A 3D Printed Micro Simulated Moving Bed Chromatography System – Development, Modeling and Application

Zur Erlangung des akademischen Grades einer
DOKTORIN DER INGENIEURWISSENSCHAFTEN (Dr.-Ing.)

von der KIT-Fakultät für Chemieingenieurwesen und Verfahrenstechnik
des Karlsruher Instituts für Technologie (KIT)
genehmigte

DISSERTATION

von
Juliane Annika Diehm, M. Sc.
aus Schwäbisch Hall

Tag der mündlichen Prüfung: 23.06.2025

Erstgutachter: Prof. Dr.-Ing. Matthias Franzreb
Zweitgutachter: Prof. Dr. Jürgen Hubbuch

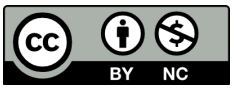

"don't let the future hold you back"

– *Laser 3.14*

Danksagung

An erster Stelle möchte ich mich ganz herzlich bei Prof. Dr.-Ing. Matthias Franzreb bedanken, der mir die Möglichkeit gegeben hat, dieses spannende Thema in seiner Gruppe zu bearbeiten. Vielen Dank für die hervorragende wissenschaftliche Betreuung, die Unterstützung in den vergangenen Jahren und den großen wissenschaftlichen Freiraum, den du mir während dieser Zeit gewährt hast. Dank dir würde ich mich jederzeit wieder für diese Promotion entscheiden.

Mein besonderer Dank gilt auch Prof. Dr. Jürgen Hubbuch für die Übernahme des Korreferats. Deine Vorlesungen haben meine Begeisterung für Chromatographie geweckt und mich letztendlich zu meinem Promotionsthema geführt.

Dem Cusanuswerk danke ich für die Förderung dieses Projekts, die weit über finanzielle Unterstützung hinausgeht.

Ein besonders großes Dankeschön gilt meinen Studenten Verena, Tim, Kai, Carolin, Rafaela, Wienke, Lennart, Ildi und David. Danke für eure Zeit, eure Ideen und Kreativität und dafür, dass ihr einen Teil meines Projekts zu eurem eigenen gemacht habt. Ohne euch hätte ich vieles nicht umsetzen können, und die Zusammenarbeit mit euch war einer der schönsten Aspekte meiner Arbeit.

Allen Kolleginnen und Kollegen in der AG Franzreb danke ich für die tolle Arbeitsatmosphäre, die gegenseitige Unterstützung und die zahlreichen Motivationskuchen – ihr seid die Besten!
Besonderer Dank gilt meinen Bürokolleginnen und -kollegen Ruijie, Tram, Magdalena, Marcel und Sefkan. Danke, dass ihr immer die Ersten wart, die sich mit mir gefreut haben, wenn ein Experiment gelungen ist, und für die vielen hilfreichen Anregungen, wenn es mal gehakt hat.
Sefkan – ich hätte mir niemanden Besseren an meiner Seite wünschen können, um die „fünf Phasen einer Doktorarbeit“ parallel zu durchleben.
Vielen Dank auch an André – von Arbeitsfragen bis „Törtchentaxi“ bist du eine der hilfsbereitesten Personen, die ich kenne, und eine riesige Bereicherung für diese Gruppe.

Der Analytikabteilung, insbesondere Frank, danke ich für die große Unterstützung bei den Massenspektrometermessungen.

Steffi, Angela und Gerald – vielen Dank, dass ihr immer ein offenes Ohr für große und kleine Anliegen habt!

A special thanks for the inspiring talks, discussions, and the encouragement goes out to all my fellow PhD students from SoCSS. It was a pleasure to meet you and I look forward to seeing you all again.

Am Ende möchte ich meinen Freunden und meiner Familie danken – ohne eure Unterstützung, egal ob wissenschaftlicher oder anderweitiger Natur, wäre diese Arbeit nach wie vor nur eine Idee und hätte ihren Weg nie zu Papier gefunden.

Gina und Till – wenn ich an Karlsruhe denke, denke ich an euch. Ohne euch wären Studium und Promotion nicht dasselbe gewesen, und es ist einfach wunderbar, Freunde wie euch zu haben, auf die man sich in jeder Situation verlassen kann. Danke, dass ihr jeden Schritt an meiner Seite wart.

Cari – du bist immer nur einen Anruf entfernt und warst schon immer mein größter Fan. Danke dafür!

Gabi, Thomas, Carina und Manu – vielen Dank für euer Intresse, wenn Chris und ich wieder in Arbeitsgespräche abgedriftet sind, und für die vielen schönen Momente, in denen wir einfach mal nicht an die Arbeit gedacht haben.

Micha – von deiner Fähigkeit, die komplexesten Sachverhalte gutverständlich erklären zu können, würde ich mir gerne eine Scheibe abschneiden. Danke, dass du ein begeisterter und überzeugter Wissenschaftler bist.

Katha – du warst schon immer mein größtes Vorbild. Dich in den letzten Jahren um mich zu haben, mich mit dir austauschen zu können und immer zu wissen, dass ich auf dich zählen kann, ist eines der größten Geschenke überhaupt.

Danke an meinen Eltern - ihr habt in mir den Spaß am Lernen entfacht und mir das Gefühl gegeben, dass ich alles schaffen kann. Danke, dass ihr immer für mich da seid und immer an mich glaubt.

Und zuletzt möchte ich Chris danken. Es ist unbezahlbar, jemanden an seiner Seite zu wissen, mit dem man über alles reden kann – danke, dass du mich verstehst, egal ob es gerade um die Arbeit geht oder nicht und immer für mich das bist – ohne dich wäre das alles die letzten Jahre unvorstellbar gewesen.

Abstract

Continuous processes offer significant advantages over batch operations in biopharmaceutical manufacturing, including reduced resource consumption, increased efficiency, and a smaller facility footprint. Despite these benefits, adoption at the production scale remains limited, even though they could significantly reduce manufacturing costs. One key obstacle is the lack of miniaturized continuous systems that can be operated over extended periods with minimal material consumption. Another major challenge is the implementation of fast and reliable process analytics to ensure consistent product quality.

Chromatography, as the primary purification step in biopharmaceutical production, plays a central role in both manufacturing and analytical workflows, and simulated moving bed chromatography (SMB) is a common continuous implementation. However, commercial lab-scale SMB systems are too large to allow for efficient early-stage process development, requiring further downscaling. This thesis aims to contribute to resource-efficient small-scale process development for continuous applications and improved process analytics by developing a 3D printed micro simulated moving bed (µSMB) chromatography system.

A key challenge in downscaling SMB systems is to minimize the system volume and its negative impact on separation performance. Unlike conventional laboratory SMB setups that employ multiple valves for flexibility, this work uses a single central valve to reduce dead volume, which was developed with 3D printing to enable the rapid prototyping of customized systems. By systematically selecting and optimizing sealing concepts, a modular and robust design was developed that withstands pressures up to 8 bar and supports rapid, flexible adaptation to different continuous multi-column processes.

A µSMB setup was built with this 3D-printed valve system and applied in two proof-of-concept studies. First, the system continuously desalted a protein using size-exclusion chromatography, achieving consistent desalting levels above 94%, and up to 99% at reduced yields. At the lowest tested feed flow rate of 15 µL/min, the process would require only 151.2 mL of sample material for a full week of continuous operation, highlighting the system's suitability for resource-efficient long-term experiments. To the best of the author's knowledge, these are the smallest SMB experiments ever conducted.

Second, the µSMB was used for continuous sample preparation in electrospray ionization mass spectrometry (ESI-MS) by continuously exchanging the buffer of a protein solution. Even with poor separation performance of the single columns, the µSMB achieved a buffer exchange of 98%,

which improved quality of MS measurements significantly. Thus, this case study demonstrates how the µSMB enables the integration of MS in a fast and reliable manner for process analytics, facilitating access to this important and powerful analytical method more effectively.

In both studies, the respective process conditions were optimized solely on the basis of chromatography column models, without accounting for system volume. The hydrodynamic effects in the µSMB's system volume differ from those in larger systems, and there is currently no suitable model capable of describing these effects (e.g., Taylor-Aris dispersion) in multi-column chromatography at a manageable computational cost. Consequently, a new approach was developed that balances precision and computational effort by reducing the dimensionality required to describe the fluidic effects from 3D to 2D by adjusting the applied flow rate profile. When considering only the system volume, this approach significantly improves results; however, in modeling the overall system, it shows no advantage over existing models. Therefore, the columns themselves appear to have a far greater impact on the entire process, and any discrepancies between simulations and experiments have to be attributed to other factors, such as transitions between columns and system volume.

Overall, these studies show that the system's performance is governed primarily by the separation efficiency of the individual columns rather than by system volume effects. Consequently, further downscaling was investigated by integrating ion-exchange monolithic capillary columns directly into the valve rotor. This reduced the channel volume in the valve from 46.7 µL to 26.8 µL and the column volume from 353 µL to 22.1 µL, which equals a reduction in column volume by more than a factor of 15 and consequently leads to a significant reduction in residence time. Under these extremely miniaturized conditions, mixing between separation zones occurred, preventing meaningful SMB operation; hence, SMB downscaling reached its limit under the given conditions. To overcome this issue, the valve's modular design was applied to investigate a different continuous multi-column setup, where the columns were operated in parallel. With this setup, promising separation results with yields above 60% and purities above 80% were achieved, suggesting that different setups should be considered for miniaturization.

The 3D-printed µSMB system presented in this thesis enables resource-efficient process development and shows great potential for process analytical technology. Due to its modular design, it can also be easily adapted to various multi-column chromatography processes beyond SMB. Thereby, it provides insights into how emerging fabrication technologies and innovative analytical methods can support the broader shift toward continuous bioprocessing. In combination with other miniaturized continuous unit operations, this system could be used for a complete miniaturized manufacturing process in the future, thus making a valuable contribution to the advancement of integrated biomanufacturing.

Zusammenfassung

Kontinuierliche Verfahren bieten zahlreiche Vorteile gegenüber Batch-Prozessen, zum Beispiel einen geringeren Ressourcenverbrauch, eine höhere Effizienz und einen kleineren Anlagen-Footprint. Dennoch werden sie bislang nur vereinzelt zur Produktion von Biopharmazeutika eingesetzt – obwohl sie maßgeblich zur Senkung der Herstellungskosten beitragen könnten. Ein Hauptgrund hierfür ist, dass es für viele Prozessschritte keine miniaturisierten Systeme in einem für die Prozessentwicklung geeigneten Maßstab gibt. Eine weitere Herausforderung stellt die Implementierung schneller und verlässlicher Prozessanalytik dar, die für die Sicherstellung einer konstant hohen Produktqualität erforderlich ist.

Chromatographie ist der zentrale Aufreinigungsschritt in biopharmazeutischen Prozessen und spielt sowohl in der Produktion als auch in der Analytik eine Schlüsselrolle. Die Simulated-Moving-Bed-Chromatographie (SMB-Chromatographie) ist ein etabliertes kontinuierliches Chromatographieverfahren, kommerziell erhältliche Laborsysteme sind allerdings zu groß für eine materialsparende Prozessentwicklung oder analytische Anwendungen und somit ist eine weitere Miniaturisierung erforderlich. Ziel dieser Arbeit ist es daher, durch die Entwicklung eines 3D-gedruckten mikro-Simulated-Moving-Bed-Chromatographiesystems (µSMB-Chromatographiesystems) zur effizienten Entwicklung kontinuierlicher Prozesse und zur Verbesserung von Prozessanalytik beizutragen.

Ein zentraler Faktor beim Downscaling von SMB-Systemen ist die Minimierung des Anlagenvolumens, da große Volumina die Trennleistung durch Dispersionseffekte negativ beeinflussen. Das Ventilsystem trägt maßgeblich zum Gesamtvolumen bei; kommerzielle Labor-SMB-Systeme verwenden meist mehrere Ventilblöcke, da so verschiedene Mehrsäulenchromatographieprozesse auf einem System implementiert werden können. In dieser Arbeit wird stattdessen ein Zentralventil genutzt, da dies das Systemvolumen deutlich verkleinert. Dieses Zentralventil wurde mittels 3D-Druck gefertigt und ist dank seines modularen Designs flexibel an verschiedene Anwendungsanforderungen und Chromatographieprozesse angepassbar. Durch die systematische Auswahl und Optimierung verschiedener Dichtkonzepte kann das Zentralventil bis zu einem Druck von 8 bar betrieben werden.

Das Ventil wurde zum Aufbau eines µSMB-Systems genutzt und in zwei Proof-of-Concept-Studien eingesetzt. Zunächst wurde das System für die kontinuierliche Entsalzung einer Proteinlösung mittels Größenausschlusschromatographie angewendet und erzielte dabei konstante Entsalzungsgrade von über 94% bzw. bis zu 99% bei reduzierten Ausbeuten. Die niedrigste getestete

Feed-Flussrate betrug 15 µL/min, was einen einwöchigen Testbetrieb mit einem Probenvolumen von lediglich 151,2 mL ermöglicht und die Fähigkeit des µSMB-Systems ressourcenschonende Langzeitexperimente durchzuführen demonstriert. Nach aktuellem Wissensstand stellen dies die kleinsten jemals durchgeführten SMB-Experimente dar.

In der zweiten Studie wurde das µSMB-System zur kontinuierlichen Probenvorbereitung für Elektrospray-Ionisations-Massenspektrometrie-Messungen genutzt, indem der Puffer einer Proteinlösung kontinuierlich ausgetauscht wurde. Trotz der begrenzten Trennleistung der Einzelsäulen wurde ein Pufferaustauschgrad von 98% erreicht, wodurch die Qualität der Massenspektrometrie-Messungen signifikant verbessert werden konnte. Dieses Ergebnis zeigt, dass das µSMB-System Massenspektrometer-Analysen auf eine einfache und zuverlässige Weise in die Prozessanalytik integrieren kann und so den Zugang zu dieser wichtigen Analysemethode erleichtert.

In beiden Studien wurden die Prozessbedingungen auf Basis von Chromatographiesäulenmodellen optimiert, wobei andere Systemkomponenten zunächst vernachlässigt wurden. Da sich die hydrodynamischen Effekte im Systemvolumen der µSMB von denen in größeren SMB-Anlagen unterscheiden, wurde untersucht, welche Auswirkungen diese Vereinfachung hat. Derzeit existiert kein Modellansatz, der diese Effekte mit einem für Mehrsäulenchromatographieprozessen vertretbaren Rechenaufwand abbilden kann. Daher wurde ein neues Modell entwickelt, der einen Kompromiss zwischen Genauigkeit und Rechenaufwand bietet, indem die Dimension, die zur Beschreibung der Strömungseffekte erforderlich ist, durch Anpassung des modellierten Flussratenprofils von drei auf zwei Dimensionen reduziert wurde. Während dieser Ansatz die Modellierung des Systemvolumens deutlich verbessert, zeigte er für das Gesamtsystem keinen Vorteil gegenüber bestehenden Modellen. Dies deutet darauf hin, dass die Trennleistung primär von den Säulen selbst und weniger vom Systemvolumen beeinflusst wird. Abweichungen zwischen Simulation und Experiment lassen sich daher eher auf andere Faktoren zurückführen, wie etwa den Übergang zwischen den Säulen und dem Systemvolumen.

Da die Trennleistung des µSMB-Systems hauptsächlich von den verwendeten Einzelsäulen abhängt, wurde untersucht, ob eine weitere Miniaturisierung möglich ist. Hierzu wurden monolithische Ionenaustausch-Kapillarsäulen direkt in den Ventilrotor integriert. Dadurch konnte das interne Ventilvolumen von 46,7 µL auf 26,8 µL und das Säulenvolumen von 353 µL auf 22,1 µL reduziert werden. Dies stellt eine Reduktion des Säulenvolumens um mehr als den Faktor 15 dar und führt folglich auch zu einer deutlichen Reduktion der Verweilzeit im System. In diesem extrem kleinen Maßstab traten unerwünschte Vermischungen zwischen den SMB-Zonen auf, die einen sinnvollen Betrieb verhinderten – das Downscaling des SMB-Prinzips hat unter diesen Bedingungen sein Limit erreicht. Um dieses Problem zu umgehen, wurde das modulare Design des 3D-gedruckten Ventils genutzt, um das System auf einen alternativen kontinuierlichen Mehrsäulenchromatographieprozess anzupassen, bei dem die Säulen parallel betrieben werden. Mit diesem Ansatz wurden vielversprechende Trennergebnisse mit Ausbeuten über 60% und Reinheiten über 80% erzielt. Dies verdeutlicht, dass das µSMB-System direkt für die Miniaturisierung von anderen kontinuierlichen Chromatographieprozessen genutzt werden kann.

Das in dieser Arbeit entwickelte 3D-gedruckte µSMB-System ermöglicht nicht nur eine ressourcenschonende Prozessentwicklung und bietet großes Potenzial für die Prozessanalytik, sondern lässt sich durch sein modulares Design auch flexibel an verschiedene Mehrsäulenchromatographieprozesse über SMB hinaus anpassen. Darüber hinaus liefert die Arbeit wertvolle Einblicke, wie neue Fertigungstechnologien und innovative Analysemethoden den Wandel hin zu kontinuierlichen Prozessen in der biopharmazeutischen Industrie unterstützen können. In Kombination mit anderen miniaturisierten kontinuierlichen Prozesseinheiten kann dieses System einen vollständigen miniaturisierten Prozess für die kontinuierliche Bioproduktion bilden und so einen wertvollen Beitrag zur Weiterentwicklung integrierter Herstellungsmethoden leisten.

Contents

List of Tables

List of Figures

List of Symbols

Latin Characters

$a_{0.1}$	min	Width of left side of the peak at 10% peak height
a_i^{wv}	g/(L · mAU)	Coefficient of calibration curve
A	(min·mg)/mL or similar	Peak area
A_i	cm	Coefficient in the van Deemter equation
A_C	m^2	Column cross-section area
$A(k)$	m^2	Column cross-section area of radial element k
$b_{0.1}$	min	Width of right side of the peak at 10% peak height
b_i^{wv}	g/L	Coefficient of calibration curve
B_i	cm^2/s	Coefficient in the van Deemter equation
BC	mL/mL	Buffer consumption
c_i	g/mL or $\mathrm{mol}/\mathrm{m}^3$	Concentration
C_i	s	Coefficient in the van Deemter equation
CVS		Column void volume per switch
d	m	Diameter
d_cap	m	Capillary diameter
d_p	m	Particle diameter
$D_{\mathrm{app},i}$	m^2/s	Apparent dispersion coefficient
$D_{\mathrm{ax},i}$	m^2/s	Axial dispersion coefficient
D_ECV	m^2/s	Dispersion coefficient in the ECV
$D_{\mathrm{m},i}$	m^2/s	Molecular diffusion coefficient
$D_{\mathrm{P},i}$	m^2/s	Pore diffusion coefficient
$D_{\mathrm{S},i}$	m^2/s	Surface diffusion coefficient
DE	%	Desalting efficiency
DL	%	Dilution
Dn		Dean number
eqV	µL	Equivalent volume
F_i		Pore accessibility coefficient, identical to $K_{\mathrm{SEC},i}$
FRD		Flow rate distribution
FRD^*		Equivalent radial flow rate distribution
h	g/mL or similar	Peak height

H_i		Henry coefficient
$HETP_i$	cm	Height of an equivalent theoretical plate
$I_{PI,t}$		Integration term of PI controller
k		Radial element
$k_{\mathrm{a},i}$	1/s	Adsorption coefficient
k_{AS}		Penalty factor of AS yield constrained
k_{BSA}		Penalty factor of BSA yield constrained
$k_{\mathrm{d},i}$	1/s	Desorption coefficient
$k_{\mathrm{film},i}$	m/s	Film transfer coefficient
$k_{\mathrm{eff},i}$	m/s	Effective film transfer coefficient
k_{h}		Penalty factor peak height
k_{I}		Tuning parameter of PI controller
k_i'		Retention factor
K_i		Equilibrium constant
k_{P}		Tuning parameter of PI controller
k_{PA}		Penalty factor peak area
k_{ret}		Penalty factor retention time
$K_{\mathrm{SEC},i}$		Partition coefficient, identical to F_i
L	cm or m	Length
L_{C}	cm or m	Column length
L_{crit}	cm or m	Critical length
L_{ECV}	cm or m	Length of the ECV
m_j		Flow rate ratio
MW_i	g/mol	Molecular weight
m/z		Mass to charge ratio
N_{ECV}		Number of grid points for DPFR models
N_i		Number of plates / column efficiency
n_{rad}		Number of radial cells
p	mbar	Pressure
$P_{\mathrm{PI},t}$	mbar	Proportional term of PI controller
P	mL/(mL·h)	Productivity
q_i	mg/mL	Loading of stationary phase
Q	µL/min or m^3/s	Volumetric flow rate
r		Radial coordinate
R		Resolution
R_{p}	cm or m	Particle radius
R^2		Regression coefficient
R_{c}	cm or m	Curvature radius
R_{cap}	cm or m	Capillary radius
Re_{p}		Reynolds number (particle)
Re_{cap}		Reynolds number (capillary)

s		Flow rate division ratio
$\dot{S}_{\text{solid},j}$	mL/min	Net movement of stationary phase in zone j
Sc		Schmidt number
t	min	Time
T		Peak asymmetry
t_0	min	Retention time of a small non-interacting tracer that can enter all pores
$t_{0,\text{int}}$	min	Retention time of a larger non-interacting tracer that can enter no pores
t_{end}	min	Overall process time
t_{inj}	min	Injection time
$t_{\text{ret},i}$	min	Retention time
$t^j_{\text{ret},i}$	min	Retention time in zone j
$t_{\text{ret},i,\text{net}}$	min	Net retention time
t_{sys}	min	System retention time
t_{s}	min	Switching time
$t_{\text{ret,max}}$	min	Maximum retention time
$t_{\text{ret,mean}}$	min	Mean retention time
u_{int}	m/s	Interstitial velocity
u_{e}	m/s	Effective velocity
u_{mean}	m/s	Mean linear velocity
V	mL	Volume
V_{C}	mL	Column volume
V_{CSTR}	mL	CSTR volume
$\dot{V}_{\text{liquid},j}$	mL/min	Net volumetric liquid flow in zone j
w_i	min or mL	Peak width
$w_{0.1}$	min or mL	Peak width at 10% peak height
y		Value of objective function
Y	%	Yield
z	cm or m	coordinate

Greek Characters

α		Selectivity
ε_{int}		Interstitial porosity
ε_{p}		Particle porosity
ε_{T}		Total porosity
η	mPa·s	Dynamic viscosity
κ		Coefficient for determination of D_{ECV}
μ_t		First moment
ρ	kg/m^3	Density

σ_t		Standard deviation
τ	min	Average residence time

Indizes & Superscripts

0	Unretained
0.1	at 10% peak height
1,2,3,4	SMB zones
a	Adsorption
A	Component A
app	Apparent
AS	Ammonium sulfate
ax	Axial
B	Component B
BSA	Bovine serum albumin
c	Curvature
cal	Calculated
C	Column
CFD	CFD simulation
CSTR	Continuously stirred tank reactor
crit	Critical
D	Diluent stream
e	effective
E	Extract stream
ECV	Extra column volume
eff	Effective
exp	Experimental
F	Feed stream
film	Film transfer
h	Height
H_2O	Water
i	Species
in	Inlet
inj	Injection
int	Interstitial
j	Zone of SMB system
m	Molecular
max	Maximum
mean	Mean
meas	Measured value
min	Minimal

net	Net
out	Outlet
p	Particle
P	Pore
PA	Peak area
PI	PI controller
R	Raffinate stream
rad	Radial
ret	Retention
s	Switching
S	Surface
SC	Sensor comparison
set	Set value
sim	Simulated
sys	System
t	Current time step
$t-1$	Last time step
T	Total
W	Waste stream
wv	Wavelength

Abbreviations

ABS	acrylonitrile butadiene styrene
AIBN	azobisisobutyronitrile
apoMb	dissociated myoglobin
AS	ammonium sulfate
BSA	bovine serum albumin
CAD	computer aided design
CADET	Chromatography Analysis and Design Toolkit
CFD	computational fluid dynamics
CIP	cleaning in place
CLIP	continuous liquid interface production
CMCC	continuous multi-column chromatography
CSS	cyclic steady state
CQA	critical quality attribute
CSTR	continuously stirred tank reactor
DBC	dynamic binding capacity
DC	direct-current
DART	direct analysis in real time
DLP	digital light processing
DMD	digital micromirror device
DPFR	dispersed plug flow reactor
DSP	downstream processing
ECV	extra column volume
EDM	equilibrium dispersive model
EGDMA	ethylene glycol dimethylacrylate
eqFRD	equivalent radial flow rate distribution
ESI	electrospray-ionization
ESI-MS	electrospray ionization mass spectrometry
FDA	Food and Drug Administration
FDM	fused deposition modeling
FFF	fused filament fabrication
FT-ICR	Fourier transform ion cyclotron resonance
FTIR	Fourier-transform infrared

GMA	glycidyl methacrylate
GRM	general rate model
GUI	graphical user interface
holoMb	native myoglobin
HPLC	high-performance liquid chromatography
HTPD	high-throughput process development
HTS	high-throughput screening
ICP-MS	inductively coupled plasma mass spectrometry
IDA	iminodiacetic acid
IEX	ion-exchange chromatography
IM	ideal model
LC	liquid chromatography
LHS	liquid handling station
mAb	monoclonal antibody
MALS	multi-angle light scattering
MALDI	matrix-assisted laser desorption/ionization
Mb	myoglobin
MCP	microchannel plate
MCSGP	multi-column countercurrent solvent gradient purification
MIR	mid-infrared
MS	mass spectrometry
MVDA	multivariate data analysis
NIR	near-infrared
PAT	process analytical technology
PCC	periodic countercurrent
PDMS	polydimethylsiloxane
PEEK	polyether ether ketone
PFR	plug flow reactor
PLA	polylactic acid
PLS	partial least squares
PP	polypropylene
PTFE	polytetrafluoroethylene
RF	radio-frequency
SEC	size-exclusion chromatography
SMA	steric mass action
SMB	simulated moving bed
TDM	transport dispersive model
TMB	true moving bed
ToF	time of flight
UF/DF	ultrafiltration/diafiltration
USP	upstream processing

UV	ultraviolet
µSMB	micro simulated moving bed

1. Introduction and Research Proposal

In 1982, the first modern biopharmaceutical product – recombinant human insulin – was approved by several regulatory agencies [1]. Less than fifty years later, a variety of biopharmaceutical modalities have emerged, including recombinant peptides and proteins (e.g., monoclonal antibodies (mAbs), growth factors, and fusion proteins), nucleic acid-based therapeutics, cell therapies, and various vaccines [2]. By 2023, eight of the top ten global drugs by sales were biopharmaceuticals, including six mAbs [3]. These therapeutics often address previously unmet medical needs, targeting conditions that were once considered untreatable [4].

Despite these remarkable achievements, biopharmaceuticals are often criticized for their high cost [5–7]. Consequently, there is an ongoing discussion about the need to radically change production strategies to increase cost efficiency while maintaining high product quality standards [8]. With increasing product titers in recent years, the focus on efficient process strategies has shifted from upstream processing (USP) to downstream processing (DSP) [9]. As chromatography is one of the most frequently applied unit operations in DSP, there is growing interest in optimizing chromatographic steps [10].

A prominent concept for enhancing manufacturing efficiency is the transition from batch to continuous processes, as it addresses several challenges simultaneously: Implementing continuous manufacturing can increase a facility's output by a factor of ten, enabling either higher production quantities or the option to scale down manufacturing units for greater flexibility [11]. Moreover, continuous processing reduces facility downtime, ensures consistent product quality without batch-to-batch variability, enhances process efficiency, lowers overall manufacturing costs, and reduces the environmental footprint of production [11–13].

Continuous chromatography processes have been successfully implemented in the petrochemical [14] and sugar industry [15], among others. Numerous case studies also demonstrate the benefits of continuous manufacturing of biopharmaceuticals [12,16,17], nevertheless, continuous processes remain the exception rather than the norm in industrial biopharmaceutical production.

One major obstacle is that current lab-scale systems are too large to conduct long-term studies with a reasonable product amounts, as the increased throughput of continuous chromatography makes them too material-intensive for early-stage process development. Among other factors, the absence of readily available scale-down equipment has been identified as a key barrier to the transition from batch to continuous manufacturing [11].

Another major challenge for the implementation of continuous processes is the availability of reliable process analytics. In continuous manufacturing, process analytical technology (PAT) is essential to ensure high product quality through real-time monitoring and active process control [13]. Yet, widely used PAT applications typically exclude the most common off-line analytics, such as high-performance liquid chromatography (HPLC) or mass spectrometry (MS), due to long analysis times and the need for sample pre-processing [18]. Still, these methods could play a crucial role in monitoring critical quality attributes (CQAs), especially in the context of real-time release [19]. Miniaturized systems offer a promising solution by significantly reducing analysis time, making these techniques more accessible for PAT applications [11].

In recent years, 3D printing has emerged as a powerful technology for the rapid prototyping of customized, miniaturized systems [20, 21]. The ongoing development of new printable materials continues to expand its applications in biological and chemical research [22]. By enabling the fabrication of complex parts with integrated channel systems, 3D printing is increasingly being used for microfluidic systems [21, 23]. However, its potential to manufacture miniaturized continuous chromatography systems remains largely unexplored.

This thesis seeks to address the current lack of miniaturized continuous chromatography systems with 3D printing by answering the following central research questions:

- Can 3D printing bridge the existing gap in miniaturized continuous chromatography equipment and enable the rapid prototyping of application-specific miniaturized process equipment?
- Can continuous chromatography processes be scaled down to the extent that they enable resource-efficient process development?
- Can these miniaturized systems be effectively used for PAT applications, and do they add value to the existing pool of PAT tools and process monitoring technologies?

To answer these questions, simulated moving bed (SMB) chromatography, one of the most widely applied continuous chromatography processes, is used as a case study. First, critical system components for miniaturized SMB setups are identified, and suitable 3D printing manufacturing procedures are developed in Chapter 4. In Chapter 5, it is investigated whether downscaling to the micro-scale is feasible by conducting a proof-of-concept study using the system for continuous protein desalting. After successful proof-of-concept, the system's potential as a PAT tool is investigated by applying it to continuous sample pre-processing for MS analysis in Chapter 6. Finally, in Chapter 7 a detailed system model is built to increase process understanding and improve process optimization. The focus of this study is on the modeling of the system volume, as hydrodynamics and other effects often differ in miniaturized systems, complicating knowledge transfer during scale-up.

2. State of the Art and Theoretical Background

This chapter provides the theoretical foundations and reviews the current state of the art relevant to this work. The primary focus is chromatography, the core methodology employed in this work. While other unit operations are of relevance in continuous manufacturing, they fall outside the scope of this thesis.

Section 2.1 covers the fundamentals of both single-column and continuous multi-column chromatography, with particular emphasis on SMB chromatography. It also discusses key chromatographic parameters, modeling approaches, and provides a brief overview of existing miniaturized chromatography systems. Section 2.2 introduces common PAT methods, focusing on electrospray ionization mass spectrometry (ESI-MS), which, although not widely adopted for PAT in DSP, plays a central role as an analytical tool in this work. Finally, Section 2.3 provides a concise overview of the 3D printing technologies utilized in this thesis, emphasizing the role as a key enabling technology.

2.1 Chromatography

Liquid chromatography (LC) is a process in which substances are separated based on their specific interactions with a liquid mobile phase and a solid stationary phase [24]. Typically, the stationary phase consists of functionalized, porous particles in the micrometer size range that are packed into a cylindrical housing (the chromatography column) through which the mobile phase flows. Alternatively, functionalized monoliths, membrane adsorbers, or fibers can also be used as stationary phases [24].

LC is currently the most applied purification method in biopharmaceutical DSP [25]. It is used for various product classes, including mAbs [26], virus-like particles [27], and oligonucleotides [28], for different purification steps, ranging from capture to polishing [26]. This broad applicability is achieved through the targeted use of different interactions with functional groups on the stationary phase's surface, resulting in various chromatography modes, e.g., affinity, ion-exchange, hydrophobic interaction, mixed-mode, and reversed phase chromatography [24].

Besides the mode of interaction, LC can be categorized by other criteria, as illustrated in Figure 2.1. One classification is based on the elution mode. In isocratic elution, the mobile phase

composition is constant throughout the separation process, making it primarily suitable for solutes with weak interactions with the stationary phase. Strong interactions typically require changes in mobile phase composition to weaken binding and facilitate elution. This change can be done either stepwise (step elution) or as a gradient (linear gradient elution). In ion-exchange chromatography, for example, pH or salt concentration are usually adjusted for elution [24].

A typical gradient elution batch chromatography process in biopharmaceutical production consists of several consecutive steps: During equilibration, the stationary phase is flushed with a buffer to ensure that the stationary phase is in the desired binding condition. Second, the sample is injected into the mobile phase flow and onto the column, followed by optional washing steps with different buffers to remove undesired contaminants while the product is bound to the stationary phase. Next, the product(s) is/are eluted from the column, followed by optional washing and cleaning in place (CIP) steps [29]. The main focus of this work is on isocratic chromatography with size-exclusion chromatography (SEC).

SEC (sometimes also referred to as gel permeation chromatography) differs from other chromatography modes because separation is based on the hydrodynamic radius of the solutes rather than their interactions with the stationary phase. On the contrary, the stationary and mobile phase are deliberately selected to minimize (ideally eliminate) any binding between the sample and the stationary phase. Instead, the stationary phase contains a network of pores of varying sizes. Molecules with a small hydrodynamic radius can access a greater portion of this network compared to molecules with a larger hydrodynamic radius, which cannot enter the smaller pores, resulting in a shorter retention time; consequently, in SEC, molecules elute from largest to smallest [24, 30, 31].

The following sections outline the theoretical foundations essential for developing and modeling an SEC-based SMB process. Key parameters of batch chromatography are introduced first, followed by an overview of continuous chromatography processes and relevant modeling approaches. Finally, chromatography miniaturization is briefly introduced.

2.1.1 Parameters

Chromatography processes are characterized by parameters that depend on the chromatography column, the components that are to be separated (also referred to as solutes), and the overall system [24]. These parameters play an important role for the selection of suitable separation systems and subsequent process optimization. Component dependent parameters, such as the molecular weight/hydrodynamic radius or net charge, determine which chromatography methods are suitable for separation [24]. These parameters are often highly influenced by mobile phase properties, such as pH and conductivity, and must therefore be considered in the context of the entire system [24].

Column dependent parameters include the dimensions of the column, the (mean) particle size of the stationary phase, the porosity of the stationary phase, often referred to as the particle porosity ε_p, the interstitial porosity ε_int, meaning the void volume between the particles of the stationary phase, and the total porosity ε_T, describing the total void volume of the column [24].

Figure 2.1: Overview of different ways to categorize liquid chromatography with examples in each category.

The Chromatogram and Derived Parameters

While some of the parameters are easily measurable and usually provided by the column manufacturer, like the geometrical dimensions, the porosities often have to be determined with tracer experiments.

A pulse of a tracer molecule that does not interact with the stationary phase and is too large to enter the particle pores is injected into the mobile phase flow to determine ε_{int} from the resulting peak's retention time $t_{0,\text{int}}$ according to (2.1) with the volumetric flow rate of the mobile phase Q and the column volume V_{C}. Similarly, ε_{T} can be determined using a small, non-interacting tracer that can access the whole pore volume, using the retention time t_0 according to (2.2). ε_{p} can be derived with the two other porosities according to (2.3) [24].

$$\varepsilon_{\text{int}} = \frac{t_{0,\text{int}} \cdot Q}{V_{\text{C}}} \tag{2.1}$$

$$\varepsilon_{\text{T}} = \frac{t_0 \cdot Q}{V_{\text{C}}} \tag{2.2}$$

$$\varepsilon_{\text{p}} = \frac{\varepsilon_{\text{T}} - \varepsilon_{\text{int}}}{1 - \varepsilon_{\text{int}}} \tag{2.3}$$

The different porosities are important parameters for the design of a chromatography process, as they have a direct impact on the accessible volume of the different components and hence

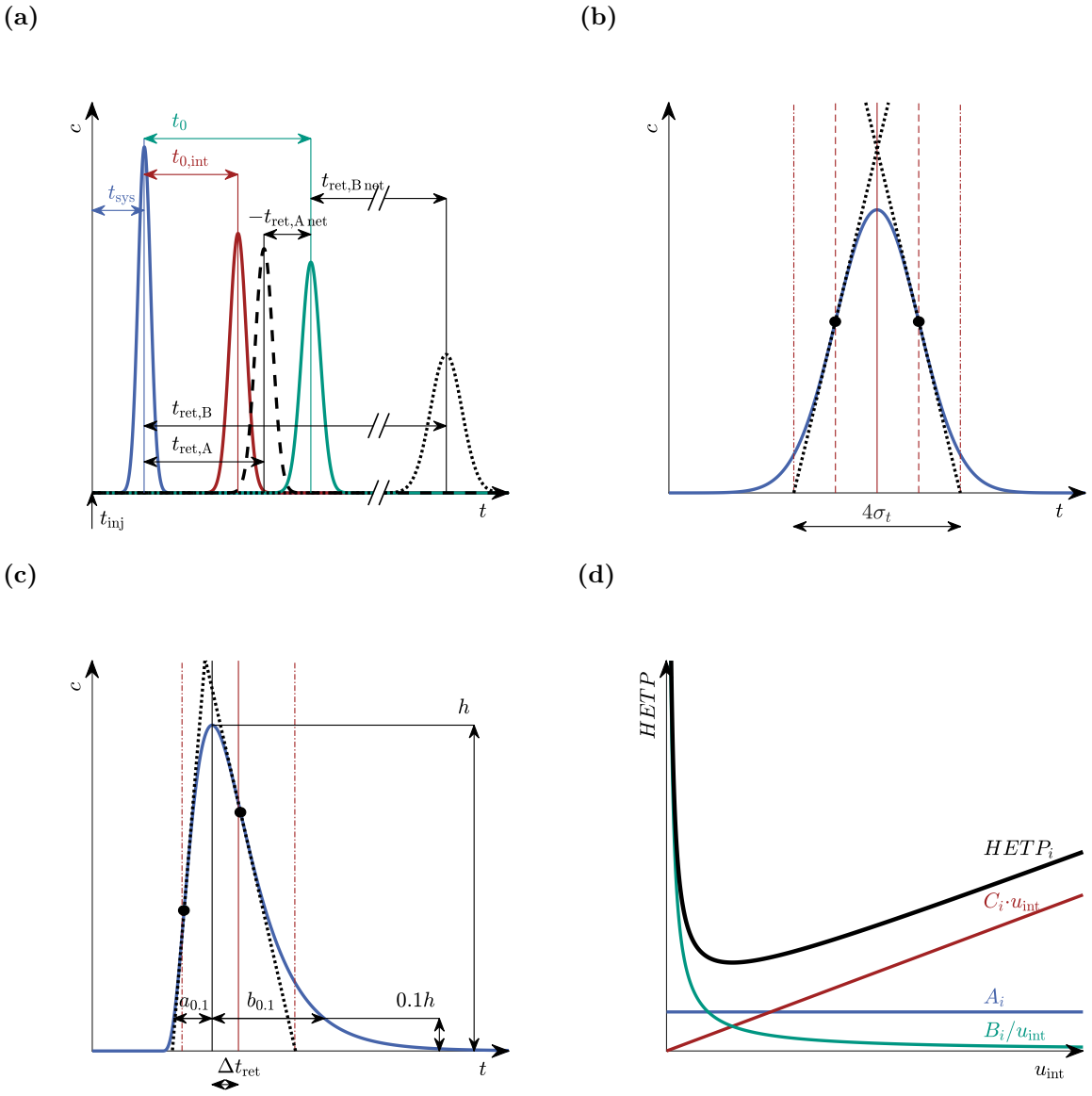

Figure 2.2: (a) Chromatogram with system retention time (blue), retention time of a large (red) and small (green) unretained molecule as well as retention time of a non-interacting (dashed black line) and interacting (dotted black line) molecule. Chromatogram of a symmetrical (b) and asymmetrical (c) peak, with center of area (red line), one standard deviation from center of area (dashed red line), two standard deviations from the center of area (dashed dotted red line), peak maximum (black line), inflection points, and inflection point tangents (dotted lines). (d) Van Deemter plot.

on retention time and are of particular relevance in SEC, where the retention time of all (non-interacting) components is always between $t_{0,\text{int}}$ and t_0 [32].

The chromatogram, which represents the time-dependent concentration $c_i(t)$ of solutes at the column outlet, is the primary tool for the determination of chromatography parameters. It is recorded with a suitable detection method, mostly ultraviolet (UV) absorbance [24]. Figure 2.2a illustrates an exemplary chromatogram for the determination of t_0 and $t_{0,\text{int}}$. Due to dispersion effects in the system and the column, a rectangular pulse injection results in a peak shaped outlet profile, which is often approximated as a Gaussian distribution. In this case, the retention time of the different solutes can be determined with the respective peak maximum. The retention time of the chromatography system (without chromatography column) t_{sys} has also to be identified for a correct evaluation. This is usually done by performing tracer experiments with a zero-dead-volume connector instead of the chromatography column [24].

A useful metric is the net retention time $t_{\text{ret},i,\text{net}}$, which accounts for the retention time relative to a non-interacting solute that can access the entire pore volume [24]. Figure 2.2a exemplifies peaks for both a non-interacting component (A, SEC) and a retained component (B). In SEC, non-interacting solutes exhibit negative net retention times since they cannot access the full pore volume. Under isocratic conditions, peak height typically decreases, and peak width increases with longer retention times due to dispersion effects in the column, leading to stronger sample dilution [24].

Besides the retention time, the peak width is an important parameter to determine the separation performance of a chromatography process. Figure 2.2b depicts a peak with Gaussian distribution where the peak width is usually approximated by multiplying the standard deviation σ_t by a factor of 4 [24], covering 95.4% of the total peak area [33]. Graphically, the peak width can be determined at the intersection point of the inflection point tangents with the baseline, as depicted in Figure 2.2b. The inflection points have a distance of σ_t to the peak center [24, 34].

However, in practical applications, chromatographic peaks are often asymmetrical and do not strictly follow a Gaussian distribution, as shown in Figure 2.2c. In such cases, the first moment μ_t (2.4) of the peak provides a more accurate measure of retention time, representing the center of the peak area. In Figure 2.2c, Δt_{ret} depicts the difference in retention time determined with the peak maximum and the first moment. Similarly, σ_t can be calculated with the second moment of the distribution according to (2.5) [24, 34]. As depicted in Figure 2.2c, the resulting peak width is not identical to the one graphically determined using the inflection points and both account for less than 95.4% of the peak area in the depicted example.

$$\mu_t = \frac{\int_0^\infty t \cdot c(t)\mathrm{d}t}{\int_0^\infty c(t)\mathrm{d}t} \tag{2.4}$$

$$\sigma_t^2 = \frac{\int_0^\infty (t-\mu_t)^2\, c(t)\mathrm{d}t}{\int_0^\infty c(t)\mathrm{d}t} \tag{2.5}$$

The peak width w at a specific height h, such as at 10% of the peak height ($w_{0.1}$), is often used instead. The peak asymmetry T assesses how well a peak conforms to a Gaussian distribution. It is calculated with the ratio of the peak widths $a_{0.1}$ and $b_{0.1}$ measured from the peak maximum

according to (2.6). The peak asymmetry of a non-interacting solute is often used as general measure for the quality of the chromatography bed [24].

$$T = \frac{b_{0.1}}{a_{0.1}} \tag{2.6}$$

Isotherm and Kinetics

Two characteristics, the isotherm and kinetic, are usually acquired to characterize the interactions of a component with the stationary phase under specific conditions. The isotherm describes the ratio between the concentration of the component in the mobile phase to the component bound to the stationary phase under equilibrium conditions, while the kinetic describes the time required to reach equilibrium. In many cases, the kinetic is neglected, because it is assumed that adsorption and desorption processes during the chromatography experiment happen fast and are not time limiting [24].

There are various isotherm models that differ greatly in their complexity. The simplest is the Henry isotherm, which assumes a linear relationship between the concentration of a component i in the mobile phase c_i and the resulting loading of the stationary phase q_i according to (2.7). The Henry constant H_i (sometimes also named the equilibrium constant K_i) is a measure of the affinity of the respective component to the stationary phase, the higher H_i, the higher the affinity to the stationary phase [24].

$$q_i = H_i c_i \tag{2.7}$$

Equation (2.7) is in quasi-stationary form. If the kinetic of the adsorption process is to be considered, the kinetic form of the isotherm (2.8) with the adsorption coefficient $k_{\mathrm{a},i}$ and desorption coefficient $k_{\mathrm{d},i}$ can be applied. The adsorption and desorption rates are linearly correlated with the equilibrium constant (2.9). Alternatively, different kinetic models, such as the linear driving force model, can be used [35].

$$\frac{\mathrm{d}q_i}{\mathrm{d}t} = k_{\mathrm{a},i} c_i - k_{\mathbf{d},i} q_i \tag{2.8}$$

$$K_i = \frac{k_{\mathrm{a},i}}{k_{\mathrm{d},i}} \tag{2.9}$$

The Henry isotherm is primarily used for analytical purposes, as many systems follow this linear correlation at low concentrations as it is favored for quantitative analysis [24].

Another frequently applied isotherm model is for example the Langmuir isotherm, which features a maximum loading capacity besides the equilibrium constant. If several components interact, this isotherm can also be defined in a multi-component form [24]. For ion-exchange chromatography, the steric mass action (SMA) isotherm is often used, as it additionally includes the salt displacement effects and shielding effects of the bound component on the stationary phase's surface [24, 36].

There are different methods to determine the isotherm parameters. In case of the linear isotherm, the Henry constant can be calculated from the solute's retention time relative to the one of a small, non-interacting component according to (2.10) [24].

$$H_i = \left(\frac{t_{\mathrm{ret},i}}{t_0} - 1 \right) \frac{\varepsilon_\mathrm{T}}{1 - \varepsilon_\mathrm{T}} \tag{2.10}$$

In case of SEC, however, this equation leads to a negative Henry constant. This results from the definition of the net retention time as depicted in Figure 2.2a as the sum of the retention time of a non-interacting component and a retention, which increases linearly (in this case) with the equilibrium constant [37]:

$$t_{\mathrm{ret},i} = t_0 + H_i \cdot t_0 \frac{1 - \varepsilon_\mathrm{T}}{\varepsilon_\mathrm{T}} \tag{2.11}$$

In SEC, $t_{0,\mathrm{int}}$ is more appropriate representative of the retention time of a non-interacting component compared to t_0, since not all components can access the whole pore volume. Thus, (2.11) must be adapted to:

$$t_{\mathrm{ret},i} = t_{0,\mathrm{int}} + K_{\mathrm{SEC},i} \left(t_0 - t_{0,\mathrm{int}} \right) \tag{2.12}$$

$K_{\mathrm{SEC},i}$ is the partition coefficient that is often used instead of H_i for SEC and is a measure for the pore volume accessible to a component; it always has a value between 0 and 1 [32]:

$$K_{\mathrm{SEC},i} = \frac{t_{\mathrm{ret},i} - t_{0,\mathrm{int}}}{t_0 - t_{0,\mathrm{int}}} \tag{2.13}$$

For other isotherms, the process of parameter determination is more elaborate, and there are several approaches to determine the parameters with either static or dynamic methods [24].

Performance Parameters

There are several parameters that are widely applied to assess the separation performance of chromatography processes. The retention factor k_i' describes the retention of a solute relative to a non-interacting component according to (2.14). It depends on the distribution of the solute between the stationary and mobile phase and enables the evaluation of the retention behavior independent of the chosen mobile phase flow rate [24].

$$k_i' = \frac{t_{\mathrm{ret},i} - t_0}{t_0} \tag{2.14}$$

Another important parameter is selectivity α, which is the ratio of retention factors between two solutes (2.15), alternatively it can be calculated based on the Henry coefficients (2.16). It provides an initial assessment whether the interaction with the stationary phase differs between the solutes and hence whether the investigated method is suitable for the separation process [24].

$$\alpha = \frac{k'_{\mathrm{B}}}{k'_{\mathrm{A}}} = \frac{t_{\mathrm{ret,B}} - t_0}{t_{\mathrm{ret,A}} - t_0} \tag{2.15}$$

$$\alpha = \frac{H_{\mathrm{B}}}{H_{\mathrm{A}}} \tag{2.16}$$

However, a difference in net retention time alone is not sufficient for an efficient separation process, the peak width w must also be considered. The resolution R (2.17) combines the information of retention time and peak width and depends on the selectivity, retention factors and column efficiency. For Gaussian peaks, a resolution of 1.5 equals a baseline separation, meaning both components are completely separated. At lower resolutions, there is still an overlapping peak area, e.g., of 3% at a resolution of 1, meaning that this amount of product will not be purified in the process. Chromatography processes are typically optimized to operate close to baseline separation since lower resolutions decrease either yield or purity, while higher resolutions reduce efficiency [24].

$$R = \frac{2\left(t_{\mathrm{ret,B}} - t_{\mathrm{ret,A}}\right)}{w_{\mathrm{A}} + w_{\mathrm{B}}} \tag{2.17}$$

According to (2.17), a smaller peak width enables the separation of components with a smaller difference in retention times, hence, it is desirable to keep the peak width as low as possible. The peak width is increased by different dispersion effects occurring in the chromatography system as well as in the chromatography column. The ability of a column to produce narrow peaks, also referred to as the column efficiency, can be quantified with the plate number N_i, where a high plate number equals a high column efficiency. N_i can be calculated with the first and second moment of a peak (2.18) and can be converted to the height equivalent to a theoretical plate $HETP_i$ by dividing the column length L_{C} by N_i (2.19). $HETP_i$ is a sum parameter for different dispersion effects occurring in the column, and is further discussed in the next paragraph [24].

$$N_i = \frac{\mu_{t,i}^2}{\sigma_{t,i}^2} \tag{2.18}$$

$$HETP_i = \frac{L_{\mathrm{C}}}{N_i} \tag{2.19}$$

Van Deemter Equation

The van Deemter equation (2.21) describes the impact of different dispersion effects on $HETP_i$ as a function of the interstitial flow velocity u_{int} [38]. u_{int} can be derived from the volumetric flow rate with the column cross section area A_{C} and $\varepsilon_{\mathrm{int}}$ according to (2.20) [24]. The van Deemter equation features three different terms (2.21): The A-term is the Eddy diffusion, which describes dispersion caused by molecules taking different paths through the packed bed. Eddy diffusion is a stochastic process; thus, it is independent of the flow rate. Instead it is proportional to the particle diameter and can hence be reduced with the usage of small particles. The B-term describes the influence of longitudinal diffusion on overall dispersion. It increases with decreasing flow rate due to a longer residence time in the column. The C-term describes the mass transfer

resistance. It increases with increasing flow rate, as there is less time for components to diffuse into the pores of the particles of the stationary phase, resulting in different interaction times of molecules with the stationary phase [24, 38].

$$u_{\text{int}} = \frac{Q}{A_{\text{C}} \cdot \varepsilon_{\text{int}}} \tag{2.20}$$

$$HETP_i = A_i + \frac{B_i}{u_{\text{int}}} + C_i \cdot u_{\text{int}} \tag{2.21}$$

Figure 2.2d gives a graphical representation of the different terms and the resulting $HETP_i$ in dependence of the flow rate. It can be clearly seen that there is an optimal flow rate for efficient operation of a chromatography process, however, in preparative chromatography, the columns are commonly operated at higher flow rates under non-optimal conditions to increase the productivity [24].

2.1.2 Continuous Chromatography

Although batch chromatography remains the state-of-the-art separation method in DSP of biopharmaceuticals, significant performance enhancements can be achieved with continuous, countercurrent operation. This approach increases resin utilization while minimizing product loss, reduces mobile phase consumption, and enhances overall process productivity [10]. There are different approaches to performing chromatography in a quasi- or semi-continuous mode, which are outlined in the following sections.

2.1.2.1 Simulated Moving Bed Chromatography

Theoretically, chromatography can be operated in a continuous countercurrent mode, as illustrated in Figure 2.3. With this concept, known as true moving bed (TMB) chromatography, a binary mixture of components A and B, where B interacts stronger with the stationary phase than A, is continuously separated by moving the stationary phase countercurrent to the mobile phase. The velocity of the stationary phase is chosen between the propagation velocities of the two components, consequently, the resulting net velocities of the two components are in different directions in relation to the feed inlet, and the weaker interacting component A is transported with the mobile phase and the stronger interacting component B is transported with the stationary phase in the opposite direction. This way, the purified components can be continuously

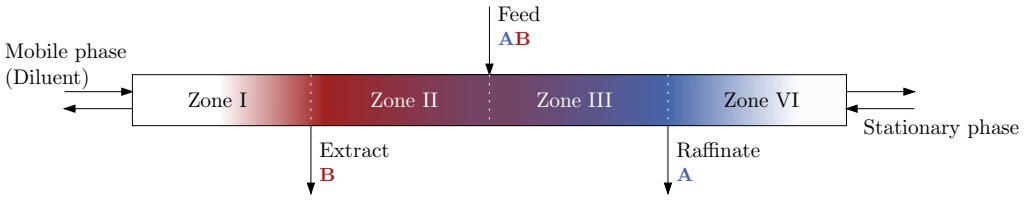

Figure 2.3: The TMB principle: an indefinitely long stationary phase with the feed inlet at its center is transported in opposite direction to the mobile phase flow. The flow rates of stationary and mobile phase are chosen in a manner that the net flow rates of the two components in the feed stream are in opposite directions, resulting in a continuous binary separation.

collected at the raffinate port (component A) and extract port (component B). In total, a TMB system has two inlet ports, the mobile phase (diluent/eluent) and the feed inlet, as well as two outlets, the raffinate and extract streams. The addition and withdrawal of these streams divide the system into four distinct zones with varying mobile phase flow rates, each with a specific role in the separation process. Despite its theoretical advantages, the TMB concept has limited practical applications due to the difficulty of physically moving the stationary phase without compromising packing integrity or causing excessive abrasion [39, 40].

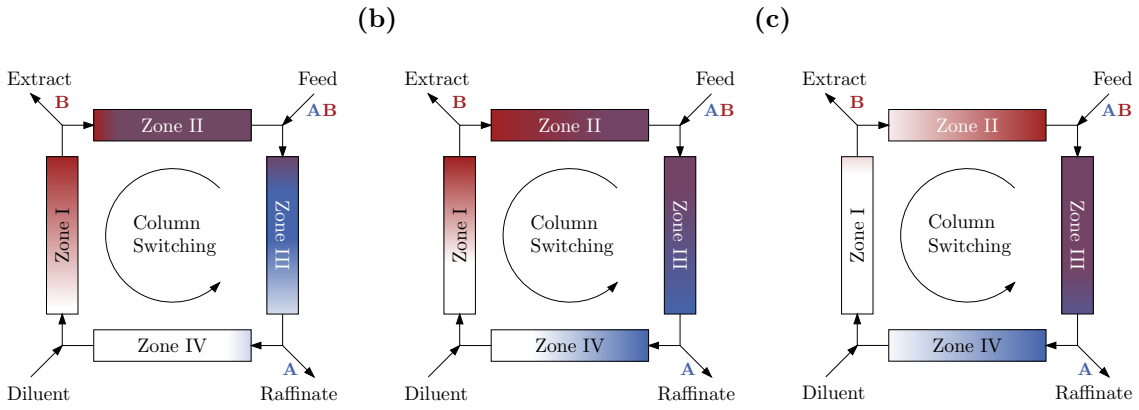

Figure 2.4: The SMB principle: the indefinite long stationary phase of a TMB process and its continuous movement is approximated by using separate columns for each zone. Depicted are the concentration profiles of two components A and B, where A is the less retained component, during cyclic steady state at the beginning (a), middle (b) and end (c) of a switching interval.

Instead, SMB is the practicable alternative to TMB processes that has been established for many industrial processes [40]. The first commercial SMB processes, the Sorbex processes, were introduced in the 1960s by Universal Oil Products, for example for the separation of para-xylene from aromatic hydrocarbon mixtures [14, 40, 41]. Today, SMB is widely used not only in the petrochemical industry but also in sugar processing [15] and pharmaceutical applications [39], particularly for enantiomer separations [42].

Unlike TMB, SMB does not require the continuous movement of the stationary phase. Instead, the packed bed is divided into multiple sections, typically using separate chromatography columns. The countercurrent movement between the stationary and mobile phases is simulated by periodically shifting either the positions of the columns in the opposite direction to the mobile phase flow or the inlets and outlets in the direction of the mobile phase flow. This periodic switching results in a semi-continuous operation that does not reach a true steady state but instead operates under a cyclic steady state, where outlet concentrations fluctuate periodically [39,40,43].

Similar to TMB, SMB processes are typically operated in an isocratic mode for the separation of binary mixtures with an identical four-zone configuration. Each of these zones fulfills a certain role during the process: the separation process takes place in zones II and III, zone I is for the regeneration of the stationary phase while zone IV is for the regeneration of the mobile phase [39, 40].

The principle of the process is depicted in Figure 2.4, showing the concentration profiles of the two components at the beginning (Figure 2.4a), the middle (Figure 2.4b), and the end

(Figure 2.4c) of a switching interval. An example concentration profile of the components at the end of a switching interval is also depicted in Figure 2.5a, while Figures 2.5b and 2.5c show the resulting outlet profiles of both components at the raffinate and extract port. The outlet profiles show the start-up behavior of the process as well as the cyclically repeating peak shapes in cyclic steady state. In both outlets, the switching of the columns leads to an abrupt change in the outlet concentration. Notably, component A reaches the raffinate outlet within the first switching cycle, whereas component B requires two column switches before appearing in the extract stream. In the depicted example, the concentration of component B does not reach zero in zone IV, resulting in an impure raffinate stream; the process parameters need to be adapted to improve the raffinate purity. A basic concept for the determination of process parameters of SMB processes is discussed in the next paragraph.

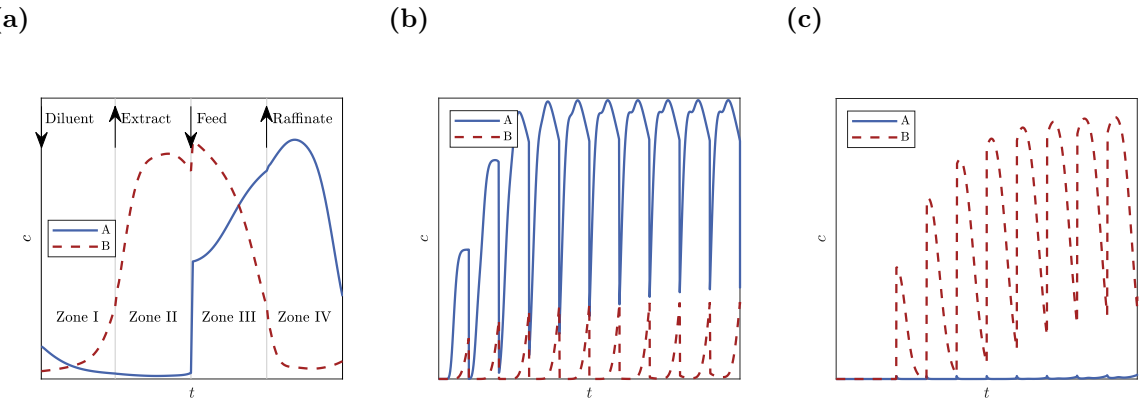

Figure 2.5: (a) Concentration profile of components A and B in the different zones right before the next switching. Outlet concentration profiles of A and B in the raffinate (b) and extract (c) stream during the first ten switching steps (2.5 cycles).

Process Point Determination

Certain conditions have to be met for each SMB zone to function effectively: For a complete regeneration of the stationary phase in zone I, all components have to be eluted from the column before the columns are switched or, in other words, the retention time of the component has to be shorter than the column switching time t_s. Since component B has a longer retention time than A, component A can be neglected for process optimization in this zone. In zones II and III, where the separation of the components takes place, component A has to elute completely while component B is retained, meaning t_s has to be between their retention times. In zone II, the condition for completely eluting component A is critical, as remaining component A will contaminate the extract stream after switching, while for zone III the complete retention of component B ensures a pure raffinate stream. In zone IV all components have to be retained completely for the regeneration of the mobile phase. In contrast to zone I, component A is the critical component in this case. The conditions described here are summarized in Equations (2.22)-(2.25) [44, 45].

$$t^1_{\mathrm{ret,B}} < t_\mathrm{s} \tag{2.22}$$
$$t^2_{\mathrm{ret,A}} < t_\mathrm{s} < t^2_{\mathrm{ret,B}} \tag{2.23}$$
$$t^3_{\mathrm{ret,A}} < t_\mathrm{s} < t^3_{\mathrm{ret,B}} \tag{2.24}$$
$$t_\mathrm{s} < t^4_{\mathrm{ret,A}} \tag{2.25}$$

In a four zone SMB process, five independent parameters can be adjusted to fulfill these conditions: the flow rates of the diluent Q_D, extract Q_E, feed Q_F, and raffinate Q_R stream as well as t_s. Several methods exist for determining a suitable process point, with the triangle theory being the most common one [39, 46, 47]. Alternative approaches include the standing wave design [48] and various (model based) optimization methods [49].

The triangle theory assumes ideal chromatography without dispersion or peak broadening and was developed for linear (Henry) and non-linear (e.g., Langmuir) isotherms [47, 50]. Its key advantage is that required parameters, such as column porosities and retention times, can be determined from single-column batch chromatography experiments.

Generally, the mean retention time of a component can be calculated with the first moment of an outlet concentration profile according to (2.4). In case of ideal chromatography, this can be simplified to [34]:

$$t_{\mathrm{ret},i} = \mu_1 = t_0 \left[1 + \frac{1-\varepsilon_\mathrm{T}}{\varepsilon_\mathrm{T}} \frac{\partial q_i}{\partial c_i}\right] \tag{2.26}$$

In the case of a linear isotherm, the change of loading of the stationary phase with mobile phase concentration can be replaced with the Henry coefficient [24]:

$$\frac{\partial q_i}{\partial c_i} = H_i \tag{2.27}$$

With (2.22), this leads to the following equation for component B in zone I:

$$t^1_{\mathrm{ret,B}} = t_0 \left[1 + \frac{1-\varepsilon_\mathrm{T}}{\varepsilon_\mathrm{T}} H_\mathrm{B}\right] < t_\mathrm{s} \tag{2.28}$$

Rearranging to H_B and expanding with V_C results:

$$\begin{aligned} H_\mathrm{B} &< \frac{\frac{V_\mathrm{C}\varepsilon_\mathrm{T}}{t_0} t_\mathrm{s} - V_\mathrm{C}\varepsilon_\mathrm{T}}{V_\mathrm{C}\left(1-\varepsilon_\mathrm{T}\right)} \\ &= \frac{Q_1 - \frac{V_\mathrm{C}\varepsilon_\mathrm{T}}{t_\mathrm{s}}}{\frac{V_\mathrm{C}(1-\varepsilon_\mathrm{T})}{t_\mathrm{s}}} \\ &= \frac{\dot{V}_{\mathrm{liquid},1}}{\dot{S}_{\mathrm{solid},1}} = m_1 \end{aligned} \tag{2.29}$$

m_j is defined as the ratio of net volumetric liquid flow in zone j $\dot{V}_{\text{liquid},j}$ to the net movement of stationary phase $\dot{S}_{\text{solid},j}$ in the opposite direction [46]. The portion of the mobile phase that is in the pores of the chromatography column during the switching process is moved with the stationary phase in the opposite direction to the mobile phase flow, hence $\dot{V}_{\text{liquid},j}$ is always smaller than Q_j [50]. The inequalities for all zones can be derived in the same way:

$$H_{\text{B}} < m_1 \tag{2.30}$$

$$H_{\text{A}} < m_2 < m_3 < H_{\text{B}} \tag{2.31}$$

$$-\frac{\varepsilon_{\text{T}}}{1-\varepsilon_{\text{T}}} < m_4 < H_{\text{A}} \tag{2.32}$$

m_3 is always greater than m_2 as the feed stream is added between the zones and hence Q_3 is greater than Q_2 [46]. Theoretically, m_1 has no upper limit, but in practice, it is limited by the maximum linear velocity recommended for the used chromatography columns. Also, for an efficient process with low buffer consumption, it is favorable to chose a small m_1 [50]. The lower limit of m_4 is derived by setting Q_4 to zero, resulting in no recycling of the mobile phase [46].

Suitable m_j-values can be chosen with the triangle plot, see Figure 2.6, which also gives the procedure its name. When plotting m_3 over m_2 (Figure 2.6a), a triangle is formed in which (2.31) is fulfilled and both components are pure in the extract and raffinate stream, respectively [46]. The apex of the triangle (point c) indicates the point with the highest productivity, but this point is also the most susceptible for fluctuations to impact purity. In contrast, process points close to the diagonal are less efficient but more robust [24]. Similarly, m_1 and m_4 can be plotted to determine a process point with sufficient regeneration of the mobile and stationary phase (Figure 2.6b), with a rectangle giving the area of complete regeneration and point (d) being the most efficient process point [24, 45].

By selecting suitable values for all m_js and one other parameter, e.g., the feed flow rate that is often predetermined by the process, all other process parameters can be determined using the definition of m_j (2.29) and the node mass balances link the internal flow rates to the external ones (2.33)-(2.36) [45].

$$Q_1 = Q_4 + Q_{\text{D}} \tag{2.33}$$

$$Q_2 = Q_1 - Q_{\text{E}} \tag{2.34}$$

$$Q_3 = Q_2 + Q_{\text{F}} \tag{2.35}$$

$$Q_4 = Q_3 - Q_{\text{R}} \tag{2.36}$$

However, as mentioned before, the triangle theory is based on an ideal chromatography model, neglecting all dispersion effects. Consequently, safety margins are frequently applied when selecting a process point to ensure sufficient product purity [24]. Additionally, processes are further optimized based on criteria such as the product purity or the yield in the respective streams,

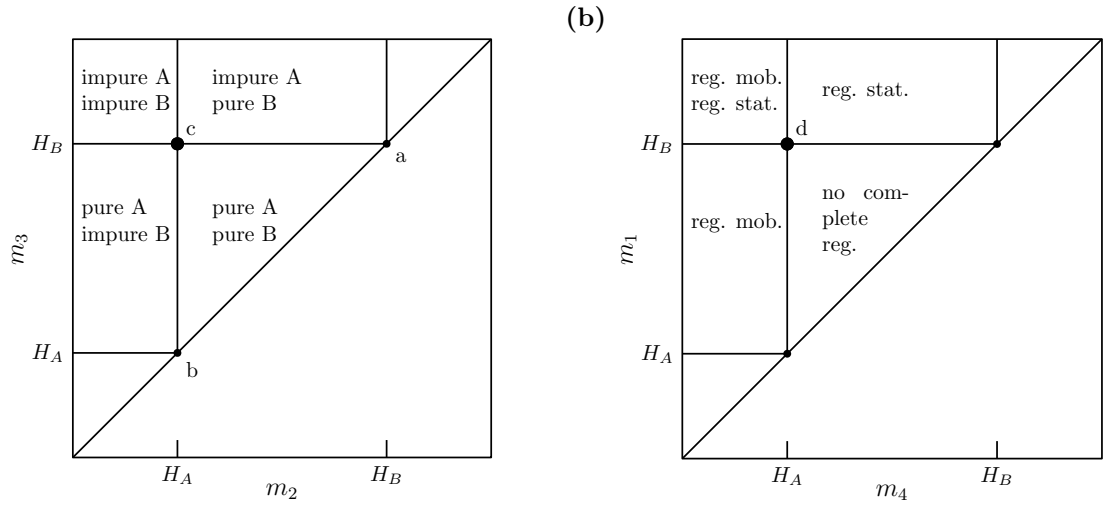

Figure 2.6: Triangle plot for m_2/m_3 (a) and m_4/m_1 (b): With the Henry coefficients of both components and the conditions $m_3 > m_2$ and $m_1 > m_4$, different areas for complete/incomplete separation of the different components and regeneration of the phases can be defined. The points c and d give the most efficient and productive process. reg. – regeneration, stat. – stationary phase, mob. – mobile phase.

using the component node balances (2.37)-(2.40) [45].

$$c_{i,1}^{\text{in}} = \frac{Q_4 c_{i,4}^{\text{out}} + Q_{\text{D}} c_{i,\text{D}}}{Q_1} \tag{2.37}$$

$$c_{i,2}^{\text{in}} = c_{i,1}^{\text{out}} \tag{2.38}$$

$$c_{i,3}^{\text{in}} = \frac{Q_2 c_{i,2}^{\text{out}} + Q_{\text{F}} c_{i,\text{F}}}{Q_3} \tag{2.39}$$

$$c_{i,4}^{\text{in}} = c_{i,4}^{\text{out}} \tag{2.40}$$

Process Variants

While the standard SMB process offers numerous advantages, it is limited to binary separations. Over the years, various adaptations of the SMB principle have been developed not only to extend its applicability to more complex mixtures but also to further enhance efficiency and productivity [40]. This section provides a brief overview of the most common modifications.

One of the most frequent adaptations involves modifying the number of columns per zone. Commonly multiple columns are used per zone, and the number of columns per zone does not have to be identical for all zones. With an increasing number of columns per zone, the SMB process approaches the TMB process [24]. A common variation is the VariCol process, in which the number of columns per zone changes dynamically throughout a cycle by asynchronously switching ports. This reduces the total number of required columns and saves stationary phase material [24, 51].

Another modification involves changing the number of zones. One prominent example is the three-zone open-loop SMB, where zone four is omitted because the mobile phase is not regenerated. Although this setup increases buffer consumption, it can be advantageous in scenarios

where minimizing cross-contamination is a priority, for example, when dealing with fluctuating or unknown feed compositions [40]. In some cases, SMB setups have been reduced to one or two zones for specific separation tasks [52, 53]. On the other hand, there are applications with an increased number of zones, mainly to separate ternary or pseudo-ternary mixtures [40]. For this purpose, open-loop SMB systems with 5 zones [54] or closed-loop setups with 8 zones [40] have been reported. Another approach for handling multi-component separations is the multi-stage SMB configuration, where multiple SMB units are arranged in series and use the raffinate or extract stream of one unit as the feed for the next [55]. Here, setups with up to 14 zones have been reported [56].

Other process variants increase the performance by either adapting the feed concentrations of the components during the process or varying the outlet and zone flow rates. One example is the ModiCon process, where the feed concentration is varied over the course of one cycle, which influences the propagation velocity of the components and can lead to sharper peak fronts and tails, reducing cross-contamination. Since the propagation velocity is independent of the concentration for components with linear isotherm, the ModiCon process is not beneficial in this case [40, 57]. Another approach is the PowerFeed principle, which changes the feed flow rate during the process [40, 58]. In Partial Discard implementations, portions of the extract and/or raffinate stream are selectively discarded to improve purity. As is depicted in Figures 2.5b and 2.5c, impurity breakthrough typically occurs at the beginning of a switching interval for the extract and at the end of a switching interval for the raffinate. By discarding these fractions, purity can be enhanced [40, 59]. This method can also be combined with ModiCon or PowerFeed strategies, where discarded fractions are recycled back into the feed stream [40].

These advanced SMB variations introduce additional process parameters, making analytical optimization impractical. Instead, process modeling and optimization algorithms, such as genetic algorithms, are often employed to determine optimal operating conditions [40].

One variant that particularly broadens the application range of SMB processes is gradient SMB. In the most common implementation, a stronger eluent is used in the diluent stream compared to the feed stream, thereby increasing the elution strength in zones I and II. This enhances the recovery of strongly retained components in the extract stream [40]. This principle was among others successfully applied for the separation of proteins using ion-exchange chromatography [60, 61]. Alternatively, stimuli other than elution strength can be used to generate a gradient across zones, for example using supercritical fluids as mobile phase and varying pressure [62], or with magnetic chromatography applying different magnetic field gradients [63].

These SMB variants represent only a subset of the many possible process modifications. Additional approaches combine multiple adaptations or integrate parallel columns within specific zones [40, 64]. Moreover, SMB systems can be coupled with external units, such as concentration or reaction units, to create hybrid processes [40]. Given these possibilities, the number of potential SMB-like process configurations is virtually limitless.

Implementation and Equipment

The implementation of an SMB system can vary significantly, with one of the key distinctions being whether the movement of the stationary phase is simulated by switching the columns

themselves or by switching the port positions. The core component enabling this switching mechanism is the valve system, which can be implemented in different ways: It can either be one single central valve, as depicted in Figure 2.7a, several manifold valves as depicted in Figure 2.7b, or multiple 3/2-way valves as depicted in Figure 2.7c [43].

Each of these implementations has its advantages. The first SMB implementations used a central valve systems, resulting in a less complex overall system [65]. Figures 2.8a and 2.8b show the differences between central valves that switch the chromatography columns and central valves that switch the in- and outlet ports. For central valves switching the columns, the columns are connected to the valve rotor, while the in- and outlets are connected to the stator. The advantage of this implementation is its relatively low extra column volume (ECV), as only short channels in the valve system are required [43]. The alternative approach circumvents the need to physically move the columns by switching the ports instead. Here, both the columns and the in- and outlet ports are connected to the valve stator. Thus, this approach requires transfer lines to ensure all ports can connect to all columns. These additional connections can increase system volume and introduce cross-contamination risks [43].

Especially in (bio-)pharmaceutical applications, systems with manifold or 3/2-way valves are much more common [43, 66]. One advantage of these systems is their flexibility, enabling the implementation of different processes on one system [67,68]. The disadvantages of these systems are their greater complexity and increased system volume, though new developments in special manifold valve systems have significantly reduced system volume [43].

Beyond the valve system, pumps play a crucial role in SMB operation. In all implementations shown in Figure 2.7, the position of the recycle pump is switched together with one column, meaning that during a complete cycle, it operates in all zones with variable flow rate. Consequently, the flow rate of the recycle pump must be adjusted dynamically [43]. Alternatively, the recycle pump can be in a fixed position in one zone with constant flow rate, however, this requires an extra set of valves in the multi-port valve and 3/2-way valve implementation because it is necessary to interconnect the recycle pump in the same way as the chromatography columns [43].

2.1.2.2 Further Continuous Chromatography Methods

Besides SMB, several other semi- and quasi-continuous chromatography techniques exist, among which PCC is the most developed multi-column chromatography technique for DSP of biopharmaceuticals [25]. Due to the wide range of SMB and periodic countercurrent (PCC) variants, the distinction between these methods is often fluid, with some implementations falling between the two.

A minimum of two columns is required for PCC, and while there is no theoretical upper limit, it is desirable to keep the number of columns and consequently the resin consumption and resulting investment costs as low as possible [25]. The focus of PCC development is on mAb capture processes with protein A chromatography [25, 69]. If a continuous feed application is required, a minimum of three columns are needed for a PCC setup, as depicted in Figure 2.9 [25]. Here, the first two columns are interconnected and loaded with the feed solution, the flow through of the first column being directly fed to the second column. This way, the resin utilization of the first column can be maximized without product loss, as the flow through will be used to pre-load

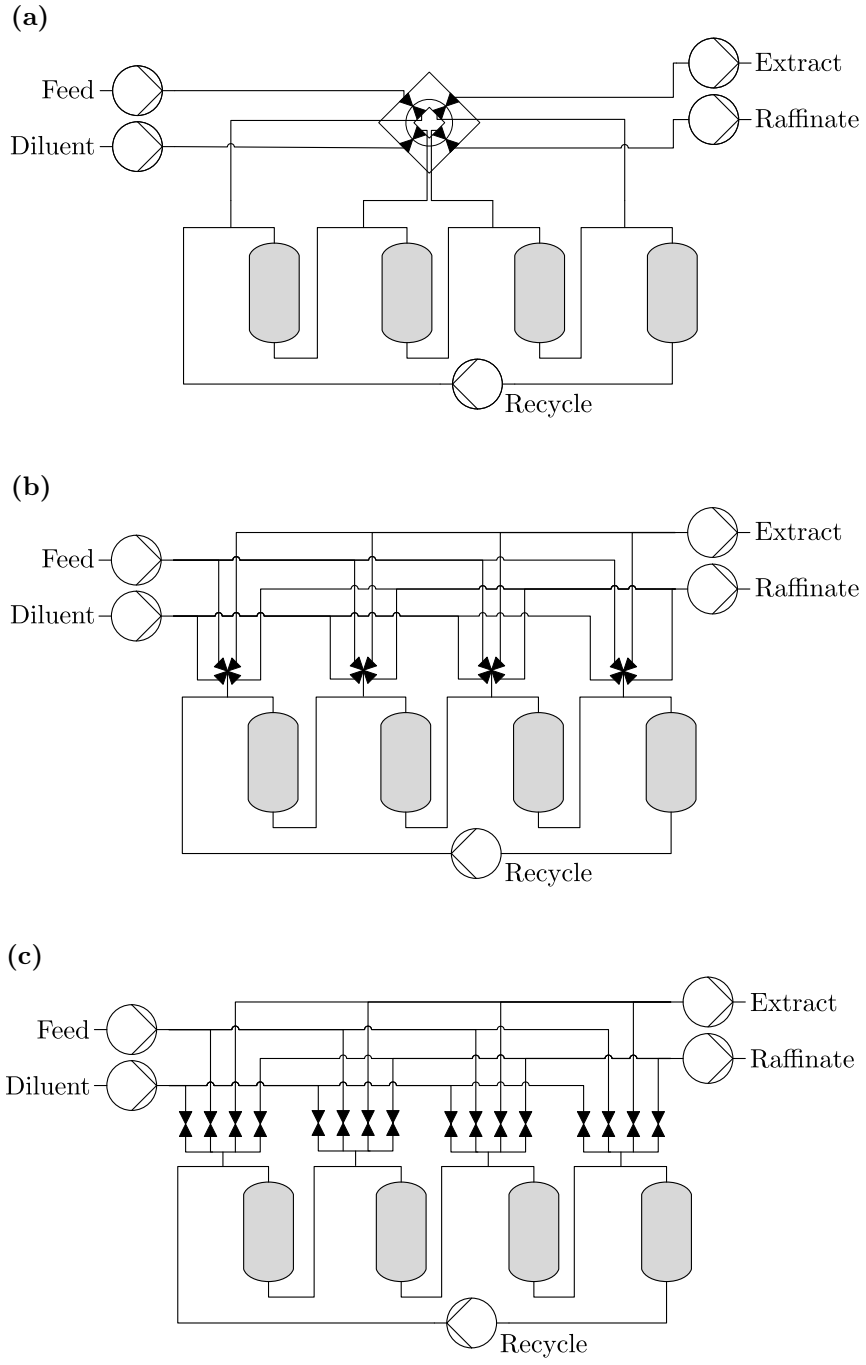

Figure 2.7: Basic implementation concepts of an SMB process: (a) all in- and outlet streams as well as columns are connected to one central valve. The number of ports of the central valves differs according to the number of used columns. (b) One multi-port valve per column is applied to connect the respective in- or outlet stream between two columns. The number of required valves increases with the number of chromatography columns. (c) A set of 3/2-way valves is applied to connect the respective in- or outlet stream between two columns. For each column, one set of valves is required, hence the set of valves increase with the number of columns. The recycle pump is switched together with a column in all depicted implementations.

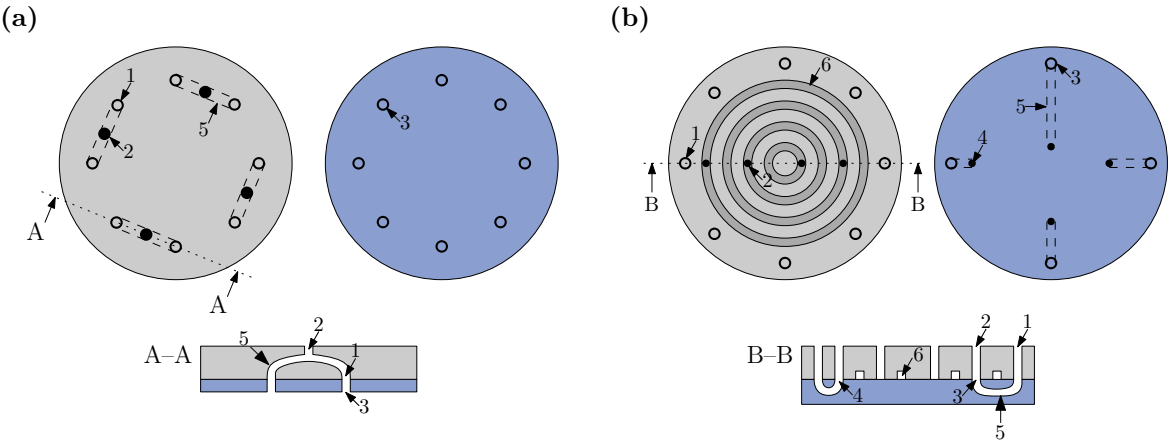

Figure 2.8: Schematic of a central valve stator (gray) and rotor (blue) with one column per zone with moving (a) and static (b) columns. 1: column in-/outlet stator, 2: in-/outlet stream stator, 3: column in-/outlet rotor, 4: in-/outlet stream rotor, 5: connecting channel, 6: transfer lines.

column two. Once column one is fully loaded or product breakthrough is detected at the outlet of column two, the column positions are rotated. Column one moves to position three, where it undergoes washing, elution, CIP, and re-equilibration while the other columns are loaded. Column two moves to position one, and a freshly regenerated column from position 3 takes its place at position two for the next cycle. Ideally, the time required for column loading matches the time needed for the elution and regeneration steps. Otherwise, either the feed must be paused, or additional columns must be added to maintain continuous operation [25].

A widely known two-column PCC process variant with semi-continuous feed flow is CaptureSMB [25]. The process has two alternating phases: in one, the columns are interconnected, while in the other, they operate in batch mode. During the interconnected steps, the columns are loaded in an identical way to the previously described 3 column PCC setup. When the first column is fully loaded, the feed is briefly stopped and the columns are washed interconnected, ensuring complete product capture in column two. While the first column is eluted and re-equilibrated (identical to position three in the PCC setup), the second column is loaded at a lower flow rate to prevent product loss. [70]

Multi-column countercurrent solvent gradient purification (MCSGP) process are closely related to open-loop SMB setups, but incorporate a step or linear gradient. This is realized by modulating the elution strength of the mobile phase between multiple zones. The number of zones is often greater than four, with multiple inlets and outlets allowing for fractionation of different components from the feed. The resulting systems are highly complex and it is elaborate to identify suitable operation parameters. The resulting productivity is not necessarily higher compared to batch-processes, but the process features a high yield, making it particularly attractive for high-value products [25, 71, 72].

While all the aforementioned methods use some form of countercurrent operation, there are also twin-column chromatography processes without an interconnected phase. In these setups, one column is loaded while the other one undergoes the wash, elution, CIP, and re-equilibration steps,

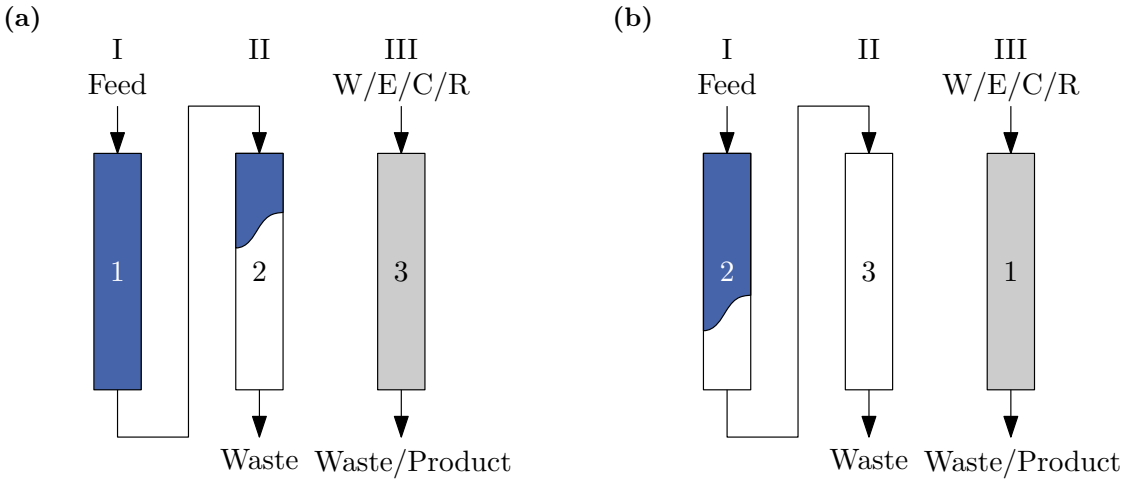

Figure 2.9: 3 column PCC setup: (a) column 1 is fully loaded and moved to position three in the next step (b), while column two is pre-loaded and moved to position one. Column three is fully eluted and re-equilibrated and moved to position two. Arabic numbers – column numbers, roman numbers – position numbers, W – wash, E – elution, C – cleaning in place, R – re-equilibration.

providing a simple continuous chromatography setup. Such setups are of interest in flow-through applications, such as mAb polishing or intermediate conditioning steps (e.g., desalting) [73].

Beyond the above-mentioned quasi or semi-continuous methods, there are also fully continuous chromatography techniques, including continuous countercurrent tangential chromatography [74], fluidized bed riser adsorption systems [75] or conveyor belt chromatography [11]. However, these have not yet found significant application in industrial chromatography [11].

2.1.3 Chromatography Modeling

Chromatography models are essential for optimizing continuous chromatography processes and are also widely used to enhance the efficiency of batch chromatography process development [40, 76, 77]. Additionally, process models play a crucial role in implementing automated process operation and real-time decision-making [78].

There are several types of chromatography models, including data-driven models [79], mechanistic models [77] and hybrid models combining both approaches [80]. Rate models are the most commonly applied mechanistic chromatography models and are also used in this thesis. A detailed overview of the relevant models for this work is presented in the following section.

2.1.3.1 Column models

Mechanistic rate models describe the thermodynamic and transport processes within a chromatography column with varying levels of complexity. To simplify modeling, common assumptions include radial homogeneity of the columns (with changes occurring only in the z-direction), constant density and viscosity of the mobile phase, absence of convection inside the porous network, and no adsorption of the eluent to the stationary phase [24].

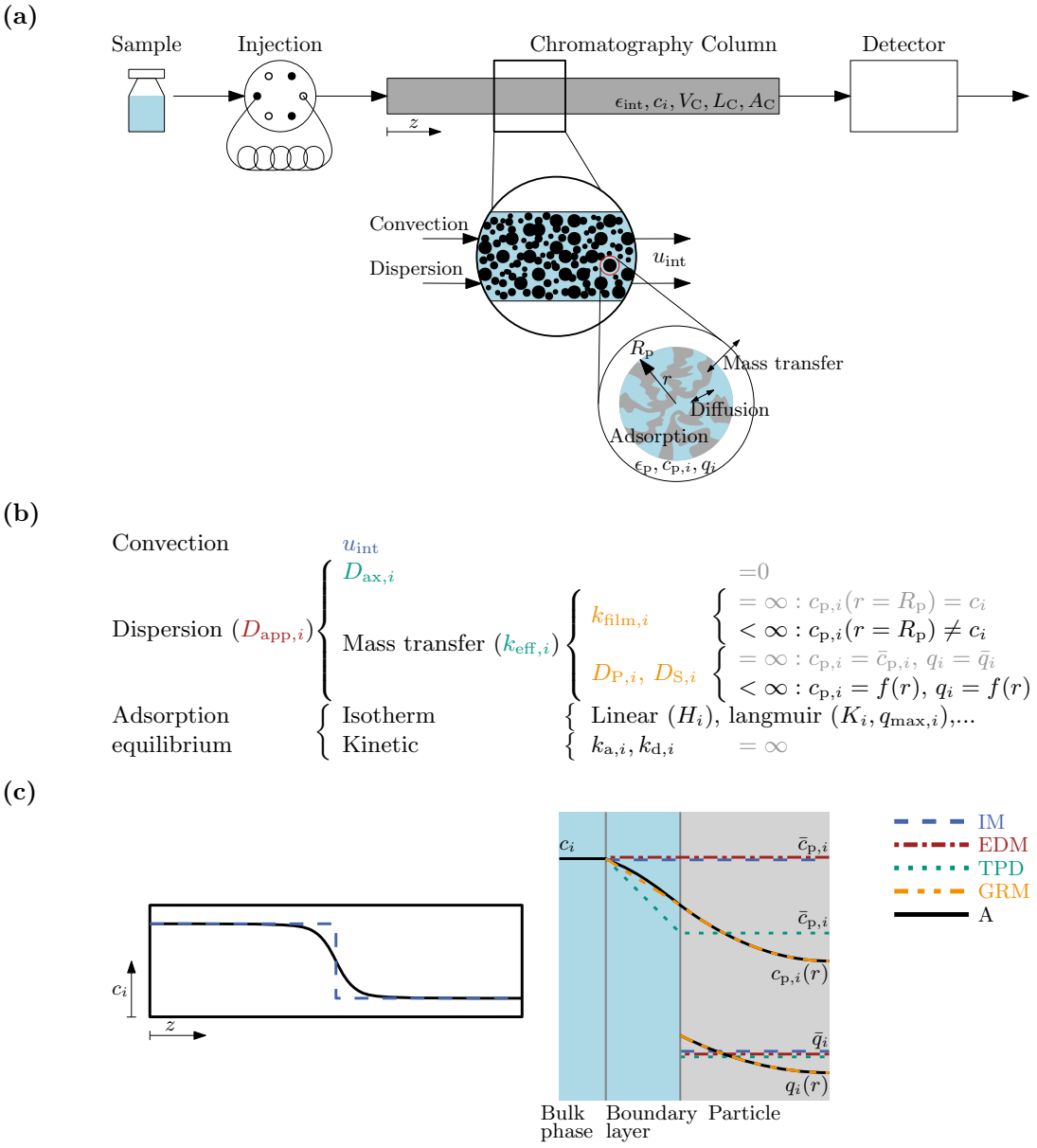

Figure 2.10: Overview of key parameters in chromatography column modeling: (a) Schematic representation of a chromatography setup highlighting key column model parameters. (b) Relationship between the model parameters of different chromatography models. The assumptions for neglecting a specific parameter are indicated in gray. (c) Qualitative concentration profiles in the column (left) and at the liquid-particle interface (right) for different column models. IM – ideal model; EDM – equilibrium dispersive model; TPD – transport dispersive model; GRM – general rate model; A – actual concentration profile.

Figure 2.10a provides an overview of the transport processes inside a chromatography column. Mass transport in the mobile phase occurs via convection and dispersion, while mass transfer to the stationary phase takes place through the boundary layer of stagnant fluid surrounding the particles. Within the stationary phase, solutes diffuse into particle pores and interact with the stationary phase [24].

Consequently, a chromatography process can be described by two differential mass balances, one for a differential volume element of the bulk mobile phase in the chromatography column and one for the stagnant fluid in the particles. In addition, an isotherm (see Section 2.1.1) describing the relationship of protein concentration in the liquid phase and protein loading to the stationary phase is required [24]. Mechanistic rate models are derived from these differential mass balances and varying levels of complexity are implemented by either neglecting certain mass transport effects or lumping multiple effects together.

The ideal model (IM) is the simplest model. It assumes that the column has infinite efficiency, meaning there is no axial dispersion, mass transfer effects are neglected, and the mobile and stationary phases are always in equilibrium. It can be analytically solved for many isotherm models, offering important insights into thermodynamics of phase equilibria. Thus, it is especially useful for highly efficient columns used with large sample sizes, i.e., operated in the non-linear range, when effects of the non-linear isotherm are dominant compared to mass transfer and dispersion effects [34].

Since mass transfer effects are neglected, one partial differential equation is sufficient to describe the components' concentration in the IM. There are two forms of this equation, depending on whether the interstitial volume or the total void volume of the column are selected as control volume. The equations can be converted into one another using the definition of the effective velocity u_e of a non-retained solute with a pore accessibility of 1 (2.43) [24]. Besides the change of the component concentration with time, the IM features a convection term and a term for the change of loading of the stationary phase with time [24].

$$\frac{\partial c_i}{\partial t} + u_\mathrm{int}\frac{\partial c_i}{\partial z} + \frac{1-\varepsilon_\mathrm{int}}{\varepsilon_\mathrm{int}}\left(\varepsilon_\mathrm{p}\frac{\partial c_i}{\partial t} + (1-\varepsilon_\mathrm{p})\frac{\partial q_i}{\partial t}\right) = 0 \tag{2.41}$$

$$\frac{\partial c_i}{\partial t} + u_\mathrm{e}\frac{\partial c_i}{\partial z} + \frac{1-\varepsilon_\mathrm{T}}{\varepsilon_\mathrm{T}}\frac{\partial q_i}{\partial t} = 0 \tag{2.42}$$

$$u_\mathrm{e} = \frac{\varepsilon_\mathrm{int}}{\varepsilon_\mathrm{T}}u_\mathrm{int} \tag{2.43}$$

The equilibrium dispersive model (EDM) considers one additional band broadening effect based on apparent dispersion [24]. The apparent dispersion coefficient $D_{\mathrm{app},i}$ lumps all mass transfer and dispersion effects together. It is considered to be constant and independent of sample concentration, and hence not applicable for highly viscous samples [34]. The EDM is suitable if mass transfer is fast but finite and peak broadening is primarily influenced by molecular diffusion, assuming mass transfer between the mobile and stationary phases is fast [34].

Comparable to the IM, the EDM only requires one partial differential equation to describe a time-dependent concentration profile, which can be expressed either in regard to ε_int (2.44) or ε_T

(2.45). Note that the apparent dispersion coefficient differs between the two forms (2.46) [24]. It can be estimated based on the $HETP_i$ value (2.47) [24].

$$\frac{\partial c_i}{\partial t} + u_{\text{int}} \frac{\partial c_i}{z} + \frac{1-\varepsilon_{\text{int}}}{\varepsilon_{\text{int}}} \left(\varepsilon_{\text{p}} \frac{\partial c_i}{\partial t} + (1-\varepsilon_{\text{p}}) \frac{\partial q_i}{\partial t} \right) = D_{\text{app},i} \frac{\partial^2 c_i}{\partial z^2} \tag{2.44}$$

$$\frac{\partial c_i}{\partial t} + u_{\text{e}} \frac{\partial c_i}{z} + \frac{1-\varepsilon_{\text{T}}}{\varepsilon_{\text{T}}} \frac{\partial q_i}{\partial t} = D^*_{\text{app},i} \frac{\partial^2 c_i}{\partial z^2} \tag{2.45}$$

$$D^*_{\text{app},i} = \frac{\varepsilon_{\text{int}}}{\varepsilon_{\text{T}}} D_{\text{app},i} \tag{2.46}$$

$$D_{\text{app},i} = \frac{HETP_i \cdot L_{\text{C}}}{2t_0} \tag{2.47}$$

The transport dispersive model (TDM) separates band broadening effects into axial dispersion with the axial dispersion coefficient $D_{\text{ax},i}$ and effective mass transfer resistance, with the mass transfer coefficient $k_{\text{eff},i}$, which is a sum parameter for film transfer, pore diffusion and surface diffusion. Consequently, different equations are required for the concentration profile in the mobile phase (2.48) and the stationary phase (2.49), with the radius of the stationary phase particles R_{p} and the concentration in the stagnant fluid inside the particle pores $c_{\text{p},i}$. The here presented equations use a linear driving force approach for the mass transfer term, alternative approaches exist in literature [81].

$$\frac{\partial c_i}{\partial t} + u_{\text{int}} \frac{\partial c_i}{z} + \frac{1-\varepsilon_{\text{int}}}{\varepsilon_{\text{int}}} \left(\varepsilon_{\text{p}} \frac{\partial c_{\text{p},i}}{\partial t} + (1-\varepsilon_{\text{p}}) \frac{\partial q_i}{\partial t} \right) = D_{\text{ax},i} \frac{\partial^2 c_i}{\partial z^2} \tag{2.48}$$

$$\varepsilon_{\text{p}} \frac{\partial c_{\text{p},i}}{\partial t} + (1-\varepsilon_{\text{p}}) \frac{\partial q_i}{\partial t} = k_{\text{eff},i} \frac{3}{R_{\text{p}}} (c_i - c_{\text{p},i}) \tag{2.49}$$

The general rate model (GRM) is the most elaborate rate model and is mainly applied for large molecules, such as proteins, due to their comparatively slow mass transfer [34]. The GRM aims to account for all the different mass transfer processes and features a mass balances for the bulk mobile phase (2.50) and the stagnant mobile phase and stationary phase (2.51), with the film transfer coefficient $k_{\text{film},i}$, the pore diffusion coefficient $D_{\text{P},i}$, and the surface diffusion coefficient $D_{\text{S},i}$ [24].

$$\frac{\partial c_i}{\partial t} + u_{int} \frac{\partial c_i}{\partial z} + \frac{1-\varepsilon_{\text{int}}}{\varepsilon_{\text{int}}} \frac{3}{R_{\text{p}}} k_{\text{film},i} (c_i - c_{\text{p},i}(r = R_{\text{p}})) = D_{\text{ax},i} \frac{\partial^2 c_i}{\partial z^2} \tag{2.50}$$

$$\varepsilon_{\text{p}} \frac{\partial c_{\text{p},i}}{\partial t} + (1-\varepsilon_{\text{p}}) \frac{\partial q_i}{\partial t} = \frac{1}{r^2} \frac{\partial}{\partial r} \left[r^2 \left(\varepsilon_{\text{p}} D_{\text{P},i} \frac{\partial c_{\text{p},i}}{\partial r} + (1-\varepsilon_{\text{p}}) D_{\text{S},i} \frac{\partial q_i}{\partial r} \right) \right] \tag{2.51}$$

Figure 2.10b provides an overview of the parameters required for the different models, how they are lumped together for simplifications and which assumptions are frequently made to neglect the influence of a specific parameter on peak broadening [24].

Additionally, Figure 2.10c qualitatively shows the assumed concentration profiles in the column itself, the bulk of the mobile phase, the boundary layer around the particles of the stationary phase, and the stagnant fluid inside the pores in comparison to an actual concentration profile.

Independent of the chosen model, initial and boundary conditions are required to numerically solve the respective partial differential equations. For the initial conditions it is usually assumed that the column is re-equilibrated at the beginning of the experiment, which can be expressed through Equations (2.52) [34]. In the case of continuous multi-column chromatography simulations, the initial conditions after a step in the chromatography process (e.g., after the switching in an SMB process) are identical to the concentration profile of the respective column in the previous process step [82].

$$\begin{aligned} c_i(z, t = 0) &= 0 \text{ for } 0 \leq x \leq L_C \\ c_{\mathrm{p},i}(r, t = 0) &= 0 \text{ for } 0 \leq x \leq R_p \\ q_i(r, t = 0) &= 0 \text{ for } 0 \leq x \leq R_p \end{aligned} \tag{2.52}$$

Danckwerts boundary conditions for the mobile phase inlet (2.53) and outlet (2.54) are usually applied, which assumes that for the column inlet the mass flux is identical to the mass flux into an empty pipe [34, 83].

$$c_i\left(t, z = 0\right) = c_{\mathrm{in},i} - \frac{D_{\mathrm{ax},i}}{u_{\mathrm{int}}} \frac{\partial c_i\left(t, z = 0\right)}{\partial z} \tag{2.53}$$

$$\frac{\partial c_i\left(t, z = L_{\mathrm{C}}\right)}{\partial z} = 0 \tag{2.54}$$

Additional boundary conditions for the adsorbent phase are required for the GRM. A frequently used set of boundary conditions was proposed by Ma et al. [24, 84]:

First, it is assumed that there are no concentration gradients at the particle center due to symmetry:

$$\left.\frac{\partial c_{\mathrm{p},i}}{\partial r}\right|_{r=0} = \left.\frac{\partial q_i}{\partial r}\right|_{r=0} = 0 \tag{2.55}$$

Additionally, the different phases are linked with the following mass balance at the particle boundary:

$$k_{\mathrm{film},i}\left(c_i - c_{\mathrm{p},i}\left(r = R_{\mathrm{p}}\right)\right) = \varepsilon_{\mathrm{p}} D_{\mathrm{P},i} \left.\frac{\partial c_{\mathrm{p},i}}{\partial r}\right|_{r=R\mathrm{p}} + \left(1 - \varepsilon_{\mathrm{p}}\right) D_{\mathrm{S},i} \left.\frac{\partial q_i}{\partial r}\right|_{r=R\mathrm{p}} \tag{2.56}$$

Finally, it is stated that there is no surface diffusion outside the particles, meaning that the gradient of the corresponding flux is zero:

$$\left.\frac{\partial \dot{m}_{\mathrm{diff,S},i}}{\partial r}\right|_{r=R_{\mathrm{p}}} = \left.\frac{\partial}{\partial r}\left(\frac{\partial q_i}{\partial r}\right)\right|_{r=R_{\mathrm{p}}} = \left.\frac{\partial^2 q_i}{\partial r^2}\right|_{r=R_{\mathrm{p}}} = 0 \tag{2.57}$$

2.1.3.2 Modeling of Dead Volume

Dispersion effects are not limited to the chromatography column itself but also occur within the chromatography system, often referred to as system volume, dead volume, or ECV.

Besides the dispersion effect, the ECV introduces a time delay, primarily due to the presence of connecting capillaries. This delay is typically modeled using a plug flow reactor (PFR) [85]. Additional mixing effects, such as those caused by valves and other system components, are commonly modeled with continuously stirred tank reactors (CSTRs) [86,87]. Alternatively, time delay and dispersion effects can be accounted for using a dispersed plug flow reactor (DPFR) model, which is based on the EDM, assuming a total porosity of 1 [44].

Particularly in small-scale chromatography systems, fluid dynamics in the ECV can be more complex, requiring advanced modeling approaches [88]. A detailed comparison of different modeling strategies is provided in Section 7.2.

2.1.4 Miniaturization in Chromatography

Chromatography miniaturization is commonly employed in process development as well as for analytical purposes [89, 90]. It is an important tool for efficient process development, enabling process parameter screening and the determination of chromatography parameters required for chromatography models with small product quantities [89]. Often, it is combined with high-throughput screening (HTS) or high-throughput process development (HTPD) [89]. Interestingly, the same methods are also used for purifying samples originating from cell culture process development [91].

A widely used scale-down approach is microtiter filter plates packed with a fixed volume of resin (e.g., 96-well format) [89], which enable the parallel evaluation of different conditions, often in a highly automated manner through liquid handling stations (LHSs) [89, 91]. Although these are used for a broad range of applications, such as resin screening, optimization of binding conditions, or determination of isotherm parameters [89, 91, 92], it is important to consider that their hydrodynamic properties differ from those of standard chromatography columns, which can affect the transferability of results to larger scales [93]. Moreover, SEC cannot be performed in this format [91].

Another option for chromatography miniaturization is the application of mini-columns that can often be operated with LHSs. Although mini-columns generally require larger sample volumes than filter plates, they offer the advantage of capturing the dynamic properties of chromatography [91].

Microfluidic chromatography chips represent an approach that requires the smallest amounts of resin and sample. Silva et al. developed a microfluidic chromatography chip with a column volume of 200 nL for the estimation of adsorption isotherm parameters [89]. While this method can be highly advantageous for high-value products, current implementations are often not integrated into automated setups, and additional work on parallelization and automation is needed to fully realize the potential of this approach [89].

Continuous chromatography processes, such as SMB, were initially developed for lower-value products compared to biopharmaceuticals and conducted at much larger scales [41]. Consequently, lab-scale SMB systems are sometimes regarded as a form of miniaturization, which has led to potentially confusing names, such as ultra-micro SMB for systems with column volumes of several mL [94].

Miniaturizing continuous chromatography to levels comparable to batch chromatography is less common. One reason is the lack of readily available equipment [11]. In addition, many parameters relevant to process development can be determined using miniaturized batch chromatography. For instance, suitable process conditions for SMB can usually be identified solely through batch chromatography experiments [11]. However, certain aspects, such as resin fouling during long-term continuous operation, must be investigated experimentally, highlighting the need for small-scale continuous chromatography systems [11].

In this context, 3D printing shows great potential to fill the gap in required equipment. Beyond the work presented in this thesis on miniaturizing SMB through 3D printing, Kortmann et al. recently showcased a 3D-printed miniaturized PCC system designed for the continuous purification of mAbs [95].

Naturally, analytical chromatography generally operates at smaller scales than preparative applications. Nonetheless, there is an ongoing trend toward further miniaturization in analytical chromatography, aiming to reduce the required sample volume, lower mobile phase consumption, and enhance measurement sensitivity [90]. Analytical chromatography is categorized according to the column diameter and applied flow rates into analytical-flow (2.1 mm–4.6 mm i.d., $Q > 200\,\mu L/min$), micro-flow (0.5 mm–1.0 mm i.d., $10\,\mu L/min < Q < 200\,\mu L/min$), capillary-flow (0.15 mm–0.3 mm i.d., $1\,\mu L/min < Q < 10\,\mu L/min$), and nano-flow (0.05 mm–0.1 mm i.d., $Q < 1\,\mu L/min$) [96]. Applied columns can either be packed beds, monoliths, or microchip based pillar arrays [96]. Choosing the optimal analytical scale depends on the sample. For example, while nano-flow chromatography provides the highest sensitivity, it is also less robust and larger-scale systems are generally easier to automate [90, 96].

2.2 Process Analytical Technology

More than a decade after the Food and Drug Administration (FDA) published its guidance on PAT [97], the development and implementation of PAT tools continue to be an active research area. According to this guidance, PAT is defined as "a system for designing, analyzing, and controlling manufacturing through timely measurements (i.e., during processing) of critical quality and performance attributes of raw and in-process materials and processes, with the goal of ensuring final product quality" [97]. Accordingly, PAT encompasses both the analytical dimension and advanced process control strategies to ensure product quality based on real-time or near-real-time measurements.

The primary objectives of PAT include increasing process understanding, improving efficiency, reducing batch failures, enhancing automation, enabling real-time release, and facilitating continuous manufacturing [97]. While these benefits apply to any manufacturing strategy, PAT is particularly critical for continuous bioprocessing, where it ensures consistent product quality over extended production periods by allowing for a timely reaction to process fluctuations [81].

A critical factor in this context is the analysis time, as a shorter analysis time extends the available decision window for corrective actions [98]. To optimize this, PAT strategies focus on reducing the time required for measurements by shifting analytical procedures closer to the process stream. Instead of relying on traditional off-line analyses performed in dedicated laboratories, PAT employs in-line, on-line, or at-line measurements (see Figure 2.11) instead of traditional off-line analyses, enabling real-time or near-real-time process monitoring. In-line measurements are performed directly within the process stream (either invasively or non-invasively), while on-line methods divert a portion of the process stream for analysis, sometimes returning it to the main process line. At-line measurements still require sample withdrawal but are performed at the production site, in close proximity to the process stream [97].

The next section provides a brief introduction to current PAT applications in DSP for biopharmaceuticals.

2.2.1 Current PAT Applications

Off-line analytical methods for DSP are mainly based on different HPLC measurements for CQAs ranging from product titer to charge profile [18]. However, recent PAT applications have increasingly employed spectroscopic methods, including Raman spectroscopy, near-infrared (NIR) spectroscopy, mid-infrared (MIR) spectroscopy, Fourier-transform infrared (FTIR) spectroscopy, UV/Vis spectroscopy, fluorescence spectroscopy, and light scattering techniques [7,18,99]. These methods are well-suited for PAT, because they allow for in-line or on-line analysis without requiring extensive sample preparation and provide results in near real time [99]. Among these techniques, Raman spectroscopy is gaining popularity due to its high sensitivity to a broad spectrum of CQAs [7].

Many attributes, however, cannot be measured directly. In such cases, software tools based on multivariate data analysis (MVDA) are utilized. The application of MVDA usually includes data pre-processing as well as model building and validation, for example using partial least squares (PLS) regression. Once validated, the model can predict targeted CQAs in real time from process sensor data [99].

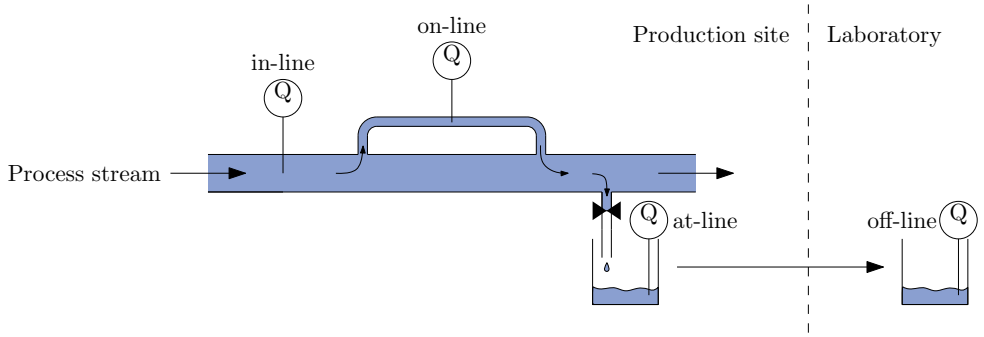

Figure 2.11: PAT measurement concepts: in-line – sensor is placed directly in the product stream; on-line – split stream of the product stream is analyzed; at-line – samples are taken from the process stream and analyzed on-site; off-line (not a PAT concept) – samples are taken from the process stream and analyzed in analytical laboratories. Q – Quality.

Several case studies demonstrate the successful application of PAT tools for monitoring CQAs in different unit operations, especially chromatography. For instance, Rüdt et al. employed UV/Vis measurements with a PLS model to automatically terminate the loading phase of a protein A capture step for a mAb [100]. Pathak and Rathore used fluorescence measurements to monitor protein A resin fouling [101]. Rolinger et al. applied multiple techniques, including UV/Vis and light scattering, to monitor concentration, molecular weight, and buffer exchange during ultrafiltration/diafiltration (UF/DF) of an mAb [102].

In some scenarios, multimodal or multiple sensors are combined to measure a single parameter [99]. For example, multi-angle light scattering (MALS) is used for in-line protein aggregation monitoring. Because light-scattering signals depend on both molecular weight and analyte concentration, Patel et al. applied UV measurements for determination of concentration in combination with MALS to determine real-time aggregate levels of an mAb during hydrophobic interaction chromatography [103].

When multiple or multimodal sensors are employed, data fusion methods are required to integrate the different data sources into a coherent analytical framework. Data fusion can be implemented at different levels: low-level fusion involves direct concatenation of data from different sensors, mid-level fusion combines extracted features, and high-level fusion integrates outputs from separate models rather than merging the data itself [99]. It is also possible to fuse the measured data with a (mechanistic) process model (e.g., using Kalman filters) to form hybrid models that have benefits such as enhanced signal-to-noise ratio [104]. Such comprehensive PAT implementations are crucial not only for real-time control but also for developing digital twins, which merge real-time data, mechanistic models, and control algorithms to enable automated, data-driven process optimization [105].

Traditional analytical approaches generally monitor one CQA at a time. Given the complexity of biopharmaceuticals and their numerous CQAs, this single-attribute focus often translates into substantial time and resource demands. Consequently, methods capable of simultaneously measuring multiple CQAs are of significant interest [19].Recently it was shown that Raman spectroscopy can be used to monitor several product attributes, such as concentration, high and low molecular weight species, or HCP content, in parallel during protein A capture chromatography [106, 107].

Beyond spectroscopic methods, multi-attribute monitoring has emerged as a PAT approach that combines LC with MS to measure multiple CQAs within a single workflow [19]. First studies showcasing the application of multi-attribute monitoring as at-line analytics have already been published [108, 109], and while MS has traditionally been associated with PAT for USP, these studies highlight its growing relevance in DSP.

The following section provides a concise overview of the mass spectrometry principles applied in this work.

2.2.2 Electrospray Ionization Mass Spectrometry

MS is an important analytical technique used to characterize molecules based on their mass-to-charge ratio (m/z) [110]. By measuring m/z, MS can analyze a wide range of molecule classes,

ranging from small compounds to large proteins, allowing the elucidation of many molecular attributes [110]. In general, MS measurements can be divided into three main steps: ionization, separation, and detection (see Figure 2.12), with different technological implementations for each step [111].

Because biomolecules often require minimal fragmentation during ionization, soft ionization techniques such as electrospray ionization (ESI) under native conditions and matrix-assisted laser desorption/ionization (MALDI) are commonly used [110]. In recent years, ESI has become more prevalent in the biopharmaceutical field than MALDI, partly because it supports continuous measurement modes and allows direct infusion of liquid samples [111, 112]. This feature facilitates rapid analyses, for instance using flow injection analysis (FIA-ESI-MS) [113], and enables direct coupling to other unit operations such as LC [110]. LC-ESI-MS is frequently applied with various chromatography modes, such as SEC [114, 115] to separate analytes prior to mass detection. The hyphenation of LC with ESI-MS is often referred to as online LC-MS in respect to the direct coupling of the two methods [110, 115], which can be confusing in the PAT context, since as for now LC-MS is usually implemented as at-line or off-line analytic [108, 116].

The following section provides a short overview of the measurement principles relevant to this work, focusing on ESI as the ion source.

2.2.2.1 Measurement Principle

Ion Source

All MS systems consist of three major components: an ion source, one or more mass analyzers, and a detector. In this work, ESI served as the ion source for protein characterization. As shown in Figure 2.13, a high voltage (typically $\pm$ 2–6 kV) is applied between the spraying nozzle and the metal capillary leading to the mass analyzer. Under this strong electric field, a Taylor cone forms at the nozzle tip, continuously emitting highly charged droplets. The droplets shrink due to solvent evaporation, often aided by a sheath gas (e.g. nitrogen), until they reach the Rayleigh limit, triggering Coulomb fission. This cycle of evaporation and fission repeats until solvent-free ions are released into the gas phase [111]. For the formation of solvent-free charged analyte ions, two principal mechanisms have been proposed. In the charged residue model it is

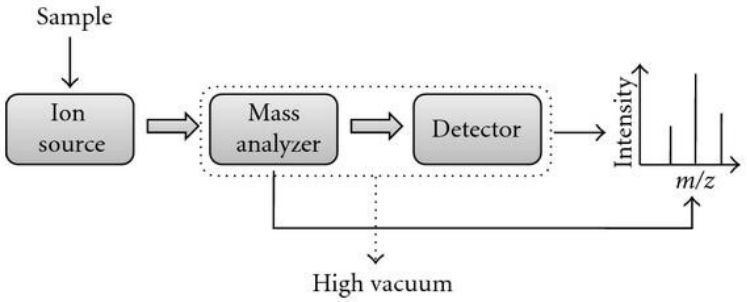

Figure 2.12: Schematic of the MS measurement principle: the sample is ionized (at atmospheric pressure in the case of ESI) and then introduced into a high-vacuum region for mass analysis and detection. Reprinted from [111] under the terms of the Creative Commons Attribution License.

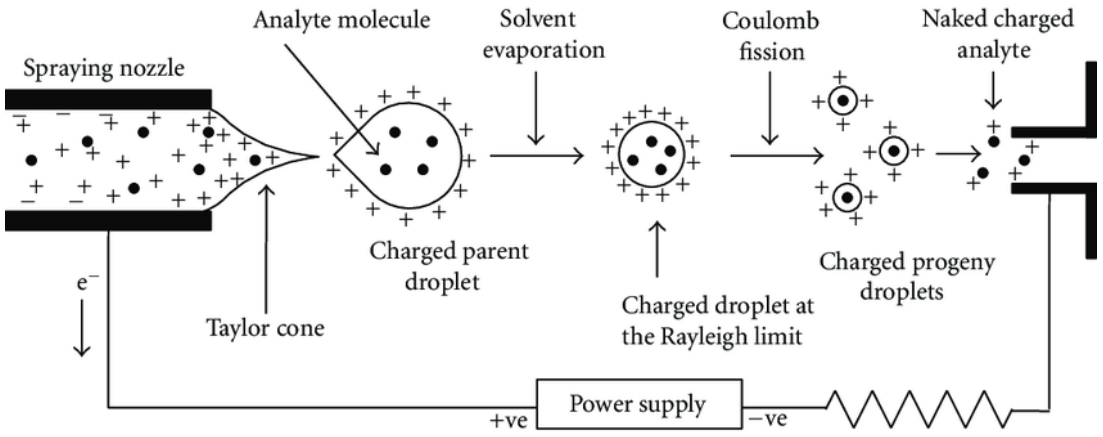

Figure 2.13: Electrospray ionization in positive mode: a high-voltage power supply is connected to the spraying nozzle and a heated metal capillary. The high charge density at the nozzle tip results in the formation of a Taylor cone, releasing highly charged droplets. These droplets shrink due to solvent evaporation until they reach the Rayleigh limit, causing Coulomb fission. This process repeats until only the charged analytes remain. Reprinted from [111] under the terms of the Creative Commons Attribution License.

assumed that the subsequent steps of solvent evaporation and Coulomb fission are repeated until only one analyte molecule remains per droplet, which carries the net charge when the remaining solvent evaporates. In contrast, the ion evaporation model assumes ion emission from the charged droplets due to high electric fields occurring at high surface charge densities [111]. Nowadays it is assumed that both mechanisms can occur simultaneously, though the charge residue model is more relevant for large molecules such as proteins while ion evaporation usually is the dominant effect for small molecules. During analyte-ion formation, the droplets migrate from the spraying nozzle to the heated metal capillary connecting ion source and mass analyzer driven by the high voltage. Additionally, ion optics are usually applied to guide and focus the ion beam [111].

A key advantage of ESI for protein analysis is that it often produces multiply charged ions, effectively lowering the observed m/z range for large molecules and allowing mass analyzers with limited mass ranges, such as quadrupoles, to be used for large molecules [111].

Depending on the polarity of the applied voltage, cations or anions can be formed, with the detection of cations in positive mode being more common. The formation of charged species in ESI typically involves protonation (positive mode) or deprotonation (negative mode), while redox processes can occur at the nozzle for redox-active analytes or solvents. Suitable solvents include water, methanol, and acetonitrile [111].

One limitation of ESI is its incompatibility with most non-volatile buffers widely used for biomolecules. The ions of these buffers can form ion-pairs with the analytes, generating multiple signals with varying m/z values and complicating data interpretation. They can also accumulate in the ion source, especially at higher concentrations, decreasing sensitivity [111]. Consequently, volatile buffers such as ammonium acetate or ammonium bicarbonate are commonly employed for ESI-MS, necessitating buffer exchange or sample dilution when working with standard biological buffers [110].

Mass Analyzer and Detector

There are various mass analyzers, all separating ions based on their behavior in electromagnetic fields [110]. In the present work, a mass spectrometer featuring quadrupole and time of flight (ToF) mass analyzers was employed. Other mass analyzers that are frequently applied for protein analysis due to their high resolution are Orbitrap and Fourier transform ion cyclotron resonance (FT-ICR) mass analyzers [117].

Quadrupole analyzers feature four parallel rods: two connected to a direct-current (DC) source and two to a radio-frequency (RF) potential [118]. Ions will move to the oppositely charged rod; however, as the polarity is changed frequently, the ions move on an oscillating trajectory between the rods. In order for the ions not to collide with the rods, the polarity of the rods have to change in the right frequency in regard to the m/z ratio of the ion. Ions with different m/z ratios will eventually collide with the rods. This allows the user to isolate or scan through different m/z ranges [118]. Quadrupoles are relatively inexpensive, compact, and easy to maintain but have limited mass ranges [118].

ToF analyzers, by contrast, separate ions according to their flight times over a fixed distance [118]. After being accelerated by a uniform electrostatic field, ions with different m/z values travel at different velocities and thus arrive at the detector at different times [110].

If multiple (different) analyzers are available in a mass spectrometer, MS/MS experiments – commonly referred to as tandem MS – can be performed. In these experiments, ions are selected, fragmented, and subsequently analyzed in successive stages, providing structural and compositional information [111]. One frequent implementation of tandem MS systems are triple quadrupoles, where a precursor ion is selected with the first quadrupole, fragmented in the second quadrupole and the fragments are analyzed in the third one. The detected fragment patterns serve as a molecular fingerprint, enabling confident identification of molecules with similar masses [111].

Finally, MS detectors include Faraday cups or electron multipliers, such as discrete-dynode electron multipliers or microchannel plates (MCPs), which amplify ion signals. Modern instruments often favor electron multipliers due to their high sensitivity [111]. Alternatively, some systems (Orbitrap, FT-ICR) detect the ions indirectly via resonance or induction, providing highly accurate detection results.

2.2.2.2 Applications in Biopharmaceutical Characterization

MS is widely regarded as one of the most versatile and powerful analytical methods [110, 119]. Its unique strength lies in the ability to detect and characterize a broad range of CQAs, and both product- and process-related impurities [110].

Rogstad et al. examined electronically submitted biologics license applications to the FDA between 2000 and 2015 and found a steady increase in MS usage [112]. Between 2012 and 2015, over half of these applications relied on MS to analyze amino acid sequences, molecular masses, deamidation, oxidation, glycosylation, disulfide bonds, and both N- and C-terminal sequence variants.

Although MS is not yet widely adopted as a PAT tool in DSP [18, 116], mainly due to the longer analysis times compared to spectroscopic methods (e.g. Raman) [18], it has been considered

in USP [108, 109], where decision times are usually longer [110]. Nonetheless, MS is increasingly viewed as a promising PAT tool for DSP, particularly in combination with SEC or other chromatographic methods for sample pre-treatment and buffer exchange [110].

Beyond manufacturing, MS also plays a critical role in product discovery and development [109]. In these early stages, it is widely used in large-scale proteomic and metabolomic screens to identify and optimize potential therapeutic targets [110]. Furthermore, MS helps enhance process understanding, for example by identifying critical host cell proteins that affect product stability [120].

2.3 3D Printing Techniques

3D printing, also known as rapid prototyping or additive manufacturing, is becoming a game-changer for biotechnological applications by enabling the rapid fabrication of prototypes [121]. Chuck Hull invented the first 3D printing concept with stereolithography, which he patented in 1986 [122]. Since then, various other techniques, such as fused deposition modeling (FDM) and selective laser sintering, have emerged, allowing the use of a diverse range of materials [121]. With key patents expiring in the early 2000s, an open-source 3D printing community emerged [123]. Combined with decreasing costs and increasing accessibility, this has led to an increased number of applications [124].

Most 3D printing methods build objects layer by layer using thermoplastics, liquid monomers, or fine powders [123]. The choice of printing material and technique depends on the part's geometry and application-specific requirements [121]. The following sections provide an overview of the 3D printing techniques used in this thesis.

2.3.1 Fused Deposition Modeling

FDM, also often referred to as fused filament fabrication (FFF), is one of the most widely used 3D printing techniques. It mostly employs thermoplastic polymer filament, which is melted and deposited in a controlled manner. A schematic of the printing principle is depicted in Figure 2.14a. The system has two main units: An extruder that continuously transports, melts, and deposits the 3D printing material, and a three-axis positioning system for exact positioning of the extruder. Layering the round polymer strands on top of each other produces a corrugated surface; to improve the surface quality, 3D-printed parts are frequently post-processed, for example, with acetone vapor treatment [125, 126].

FDM supports a broad range of materials, with polylactic acid (PLA), acrylonitrile butadiene styrene (ABS), and polypropylene (PP) being the most common ones [126,127]. It is also possible to print biocompatible and chemical resistant materials like polyether ether ketone (PEEK), though this requires a high printing temperature above 360°C [128, 129].

Mechanical properties of the printed parts are influenced not only by the chosen material but also by the infill pattern and density. Typically, only the outer shell is printed at 100% density, while the interior follows a structured infill pattern to optimize weight, strength, and printing time [126].

FDM is the most cost-effective printing technique but also has a lower precision compared to other methods. In this work, it is mainly used for fabricating housings and other structural components.

2.3.2 Digital Light Processing

Digital light processing (DLP) is a photopolymer-based 3D printing technique that cures a liquid monomer/photoinitiator mixture using UV-induced radical polymerization [130]. Unlike many other printing techniques, DLP prints an entire layer of the part at once [131].

As illustrated in Figure 2.14b, DLP printers typically print upside down, beginning with the bottom layer attached to the print platform. The platform is submerged in a vat of liquid resin, leaving a thin gap with the height of one z-layer, where polymerization occurs. A transparent vat bottom allows for UV exposure, curing the desired regions [130].

The light exposure is more intense at the bottom of the vat, leading to stronger polymerization, which can result in a corrugated outer surface. This effect can be minimized by printing with small z-layer heights. Additionally, the overall printing accuracy can be improved by adding light-absorbing additives, minimizing light scattering and hence unwanted polymerization [23].

Moreover, the properties of the printed material can be adjusted by adding further components to the photoinitiator/photoabsorber/monomer mixture. This way, it is for example possible to print porous materials by adding suitable porogens [132], or glass [133] and ceramics [134] with subsequent post-processing of the printed parts by adding fine particles. Multifunctional monomers with different functional groups can be used to functionalize the material, either for further chemical reactions [135] or to use it as an adsorbent [136].

In the schematic depicted in Figure 2.14b, the UV-light exposure is implemented with a projector and a digital micromirror device (DMD). The DMD consists of numerous rectangular mirrors that can be tilted to control light exposure. The number of mirrors in the DMD equals the pixels usable for the printing process [130]. There are similar printing techniques that use LCD screens for irradiation instead of the combination of projector and DMD [23].

Stereolithography printing is also a closely related technique, polymerizing not layer-by-layer but point-by-point, using a laser as a UV light source [121]. The continuous liquid interface production (CLIP) method, where the polymerization process and z-axis movement are continuous instead of step-wise, reduces the required printing time and produces smoother surfaces compared to the other methods [137, 138].

DLP is widely used for high-precision applications, such as microfluidic devices, where it enables the fabrication of microfluidic channels without the need for support material [23].

2.3.3 Multijetting

Multijetting, or PolyJet printing, also utilizes a liquid monomer/photoinitiator mixture that is polymerized with radical UV-polymerization. The principle is similar to an inkjet printer, as depicted in Figure 2.14c: The printing nozzles spray a thin layer of the material on the printing platform, followed by UV-induced polymerization [121]. Different nozzles can dispense various

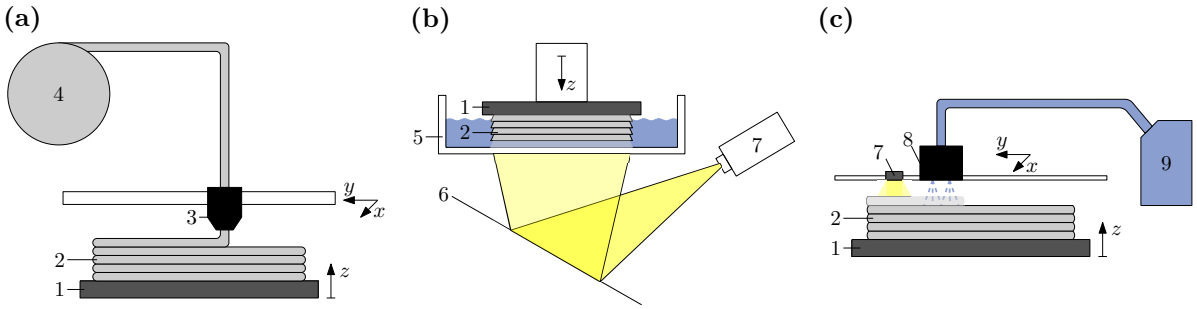

Figure 2.14: Schematics of 3D printing methods used in this thesis: (a) fused filament fabrication; (b) digital light processing; (c) polyjet/multijet. 1 – printing platform, 2 – 3D printed object, 3 – extruder with printing nozzle, 4 – printing material, 5 – vat with transparent bottom containing 3D printing material, 6 – mirror (array), 7 – UV-light source, 8 – printing head, 9 – material tank.

resins simultaneously, enabling not only multi-material printing, but also the mixing of several materials in different ratios. Thus, it is possible to change the properties of the 3D printed parts, such as stiffness or color, gradually [139]. However, unlike DLP, support structures are required for overhangs and internal cavities, which can be challenging to remove in complex geometries such as long, winding channels [121].

3. Manuscript Overview

This thesis aims to improve continuous process development and process analytics by providing insights into the development, manufacturing, application, and modeling of a micro simulated moving bed (µSMB) system. The main body of this work is based on five publications, each focusing on different aspects of the system and its applications. This chapter provides a brief overview of these publications and their contributions.

Chapter 4: Configurable 3D Printed Microfluidic Multiport Valves with Axial Compression

Juliane Diehm, Verena Hackert, Matthias Franzreb

Micromachines, `https://doi.org/10.3390/mi12101247`

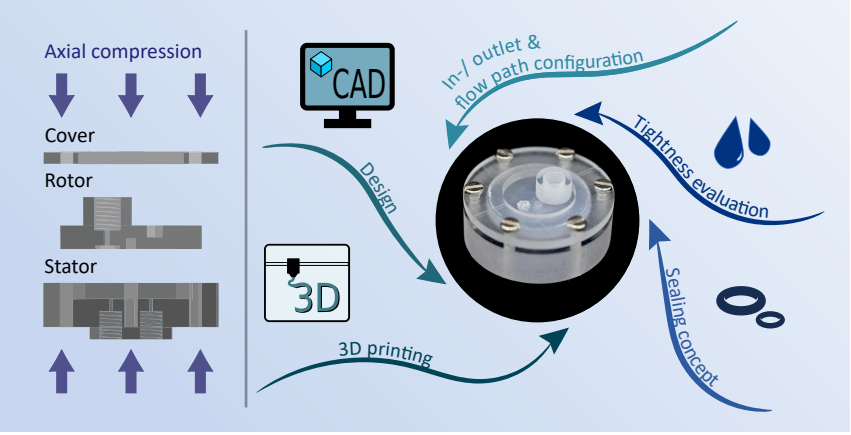

Figure 3.1: Graphical abstract to Chapter 4: Left side – principle of an axial compressed rotor-stator valve system; right side – development process of the system.

A key question addressed in this thesis is whether 3D printing is a viable manufacturing technology for miniaturized continuous chromatography systems, using SMB as an example. The valve system is the central unit for the design and implementation of any SMB system, as outlined in Section 2.1.2.1. In this work, a central valve was selected, because it ensures the connection of different columns with minimal ECV. Chapter 4 is based on the paper *'Configurable 3D Printed Microfluidic Multiport Valves with Axial Compression'* and provides insights into the design and

manufacturing process of the 3D-printed central valve. The graphical abstract is depicted in Figure 3.1, showing a smaller 3/2-way test-valve that was used throughout the development process. The valve is based on a rotor-stator principle with axial compression, as shown on the left side of Figure 3.1. The focus of this chapter is on establishing and characterizing a sealing concept for the valve system. The development process is depicted on the right side of Figure 3.1, starting with the definition of in- and outlets as well as required flow paths inside the valve, the resulting design, followed by fabrication using 3D printing and the evaluation of different sealing concepts.

Chapter 5: Development of a 3D Printed Micro Simulated Moving Bed Chromatography System

Juliane Diehm, Tim Ballweg, Matthias Franzreb

Journal of Chromatography A, `https://doi.org/10.1016/j.chroma.2023.463928`

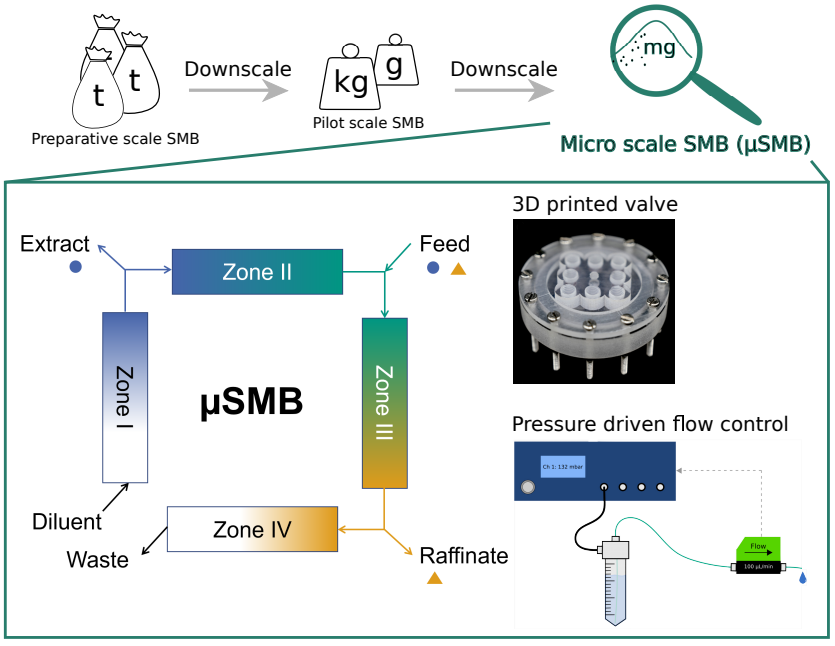

Figure 3.2: Graphical abstract to Chapter 5: An open-loop four zone µSMB setup was developed and evaluated using the-3D printed valve system presented in Chapter 4 and a pressure-driven microfluidic flow control system as its central units.

In the following chapter, the developed valve system is used to build a µSMB system in its entirety. It is based on the paper *'Development of a 3D Printed Micro Simulated Moving Bed Chromatography System'*, the graphical abstract is shown in Figure 3.2. Besides the 3D-printed valve, pressure driven flow control is a central part of the µSMB system, providing accurate flow rates in the µL/min range. Additionally, software with a graphical user interface (GUI) was implemented to control all actors (flow control and column switching) and collect and store data from all sensors. In Chapter 5 the results of a first proof-of-concept study, where bovine serum albumin (BSA) was successfully desalted from ammonium sulfate (AS), are presented,

showcasing its applicability for resource-efficient process development.

Chapter 6: Micro Simulated Moving Bed Chromatography-Mass Spectrometry as a Continuous On-line Process Analytical Tool

Juliane Diehm, Lennart Witting, Frank Kirschhöfer, Gerald Brenner-Weiß, Matthias Franzreb

Analytical and Bioanalytical Chemistry, https://doi.org/10.1007/s00216-023-05023-9

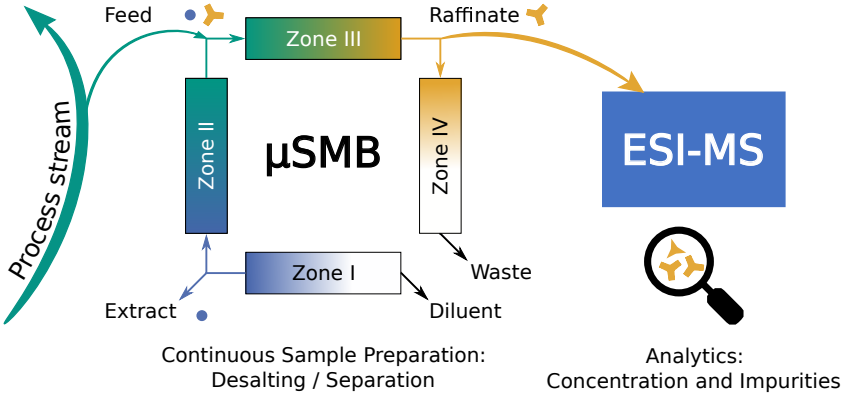

Figure 3.3: Graphical abstract to Chapter 6: The µSMB system presented in Chapter 4 is adapted so it can be directly coupled to an ESI-MS system, allowing for continuous on-line analytics by combining the detection power of ESI-MS with continuous sample pre-processing of the µSMB.

While Chapter 5 focuses on a general proof-of-concept and demonstrates the low sample amount required to operate the system, Chapter 6 investigates a different application as a continuous analytical tool in combination with ESI-MS, as schematically shown in Figure 3.3. It is based on the paper *'Micro Simulated Moving Bed Chromatography-Mass Spectrometry as a Continuous On-line Process Analytical Tool*, where the µSMB was used for continuous sample preparation for the MS measurements. In this chapter the requirements and adaptations of the µSMB that had to be done to enable the direct coupling to the ESI-MS are discussed. The results show the successful on-line measurements and highlight the improvement in signal quality with the sample pre-processing.

Chapter 7: Modeling the Extra Column Volume of a Micro Simulated Moving Bed Chromatography System: Introducing the Equivalent Radial Flow Rate Distribution

Juliane Diehm, Matthias Franzreb

Journal of Chromatography A, https://doi.org/10.1016/j.chroma.2024.465543

Modeling is an important step for process optimization of continuous chromatography processes,

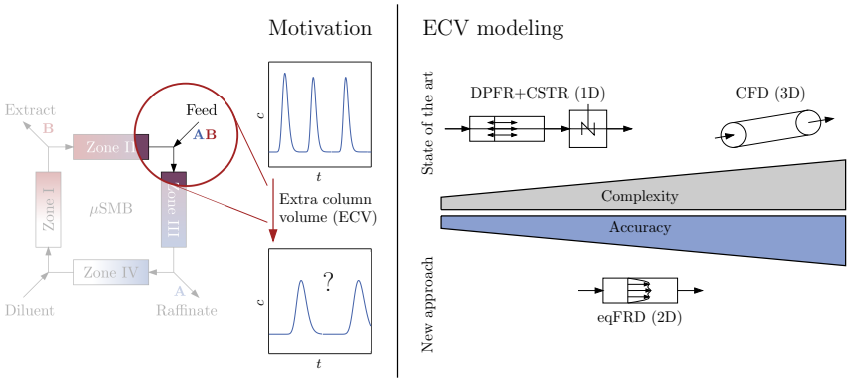

Figure 3.4: Graphical abstract to Chapter 7: The ECV can impact the retention time and peak shape in the µSMB system, influencing achieved yields and purities. Different approaches exist to account for ECV; the equivalent flow rate distribution (eqFRD) presented here is a compromise between complexity and accuracy tailored for miniaturized multi-column systems.

as outlined in Section 2.1.2. Chapter 5 already included simulations based on chromatography column models, but the other parts of the µSMB system, the ECV, was neglected. However, the ECV can greatly impact retention time and peak shape, as depicted in Figure 3.4 on the left-hand side, and should be considered to enhance process optimization. There are different approaches for the modeling of ECV, varying in complexity and accuracy, as depicted in Figure 3.4 on the right-hand side. While ECV models for miniaturized single-column chromatography systems usually aim for high accuracy, approaches with low complexity are usually applied for preparative multi-column setups. With the eqFRD, a new method was developed for the application in miniaturized multi-column setups. It is introduced in Chapter 7, which is based on the paper *'Modeling the Extra Column Volume of a Micro Simulated Moving Bed Chromatography System: Introducing the Equivalent Radial Flow Rate Distribution'*. Additionally, Chapter 7 features a comparison of this new approach with common ECV models of varying complexity for different ECVs.

Chapter 8: Integration of Capillary Chromatography Columns into a 3D Printed Microfluidic Multiport Valve for Miniaturized Multi-Column Chromatography

Juliane Diehm, David Achauer, Matthias Franzreb

Journal of Chromatography A, `https://doi.org/10.1016/j.chroma.2025.466245`

Although the µSMB system developed in this thesis is significantly smaller than conventional multi-column chromatography systems, it remains large compared to single-column micro-chromatography, where columns with diameters below 1 mm are applied. Further downscaling to these dimensions could also be beneficial for multi-column chromatography systems, for example to reduce response times in analytical applications. Chapter 8 explores further miniaturization by integrating capillary monolith columns directly into the 3D-printed valve system (Chapter 4), as depicted in Figure 3.5.

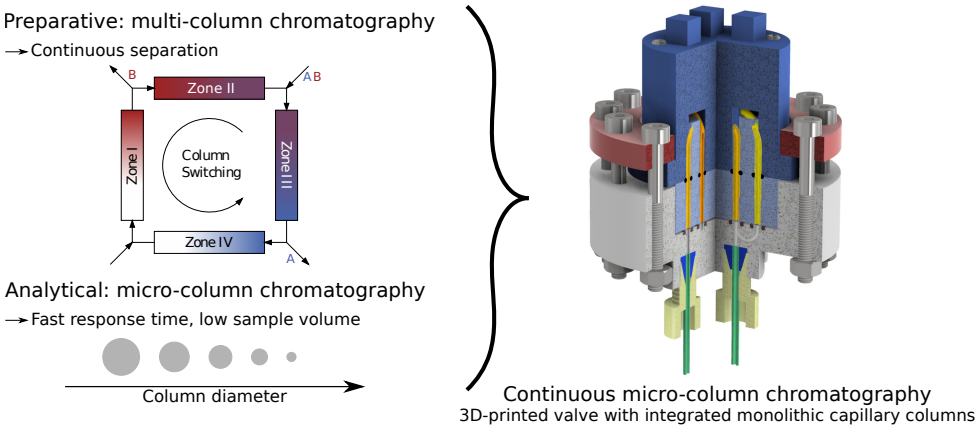

Figure 3.5: Graphical abstract to Chapter 8: To combine the strength of continuous chromatography with analytical micro-column chromatography, monolithic capillary columns are directly integrated into a 3D-printed valve system.

This study identifies the limitations of extreme downscaling for SMB applications and discusses alternative semi-continuous multi-column strategies that are be more feasible at this scale.

4. Configurable 3D Printed Microfluidic Multiport Valves with Axial Compression

Juliane Diehm[1], Verena Hackert[1] and Matthias Franzreb[1,*]

[1] Institute of Functional Interfaces, Karlsruhe Institute of Technology, Eggenstein–Leopoldshafen, 76344, Germany

Abstract

In the last decade, the fabrication of microfluidic chips was revolutionized by 3D printing. It is not only used for rapid prototyping of molds, but also for manufacturing of complex chips and even integrated active parts like pumps and valves, which are essential for many microfluidic applications. The manufacturing of multiport injection valves is of special interest for analytical microfluidic systems, as they can reduce the injection to detection dead volume and thus enhance the resolution and decrease the detection limit. Designs reported so far use radial compression of rotor and stator. However, commercially available nonprinted valves usually feature axial compression, as this allows for adjustable compression and the possibility to integrate additional sealing elements. In this paper, we transfer the axial approach to 3D printed valves and compare two different printing techniques, as well as six different sealing configurations. The tightness of the system is evaluated with optical examination, weighing, and flow measurements. The developed system shows similar performance to commercial or other 3D printed valves with no measurable leakage for the static case and leakages below 0.5% in the dynamic case, can be turned automatically with a stepper motor, is easy to scale up, and is transferable to other printing methods and materials without design changes.

Keywords
rotatory valve; rapid prototyping; polyjetting; digital light processing (DLP); sealing

published in *Micromachines*, https://doi.org/10.3390/mi12101247, licensed under a Creative Commons Attribution 4.0 International License (CC BY 4.0)

CRediT authorship contribution statement

Juliane Diehm: Conceptualization, Investigation, Visualization, Writing – original draft. Verena Hackert: Conceptualization, Investigation, Visualization. Matthias Franzreb: Conceptualization, Writing – review & editing.

4.1 Introduction

3D printing became a game-changer for the manufacturing of microfluidic chips [140, 141]. It not only simplifies manufacturing processes, but also enables the usage of microfluidic systems for a wide range of applications by combining increased configurability with high economic efficiency, especially for the manufacturing of prototypes [140, 142, 143]. While 3D printing was initially mainly used for the fabrication of molds and simple parts, complex chip designs and active components such as valves and pumps, which are essential for many microfluidic applications [144], can also be produced using 3D printing nowadays [23, 142].

For the 3D printing of microfluidic valves, two core approaches exist: for applications that allow an implementation with 2/2-way valves or a combination thereof, there is a broad spectrum of developed mechanisms, including but not limited to 4D printing, and new methods tailored to specific applications are constantly being further developed. 4D-printed valves react to an external stimulus like magnetic fields [145, 146], pH [147], or temperature [148] and thus change their switch position. Other mechanisms include membrane-like valves [149–151] and slope valves [152]. Further approaches can be found in numerous review articles [153–155].

In applications where 2/2-way valves cannot be used, e.g., when connections between different channels are to be changed, the rotor-stator principle, which is also utilized in many commercial valves, is employed: Morioka et al. developed a 3D printed stator in combination with a polydimethylsiloxane (PDMS) microfluidic chip and improved the response time and minimized band-broadening effects in a flow injection analysis system [156]. Su et al. developed a 3D printed flow injection system for coupling with inductively coupled plasma mass spectrometry (ICP-MS) [157], Chan et al. designed pump and valve systems for point-of-care diagnostics [158], and Munshi et al. designed a valve for sample injection volumes as low as 195 nL [159]. All those systems use radial compression of rotor and stator (only Su et al. used a combination of radial and axial compression by a slanted sealing surface [157]) in contrast to commercial valves, like Rheodyne® valves, that are usually compressed in the axial direction [160–162]. The difference between both approaches is illustrated in Figure 4.1. For the radial approach, the cylinder jacket surface of the rotor is the sealing surface and the compression of rotor and stator, and thus, the sealing is achieved by choosing the right fit for the manufacturing process. For the axial approach, the sealing surface corresponds to the base plate of rotor and stator. Although this design requires additional parts to compress rotor and stator, there are many advantages that accompany external compression: the compression can be adjusted, e.g., adapted to increasing wear-effects, it is easier to combine different materials as a precise fit is not as important as in the radial variant, and external sealing elements can easily be used to improve the sealing performance of the system.

In some cases, especially for applications requiring numerous switching operations between different valve positions, commercial axial compressed valves were integrated into 3D printed chips, e.g., for lab-on-valve systems: Mattio et al. developed a lab-on-valve platform with a 3D printed chip and demonstrated its applicability for the detection of cadmium and lead in water [163]. Cocovi–Solberg et al. used a similar system for various biochemical assays [143]. In all cases, a 3D printed stator was combined with a commercial rotor system, utilizing the rotor seal for sealing the system. While this approach is straightforward, it still has drawbacks since the rotor

has to be used as is, thus limiting designs to available configurations. In our opinion, this does not exploit the great potential of 3D printing entirely; at the same time, it is not trivial to design suitable 3D printed valves for applications where the valves need to be turned frequently and have high requirements on tightness and wear-resistance.

In this work, we adapted and tested the axial compression approach for 3D printing using polyjetting and DLP as printing techniques. In total, six different sealing concepts are tested. The tightness of the resulting system is evaluated using three different techniques. This approach enables the integration of 3D printable components like merges, diverges, and mixers in the stator as well as the rotor, thus we hope to further increase the impact of 3D printing on microfluidic chip fabrication and expand the field of applications.

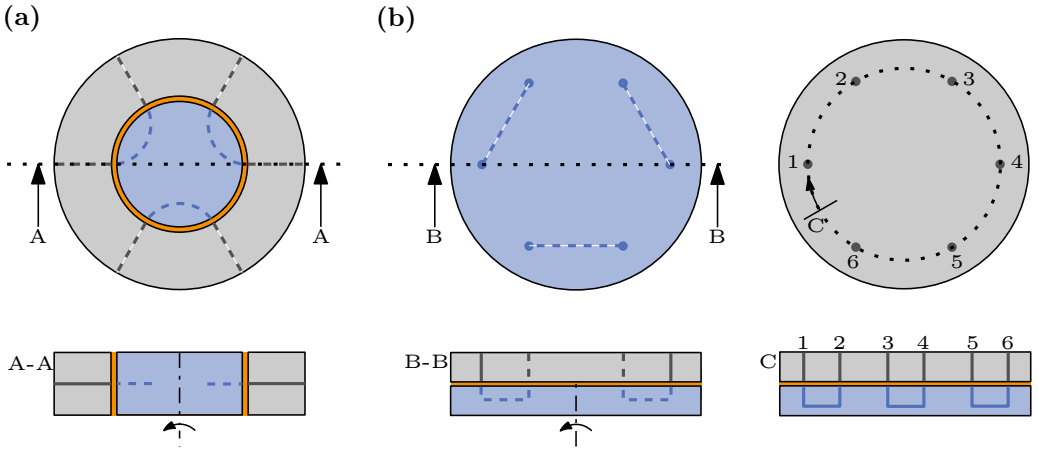

Figure 4.1: Schematic top and section view of a 6-port injection valve with radial compression (a) and axial compression (b). The rotor is shown in blue, stator in gray, and sealing gap in orange. For the axial compressed valve, an additional circular sectional view C is given, displaying interconnections of rotor and stator along dotted circle. To achieve tightness, additional parts are needed for compression with axial approach.

4.2 Materials and Methods

4.2.1 Valve Design and Fabrication

The valves were designed with the computer aided design (CAD) software Inventor Pro 2020 (Autodesk Inc., San Rafael, CA, US) and exported as stl-files for 3D printing. A 3/2-way valve (referred to as test valve) was designed to evaluate the different sealing concepts. The basic flow paths in rotor and stator can be seen in Figures 4.2a and 4.2c, detailed technical drawings of all parts are included in Appendix A (Figures A.1-A.3). All flow channels had a diameter of 800 µm. After a first assessment of different sealing concepts, an upscaled 13/4-way valve was designed based on the same concept; a basic connection scheme is given in Figures 4.2b and 4.2d, technical drawings are provided in Appendix A (Figures A.4-A.6). In this study, two different 3D printing techniques, polyjetting and DLP printing, were used to evaluate six different sealing concepts, which are explained in more detail in the following subsections.

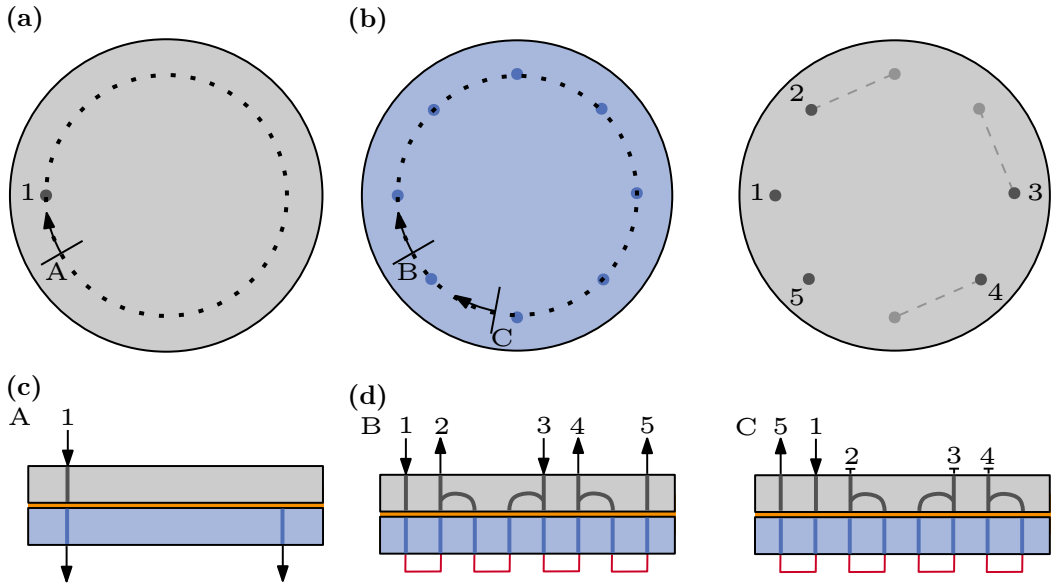

Figure 4.2: Schematic views of test setups. The stator is depicted in gray, the rotor in blue. (a) Top view of stator and (c) circular sectional view of a test valve with one inlet and two outlet options. (b) Top view of rotor and stator of an upscaled valve; rotor features 8 inlet/outlet connections, stator features 5 with additional merging/diverging channels integrated into stator plate. (d) Circular sectional views of two connection schemes of the upscaled valve. In both cases, the inlet/outlet connections of the rotor are short-circuited (no external connections). Left-hand side shows a case where all in- and outlets are used, and on the right-hand side, only one in- and outlet are connected.

4.2.1.1 Polyjet 3D Printing

For polyjetting an Object EDEN 360V (Stratasys, Rechovot, IL) was used. VeroClear was selected as printing material and SUP705 as support material (both produced by Stratasys as well). After printing, the parts were mechanically cleaned from support structures, and then put in a 2 M sodium hydroxide (Merck KGaA, Darmstadt, DE) solution for 1 h to dissolve remaining support material inside the microfluidic channels. Subsequently, the parts were cleaned with deionized water and dried before further usage.

4.2.1.2 DLP 3D Printing

For DLP printing, an ASIGA Max X35 (385 nm) (Asiga, Alexandria, AU) was used. Basic valve parts were printed with BV-007 microfluidic resin (Young Optics, Jena, DE). For 3D printed sealing elements, a highly fluorinated methacrylate based resin was prepared according to Kotz et al. [22] with Fluorolink MD700 (Solvay speciality polymers italy, S.p.A., Bollate, IT), 5 mg/mL phenyl-bis-(2,4,6-trimethylbenzoyl)-phosphinoxid (Sigma-Aldrich, St. Louis, MO, US) and 0.2 mg/mL Sudan Orange G (Sigma-Aldrich, St. Louis, MO, US). After printing, the parts were cleaned with isopropanol in an ultrasonic bath for 5 min twice. Printed support structures were removed and the parts were postcured with an Otoflash G171 polymerization device (NK Optik GmbH, Baierbrunn, DE). Independent of the used printer, 1/4-28" UNF threads were drilled after the printing process for external fluid connections with flangeless fittings, as this proved to be more durable than direct printing in previous work.

4.2.1.3 Sealing Concepts

All tested valves consist of three basic parts: a stator, a rotor and a cover used to compress the rotor and stator in axial direction with screws. A CAD-drawing of those parts as well as an example of the printed parts are given in Figures 4.3a and 4.3b. Depending on the respective concept, the parts were used as is, postprocessed, or additional sealing elements were inserted. For postprocessing, the 3D printed parts were polished with sanding sponge (3M Softback Sanding Sponge Grade Micro Fine, 3M, Saint Paul, MN, US) attached to an insert of a rotatory tool (NL). O-rings (FKM, 3 × 1 mm, Dichtomatik, Hamburg, DE), a silicone mat (1 mm, 40° shore A, exact plastics GmbH, Bröckel, DE), DLP printed sealings mats and combinations hereof were evaluated regarding their functionality as sealing elements. The 3D printed sealing mats had integrated O-ring-like structures, as can be seen in Figure 4.3c. Loctide 401 (Henkel AG & Co. KGaA, Düsseldorf, DE) was used to glue the respective sealing mats to the printed parts. In total, six different sealing concepts were tested; an overview is given in Table 4.1. Figure 4.3d shows an assembled test valve as well as a section and exploded view displaying the configuration of sealing concept 5 in detail. To evaluate the performance of the different concepts, sealing tests (see Section 4.2.2) as well as light microscope imaging of sealing surfaces and O-rings were performed. Microscope images were obtained using a Leica DM 2500M microscope (Leica Microsystems GmbH, Wetzlar, DE) in dark field mode.

Concept 5 was chosen for the design of the upscaled valve using polyjetting for printing. The upscaled valve has 8 instead of 1 intra-valve connections, and the sealing area is 2.7-times larger compared to that of the test valve. The single components and the assembled valve can be seen in Figure 4.4.

Table 4.1: List of tested sealing concepts.

Sealing Concept No	3D printer	Sealing Elements
1	Polyjet/DLP	-
2	Polyjet	-/Postprocessed: polished
3	Polyjet	Silicone mat
4	Polyjet	O-ring
5	Polyjet/DLP	Silicone mat & O-ring
6	DLP	Printed sealing mats

4.2.2 Sealing Tests

To evaluate the tightness of the 3D printed system, sealing tests with three different setups were performed. The details are given in the following subsections.

4.2.2.1 Static and Dynamic Sealing Test

For an initial static sealing test, the test valve was assembled (see Figure 4.3d) and the screws were tightened such that the resulting torque needed to turn the valve was between 80 and 100 Ncm. The inlet of the test valve was then connected to an Äkta Purifier system (Cytiva Europe GmbH, Freiburg, DE). The tightness of the valve was tested at different pressures, and the pressure was adjusted by increasing the flow of water through the valve with the pump of the

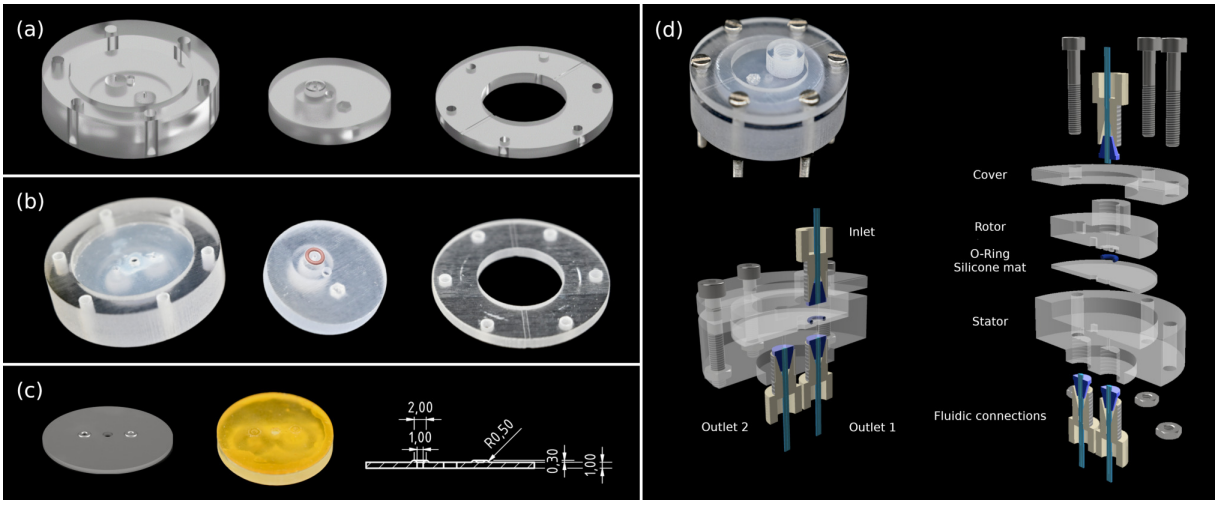

Figure 4.3: Design and implementation of the test valve: (a) CAD drawing of stator, rotor, and cover; (b) 3D printed rotor, stator, and cover: sealing area of the rotor is covered with a silicone mat, and an O-ring is placed in respective groove in rotor. Parts were printed with polyjetting; (c) from left to right: CAD drawing of a 3D printed sealing mat with integrated O-ring-like structures, 3D printed sealing mat, technical drawing of the sealing mat; (d) top-left: assembled 3D printed test valve; bottom-left and -right: section and exploded view of a CAD drawing of sealing concept 5 showing placement of respective sealing elements.

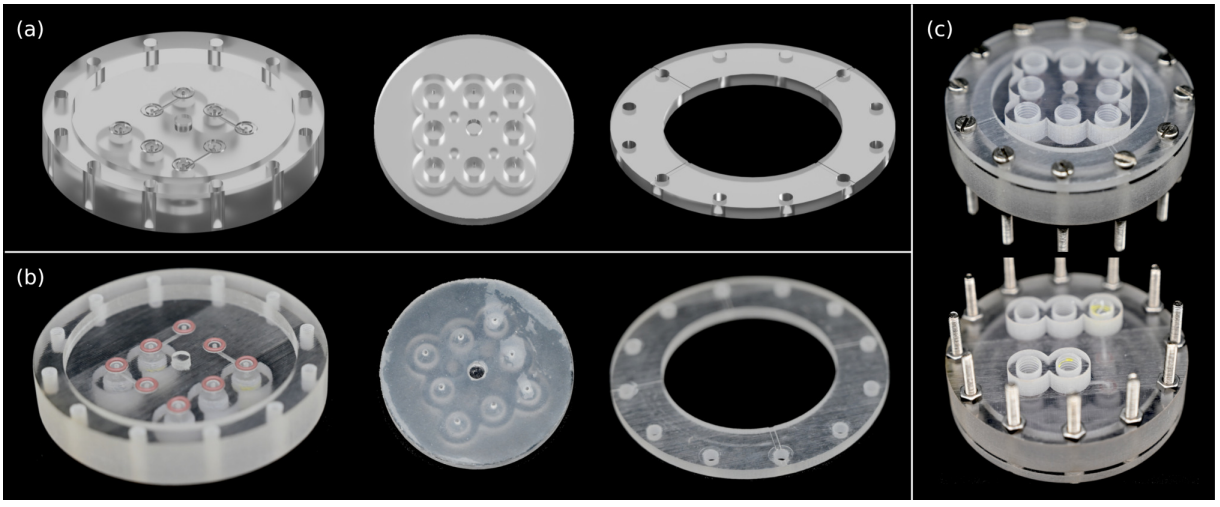

Figure 4.4: Design and implementation of the upscaled valve: (a) CAD drawing of stator, rotor, and cover; (b) 3D printed rotor, stator, and cover: sealing area of rotor is covered with a silicone mat, and O-rings are placed in respective grooves in stator; parts were printed with polyjetting; (c) top and bottom view of assembled upscaled valve.

Äkta. Each pressure was kept for 10 min before increasing to the next level (approximately 1 bar steps). The leakage of the valve was determined by optical examination, which was possible as all valve parts were printed with transparent materials. This method is less accurate than the other methods used, but nonetheless gives a first impression whether a concept is suitable at all. The experiment was stopped if a maximum pressure of 15 bar was reached without the observation of leakage. This test was repeated with test valves of all sealing concept configurations.

In the next step, the abrasion of the respective sealing elements was tested with the dynamic sealing test. This experiment was performed with all test valves that were tight at a pressure of 15 bar in the previous static test. The setup was as described before, but the pressure was kept constant at 8 bar, and every 30 s the valve was manually switched from outlet 1 to outlet 2 (compare Figure 4.3d) until 5 complete rotations were reached. The flow was stopped during the rotation.

4.2.2.2 Influence of Compression and Pressure

For further tests, to determine the influence of compression and pressure on the sealing performance, the upscaled valve was used. The valve was connected to an OB1 MK3+ (4 channels, −1,000–6,000 mbar) microfluidic flow controller (Elvesys, Paris, FR) as depicted in Figure 4.2d (left-hand side). The leakage of the system was determined by weighing the valve before and after the experiment with an analytical balance (Adventurere AX224, OHAUS Corporation, Parsippany, NJ, US). To compensate for swelling effects of the 3D printed material, the system was initially flushed with water for 1 h at a pressure of 500 mbar. Firstly, the pressure provided by the microfluidic flow controller was kept constant at 500 mbar, while the axial compression of the valve was varied so that the required torque needed to turn the rotor was between 20–100 Ncm. The valve was rotated every 30 s by 90° for 10 min using a stepper motor (PD60-3-116-TMCL, TRINAMIC Motion Control GmbH & Co. KG, Hamburg, DE). The experiment was run for 10 min and was performed in triplicates. As a control, the same experiment was performed without switching the valve.

In a second test series, the torque was kept constant at 30 Ncm and the pressure was varied between 50 and 1,000 mbar. The valve was again turned by 90° every 30 s, and the experiment was run for 10 min and performed in triplicates.

4.2.2.3 Interplay between Valve and Flow Source

In a third sealing test, the valve's performance was evaluated using flow sensors (SLI-1000, Sensirion AG, Stäfa, CH) connected to both the inlet and the outlet of the system. The setup was as depicted in Figure 4.2d (right-hand side) using only one inlet and outlet port of the valve stator. The microfluidic flow controller operated at 350 mbar as well as the piston pump P9 A of an Äkta Pure (Cytiva Europe GmbH, Freiburg, DE) at a flow rate of 200 µL/min were used as pressure sources. The flow rates were recorded for 10 min, while the valve was again turned by the stepper motor every 30 s. For comparison, the flow rates at the inlet and outlet of the column valve of the Äkta were measured. The column valve was switched every 30 s between position 1 and 2. Afterwards the flow rate measurements were divided into 30 s intervals for data evaluation, with one switching process taking place in each interval. To compensate for any differences of the

flow rate measurements between the used flow rate sensors, both flow rate sensors were connected in series and the flow through both sensors was measured for 10 min. The experimental results were adjusted according to the observed difference as described by Equation (4.1), with $V_{\mathrm{in,meas}}$ and $V_{\mathrm{out,meas}}$ being the total measured volume that passed through the inlet and outlet flow sensor, respectively, in a 30 s interval during an experiment and $V_{\mathrm{in,SC}}$ and $V_{\mathrm{out,SC}}$ being the total volumes measured with the respective sensors during the sensor comparison.

$$\mathrm{Leakage}(\%) = \left(\frac{V_{\mathrm{in,meas}} - V_{\mathrm{out,meas}}}{V_{\mathrm{in,meas}}} - \frac{V_{\mathrm{in,SC}} - V_{\mathrm{out,SC}}}{V_{\mathrm{in,SC}}} \right) \cdot 100\% \tag{4.1}$$

4.3 Results and Discussion

4.3.1 Evaluation of Sealing Concepts

To identify suitable sealing concepts the valve was first treated as a static system as those are less complex to seal than dynamic ones [164]. The tightness of the different systems in dependence of the applied pressure is given in Figure 4.5 on the left side. The first two sealing concepts, which do not use specific sealing elements, leaked immediately, even when no measurable pressure was applied. This observation was made regardless of the used printing technique and is caused by the rough surface of the 3D printed parts which always leads to a small gap between rotor and stator, even if both parts are strongly compressed [159]. This result is consistent with reports from literature, where either lubricants like vaseline [158], teflon spray [157] or teflon wrap [159] were used or only the rotor was 3D printed with an elastic PDMS stator that ensured sealing [156,165]. Further details such as microscope images regarding the structure of the sealing surfaces are given in Figure A.7 in Appendix A. All valve concepts using additional sealing elements were tight up to a pressure of at least 15 bar, regardless of the design, which is to the best of our knowledge the highest pressure applied to any 3D printed microfluidic valve so far and clearly shows the benefit of the external sealing elements used in this study.

Based on these results, the dynamic test was performed with designs 3–6 only to compare the wear resistance of the different sealing elements. Figure 4.5 (right-side) shows designs 4, 5, and 6 showed unchanged tightness after 5 rotations, and it was only with design 3, which uses a silicone mat, that leakage occurred after 2 rotations. Hence, the silicone mat can compensate for the roughness of the 3D printed parts in the static sealing test, but cannot be used for real-world operation. Thus, O-ring-based concepts seem to be the most promising. In our tests, we neither observed any difference between a classic O-ring and the 3D printed O-ring-like structures, nor between the two printing techniques, even though the printers have different resolutions and tolerances and different printing materials were used. Consequently, the presented concept enables not only a simple transfer to new printing methods or materials without the need for preliminary test to determine fits and tolerances, but it also allows for an easy usage of a variety of sealing elements, in contrast to the traditional radial concept, where rotor and stator are typically transitionless or press-fitted, which makes it complicated to insert additional elements into the sealing gap.

Long-term tests showed that the reusability of O-rings of sealing concept 5 is superior to sealing concept 4, as the wear of the O-rings on the rough surface of the 3D printed parts is higher

compared to that of the smoother silicone mat. Microscope images of O-rings after 20 rotations with and without a silicone mat on the opposite sealing surface show only slight deformations of the O-rings with the silicone mat and huge abrasions without. The respective images can be found in Figure A.8 in Appendix A. Therefore, concepts 5 and 6 show the best performance for long-term applications, and the 5th concept was chosen for further studies. In this particular case, concept 6 was not considered because the building platform of the DLP printer is too small for the upscaled valve. In principle, however, this approach is just as promising and has similar performance. The upscaled system is presented in Figure 4.4. In the static and dynamic sealing test, this valve shows identical performance to the test valve. For this system, the dynamic sealing test was repeated with 50 rotations without the occurrence of leakage, indicating that the system is suitable for long-term applications.

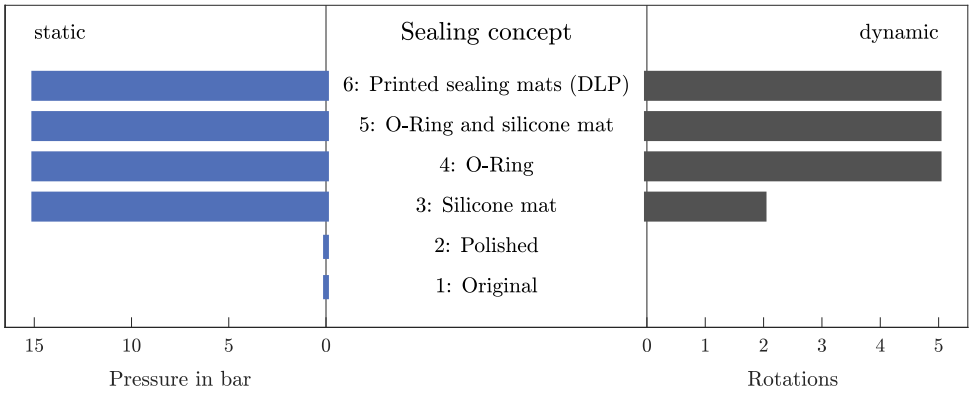

Figure 4.5: Comparison of tested sealing concepts; left: pressure stability of respective sealing concepts (static sealing test); right: influence of number of rotations on tightness of test valves (dynamic sealing test).

4.3.2 Axial Compression and Pressure

In the previous test, the flow was turned off during the switching process. This is not always practicable, and thus another test was performed with continuous flow. Simultaneously, the influence of the axial compression on the valve's tightness was evaluated. The results are given in Figure 4.6a. The leakage was calculated by dividing the measured mass gain of the valve by the overall mass flow through the valve. It was below 0.06% of the system flow in the static case with a torque ranging from 30–100 Ncm. These values are in the range of measurement inaccuracy (the average standard deviation of weighing the valve in relation to the overall mass flow is 0.04% for all performed experiments), confirming the tightness of the system in the static case and the results from the previous tests. The leakage stream increased above 0.5% at a torque of 20 Ncm, indicating that the contact pressure is too low to ensure tightness.

In the dynamic case, the leakage has a minimum at 30 Ncm with an average leakage of 0.15%. This corresponds to a leakage of 0.15 µL/min which is in the same order of magnitude as the leakage of commercial valves (e.g., leakage < 0.1 µL/min for Äkta Valve INV-907 [166]), however it has to be kept in mind that commercial valves usually are tested at higher pressures. The leakage increases for lower torques due to insufficient compression, while it increases at higher torques

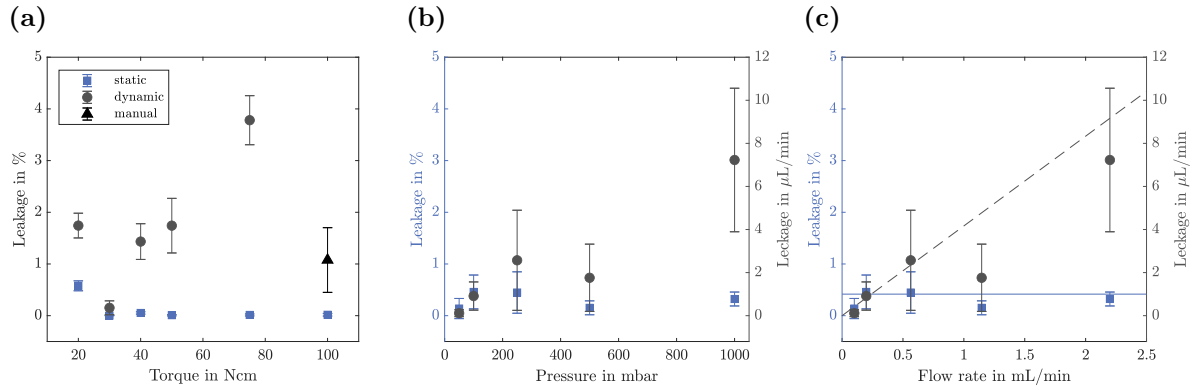

Figure 4.6: Influence of axial compression and pressure on leakage; (a) leakage stream of upscaled valve in % in dependence of torque required to rotate valve. Experiments were performed at a pressure of 500 mbar in triplicates; (b) influence of applied pressure on leakage stream of upscaled valve. Experiments were run at a torque of 30 Ncm and performed in triplicates; (c) results from (b) shown in dependence of flow rate instead of pressure. The blue line shows maximum relative dynamic leakage, and the dashed gray line maximum absolute dynamic leakage under experimental conditions.

due to the decreasing accuracy in positioning by the motor (the probability of the motor to miss steps and thus turn less than 90° increases with increasing torque). Theoretically, one would expect an increasing sealing effect with increasing contact pressure, but here the opposite is the case. To verify that this effect is indeed caused by the inaccuracy of the motor, an experiment with a manual operation at a torque of 100 Ncm was performed. Due to the increased precision in manual positioning at high torques, the leakage is lower compared to that of positioning with the motor. However, the switching time is about 8 times higher (approximately 1 s during manual operation and 0.125 s using the motor according to manufacturer specifications). This explains why the leakage is still higher with manual operation at 100 Ncm compared to that of operation with the motor at 30 Ncm.

These dependencies in combination with the complete tightness of the system in the static case lead to the assumption that leakage only occurs during the switching process. This conclusion is further confirmed by the results shown in Figures 4.6b and 4.6c, where in both cases the relative and absolute leakage is shown in dependence of pressure and flow rate, respectively. The relative leakage is below 0.5% for all cases, whereas the absolute leakage seems to increase with increasing pressure/flow rate. As the switching time is constant, it is reasonable that the relative leakage is approximately constant while the absolute leakage increases. The expected leakage streams during switching if the valve had no sealing effect during rotation can be calculated by multiplying the overall switching time with the respective flow rate. In Figure 4.6c, those expected values are given in a solid blue line for the relative leakage and in a dashed gray line for the absolute case. The mean of the measured values is about 75% of the predicted value for total leakage during switching processes; taking into account the standard deviation, the values are in the same range.

Dynamic sealing problems cannot be sealed 100% [164, 167]. A relative leakage of less than 0.5% is small compared to uncertainties in common detection methods like UV/Vis spectroscopy,

where the uncertainty is in the single-digit percentage range [168], and it is thus questionable if it would be noticeable in an experiment. At the same time, the case tested here represents an extreme test scenario in which the valve was switched more frequently than in most common applications; when used as an injection valve, for example, only one switching process is required per experiment. A visible leakage was only observed at a torque of 80 Ncm and a pressure of 1000 mbar, respectively, even then, only a thin film of liquid was visible in the sealing gap, which wouldn't be noticeable if the parts weren't transparent.

4.3.3 Interplay between Valve and Flow Source

In former studies of 3D printed radial valves, water leakage tests were performed but it is not specified how the systems tightness was determined [156, 165], making the results hard to compare. In addition, the tightness of one particular system may also be subject to the respective experimental setup, thus it is not common in literature as well as in manufacturer information to give the intrinsic leakage streams for dynamic sealing systems like valves. Nonetheless, it is of interest how different systems react during a valve switching process. For this purpose, the flow rate at the valve in- and outlet were measured during switching. This method is less accurate for the determination of leakage compared to weighing, but as the measurement can be done in-line interesting insights in processes during the switching can be obtained. In this study three different setups were compared which used either a microfluidic flow controller or a piston pump as flow source, combined with the 3D printed valve or the column valve of an Äkta.

The results are given in Figure 4.7, showing exemplarily the inlet flow rate in a solid blue line, the outlet flow rate in the red dashed line and the system pressure in a dashed dotted yellow line for the different setups. Due to different accuracies of the time stamps of used flow and pressure sensors, there is a maximum possible offset between the shown pressure and flow rate curves of 0.5 s. For the 3D printed valve, independent of the used pressure source, two different cases can be observed for the switching process, which are depicted exemplarily in Figures 4.7a and 4.7b for the valve connected to the piston pump. The corresponding graphs for the microfluidic flow controller can be found in Appendix A (Figure A.9). In Figure 4.7a, both flow rates drop at the beginning of the switching process, and afterwards, the inlet flow rate rises to almost 350 µL/min after approximately 200 ms. After 600 ms, both flow rates recover their initial level. The pressure rises above 400 mbar before dropping to the initial value again. In Figure 4.7b, both flow rates perform a double peak during the switching process, first dropping below 50 µL/min, then rising above 300 µL/min. The pressure rises above 500 mbar before dropping to the initial value again. Figure 4.7c shows that both flow rates as well as the pressure drop to a value below 50 µL/min or 50 mbar, respectively, before rising to the original value for the column valve connected to the piston pump.

When comparing Figure 4.7a to 4.7b, both curves start similarly, but then in 4.7a the inlet flow rate increases without the outlet following, indicating leakage. This is probably caused by the built-up pressure caused by the piston pump. For a tight system, a behavior as depicted in Figure 4.7b is expected. During switching, all flow paths are blocked, and thus the system pressure increases. After the flow channels are connected again, the flow can build up, the flow rates increase due to the increased pressure, thus decreasing the pressure until both flow rates

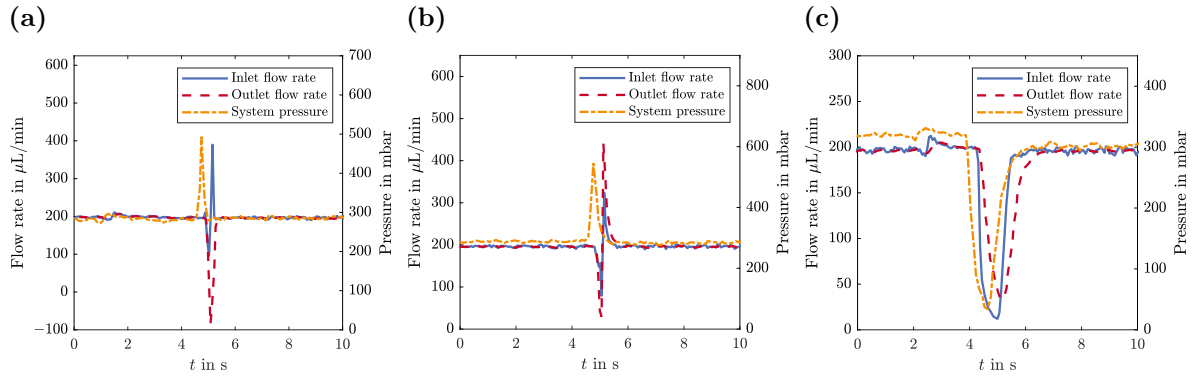

Figure 4.7: Flow rate profiles at valve in- and outlet and system pressure; (a) 3D printed valve with piston pump, not tight case; (b) 3D printed valve with piston pump, tight case; (c) Äkta column valve with piston pump. Due to different accuracies of time stamps of used flow and pressure sensors, there is a maximum possible offset between shown pressure and flow rate curves of 0.5 s.

and pressure drop to the original value. In contrast, for the Äkta system the pressure drops during the switching process. As the pressure sensor is located directly after the piston pump, the only plausible explanation for this is that the pump stops pumping during valve switching. This also causes both flow rates to drop during the switching processes without the occurrence of an overshoot of flow or pressure. While this is certainly favorable to increase the system's tightness during the switching process as well as to prevent pressure or flow spikes after the switching, it also leads to a longer switching time. In this experiment, the switching time is two-times higher compared to that of the 3D printed system.

Both scenarios depicted in Figures 4.7a and 4.7b were observed for the 3D printed valve in dependence of the current switching position but independent of the used flow source. In conclusion, leakage occurs sporadically for the 3D printed valve, indicating that the used 3D printers have a noticeable manufacturing tolerance. Nonetheless, previous experiments showed that the absolute leakage is at a very low level that won't interfere with the majority of applications. Even if it would be relevant in some cases, it can be prevented by turning the pump off during switching, as it is done by the Äkta system.

Figure 4.8 shows a comparison of observed leakages overall switching processes for the different setups. All mean values are in the range of 0.2–0.35%. The standard deviation is ±0.5% for both experiments with the 3D printed valve, and a little less (±0.3%) for the experiment with the column valve. This is in accordance to the manufacture's specifications, where the repeatability of the sensors is stated to be below 0.5% of the measured value. The mean as well as the standard deviation of the 3D printed valve is slightly larger compared to the value of the Äkta system in both tested cases, which is plausible due to higher manufacturing tolerance of 3D printing, resulting in different observed switching scenarios with leakages occurring sometimes but not always. This was not observed for the Äkta system, as the flow was stopped during the switching in this case. The difference of the leakages are too small to distinguish any differences between the setups, as all mean values as well as zero (no leakage) are in the range of the observed standard deviations. This shows that within the accuracy of our measurements the sealing of

the 3D printed valve is comparable to a commercial one. In addition, this experiment gives a good insight in the processes taking place during switching and can be used as a starting point for further optimization of the 3D printed valve system.

Table 4.2 summarizes the advantages and disadvantages of different valve manufacturing approaches and lists the features of applications that the manufacturing approaches are suitable for.

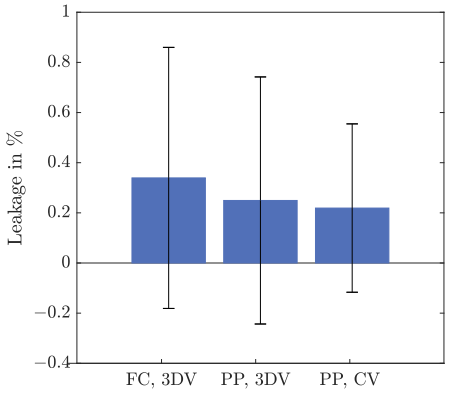

Figure 4.8: Difference in integrated in- and outlet flow for three tested setups. FC – microfluidic flow controller; 3DV – 3D printed valve; PP – piston pump; CV – column valve of Äkta system.

4.4 Conclusions

In this study, we developed and tested an axially compressed, 3D printed microfluidic multiport valve. The valve's tightness was evaluated with three methods: optical examination was used for a first qualitative analysis of the systems. Weighing proved to be the most accurate method for quantitative studies. Flow rate measurements are less sensitive for quantitative measurements if only slight differences in flow rates can be observed, but can provide additional insights into the processes during switching. The designed valve had a comparable performance to that of radial 3D printed multiport valves and the commercial valve system evaluated in this study, with no measurable leakage for the static case and leakages below 0.5% in the dynamic case. Six sealing configurations with additional sealing elements were examined. A concept using O-rings and a silicon sealing mat as external sealing elements showed the best performance, especially for long-term applications. The proposed approach could easily be transferred to other 3D printers using different printing materials without the need for preliminary experiments or the adjustment of the fit of rotor and stator. The systems performance was optimized through the adaption of the axial compression in a setup where the valve was switched automatically with a stepper motor. In addition, the valve can easily be scaled up in regard to sealing surface and number of channels and is highly costumizable, as the rotor as well as the stator are 3D printed. Thus, additional elements like merges, diverges, microfluidic mixers, or external fluidic connections can directly be integrated into all fluidic paths of the valve, minimizing the dead volume of the corresponding setup. This contributes to lab-on-valve applications where the valve is designed according to the respective application and not vice versa, increasing the versatility of 3D printed microfluidic applications.

Table 4.2: Comparison of different valve designs.

Manufacturing	**Advantages**	**Disadvantages**	**Recommended Applications**
Commercial	+ High pressures + Reliable	− Not customizable	• Standard applications • High pressure requirements
3D printed			
Radial compression	+ Customizable + Small footprint	− No external sealing elements − Adjustment of fit required	• Custom applications with flow paths of low complexity • Low pressure requirements
Axial compression	+ Customizable + Additional sealing elements	− Comparable high footprint − Additional part (cover)	• Custom applications with complex flow paths • Low to medium pressure requirements
Printing techniques			
Polyjetting	+ Planar surface		• Valves with large sealing surfaces
DLP	+ Amall channel diameter ($<$0.8 mm)		• Deadvolume is critical

5. Development of a 3D Printed Micro Simulated Moving Bed Chromatography System

Juliane Diehm[1], Tim Ballweg[1] and Matthias Franzreb[1,*]

[1] Institute of Functional Interfaces, Karlsruhe Institute of Technology, Eggenstein–Leopoldshafen, 76344, Germany

Abstract

In the 1960s, chromatography processes were revolutionized by the invention of simulated moving bed (SMB) chromatography. This method not only enhances the separation performance and resin utilization in comparison to batch-chromatography, it also has a much lower buffer consumption. While SMB chromatography nowadays is applied for a wide range of industrial applications, it was never transferred to the micro-scale (in regards to column and system volume). In our opinion a micro simulated moving bed chromatography system (µSMB) would be a useful tool for many applications, ranging from early process development and long term studies to downstream processing of speciality products. We implemented such a µSMB with a 3D printed central rotary valve and a microfluidic flow controller as flow source. We tested the system with a four zone open loop setup for the separation of bovine serum albumin (BSA) and ammonium sulfate with size-exclusion chromatography. We used four process points and could achieve desalting levels of BSA ranging from 94% to 99%, with yields ranging form 65% to 88%. Thus, we were able to achieve comparable results to common lab scale processes. With a total dead volume of 358 µL, including all sensors, connections and the valve, this is, to the best of our knowledge, the smallest SMB system that was ever built and we were able to perform experiments with feed flow rates reaching as low as 15 µL/min.

Keywords
continuous chromatography; microfluidics; µSMB; continuous buffer exchange; process miniaturization

published in *Journal of Chromatography A*, https://doi.org/10.1016/j.chroma.2023.463928,

CRediT authorship contribution statement

Juliane Diehm: Conceptualization, Methodology, Investigation, Software, Visualization, Writing – original draft. Tim Ballweg: Methodology, Investigation, Visualization, Writing – review & editing. Matthias Franzreb: Conceptualization, Writing – review & editing.

5.1 Introduction

Continuous manufacturing is of rapidly increasing importance to the biopharmaceutical industry as more product can be produced in less time and at lower costs compared to batch processes [169–171]. Within biopharmaceutical DSP, chromatography is one of the most frequently applied unit operations and hence special attention is paid to this step [10,169]. SMB is a frequently considered continuous implementation of chromatography [10, 172]. It combines the common advantages of continuous processes, like higher productivity and consistent product quality [10, 171, 173], with the high efficiency and selectivity of a counter current operation, resulting in better resin utilization and lower buffer consumption in comparison with batch chromatography [174, 175]. Due to its numerous advantages, SMB has become a state of the art separation technique for many separation tasks in different industries, like the separation of *p*-xylene from other xylenes (Parex process) in the petrochemical industry [14], the separation of isomers in the sugar industry [15], or the enantioseparation for fine chemicals and pharmaceuticals [39].

However, the advantages of the SMB principle come at a price; as a result of the greater number of design and process parameters, like number of columns per zone and the zone flow rates, the process development is more sophisticated [10]. This can be a challenge, especially for the biopharmaceutical industry, where only a limited amount of product is available at early development stages. To save product, processes are therefore usually scaled down during process development [176–178]. This approach is particularly beneficial for continuous processes, as they have higher throughput than batch processes and hence greater product amounts are required to perform one experiment, especially if the process should be run over a longer time frame in steady state. However, with current lab and pilot scale SMB devices this can only be done to a certain limit, as the instruments provide stable flow rates merely in the mL/min range and the dead volumes of the systems are too high to handle small volumes efficiently.

In our opinion, a further down scale to the µL/min range has the potential to save many resources during process development in terms of time, resin and sample, especially for long-term studies, e.g., to investigate resin reusablilty, cleaning protocols or process stability. Thus, we decided to develop a µSMB system which allows both the downscaling of the flow rates and the column volumes into the µL range. At the same time, we aim to maintain the benefits of current lab scale systems, like the easy adaptability to various process variants and the adjustment of the number of columns in a short time frame as well as the option to use the system as a disposable device.

In 2006, Subramini and Kurup showed in a theoretical study, that a downscale of the SMB principle to the µL-range in regard to column volume can separate a mixture of phenol and *o*-cresol with high yield and purity [179]. However, the study was completely theoretical and solely based on the separation performance of the columns. Important hardware considerations were not addressed and to the best of our knowledge, this theoretically study was never experimentally validated. Also some SMB equipment vendors already hold patents on so called *micro SMB systems*, but in this case the term *micro* seems to be used to distinguish from preparative SMB systems that are designed for product throughput of several tens of tons per year with column volumes in the m^3 range and not a reference to the actual scale of the system. The mentioned systems either have flow rates in the mL/min ballpark [180], or the used columns have a column

volume of several mL [94]. These systems are comparable to the aforementioned lab, pilot or small scale systems [181, 182]. Besides the commercially available systems, there are some self built SMB devices that work with lower flow rates, i.e. 200-900 µL/min, e.g., the HPLC-SMB of Pedeferri et al. [183] or the ÄKTA-SMB by Kröber et al. [184], but they still use columns with a column volume of several mL.

In this paper, we present our approach for the development of a µSMB system. First, we discuss our design considerations regarding the hardware wise implementation of the µSMB system, followed by a proof of concept study. Here, we used four process points for the desalting of the protein BSA from the salt AS by SEC-SMB to showcase the functionality of the setup. Finally, we used process modeling and simulation to assess the performance of our system.

5.2 Design Considerations

First we made a general assessment of the points that are critical for the downscale in order to maintain the SMB functionality. We won't give a detailed description of the SMB principle here, for this we refer to the extensive literature, e.g., [39, 40, 46, 185] or Section 2.1.2.1. Examples for SEC-SMB processes can be found in [186–188].

In a classical SMB setup, the binary separation of two components is achieved in zones II and III by adjusting the mean residence time in the respective zone between the retention times of both components [46]. This is achieved by cyclic switching of the columns in combination with setting different flow rates in the SMB zones. Hence, the generation of precise, fluctuation- and pulsation-free flow in each of the SMB zones is essential for the functionality. The flow rate deviation of many commercial lab scale systems is specified as $\pm 2\%$ with a working range in the mL/min scale [189, 190]. This results in absolute flow rate deviations in the $\pm 100\,\mu L/min$ scale, which is within or even above the working range of a potential µSMB system. The lab scale systems usually use piston pumps as flow source, however, they are not suitable for the miniaturization of chromatography systems, as they are comparably large and prone to pressure pulsations [191]. In the field of microfluidics, other pressure sources, like elctroosmotic pumps [192] or pressure driven microfluidic flow controllers [193,194] are more commonly applied [191]. We decided to use a pressure driven microfluidic flow controller in combination with a closed-loop flow rate control, as this system is ideal for the parallel generation of multiple flows in the µL/min range [195].

Even more important than the zone flow rates are the separation performances of the respective zones. Besides the chromatography columns itself, the system volume (also referred to as dead volume) can have a major influence on the system's separation performance [196]. The effect of dead volume on SMB processes has been extensively studied: Generally, the dead volume should be kept as low as possible, especially if high purities are required [197]. Particularly components that induce mixing effects, like check valves and pumps have a huge impact on the separation efficiency and should therefore not be placed between the columns [44]. Hence, we decided to implement the µSMB as an open-loop setup; this way it is not necessary to place a recycle pump between zones one and four. The diluent can still be recycled offline if required, e.g., by cyclical switching of waste and diluent reservoir [183].

The remaining contributions of the capillary dead volume (tubing and valve) can be divided into two portions:

(1) It causes a time delay, as the components need time to travel through the dead volume. This can be accounted for during the determination of the process point, e.g., by adapting the species retention times or by increasing the switching time [44]. Under the assumption that the dead volume is symmetrically distributed throughout all zones, this does not present a limitation for the downscale [198].

(2) It induces peak broadening while the species passes through the dead volume. This effect can decrease the separation performance of the system and thus should be considered [44]. Here, the dead volume between the chromatography columns is of particular importance [196], as it has a direct influence on the respective zone's resolution.

Usually, the chosen valve system has the greatest impact on the system's inter-column dead volume, not only due to its own volume, but also because it determines the connection scheme [43]. The first SMB systems featured one central rotary valve but nowadays common commercial lab-scale systems as well as the aforementioned custom SMB systems use valve systems consisting of either several multiport or 2-way valves [43]. These systems have the advantage that they can easily be adapted to a varying number of columns and that they can be used in various configurations, as the ports can be switched independently. This way, numerous processes can be realized on one system, which is especially useful in process development. On the other hand, these systems have the disadvantage that the connection scheme with the multiple valves requires lots of tubings which results in a higher dead volume compared to systems with a rotary central valve [43]. Hence, we decided to use the the original approach with one central rotary valve.

Besides the lower flexibility, typically mentioned disadvantages of this approach are that the systems are prone for cross-contamination and leakage. The cross-contamination results from commonly used channels for multiple streams that are necessary to connect all streams with all columns when both in- and outlet streams and columns are connected to the valve's stator. Both disadvantages have less impact in case of a µSMB: As the columns are smaller, they can be connected and turned with the valve's rotor. This enables a connection scheme without cross-over-channels, reducing the risk of cross-contamination. In addition, the whole valve is much smaller which makes the sealing of the system much easier. The reduced flexibility of rotary valves can be overcome by using 3D printing for the manufacturing of the valve system. This way, it can be easily adapted and manufactured in the time frame of one day in order to change the system to another process or a different number of columns. In the following sections, a detailed description of the system is given.

5.3 Materials and Methods

5.3.1 Experimental Setup

In this section, the general setup of the µSMB is explained. In addition, further details about the flow control and the used chromatography columns are given.

5.3.1.1 General Setup

The proposed µSMB system is a four zone open-loop setup with one column per zone. Figure 5.1 shows an instrument and piping diagram of the system. The experimental setup is depicted in

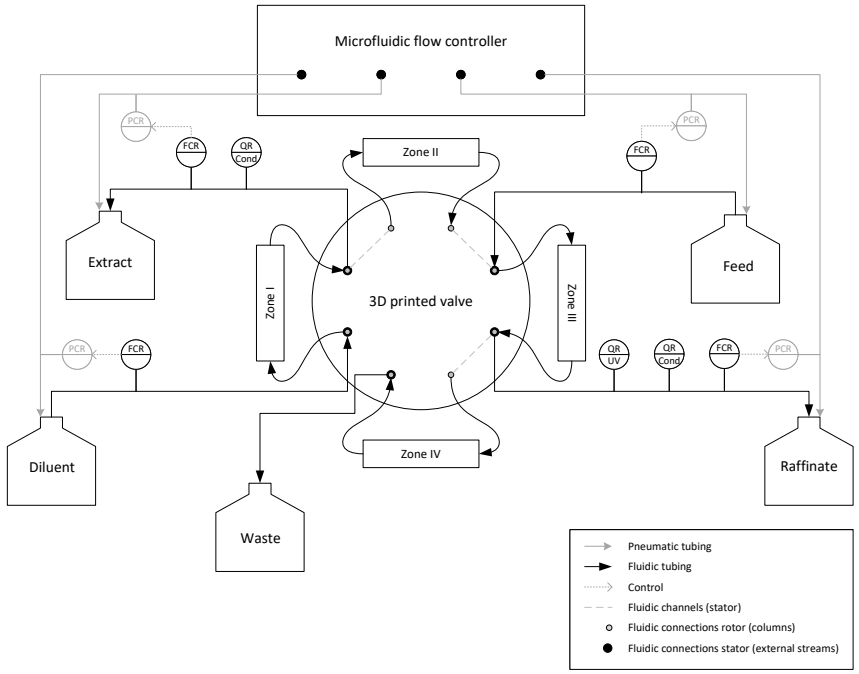

Figure 5.1: Instrumentation and piping diagram of the used SMB setup. FCR – Flow–Control–Record; PCR – Pressure–Control–Record; QR – Quality–Record.

Figure 5.2. The SMB functionality is realized with a 3D printed central rotary valve, whose manufacturing process and characterization has been described in Chapter 4. Detailed CAD drawings of all valve parts are included in Appendix A (Figures A.4-A.6). The rotary valve was implemented as a two disk design, where the columns are connected and moved with the valve's rotor, as this is in the case of miniaturization particularly promising [182]. The valve's stator contains channels to connect the chromatography columns as well as for the addition and withdrawal of external streams. On the rotor, the ports connecting the chromatography columns are organized in two concentric circles, one for the column-inlet-ports and one for the column-outlet-ports. All ports form a rectangle. This way the distance between the ports is minimized. Furthermore, the cross-contamination risk between the in- and outlets is reduced, as they follow different trajectories (for an illustration of the difference of this approach and one where all ports are placed on one circle, see also Figure B.10 in Appendix B). The chromatography columns are aligned in a horizontal rectangle and connected to the rotor and the motor shaft with a 3D printed adapter. This layout allows for an efficient connection of the columns to the valve. The valve is turned with a stepper motor (pan drive PD60-3-1161, TRINAMIC Motion Control GmbH & Co. KG, Hamburg, DE). The system flow is generated with a microfluidic flow control system (OB1 M3K+, Elveflow, an Elvesys brand, Paris, FR) in combination with flow sensors (SLI-1000, Sensirion AG, Stäfa, CF) in diluent, extract, feed and raffinate streams. The applicable flow rate range is defined by the measuring range of the flow sensors (here: 15-1000 µL/min) and the maximum pressure of the microfluidic flow controller (here: 6 bar) and can be adapted (if required) by choosing different hardware. The system is also equipped with conductivity sensors (ÄKTApurifier, Cytiva Life Sciences, Uppsala, SE) with conductivity meters (Labor-Konduktometer 703, Knick Elektronische Messgeräte GmbH & Co. KG, Berlin, DE) in

extract and raffinate stream and a UV sensor (Qmax V, Cetoni GmbH, Korbussen, DE) in the raffinate stream for process control and evaluation. The 3D printed valve has an internal volume of 46.7 µL, the volume of the tubing that is used to connect the columns to the valve is 43.2 µL and the system has a total volume (excluding chromatography columns) of 358.1 µL. Considering the used sensors, the flow sensors have the greatest contribution to the dead volume with 25 µL each. With a total column volume of 1412 µL, this corresponds to a ratio of dead volume to system volume of 25.4% for the whole system and of 6.4% for the part relevant for the separation, which consists of the valve and the capillaries connecting valve and columns. The dead volume of preparative SMB systems is usually in the range of 3% of the column volume [197]. For small scale systems, the percentage can be much higher; Gomes et al. reported 11% for their FlexSMB unit [198], and there are even some reports where the system and the column volume were in the same order of magnitude [44, 183]. However, Minceva et al. observed a significant loss of an SMB system's performance with increases in dead volume as small as 1% [196].

5.3.1.2 Flow Control

As mentioned above, a microfluidic flow controller was used as flow source. This device works by pressurizing a vessel and thereby forcing the liquid out. Thus, an accurate and pulsation free flow is generated, even in the lower µL/min range [199]. In contrast to piston pumps this presents not a volume but a pressure driven pumping approach. The pressure in a chromatography system can vary over one process, for example due to viscosity changes in the mobile phase during sample loading [200], thus a closed-loop controller is necessary for a pressure driven approach in order to keep the flow rate constant. A time-discrete PI-controller according to (5.1) was implemented for this purpose, where p_t is the current set pressure, p_{t-1} is the set pressure of the previous time step, $P_{\mathrm{PI},t}$ is the proportional term that is calculated with the difference of the set (Q_{set}) and actual flow rate ($Q_{\mathrm{meas},t}$) for each time step according to (5.2) and $I_{\mathrm{PI},t}$ is the integration term, which is the sum overall $P_{\mathrm{C},t}$ values of all time steps as shown in (5.3).

$$p_t = p_{t-1} + k_{\mathrm{P}} P_{\mathrm{PI},t} + k_{\mathrm{I}} I_{\mathrm{PI},t} \tag{5.1}$$

$$P_{\mathrm{PI},t} = Q_{\mathrm{set}} - Q_{\mathrm{meas},t} \tag{5.2}$$

$$I_{\mathrm{PI},t} = \sum_{t=0}^{t} P_{\mathrm{PI},t} \tag{5.3}$$

The parameters k_{P} and k_{I} were determined with the method of Ziegler-Nichols [201] with a single chromatography column as controlled system. After fine tuning, k_{P} was set to 0.8 and k_{I} to 0.009, respectively. The control rate was set to 300 ms. In the µSMB setup the flow rates of four streams are controlled (diluent, feed, extract, raffinate), while the fifth flow rate (waste) is adjusted automatically due to mass balance. The flow rates and thus the flow control of the four streams are not independent of each other, as they form an interconnected system in the SMB; in the next step it was therefore tested if the single channel control could also be applied for the SMB setup. A stable flow for all streams could be generated with a feed-forward control. First start values were estimated with the Bernoulli equation [202] for the pressure drop in capillaries and the valve system and the Darcy equation [203] for the pressure drop in chromatography

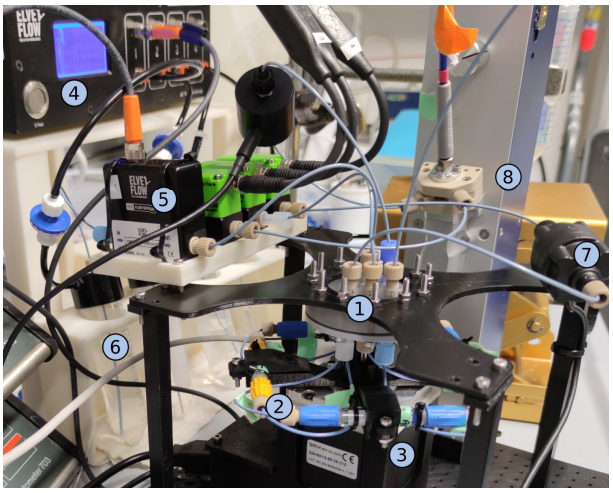

Figure 5.2: The µSMB system: 1 – 3D printed rotary valve; 2 – chromatography columns connected to the valve's rotor and the motor shaft; 3 – motor; 4 – microfluidic flow controller; 5 – flow sensors; 6 – liquid reservoirs; 7 – conductivity sensor; 8 – UV sensor.

columns. Later on, the stationary pressures from a first test run were used as start values. To further stabilize the system flow, the controllers of the different streams were not started at once but staggered, starting with the diluent stream and going counterclockwise to the raffinate stream with a time delay of 100 ms between each stream.

5.3.1.3 Chromatography Columns

Omnifit BenchMark Microbore chromatography columns (3x50 mm, column volume approx. 353 µL, Diba Industries Inc., Danbury, US) with stainless steel end pieces were used as column housings. The columns were packed with Sephadex G-25 Fine buffer exchange medium (Cytiva Life Sciences, Uppsala, SE), which has a particle size in the range from 20 µm to 80 µm in the dry and from 33 µm to 140 µm in the wet state. The slurry was prepared according to the manufacture's specifications and columns were packed using a pack adapter and deionized water as mobile phase. The column was connected to an ÄKTApurifier (Cytiva Life Sciences, Uppsala, SE) controlled with UNICORN 5.2 and the bed was compressed by increasing flow rates from 0.1 mL/min to 0.5 mL/min with a step increment of 0.1 mL/min. Each step was held for at least 10 min. Afterwards the pack adapter was removed and the column was washed for another 40 min at a flow rate of 0.3 mL/min with deionized water. In total four columns were packed.

5.3.1.4 Single Column Experiments

Single column experiments were performed to determine the column porosities and the retention times of BSA and AS. The experiments were conducted with an ÄKTApurifier at a flow rate of 0.3 mL/min with deionized water as mobile phase. For the determination of total and bed porosity, 2.5 µL of 1% (v/v) aceton or 1 g/L blue dextran solution, respectively, were injected. For the determination of the retention times of BSA and AS, 10 µL of a solution containing 1 g/L BSA (Sigma Aldrich, St. Louis, US) and 200 mM AS (Merck KGaA, Darmstadt, DE) were injected. All experiments were performed in triplicates for all columns. The hold-up volume of the system was determined by conducting the injections with a zero dead volume connector in

place of a chromatography column. The porosities and retention times were calculated for all experiments and the mean value was used for process design.

5.3.1.5 SMB Experiments

The feed solution for all SMB experiments contained 2 g/L BSA and 200 mM AS. Deionized water was used as diluent. Falcontubes ($V = 50\,\mathrm{mL}$) were used as reservoirs and connected to the flow controller with an adapter (Elveflow, an Elvesys brand, Paris, FR). The reservoirs for extract and raffinate were both filled with 2.5 mL of deionized water in order to prevent backflow of air into the SMB system during the start-up process. The system was flushed with deionized water and the feed stream was primed up to the central valve before the experiment was started. In addition, all reservoirs were weighed with a precision balance (Adventurer AX224, Ohaus Corporation, Parsippany, US) in order to calculate the mass balance of the process later on. The control of the flow rates, the switching of the valve by the motor and the data logging of the pressures, flow rates and conductivities was handled by a custom Matlab application (Matlab R2020b, Mathworks Inc., Natick, US) with a GUI (see Figure B.11 in Appendix B) during the experiments. The data logging of the UV absorption at 280 nm was done with the Qmix Elements software (Cetoni GmbH, Korbussen, DE). The flow rate control was paused for 1 s during the valve switching process and all pressures were kept constant at the last values before switching. The integral of the set point deviation (I_{PI}) was set to zero and the controller was restarted after every valve switching. After the experiment was finished, the reservoirs were weighed again and the concentrations of BSA and AS were determined with off-line UV measurements (EnSpire multiplate reader, PerkinElmer, Waltham, US) and conductivity measurements (WTW LF330 conductivity meter with WTW Tetra con 325, Xylem Analytics Germany Sales GmbH & Co. KG, WTW, Weilheim, DE), respectively. The SMB system was re-equilibrated with deionized water and then flushed with 20% ethanol for storage.

Five performance parameters were specified to assess the process points: the yield Y, the desalting efficiency DE, the dilution DL, the buffer consumption BC, and the productivity P, as defined by the following equations:

$$Y = \frac{c_{\mathrm{BSA,R}} \cdot V_{\mathrm{R}}}{c_{\mathrm{BSA,F}} \cdot V_{\mathrm{F}}} \cdot 100\% \tag{5.4}$$

$$DE = 1 - \frac{c_{\mathrm{AS,R}}}{c_{\mathrm{AS,F}}} \cdot 100\% \tag{5.5}$$

$$DL = \frac{c_{\mathrm{BSA,R}}}{c_{\mathrm{BSA,F}}} \cdot 100\% \tag{5.6}$$

$$BC = \frac{V_{\mathrm{D}}}{V_{\mathrm{F}}} \tag{5.7}$$

$$P = \frac{V_{\mathrm{F}}}{4V_{\mathrm{C}} \cdot t_{\mathrm{end}}} \tag{5.8}$$

All parameters were calculated using the results of the off-line measurement, with the concentrations of AS (c_{AS}) and BSA (c_{BSA}) in the reservoirs of the respective streams at the end of the experiment, the total processed volumes of the respective streams (V), the column volume of a single column (V_{C}) and the overall process time (t_{end}).

5.3.2 Determination of Process Points

A process point for the first assessment of the µSMB system was determined using the triangle theory, which is commonly applied in literature [39, 46, 50]. The triangle theory is based on an ideal chromatography model, meaning the process point is solely selected based on the retention times of the pure components and all peak broadening effects are neglected [39]. The Henry coefficient of the species i H_i was calculated based on (2.10) [24].

The Henry coefficients were then used to create the triangle plot (see Figure 5.3). Note that in the case of SEC, the Henry coefficients are negative, as the retention times of the species are smaller compared to the tracer due to the partial exclusion from the pores of the stationary phase. In the triangle plot m_j stands for the ratio of mobile phase flow to simulated stationary phase flow in the respective zone j according to (2.29) [44]. For the m_2/m_3 values, a point in the blue triangle of complete separation was chosen, for the m_4/m_1 values a point of complete regeneration of mobile and stationary phase close to the point of lowest buffer consumption was selected in the red rectangle. The feed flow rate was set to 30 µL/min. With these specifications, the remaining flow rates and the switching time were calculated with (2.29) and the five node balances of the open-loop SMB process (5.9)-(5.13). Further details on the triangle theory are provided in Section 2.1.2.1

$$Q_{\mathrm{D}} = Q_1 \tag{5.9}$$

$$Q_{\mathrm{E}} = Q_1 - Q_2 \tag{5.10}$$

$$Q_{\mathrm{F}} = Q_3 - Q_2 \tag{5.11}$$

$$Q_{\mathrm{R}} = Q_3 - Q_4 \tag{5.12}$$

$$Q_{\mathrm{W}} = Q_4 \tag{5.13}$$

The determined flow rates and the switching time are given in Table 5.1. Experiments were also performed with halved flow rates and doubled switching time (0.5xTT) and doubled flow rates and halved switching time (2xTT), to show the robustness of the system. These process points all relate to the same positions in the triangle plot and thus should lead to the same results for an ideal process. To account for non-idealities, a process point was also determined using the GRM (see row "Optimized" in Table 5.1). For this, the modeling and optimization tool Chromatography Analysis and Design Toolkit (CADET)-SMB was used [204, 205]. Details on the modeling process are given in the next section. The position of this process point in the m_1/m_4 and the m_2/m_3 plane is also depicted in Figure 5.3.

5.3.3 Process Modeling

The SMB processes at the respective process points were modeled using CADET-SMB (version 2.12) with CADET (version 3.2.1), in order to obtain comparative values for the experimental performance. Matlab Version R2020b was used for all simulations. A detailed description of the model procedure is given in the following sections. In addition, a tabular overview of all model input parameters is given in Table B.1 in Appendix B.

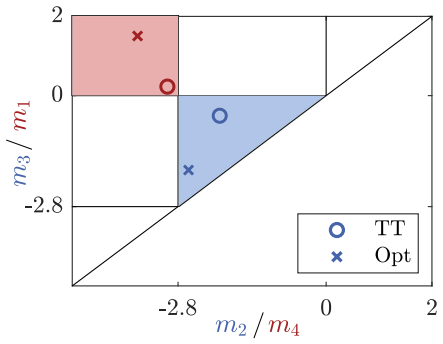

Figure 5.3: Position of the process points in the m_2/m_3 and m_4/m_1 plane of the triangle plot. The area of complete separation in the m_2/m_3 is depicted in blue and the area of complete regeneration of mobile and stationary phase in the m_4/m_1 plane is depicted in red.

Table 5.1: Overview of tested process points

Process Point	Q_D in µL/min	Q_E in µL/min	Q_F in µL/min	Q_R in µL/min	t_s in s
Triangle Theory (TT)	113	45	30	50	165
Optimized (opt)	285	169	30	70	80
2xTT	226	90	60	100	82.5
0.5xTT	56.5	22.5	15	25	330

5.3.3.1 Single Column Modeling

As a first step, model parameters of a single column experiment were determined. For this the data of the single column experiments with BSA and AS described in Section 5.3.1.4 were used. In addition, the experiments were repeated at different flow rates (0.05 mL/min, 0.1 mL/min, 0.2 mL/min, 0.3 mL/min) to obtain the influence of the flow rate on the axial dispersion coefficient.

A series of CSTRs was implemented into the single column model (see Figure B.12) to account for the peak broadening effects of the Äkta system. The GRM was chosen as chromatography model. The mass balances for the mobile and stationary phase are given in (2.50) and (2.51), further details on the model equations and solver can be found in [206, 207] and the CADET documentation [208]. The porosities were calculated based on the retention times of the tracer molecules. The pore accessibility F was determined with the retention times of BSA and AS. The mass transfer parameters axial dispersion D_{ax}, film transfer coefficient k_{film} and pore diffusion coefficient D_p were estimated by adjusting the modeled chromatogram to the experimental one. D_p was set to zero for BSA, as it cannot penetrate the particle pores. The optimization was done with the genetic algorithm of the global optimization toolbox of Matlab. The population size was set to 100 with a maximum of 500 generations. The optimization parameters were the difference in simulated and experimental peak area A, the difference in retention time t_{ret} and the difference in peak height h. The objective function was defined as follows:

$$y = k_{PA} \left| A_{sim} - A_{exp} \right| + k_{ret} \left| t_{ret,sim} - t_{ret,exp} \right| + k_h \left| h_{sim} - h_{exp} \right| \tag{5.14}$$

The penalty factors were set to $k_{PA} = 1$, $k_{ret} = 2$ and $k_h = 10$. First, the optimization was performed separately for BSA and AS. As it is only possible to enter the same D_{ax} for both components in CADET-SMB, the average of the determined D_{ax} of both components was calculated and used as a set value. A second optimization was performed to refine k_{film} for BSA and k_{film} and D_p for AS. D_{ax} was determined for all four flow rates, k_{film} and D_p were treated as independent of the flow rate.

5.3.3.2 SMB Modeling

CADET-SMB (version 2.1.2) was used for the simulation and optimization of the SMB process. The script was adapted to a four zone open-loop system. A simulation was performed for all process points given in Table 5.1. For comparison with the experimental mass balance, the simulated trajectories of both components in the different streams were integrated for the duration of the respective experiment. In addition, the integral over one cycle in cyclic steady state was calculated. The built-in script of CADET-SMB using the differential evolution algorithm with a population size of 50 and a maximum number of generations of 200 was applied for the process point optimization. The aim of the optimization was to maximize purity of BSA in the raffinate stream. Thus, the objective function was defined to maximize yield of BSA in the raffinate ($Y_{BSA,R}$) and minimize yield of AS in the raffinate ($Y_{AS,R}$) at the same time:

$$y = k_{AS} Y_{AS,R} + k_{BSA} \left(Y_{BSA,R,min} - Y_{BSA,R} \right) \tag{5.15}$$

The penalty factors k_{BSA} and k_{AS} were set to 1 and 10, respectively. The required yield of BSA in the raffinate ($Y_{BSA,min}$) was set to 0.99.

5.4 Results and Discussion

5.4.1 Model Parameter Estimation

The parameters that were determined for the simulation of the single column experiment are given in Table 5.2. The pore accessibility F and the porosities were calculated with the retention times of the components and the tracers, respectively. BSA is excluded from all pores, nonetheless for the simulations a value of 1.0×10^{-5} was used for the pore accessibility, since it can't be zero for mathematical determinacy. In contrast to that, AS is able to access the whole pore volume. In addition to the determined values for the mass transfer parameters, Table 5.2 shows the values calculated with empirical correlations. D_{ax} was calculated with the correlation of Chung and Wen [209], k_{film} was derived from the correlation by Wilson and Geankoplis [210] and D_p was calculated according to Satterfield et al. [211]. All experimentally determined parameters, except for the film transfer coefficient of AS, are in the same order of magnitude as the values predicted by the empirical correlations and thus are considered to be reasonable. The film transfer coefficient of AS is two orders of magnitude smaller compared to the correlation and it is even lower than the one of BSA. This is unlikely, as BSA has a higher molecular mass and therefore a lower diffusion coefficient.

From the chromatogram in Figure 5.4 it is clearly visible that the second peak, which is detected by the conductivity measurement and hence caused by AS is much broader than the first peak,

Table 5.2: Model parameters for the simulation of the separation of BSA and AS with the used columns. Values marked with * were directly calculated from the chromatograms, values marked with + are comparative values that were calculated with empirical correlations from literature. All other values were obtained from parameter fitting.

	BSA	AS
F^*	0 (1.0×10^{-5})	1
ε_t^*	0.844	
ε_p^*	0.743	
ε_{int}^*	0.394	
D_{ax} in m^2/s	$5.21 \times 10^{-6} \cdot Q$ [mL/min]	
	5.21×10^{-7} (@ 0.1 mL/min)	
D_{ax}^+ in m^2/s	1.17×10^{-7} (@ 0.1 mL/min)	
k_{film} in m/s	1.14×10^{-5}	3.00×10^{-6}
k_{film}^+ in m/s	1.75×10^{-5}	1.46×10^{-4}
D_p in m^2/s	–	2.31×10^{-10}
D_p^+ in m^2/s	–	2.30×10^{-10}

which is visible in the UV signal and thus represents BSA. Most likely another effect is lumped into the value of k_{film} in order to account for this peak broadening. This could for example be caused by the longer residence time or the tortuosity of the pore system of the beads. Even though this value does not represent the physical value of AS's film transfer coefficient, the simulation is nonetheless able to reflect the experimental results, as it is shown exemplary for a flow rate of 0.3 mL/min in Figure 5.4. Both, the retention time and the peak height are predicted precisely. There are deviations at the slopes, particularly at the descending slope of AS; nonetheless, the fit quality is sufficient to calculate comparative values for the SMB experiments. Figure 5.4 also shows that there is no baseline separation of BSA and AS; however, there are regions of pure BSA and pure AS, which is usually sufficient for a separation with SMB [44].

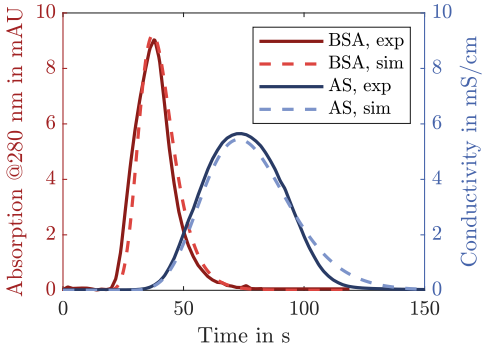

Figure 5.4: Comparison of simulation and experimental results for the separation of BSA and AS with a single column at a flow rate of 0.3 mL/min

5.4.2 Flow Rate Accuracy

The precise generation of flow rates in the µL/min range was identified as one of the critical factors for the successful implementation of a µSMB device. Thus, the flow rates were monitored and analyzed for the triangle theory process point. Figure 5.5a shows the flow rates of the four

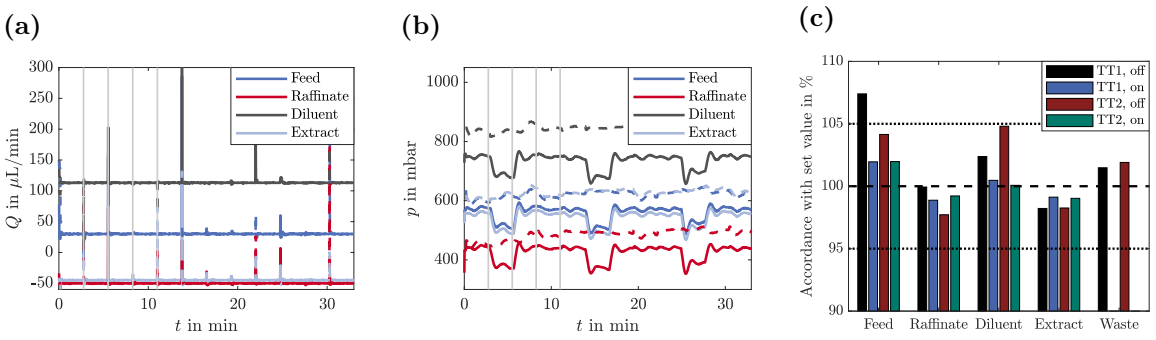

Figure 5.5: Flow rate (a) and pressure curves (b) of the four controlled in- and outlet streams of the SMB system. Depicted are the first three cycles of both runs with the TT process point (TT 1: solid line, TT 2: dashed line). The first four switches are indicated with vertical gray lines. (c) Comparison of on-line and off-line flow measurements with the set value.

controlled in- and outlet streams for the first three cycles of the experiment in duplicates. The inlet streams are shown with positive flow rates and the outlet streams with negative ones. The first four valve switches are indicated with vertical gray lines. The results of both experiments are in good accordance with the set values, however short fluctuations are occurring during the switching process. This is because the back pressure of the system changes during the switching and in contrast to most other systems, the flow is not stopped. Similar pressure spikes during the switching process were also observed by Gomes et al. but they didn't report any negative effects [198].

Figure 5.5b depicts the pressures applied by the microfludic flow controller to generate the respective flows of Figure 5.5a. The pressures follow a periodic pattern with the switching cycle, which indicates that the pressure drop differs for the four used chromatography columns. In addition, all pressures are higher for the second run, although the same columns were used. This illustrates that it is necessary to use a closed-loop control for the flow rates in this setup in order to account for the changes in pressure drop.

To assess the influence of the switching process on the overall flow rate accuracy, the mean flow rate recorded by the on-line sensors over the whole process was calculated. Additionally, off-line measurements were performed by weighing the reservoir vessels before and after the experiment. The results of the off- and on-line measurements are given in Figure 5.5c. As there was no on-line measurement for the waste stream, only the off-line measurements are depicted. There is a slight discrepancy between the off- and on-line measurements but they are all (except the first off-line measurement of the feed stream) in the accuracy range of ±5% given by the flow sensor manufacturer. A different kind of flow sensor was used during the first experiment (TT1) in the feed stream. Here, the value is above 5%, but for the second run (TT2), where the sensor was changed to a SLI-1000 sensor, the accuracy is below 5% as well. In most cases the deviation is even below ±2%. A difference between set and actual value is not only observed for the off-line, but also for the on-line measurements. This implies that there is a measurable influence of the switching process on the mean flow rate. Thus, the performance of the flow control could probably be further improved by fine tuning the PI controller for adaptions during the switching process.

On the other hand, as described before, the fine tuning of this coupled system of controllers is not trivial. In addition, the flow rate accuracy of commercial systems is in the same range (e.g., BioSMB PD: ±5% [190], Octave 12 pump: ±2% [189]), even though the minimum flow rate is higher (e.g., BioSMB PD: 0.5 mL/min [190], Octave 12 pump: 0.2 mL/min [189]). Gomes et al. measured the fluctuation in the recycle stream of their system; the flow rate was in the range between 21 mL/min and 25 mL/min in the course of one cycle, which corresponds to fluctuations of ±8% [198]. Hence, the achieved flow rate accuracy of the µSMB system is acceptable for the conduction of SMB experiments.

5.4.3 Influence of Dead Volume

Besides the flow rate control, the dead volume is an important factor for the miniaturization of an SMB system. In the following the effects of the dead volume on the µSMB experiments will be assessed with the system's mass balance, trajectories and mean concentrations in the in- and outlet streams. The experimental results in this section are a duplicate run of the process point that was determined with the triangle theory (TT1 and TT2).

In order to assess the influence of the dead volume on the system's performance, process simulations were performed to obtain comparative values. The chromatography columns were modeled with the GRM, thus the dispersion effects in the column were taken into account, but the dead volume and effects connected to it were not considered. This way, the simulated results represent an idealized system without any dead volume and the impact of the dead volume on the experiments can be estimated through comparison with the simulation.

5.4.3.1 Mass balance

Figure 5.6 shows the mass balances of BSA and AS for both runs. The experimental mass balance was calculated with the off-line concentration measurements. For comparison, the mass balance of the simulation is depicted. At first glance it is surprising that the mass balance does not reach 100% for the simulation. This is because the whole system is filled with water at the beginning of each experiment. After the experiment is stopped, part of the feed solution remains in the columns and other parts of the system, hence reducing the mass balance. This effect has less influence for longer process times, as the portion of feed solution remaining in the system compared to the overall amount of feed gets smaller. The mass balance predicted by the simulation differs for both runs since they were run for a different time: The process time of TT1 is 112 min, for TT2 it is only 88 min. The mass balance calculated with the simulation over one cycle in cyclic steady state (gray bars) is 100%. This shows that the mass conservation in the simulation is working.

In both experiments, AS has a lower recovery than BSA. This is caused by the broader peak width of AS (see Figure 5.4), which causes AS to spread over the whole system in the course of the experiment. This is different for BSA, where the concentration remains at 0 g/L in some sections (compare the chromatograms in Figure 5.8). This way more AS remains in the system when the experiment is stopped and thus the mass balance is reduced.

In addition, all experimental mass balances are lower than the simulated ones. This is due to the fact that the dead volume was not considered for the simulation but BSA and AS also remain

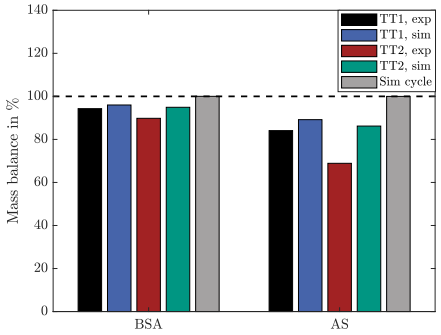

Figure 5.6: Mass balance of BSA and AS for both TT runs in comparison to the simulation and the simulation of one process cycle in cyclic steady state.

in those parts of the system when the experiment is finished. For the reasons discussed before, this effect is larger for AS. The experimental mass balance of BSA only differs 2.8% and 5.4% from the simulation, indicating only a small influence of the dead volume. For AS these values are higher with 5.7% and 20.1%. However, these values would decrease for longer process times and the samples can be recovered by flushing the system after a run is finished. Thus, they do not represent a real loss.

5.4.3.2 Trajectories and Chromatogram

The concentrations of BSA and AS at the raffinate and extract port were recorded on-line during the experiments with a sampling time of 1 s. The resulting trajectories of the first three cycles are depicted in Figure 5.7 alongside the simulated results. Figure 5.7a shows the BSA concentration in the raffinate stream, Figure 5.7b and 5.7c show the AS concentration in the raffinate and extract streams, respectively. The BSA concentration in the extract is not displayed, as no on-line measurement was performed. The switching times are indicated by the vertical gray lines in all figures.

The retention time was adjusted by the time delay caused by the dead volume between the valve system and the detectors for all measurements. In general, the results of both experimental runs are in good accordance with each other. This underlines the statement of the last paragraph, that the deviation in the mass balances is caused by the different lengths of the experiments and not by differences during the processes. All trajectories show a cyclic pattern with start up behavior, which is caused by the valve switchings and is typical for SMB processes.

The first peak of the experimental results of BSA is either misshaped or completely missing and all other peaks of the first cycle have a smaller peak area in comparison to the simulation. This behavior indicates that there is an interaction between BSA and some part of the SMB system. Most likely it is an interaction with the 3D printing material of the valve system, as this has been reported before [212]. After one cycle, BSA has been in contact with all parts of the 3D printed valve and the material is saturated, which results in a better prediction of the experimental peak shape by the simulation. After each valve switching, the BSA concentration drops abruptly. In the experiments the observed drop in concentration is neither as low nor as steep as predicted by the simulation. Additionally, the minimum BSA concentration is not reached right after the

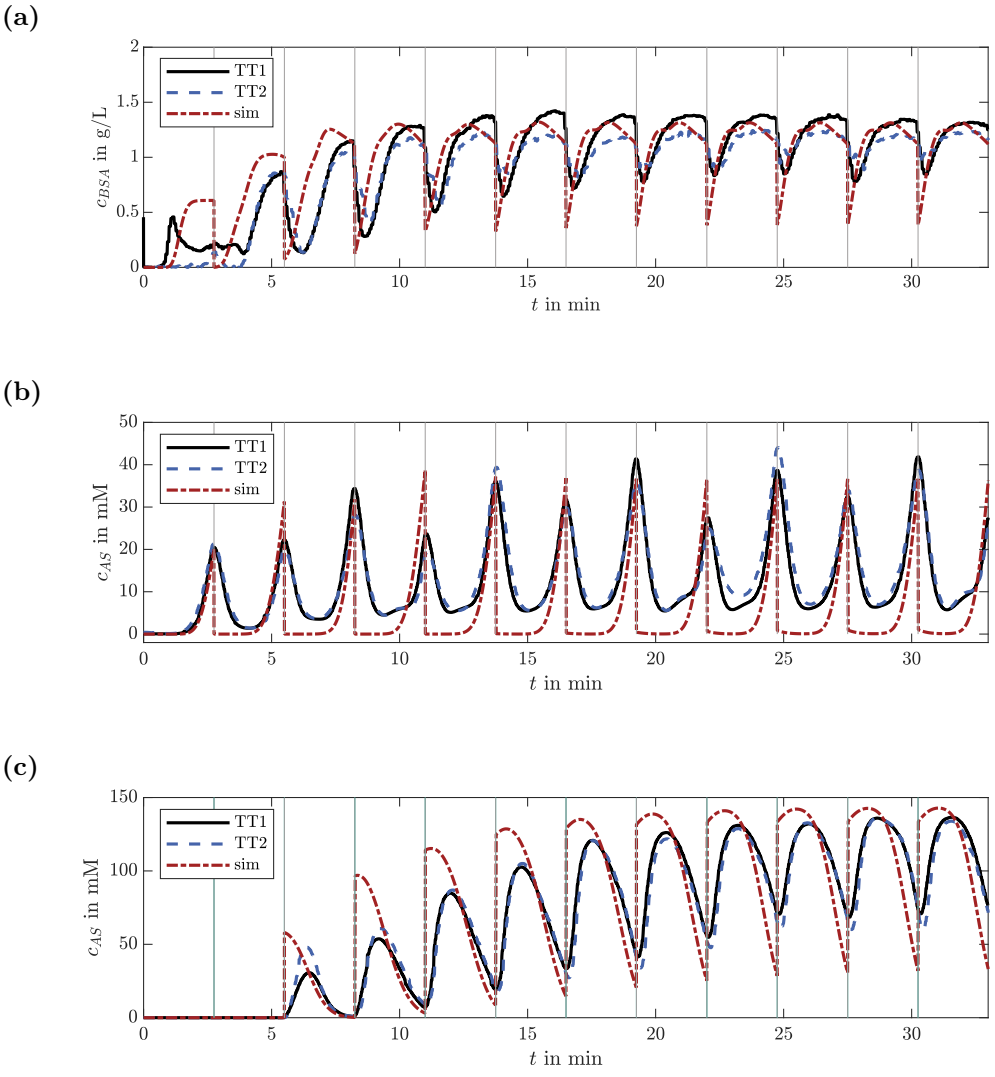

Figure 5.7: Comparison of the experimental and simulated trajectories of the TT process point: (a): BSA trajectory in raffinate stream; (b) AS trajectory in raffinate stream (c) AS trajectory in extract stream.

switching but slightly later. The latter effect is caused by the dead volume between valve and sensor. This part of the system (volume approx. 30 µL) is still filled with the solution leaving the previous column, thus there is a time delay until the effect of the switching process is measured. The remaining deviations result from peak broadening effects in the dead volume.

There is a breakthrough of AS into the raffinate stream at the end of each switching period in the experiment as well as the simulation, as it is shown in Figure 5.7b. This was to be expected, as AS has a comparably high peak width in the single column experiment. Only the position of the peak maximum and not the peak width was considered during process point determination, thus leading to this impurity level. Comparing the simulation and experiments, it can be seen that the prediction of the retention time and height of the AS peaks is quite precise. In contrast to the simulation, the AS concentration does not drop to zero after each switching process in the experiments indicating peak broadening in the dead volume. In this case, the not considered dead volume leads to a higher overall concentration of AS in the raffinate. When comparing the peak heights, it can be observed that each fourth peak is lower compared to the other ones. This indicates that one column differs from the other ones, which also explains the different back pressures observed in Figure 5.5b.

Several observations can be made for the trajectory of AS in the extract: (1) At the beginning of the experiments, the AS concentration is lower than predicted; (2) the peak shape is different, particularly the concentration increase after switching is not as steep; (3) the peaks have a longer retention time compared to the simulation which is especially evident in the first cycle. The longer retention time is most likely caused by the time delay induced by the dead volume. This also leads to the differences in peak shape: The position were the AS peak is cut by the switching is close to the peak maximum in the simulation but not in the experiments. A possible explanation for the lower AS concentration is that the regeneration of the stationary phase in zone one is not sufficient and AS is transported from zone one into zone four with the stationary phase.

Comparing the simulated and experimental trajectories, deviations in retention time and peak height that are most likely caused by the dead volume are observable. However, it is difficult to determine how much this will effectively influence the process, e.g., in terms of yield from the trajectories. Therefore, the measured (dark colors) and predicted (light colors) overall concentrations in the reservoirs after the experiment (TT1) are shown in Figure 5.8. In addition, the chromatogram of the simulated concentrations in the zones at the beginning of a cycle in the cyclic steady state and the zone flow rates are depicted. The concentration of AS is always non-zero and it increases with the column length in the fourth zone. This indicates that the regeneration of the stationary phase in zone one is indeed not sufficient and as a consequence the diluent flow rate should be increased to improve BSA purity. In accordance with the trajectories, the experimental AS concentration is lower in the extract and higher in the raffinate compared to the simulation results. While the difference in the extract is less than 2%, the measured concentration in the raffinate is twice as high as expected. This comparably high relative error is partly due to the low concentration level itself. In regard to the feed concentration, the deviation is below 3%. The same is applicable for BSA. Thus, the observed overall deviation from the simulation and therefore the influence of the dead volume is small. It gets obvious from

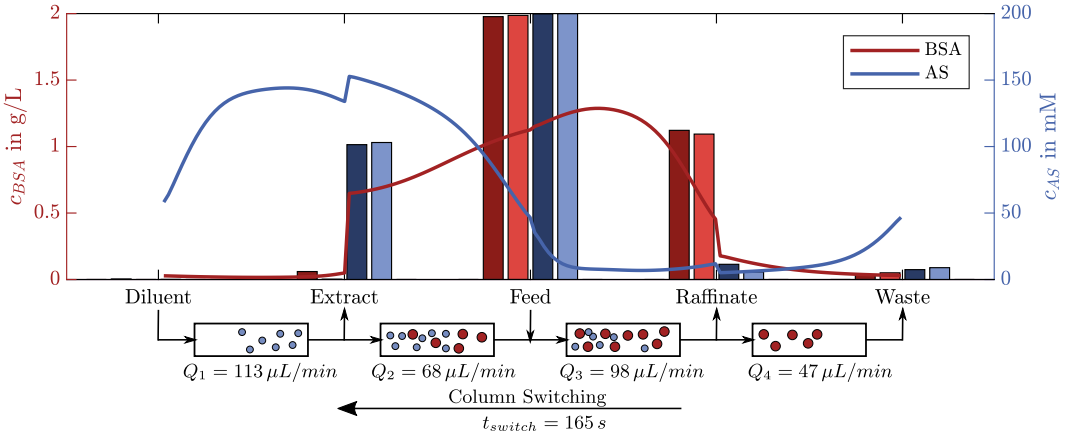

Figure 5.8: Concentrations of BSA and AS in the reservoirs of the in- and outlet streams at the end of the TT1 experiment (dark colors) in comparison to the simulated concentrations (light colors). In addition, the simulated concentration profile right after switching in cyclic steady state in the zones as well as the zone flow rates are displayed.

Figure 5.8 that the µSMB system is capable to perform the separation of BSA from AS, even though the dead volume was not considered for the process design. To improve the purity of BSA as well as for the conceptualization of further studies, it still would be of interest to do additional investigations on the dead volume's effects. For example, from the shown results it cannot be determined if the time delay or the peak broadening have a greater influence on the process. In addition, it cannot be distinguished if band broadening occurs mostly in the volume between the valve and the detector, which only influences the peak shape but not the separation performance, or in the dead volume between the columns. This information would be important if the system was adapted for different kinds of processes as well as for the process transfer to other systems.

5.4.4 Performance of the Process Points

In the two previous sections, it was shown that the system meets the necessary requirements regarding flow rate control and dead volume. To conclude, the performance of the SMB system is evaluated by comparing the defined performance parameters of the process points. In addition to the aforementioned process point determined with the triangle theory, all flow rates were either halved (0.5xTT) or doubled (2xTT) to evaluate the system's behavior under different flow conditions. Furthermore, a process point was determined using the optimization function of CADET-SMB, with the aim of achieving the highest possible desalting efficiency (Table 5.1).

The results are depicted in Figure 5.9, with Figure 5.9a showing the experimental and Figure 5.9b showing the comparative results of the respective simulation. In both figures, the results form the same pattern: 2xTT has the highest productivity, opt has the highest buffer consumption and the highest dilution, but it also has the highest desalting level and the lowest yield. In this case, the optimization algorithm traded off yield against purity.

In principle, the performance parameters can be divided into two groups. The productivity and the buffer consumption are determined by the chosen process point, while the yield, the desalting

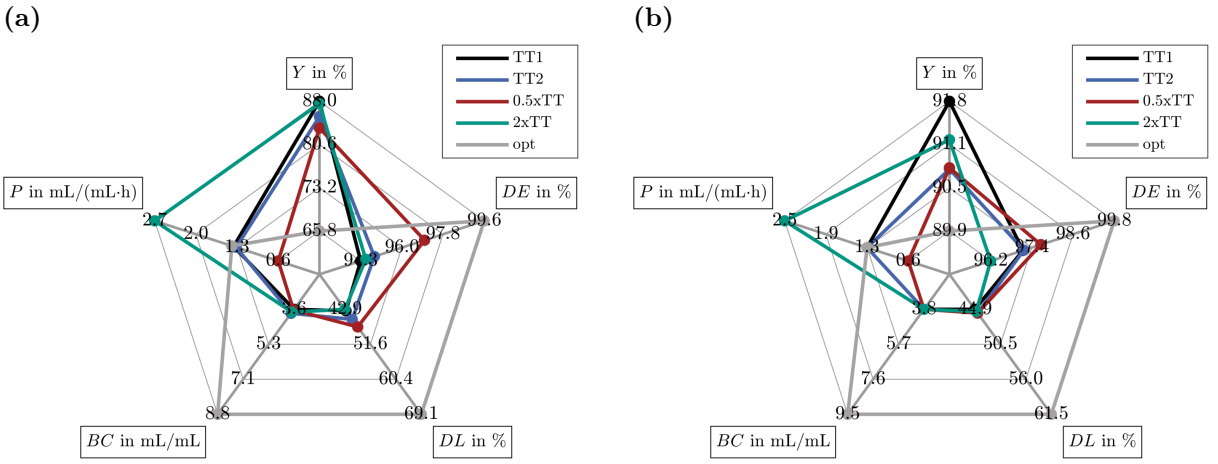

Figure 5.9: Comparison of the performance parameters for the experiments (a) and the respective simulations (b). Y – yield; DE – desalting efficiency; DL – dilution; BC – buffer consumption; P – productivity.

efficiency and the dilution depend on the separation performance. There are only slight differences between the experiments and simulations for the first group. They are caused by differences between the set and actual flow rates. As described before, this is due to disturbances during the switching process and the accuracy of the on-line flow sensors (see Section 5.4.2).

The experimental yield is lower as estimated with the simulation for all experiments. For most experiments, this deviation is in the range of 3-5% and can be explained by the portion of the BSA remaining in the dead volume of the system after the experiment is finished, as was discussed in the previous section (see Section 5.4.3). For the optimized process point, the difference is 24%, which can not be explained solely by this effect. Neither are the higher flow rates nor the shorter switching time the cause of this result, as they are comparable to 2xTT where this effect is not observable. Most likely the deviation is caused by the different ratios of the zone flow rates compared to the other experiments. The ratio of the highest to the lowest flow rate is much higher (3.8 vs 2.4), at the same time the ratio of the flow rates in zones three and two is a bit lower (1.26 vs 1.44). Due to the unconsidered inter-column dead volume, this causes more BSA to be transported in the direction of the extract port where it will be flushed out because of the high flow rate in zone one. In this case the yield can be improved, e.g., by adapting the switching time.

In an ideal, dispersion free scenario, the results for TT, 0.5xTT and 2xTT should be identical. The simulation calculates identical values for the productivity and the buffer consumption; the differences in yield were discussed before. However, the desalting efficiency increases from 96.2% to 97.7% with decreasing flow rate. This is even more apparent for the experiments, where the results range from 94.2% to 97.0%. The reason for this observation is that in the flow rate range considered here, the axial dispersion is smaller for lower flow rates (see Table 5.2), thus there is less band broadening due to mass transfer limitations and less AS contaminates the raffinate. Consequently in this case, lower flow rates are favorable for the separation process. The optimization algorithm still chose higher flow rates for the optimized process point because

dilution was not directly penalized in the objective function. From this point of view, the diluent flow rate should be infinitely high; however, a high diluent flow rate has a negative impact on the BSA yield and as this was considered in the objective function, the selected diluent flow rate is in a reasonable range.

In summary, all evaluated process points reached a desalting level above 94%, the optimized point even achieved a desalting efficiency of 99.6%. The yields were in the range from 85% to 88%, only the optimized point has a lower yield of 65.8%. These results are comparable to the ones reported by Hashimoto et al., who used comparable components with a larger setup [186]. This clearly shows that the µSMB system is capable of successfully performing separation processes under various conditions. An optimization under consideration of the dead volume could even increase the performance further in future works.

5.5 Conclusion

We were able to successfully develop a µSMB system. The main factors for downscale, flow rate accuracy and dead volume, were addressed with the use of a microfluidic flow controller and a 3D printed valve, respectively. The resulting ratio of inter-column dead volume to column volume is 6.4% for the developed system. As a proof of concept we tested the system for the separation of BSA and AS with SEC-SMB under different conditions. We were able to achieve desalting rates above 99%, reaching comparable levels to other systems [186]. Still, we saw some impact of the dead volume on the process, which should be further investigated in the future. The lowest applied feed flow rate was 15 µL/min, with the zone flow rates between 24 µL/min and 56.5 µL/min which is, to the best of our knowledge, the process with the lowest flow rates that was ever reported for a SMB experiment. The sample volume required to reach the cyclic steady state was as low as 3.3 mL.

The presented results thus provide the proof that SMB is not only a useful tool for preparative applications but can also be applied in a small scale, enabling a variety of new applications. For example, the µSMB system can be a useful tool in process development as a downscale model. For this, the comparability of the µSMB to common lab scale systems should be investigated as a next step. Furthermore, due to its low column volumes and low buffer and sample consumption, the system could be interesting for long term studies in regards to resin reusablity or cleaning protocols. One big advantage of the presented system is that the main parts, the pump and the valve, are either not in contact with the product (pump) or can be manufactured at low costs in a short time (valve). This way the system is ideal as a disposable setup and can also be used for studies with toxic components without the possibility to cross-contaminate the next process. Additionally, because of its small footprint it can easily be placed in a common lab fume hood. The 3D printed valve system enables the easy adaption of the system to multiple processes but keeps the system simple at the same time, which makes it a perfect tool for research.

6. Micro Simulated Moving Bed Chromatography-Mass Spectrometry as a Continuous On-line Process Analytical Tool

Juliane Diehm[1], Lennart Witting[1], Frank Kirschhöfer[1], Gerald Brenner-Weiß[1] and Matthias Franzreb[1,*]

[1] Institute of Functional Interfaces, Karlsruhe Institute of Technology, Eggenstein–Leopoldshafen, 76344, Germany

Abstract

Continuous manufacturing is becoming increasingly important in the (bio-)pharmaceutical industry, as more product can be produced in less time and at lower costs. In this context, there is a need for powerful continuous analytical tools. Many established off-line analytical methods, such as mass spectrometry (MS), are hardly considered for process analytical technology (PAT) applications in biopharmaceutical processes, as they are limited to at-line analysis due to the required sample preparation and the associated complexity, although they would provide a suitable technique for the assessment of a wide range of quality attributes. In this study, we investigated the applicability of a recently developed micro simulated moving bed chromatography system (µSMB) for continuous on-line sample preparation for MS. As a test case, we demonstrate the continuous on-line MS measurement of a protein solution (myoglobin) containing Tris buffer, which interferes with ESI-MS measurements, by continuously exchanging this buffer with a volatile ammonium acetate buffer suitable for MS measurements. The integration of the µSMB significantly increases MS sensitivity by removing over 98% of the buffer substances. Thus, this study demonstrates the feasibility of on-line µSMB-MS, providing a versatile PAT tool by combining the detection power of MS for various product attributes with all the advantages of continuous on-line analytics.

Keywords
µSMB-MS; process analytical technology (PAT); continuous buffer exchange; sample pre-processing; desalting; native ESI-MS

published in *Analytical and Bioanalytical Chemistry*,
`https://doi.org/10.1007/s00216-023-05023-9`, licensed under a Creative Commons Attribution 4.0 International License (CC BY 4.0)

CRediT authorship contribution statement
Juliane Diehm: Conceptualization, Methodology, Investigation, Writing – original draft. Lennart Witting: Methodology, Investigation, Writing – review & editing. Frank Kirschhöfer: Methodology, Investigation, Writing – review & editing. Gerald Brenner-Weiß: Writing – review & editing. Matthias Franzreb: Conceptualization, Writing – review & editing.

6.1 Introduction

Continuous manufacturing is state of the art for many chemical processes [213], offering numerous advantages over batch processing, such as faster time-to-market, lower cost of goods, a more consistent product quality without batch-to-batch variability, or a lower carbon footprint and is therefore of interest to the (bio-)pharmaceutical industry [10,13]. However, active process control is crucial for successful continuous processing due to potential variations in process parameters and input materials [13]. The limited number of process observations combined with long analysis times for biomolecules have been identified as a critical challenge for the next generation of biomanufacturing [214].

As a result, there has been extensive research into PAT in recent years [13]. In the field of biopharmaceuticals, spectroscopic methods, such as UV/Vis spectroscopy, NIR spectroscopy, or Raman spectroscopy, have received considerable attention as they can perform in-line measurements without the need for sample preparation while also featuring a fast measurement time [18, 99]. In contrast, commonly used off-line analytical methods, like HPLC or MS, are less considered because they either have a longer processing time (HPLC) or require sample preparation (MS) [18].

Nevertheless, the application of MS as a PAT tool is promising [116], as it is considered one of the most powerful techniques [119] capable of detecting a wide range of quality attributes, including glycosylation patterns [215, 216], charge variants [217, 218], aggregates [219, 220], as well as process-related impurities such as host cell proteins [221–223].

Wang et al. demonstrated the potential of direct analysis in real time (DART)-MS as a PAT tool, not only for process analytics [224] but also for accelerating process development [225]. However, the DART method is suitable primarily for small and medium-sized molecules [226, 227]. For biological molecules, so-called native ESI-MS measurements are of particular interest, as the structural information is preserved during the measurement [219]. It is mainly applied in combination with liquid chromatography for sample pre-processing (LC-MS), since most biological buffer systems are incompatible with ESI-MS, as they are either non-volatile or introduce significant noise [228,229]. Miniaturized LC systems are particularly promising, having a shorter analysis time [119]. This is crucial, as it increases the time available to make process adjustments, if necessary, to keep all CQAs within the specified range [13]. Therefore, CQAs should ideally be measured continuously. In the case of LC-MS, the MS measures samples at a high acquisition rate and LC is the time-limiting step. Although existing systems are often referred to as online LC-MS (due to the direct coupling of the two systems), they still rely on batch-wise LC pre-processing, which hinders true on-line implementation in terms of PAT. To address this limitation, the batch-wise LC sample pre-processing needs to be replaced by a continuous (chromatographic) method. Although continuous implementations of chromatography processes exist at a preparative scale, they have not been applied for analytical purposes so far, as the existing equipment is not designed to handle small volumes and is therefore not suitable for analytical purposes.

To overcome this limitation, we recently miniaturized SMB chromatography, a widely used continuous chromatography technique, to the micro-scale (µSMB) [230]. This study demonstrates its

effectiveness as an analytical tool for continuous on-line sample preparation coupled with on-line native ESI-MS measurements. In typical SMB processes, a series of identical chromatography columns is divided into four zones of different mobile phase flow rates by adding and withdrawing material flows between the columns. Additionally, the chromatography columns are switched in the opposite direction of the mobile phase flow such that a time discrete countercurrent movement between stationary and mobile phase results. If the flow rates in each zone as well as the column switching time interval are selected accordingly, a continuously added feed stream can be separated into two fractions, the raffinate and the extract stream [39]. Here, each zone fulfills a specific task: zone one is for the regeneration of the stationary phase, zones two and three are for the separation of the components in the feed stream and zone four is for the regeneration of the mobile phase [40]. For further details on the SMB principle, we refer to the literature [39, 40, 46] or Section 2.1.2.1.

In this proof-of-concept study, we performed a continuous buffer exchange of a protein solution based on SEC with the µSMB system. We then hyphenated the µSMB to an ESI-MS for continuous protein detection. We selected Tris buffer as an example of a biological buffer that interferes with MS measurements and continuously replaced it with a volatile ammonium acetate buffer. Myoglobin (Mb) was chosen as a protein because its non-covalently bound prosthetic heme group allows easy verification of its structural integrity during measurements [231, 232].

6.2 Materials and Methods

6.2.1 Chemicals and Buffers

All chemicals were purchased from Sigma Aldrich (St. Louis, US). Myoglobin from equine skeletal muscle had a purity of 95-100%, ammonium acetate of >99.95%, and Tris-HCl of > 99%. Buffers were prepared with ultrapure water (Milli-Q Gradient, Merck Millipore, Burlington, US) and degassed in an ultrasonic bath for at least 30 min before usage. Stock solutions of 100 mM NH_4OAc (pH 7), 1 mM Tris (pH 7), and 10 g/L Mb in 10 mM NH_4OAc (pH 7) were prepared. Feed solutions for the µSMB experiments were prepared from these stock solutions.

6.2.2 Mass Spectrometry

Mass spectrometry was performed on an X-500R QTOF mass spectrometer (AB Sciex LLC, Framingham, US). Instrument handling and data acquisition were performed using SCIEX OS Software (version 2.2, AB Sciex LLC, Framingham, US). Data processing, such as extraction of extracted-ion chromatograms, calculation of mean spectra, and baseline chromatogram extraction, was performed using the built-in Explorer Tool. A peak width of m/z ±0.02 was used for all molecules to extract extracted-ion chromatograms. The baseline chromatogram was extracted with an m/z ratio between 400 and 500. Protein reconstructions from spectra were performed using the Bio Tool Kit of the Explorer Tool with a limited input m/z range from 1700 to 2600. The output mass range was chosen from 5 kDa to 20 kDa with a step mass of 0.5 Da.

6.2.2.1 Operating Conditions

All MS measurements were performed in ToF-MS mode with positive polarity. The ToF mass range was between m/z 400 and m/z 2600 with an accumulation time of 0.25 s. The spray

voltage was set to 5000 V and the declustering potential to 40 V. The collision energy was 20 V for native measurements and 40 V for non-native measurements. Ion source gas 1 (nitrogen) was set to 50 psi, curtain gas to 25, and CAD gas to 7. The ion source temperature was set to 100 °C. The mass spectrometer was equilibrated for at least 45 min and calibrated with an external standard (electrospray-ionization (ESI) positive solution for the Sciex X500B system, Sciex) before a measurement was started.

6.2.2.2 Off-line Measurements

Samples containing 10 µg/mL Mb in 10 mM NH_4OAc buffer with varying Tris concentrations of 0, 1, 5, 10, and 100 mM were measured off-line in duplicate. A syringe pump (Harvard Apparatus Model 11 (55-1111), Holliston, US) was used to continuously infuse the sample solutions into the ESI source. The flow rate was set to 30 µL/min, corresponding to the raffinate flow rate of the µSMB experiments. Each sample was measured for 2 min; only the second minute was used for data evaluation to ensure that the system was flushed with the respective sample. The sample without Tris was measured under native and non-native conditions. All other samples were measured under native conditions only.

6.2.3 µSMB Process

The µSMB system used is a four-zone open-loop setup with one column per zone (Figure 6.1). This means that the buffer leaving the fourth zone is not recycled into the first zone. Theoretically, the fourth zone of the µSMB system is not required in this case, as it is not necessary to regenerate the mobile phase. We still decided to use four zones because this decouples the flow rate of zone three from the raffinate flow rate. Therefore, this setup enables users to freely choose and independently select the flow rate in zone three during process point development, as well as the option to set the raffinate flow rate to a specified fixed value (30 µL/min in this case). Alternatively, this could be achieved with a diverting valve, but sine this would have decreased the analyte concentration in the raffinate stream, we chose the four-zone open-loop setup. The raffinate flow rate is of particular interest as it is infused into the mass spectrometer. The µSMB system consists of a 3D printed central rotary valve, which is actuated by a stepper motor (pan drive PD60-3-1161, TRINAMIC Motion Control GmbH & Co. KG, Hamburg, DE). The valve was fabricated according to [233] (Chapter 4), with the only difference that a polytetrafluoroethylene (PTFE) sheet (PTFE Virginalfolie 0.25 V AD, Hightechflon GmbH & Co. KG, Konstanz, DE) was used for sealing instead of a silicone sheet. The in- and outlets of the chromatography columns were connected to the valve's rotor, and the system's in- and outlet streams were connected to the stator. A pressure-driven microfluidic flow controller (OB1 M3K+, Elveflow, an Elvesys brand, Paris, FR) in combination with flow sensors (SLI-1000, Sensirion AG, Stäfa, CF) was used for closed-loop control of the flow rates. Conductivity sensors (ÄKTApurifier, Cytiva Life Sciences, Uppsala, SE) with conductivity meters (Labor-Konduktometer 703, Knick Elektronische Messgeräte GmbH & Co. KG, Berlin, DE) were applied for on-line conductivity monitoring in the extract and raffinate streams. The conductivity sensors were calibrated to determine the Tris concentration with solutions containing 0, 1, 5, 10, 50, and 100 mM Tris. The resulting slopes of the calibration curves were 15.359 mM/(mS/cm) for the extract and

15.382 mM/(mS/cm) for the raffinate, with an intercept of 0.3656 mM and 0.2993 mM, respectively. The conductivity sensor in the raffinate stream was only used for stand-alone µSMB experiments to reduce the delay volume between µSMB and mass spectrometer.

The general setup of the µSMB has been described previously [230] (Chapter 5). However, in this study, some modifications had to be made for coupling to the MS system: As the raffinate is directly infused into the ESI source, it is not possible to directly control the outlet pressure of this stream and therefore it is not possible to control the raffinate's flow rate with the microfluidic flow controller. The flow rates of all other streams, including the waste stream, were controlled instead so that the raffinate stream's flow rate is adjusted automatically following the system's overall liquid flow mass balance. An instrumentation and piping diagram of the setup with all fluidic and pneumatic connections is shown in Figure 6.1.

A Matlab application with a GUI was developed with Matlab's AppDesigner (R2022a, Mathworks Inc., Natick, US) to control the flow rates and valve switching, as well as to record the sensor data of the flow and conductivity sensors and the applied pressures of the flow controller (see Figure B.11).

6.2.4 Chromatography Columns

Four Omnifit BenchMark Microbore chromatography columns (3x50 mm, column volume approx. 353 µL, Diba Industries Inc., Danbury, US) with 0.2 µm stainless steel end pieces were packed with Sephadex G-10 buffer exchange resin (Cytiva Life Sciences, Uppsala, SE) for use in the µSMB experiments. The slurry was prepared according to the manufacturer's specifications. Two columns were connected with a pack adapter and prefilled with the slurry before being connected to an ÄKTA pure 25 M system (Cytiva Life Sciences, Uppsala, SE). The columns were compressed by increasing the flow rate from 25 µL/min to 200 µL/min with a step size of 25 µL/min. Each step was held for 10 min and purified water was used as the mobile phase. Afterward, the pack adapter was replaced by an end piece and the column was again flushed for at least 40 min at a flow rate of 200 µL/min.

Next, the column and particle porosities were determined with tracer experiments. For this purpose, 2.5 µL of 1% (v/v) acetone (total porosity) or 1 g/L blue dextran (column porosity) were injected at a flow rate of 100 µL/min with water as mobile phase. Experiments were performed in triplicate for all columns. In addition, the retention times of Mb and Tris were determined by injecting 2.5 µL of a solution containing 1 g/L Mb and 10 mM Tris. Furthermore, the experiments were performed with a zero dead volume connector instead of a chromatography column to assess the system's contribution to the retention times of the different species.

6.2.4.1 Process Point Determination

A first estimate of a suitable process point was determined with the triangle theory [39], using the retention times of Mb and Tris and the calculated porosities of the single-column experiments. This process point was then used as the starting point for a process point optimization with the software CADET-SMB (version 2.12, CADET version 3.2.1, Institute of Bio- and Geosciences 1 (IBG-1) of Forschungszentrum Jülich (FZJ), DE) [204, 205]. For this, a single-column model was needed. The lumped rate model with pores was selected, as preliminary simulations showed that

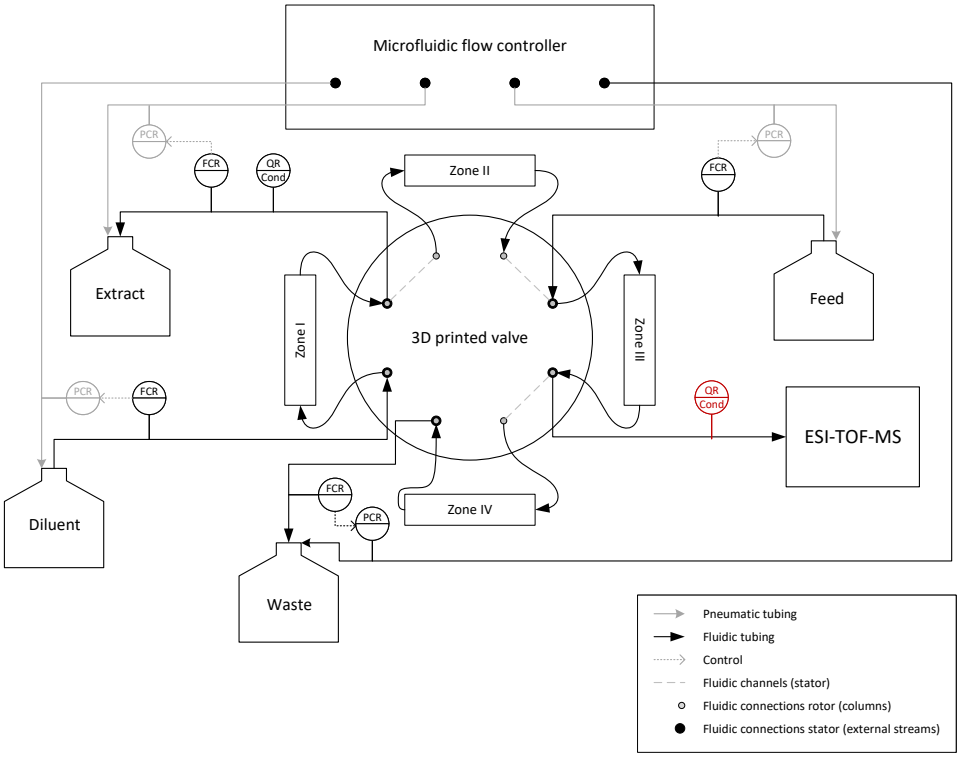

Figure 6.1: Instrumentation and piping diagram of the used µSMB setup. The conductivity sensor in the raffinate stream is only used when the µSMB is not coupled to the MS

it is not possible to distinguish the film transfer coefficient from particle diffusion based on the single-column experiments. Thus, the GRM has no advantage over the lumped rate model with pores, but has significantly longer computational times. The axial dispersion coefficient D_{ax} was estimated based on the correlation of Chung and Wen (6.1) [209], the film transfer coefficient k_{film} by the correlation of Wilson and Geankoplis (6.2) [81,210] and the molecular diffusion coefficient D_{m} according to Polson (6.3) [234] with the particle Reynolds number Re_{p} (6.4) [24], the mean particle diameter of the chromatography medium d_{p}, the interstitial velocity u_{int}, the density of water $\rho_{\mathrm{H_2O}}$, the dynamic viscosity of water $\eta_{\mathrm{H_2O}}$, the interstitial porosity of the chromatography column $\varepsilon_{\mathrm{int}}$, and the molecular weight MW of species i. The differential evolution algorithm of CADET-SMB was used for the process point optimization. An overview of all input parameters is given in Table C.2 in Appendix C.

$$D_{\mathrm{ax}} = \frac{u_{\mathrm{int}} d_{\mathrm{p}} \varepsilon_{\mathrm{int}}}{0.2 + 0.011 \left(\varepsilon_{\mathrm{int}} Re_{\mathrm{p}}\right)^{0.48}} \tag{6.1}$$

$$k_{\mathrm{film},i} = \frac{1.09 D_{\mathrm{m},i}}{d_{\mathrm{p}} \varepsilon_{\mathrm{int}}} \left(\varepsilon_{\mathrm{int}} \frac{u_{\mathrm{int}} d_{\mathrm{p}}}{D_{\mathrm{m},i}}\right)^{0.33} \tag{6.2}$$

$$D_{\mathrm{m},i} = 2.74 \cdot 10^{-9} MW_i^{-\frac{1}{3}} \tag{6.3}$$

$$Re_{\mathrm{p}} = \frac{u_{\mathrm{int}} d_{\mathrm{p}} \rho_{\mathrm{H_2O}}}{\eta_{\mathrm{H_2O}}} \tag{6.4}$$

6.2.4.2 µSMB-Experiments

All µSMB experiments were performed with the parameters determined with the process point optimization (diluent flow rate: 122 µL/min, extract flow rate: 44 µL/min, feed flow rate: 15 µL/min, raffinate flow rate: 30 µL/min, waste flow rate: 63 µL/min, switching time: 120 s). The microfluidic flow controller was operated with a feed-forward closed-loop control. Thus, initial values for the set pressures of the different process streams are required. These were determined by replacing the chromatography columns with capillaries with equivalent back pressure and starting the flow control with the desired flow rates as flow setpoints and 0 mbar for all pressure setpoints. The determined pressure start values were 1300 mbar for the diluent, 750 mbar for the extract, 1000 mbar for the feed and 600 mbar for the waste. The µSMB system with the chromatography columns was equilibrated with 10 mM NH_4OAc buffer for at least 45 min before each experiment. Then, the feed reservoir was filled with the respective feed solution and the experiment was started. After the experiment was finished, the system was first flushed with water and then with 20% (v/v) ethanol for storage.

A first µSMB experiment was performed stand-alone, without coupling to the mass spectrometer, with a feed solution containing 100 mM Tris.

6.2.5 µSMB-MS

To hyphenate µSMB and MS, the raffinate outlet port was directly coupled to the ESI interface of the MS system. To keep the delay volume between µSMB and MS as low as possible, the conductivity sensor of the raffinate was not used in this setup. Both, the µSMB and mass spectrometer, were equilibrated similarly to the stand-alone experiments. Two different experiments were performed: In the first one (run 1), the concentration of Tris in the feed solution was increased stepwise, while the concentration of Mb was kept constant at 0.2 g/L and the concentration of NH_4OAc was 10 mM. 10 mM NH_4OAc was also used as diluent. Tested Tris concentrations were 0, 1, 5, 10, 50, and 100 mM. The first section without Tris in the feed was run for eleven cycles (44 column switches) to ensure that the system runs stable. For all other concentrations, three cycles were conducted. The MS measurement continued during the exchange of the feed solution to the next higher Tris concentration, while the µSMB experiment had to be stopped.

The second experiment (run 2) was performed with a constant Tris concentration of 10 mM and Mb concentration of 0.2 g/L in the feed solution and was run for six cycles. All other conditions were identical to the first run.

6.3 Results and Discussion

Current applications of off-line MS measurements in biopharmaceutical processing range from the detection of aggregates, charge variants, and other product-related impurities to the detection of process-related impurities. In our proof-of-concept study, native myoglobin (holoMb) represents the product, and dissociated myoglobin (apoMb) alongside the heme group exemplify product-related impurities. We first verified that we are able to detect holoMb, apoMb, and heme with the MS measurement and evaluated the influence of Tris buffer, as one example of a frequently used biological buffer, on the measured signals. Subsequently, we tested whether we could reduce

the negative influence of the Tris buffer on the MS measurements by hyphenating the µSMB to the mass spectrometer.

6.3.1 Off-line MS measurements

6.3.1.1 Myoglobin

First, we performed off-line measurements with pure Mb samples to ensure that we can detect all target molecules under native conditions. The resulting spectra are depicted in Figure 6.2a. The first row shows a background spectrum of the used NH_4OAc buffer, the second row shows a spectrum of Mb under native conditions, and the last row shows the same Mb sample under non-native measurement conditions. Comparing the buffer and the native Mb spectrum, five additional peaks with three different charge states, ranging from sevenfold to ninefold, are detected. These signals are probably caused by holoMb and apoMb. Comparing these peaks with the non-native spectrum, it can be observed that the signal intensity of the peaks with the lower m/z ratio of each charge state increases while the signal intensity of the peaks with the higher m/z ratios decreases. It can therefore be concluded that the peaks with higher m/z ratios are holoMb (marked with □ in the spectra) and the peaks with lower m/z ratios are apoMb (marked with • in the spectra).

This assumption was verified by reconstructing the protein masses from the spectra; the resulting spectrum is depicted in Figure 6.2b. Two peak groups are detected, the main peak of the first one has a molar mass of 16950.5 Da and the second one of 17566.0 Da. This is in accordance with the molar masses of apoMb and holoMb reported in the literature [231,235,236], confirming their identity and our ability to measure both variants of Mb. The difference between the measured peaks is 615.5 Da, which corresponds to the mass of the dissociated heme group.

The signal of the heme group can also be observed in the non-native Mb spectrum in Figure 6.2a at m/z 616.18 and 633.16 (oxidized form) [237]. Remarkably, the heme signal has a higher intensity than the apoMb signal, although it is formed by the dissociation of holoMb to apoMb and therefore must be present at the same concentration as apoMb. However, the mass of the heme group is more than ten times smaller than that of apoMb, and since smaller molecules are generally easier to ionize, the higher signal intensity is due to a higher ion yield.

Figure 6.2b shows that there are not two single peaks detected for apoMb and holoMb, but rather two peak groups. The difference in molar mass of the individual peaks is approximately 23 Da, which equals the mass of sodium. Therefore, the peaks in one group correspond to different sodium adducts of the respective molecule.

The close-up of the main holoMb peak in Figure 6.2c shows that these sodium adducts were already present in the original native Mb spectrum in Figure 6.2a. Furthermore, each sodium adduct peak consists of multiple isotopic peaks. Therefore, in order to use all detected signals of holoMb and apoMb in the analysis of the following experiments, the integral of the protein reconstruction spectrum for the respective peak group was usually used instead of an extracted-ion chromatogram of a single signal.

(a)

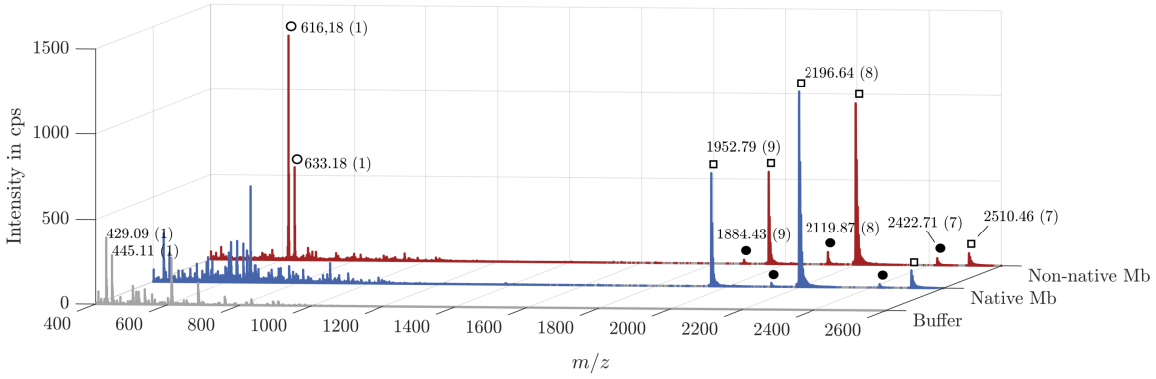

(b)

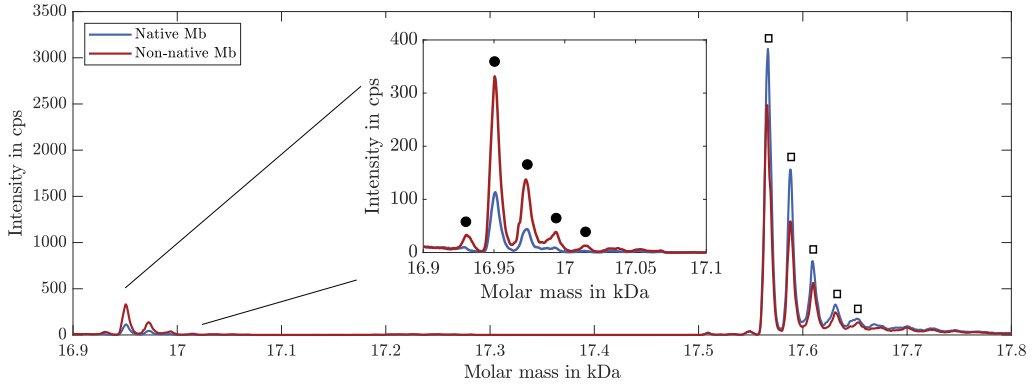

(c)

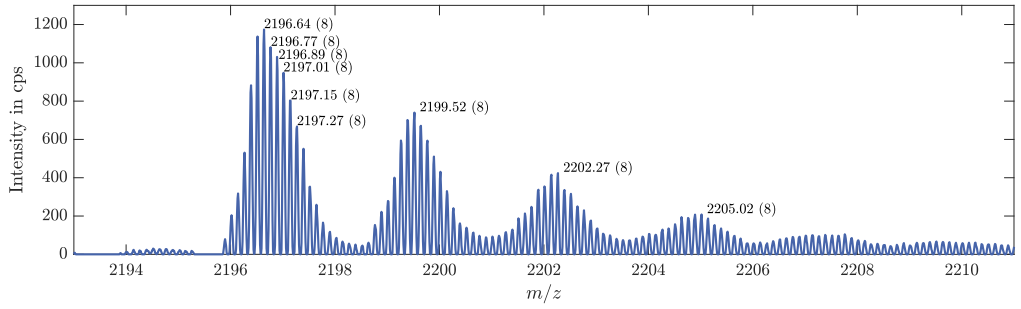

Figure 6.2: Measurement of Mb in native and non-native state: (a) background spectrum of 10 mM NH_4OAc buffer and spectra of Mb under native and non-native measurement conditions; (b) Protein reconstruction of the Mb spectra from (a); (c) close up of the Mb main peak with isotopic peaks and sodium adducts. In (a) and (c) charge states are assigned in parenthesis after m/z labels. In (a) and (b) peaks of holoMb are marked with □, of apoMb with • and of heme with ∘

6.3.1.2 Influence of Tris concentration

Most biological buffers are incompatible with ESI, as they are either not volatile or introduce a high level of noise to the background signal [228, 229]. Therefore, the influence of different concentration levels of Tris buffer on the MS detection of Mb was investigated next with off-line measurements. For this purpose, the concentration of Tris in a Mb solution was varied between 0 mM and 1 mM, as these levels of Tris buffer have been previously introduced into ESI-MS systems [228].

The resulting spectra in Figure 6.3a show no visible effect at a Tris concentration of 0.01 mM for the signals of holoMb with seven- and eightfold charge states, while the peak height of the holoMb signal with ninefold charge state slightly decreases. Starting at a concentration of 0.1 mM, the peak heights of all apoMb signals decrease. In addition, a shift towards higher sodium adducts is observed, especially for the peak corresponding to the sevenfold charged species. This effect is further enhanced in the sample containing 1 mM Tris, suggesting that sodium is a contaminant in the Tris buffer. Also, the detected amount of Mb decreases further and even the most intensive holoMb signal at m/z 2196.64 has a decreased peak height, indicating that the sensitivity of the mass spectrometer is negatively affected. Furthermore, as previously observed, Tris induces a lot of noise in a wide range of m/z ratios, with the most intensive signal at m/z 593.23 [228]. This signal reaches up to 23 kcps (a full-scale plot is included in Figure C.13 in Appendix C) which is 50 times higher than the detected signal level of the heme group, thus hindering its detection.

Figure 6.3b depicts the calibration curve of the measured Tris signal at m/z 593.23±0.2. The calibration was measured twice with independent calibration solutions and the Tris signal was normalized with the baseline chromatogram of the respective measurement. The Tris signal shows an exponential increase with concentration in the logarithmic plot, corresponding to limited growth. This is typical for an analytical system when its detection limit is reached and not only indicates that the applied concentrations are much too high, but also prevents the calculation of the exact Tris concentration from the signal. Therefore, at these concentrations, it is no longer possible to reconstruct the Mb concentration by taking the Tris concentration into account, which emphasizes the strong influence of Tris concentrations as low as 1 mM (speaking from a bioprocessing point of view, where concentrations up to 10 mM and higher are state-of-the-art) on the measurement quality.

Figure 6.3b also depicts the detected signal level of holoMb. As mentioned above, the amount of holoMb was calculated by integrating the respective peaks of the protein reconstruction chromatogram. This way, all charge variants and sodium adducts are included in the calculation and effects such as the shift to higher sodium adducts with higher Tris concentrations are not considered. Nevertheless, the total detected amount of holoMb decreases exponentially with the Tris concentration. Starting from 46.4 kcps at 0 mM Tris, the detected amount is more than 2.5 times lower at a Tris concentration of 1 mM, meaning less than 40% is detected. Even at a Tris concentration of 0.01 mM, the detection level is below 90%, underlining the severe impact on the measurement quality even at comparatively low buffer concentrations.

Figure 6.3c shows the influence of the Tris concentration on the detection of apoMb and the heme group, respectively, as two different ways to detect the product-related impurity level of our model system. While the amount of apoMb is derived from the protein reconstruction, the

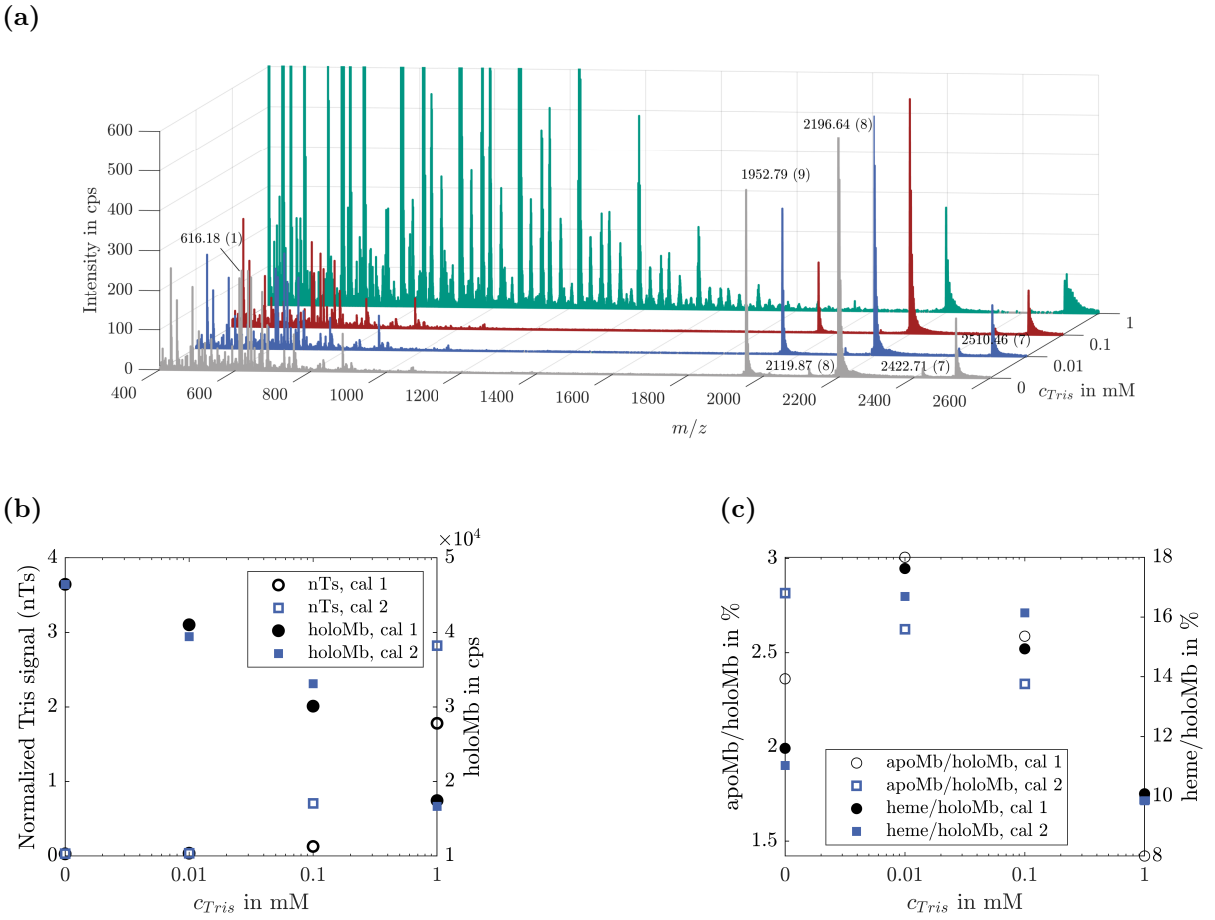

Figure 6.3: Influence of Tris buffer on MS detection of Mb: (a) Mass spectra of solutions containing 10 µg/mL Mb with increasing Tris concentrations. Charge states are assigned in parenthesis after m/z labels; (b) normalized Tris signal (m/z 593.23) and amount of detected holoMb in dependence of Tris concentration; (c) influence of Tris concentration on detected percentage of apoMb and heme group. The detected amount of apo/holoMb was calculated by integration of the respective peaks in the protein reconstruction chromatogram

amount of heme was calculated with the extracted-ion chromatogram at m/z 616.16. Overall, the amount of heme is higher than that of apoMb, which is again caused by the better ion yield. In both cases, the detected level increases at low Tris concentrations before decreasing at higher Tris concentrations. This can either mean that low Tris concentrations induce the dissociation of holoMb or increase the ion yield of the molecules. Excluding the point without Tris, both detection routes show comparable results with a drop in apoMb and heme level detection of approx. 10% from 0.01 to 0.1 mM Tris and of approx. 56% from 0.1 to 1 mM Tris.

These results clearly show that the applied ESI-MS measurements are not a suitable analytical method for samples containing Tris buffer without prior treatment. Even at concentrations as low as 0.01 mM, an effect of Tris on the measured overall concentrations of holoMb, apoMb and heme is observable. Other parameters, like the signal intensity of the Mb main Peak at m/z 2196.64, are less influenced by Tris and only show a decreased signal intensity starting at a Tris concentration of 1 mM, which is still far below the concentrations typically applied in biotechnological processes.

6.3.2 Desalting with the µSMB

In the following µSMB-MS experiments we increased the Tris concentration to higher levels up to 100 mM, which are more relevant for bioprocessing. Therefore, it is important to ensure that the µSMB provides a sufficient desalting level to prevent damage to the MS instrument during the hyphenation experiments. Thus, the desalting performance of the µSMB system was assessed stand-alone before the actual µSMB-MS experiments were performed.

Figure 6.4 depicts the measured Tris concentration in the raffinate and extract streams during an experiment with a feed solution containing 100 mM Tris. Tris is detectable in both the extract and raffinate streams; however, the mean concentration in the raffinate is more than 20 times lower compared to the extract, proving that the desalting process is working.

The concentration profiles show the typical startup behavior of SMB processes; after approx. 20 min, a cyclically recurring peak pattern is observed. This state is referred to as cyclic steady state (CSS) and is caused by column switching. Even when the CSS is reached, not all Tris peaks

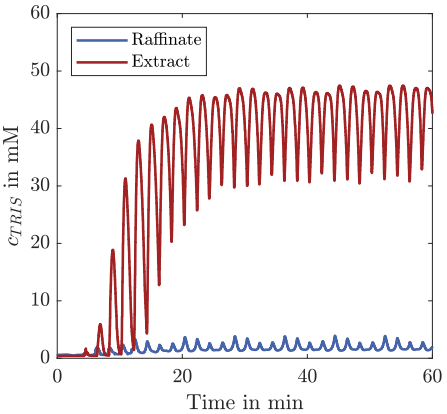

Figure 6.4: Tris concentrations in the raffinate and extract streams during a µSMB experiment with 100 mM Tris in the feed solution

have the same height, but every fourth peak is comparable. This is caused by slight performance differences between the four chromatography columns.

Since the CSS is of particular interest for continuous long-term applications, the mean desalting level was calculated for the CSS rather than for the entire process. This way, the calculated desalting level is also independent of the process time. The calculated mean Tris concentration in the raffinate in the CSS was 1.93 mM, which equals a desalting level of 98.07%.

While this already reduces the Tris concentration by almost two orders of magnitude, it is still below the desalting levels of above 99% previously achieved with the µSMB system [230]. However, these experiments were performed with a different separation system, and a comparison of the single-column chromatograms of both separation systems (see Figure C.14) shows that the lower desalting level is caused by a lower single-column performance and not by the µSMB setup.

Comparing these results with the influence of Tris on the MS measurements in the previous section shows that the µSMB is able to remove Tris to a point where it doesn't damage the MS system. Nevertheless, for the µSMB-MS experiments we expect to see an influence of Tris on the MS measurements when working with feed concentrations of 100 mM Tris, which is further investigated in the following sections.

6.3.3 µSMB-MS

6.3.3.1 Hyphenation

The first step for hyphenating the µSMB with the MS system is to generate the desired flow rates for the in- and outlet streams of the µSMB. For the µSMB-MS, it is not possible to directly control the raffinate flow rate with the pressure-driven microfluidic flow controller, as it is not possible to directly control the outlet pressure. Instead, the waste flow rate was controlled to achieve the desired raffinate flow rate based on the overall mass balance of the system.

This method for flow rate control was first validated without hyphenation to the MS system, the resulting flow rates are given in Figure 6.5a. The horizontal black lines are the respective set flow rates. Positive flow rates correspond to streams entering the system and negative ones are leaving the system. Every two minutes, during the switching process, there is a spike in the flow rates. This has been reported previously and usually has no negative effect on the separation performance due to the short time frame of occurrence [198]. In between the switching processes, the set flow rates are reached, proving the validity of the approach used.

In Figure 6.5b, the raffinate stream is directly infused into the ESI interface of the MS system. This setup is particularly challenging for the flow rate generation, as the raffinate outlet pressure is subject to additional pressure fluctuations caused by the vacuum pumps of the MS system. Some flow rate spikes have a different shape, others are higher compared to the setup without MS, and especially in the waste stream there are some minor flow rate fluctuations between the switches. Nevertheless, the mean flow rate over one switching interval corresponds to the set flow rate, ensuring that each of the SMB zones can fulfill its task. Thus, it is possible to hyphenate the µSMB and MS system hardware-wise.

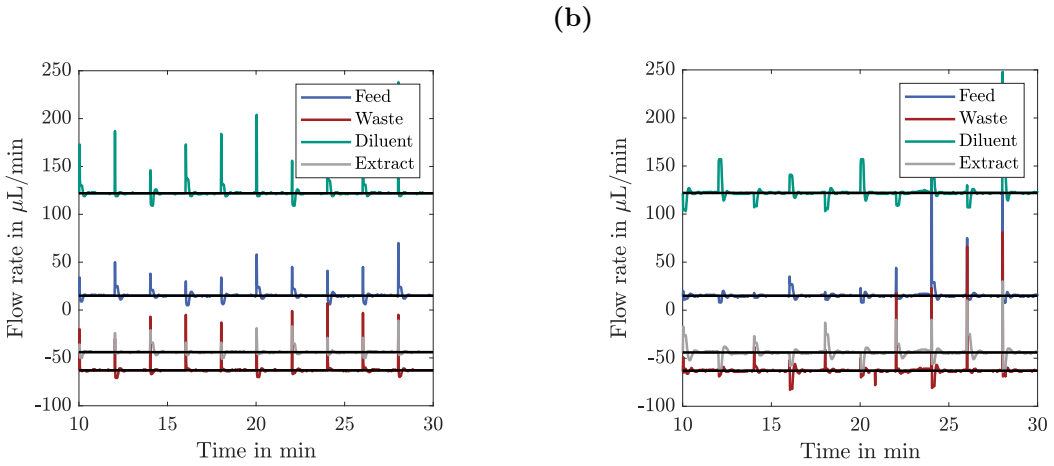

Figure 6.5: Comparison of the different in- and outlet flow rates without (a) and with (b) direct coupling of the raffinate stream to the ESI interface of the MS system

6.3.3.2 Proof-of-Concept

Two different buffer exchange experiments were performed with the µSMB-MS setup to assess whether the hyphenation can improve the MS measurement quality. In the first one (run 1), the Tris concentration in the feed solution was increased step-wise, such that the impact of Tris on the MS equipment could be assessed before further increasing the concentration. The second experiment (run 2) was performed with a constant Tris concentration in the feed.

Figure 6.6a shows the normalized extracted-ion chromatograms of holoMb (m/z 2196.64±0.02), the heme group (m/z 616.18±0.02) and Tris (m/z 593.23±0.02) throughout the experiment (run 1). The sections with different Tris concentrations are indicated in the plot. During the experiment, the flow had to be stopped several times to increase the Tris concentration in the feed solution. This resulted in an abrupt drop of the baseline signal, which caused a steep increase of the heme signal, as there are still traces of the analytes at the ESI interface and the heme group has a better ionization efficiency than the other molecules. During the phase with 0 mM Tris in the feed solution, the flow had to be stopped one additional time due to a pressure leakage in the feed reservoir. The third SMB cycle of every Tris concentration is depicted in Figure 6.6b for better comparability. The respective areas are marked with black rectangles in Figure 6.6a. Again, the typical startup behavior of SMB processes is observed. The CSS is already reached after 15 min, since only the raffinate signal is displayed, which reaches its CSS earlier than the extract signal. The peak heights of the Mb signal peaks vary throughout the experiment. As discussed previously for the Tris signal (see Figure 6.4), this is caused by differences in the chromatography columns. The first Tris signals are detected at a feed concentration of 5 mM. The peak height increases at 10 mM, where it becomes apparent that the breakthrough of Tris is countercyclical to the detection of Mb. This is interesting for on-line analytical applications, as the Tris concentration is the lowest when most Mb is eluted, resulting in less interference from Tris with the measurement compared to a constant Tris concentration with the mean value.

Up to 10 mM Tris, no adverse effects on the detection of Mb and the heme group are observed. This is in accordance with the stand-alone MS experiments depicted in Figure 6.3a, as no negative

(a)

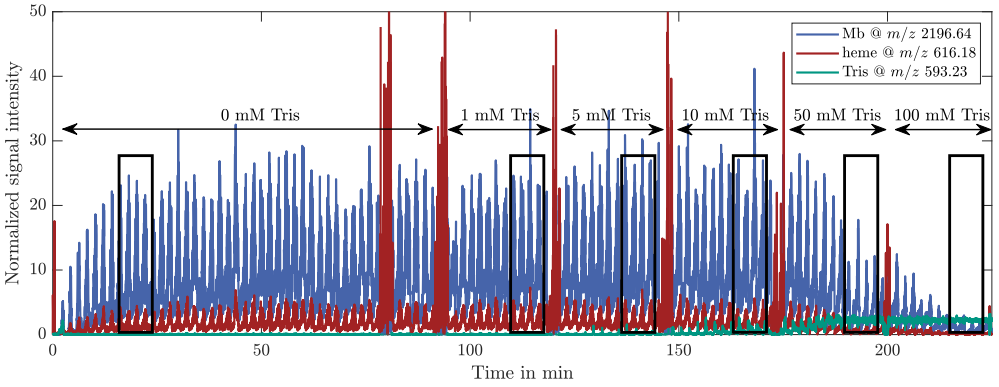

(b)

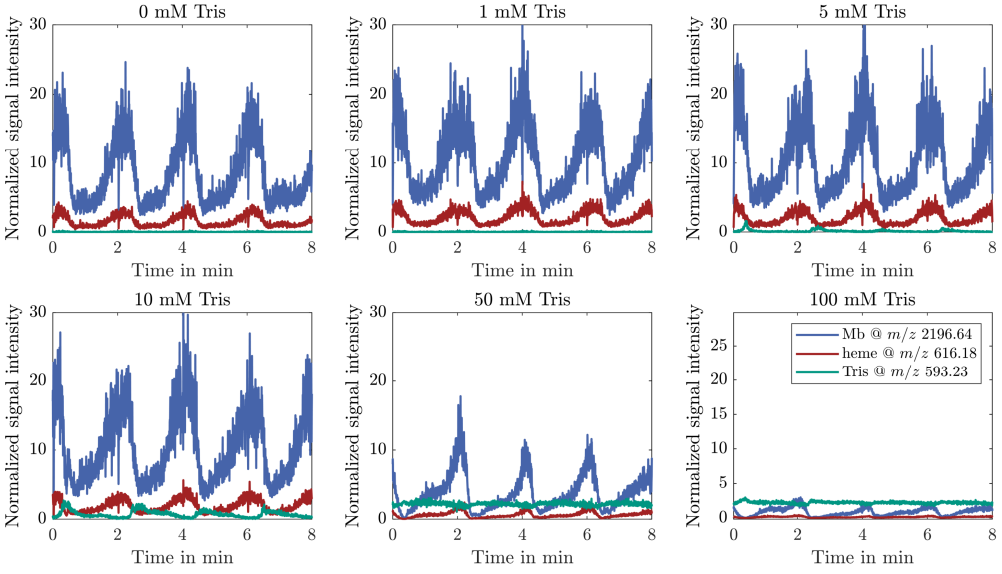

Figure 6.6: Normalized signals of Mb, heme group and Tris (a) during the entire first µSMB-MS experiment (run 1); (b) for the third process cycle at every Tris concentration (marked with black boxes in (a))

effect on the detection of the holoMb main signal was observed for Tris concentrations below 1 mM. At a higher Tris concentration of 50 mM, the detected concentrations of Mb and heme decrease significantly, similar to the previous experiments. Interestingly, the Tris signal does not increase much compared to 10 mM Tris due to the baseline correction: With an expected desalting level of 98%, the average Tris concentration in the raffinate of the 50 mM Tris µSMB experiment is 1 mM. This concentration results in a high noise level for smaller m/z ratios, as depicted in Figure 6.3a. Consequently, the baseline signal, which is recorded at m/z ratios between 400 and 500, is also affected. At such high Tris concentrations, it is not only increased, but it also fluctuates with the Tris concentration, which is why the Tris signal no longer shows a cyclic pattern at concentrations above 50 mM. This effect increases further for the 100 mM experiment. Here, the baseline signal is almost ten times higher than in the experiment without Tris. The equivalent of Figure 6.6b without baseline correction is included in Figure C.15 for reference.

While we see a significant effect of Tris concentrations exceeding 50 mM on the holoMb main peak detection, we do not observe any negative effects up to a concentration of 10 mM. Therefore, we chose this concentration for a second experiment (run 2), which was performed with a constant Tris concentration in the feed solution. When using higher Tris concentrations or when investigating other features like the ratio of holoMb to apoMb, the desalting level should be increased by adapting the µSMB system, e.g., by using more than one column per zone, by increasing the single column resolution, with further process point optimization or by applying other SMB-process variants.

Figure 6.7a depicts the mean Tris signal of the third cycle of each Tris concentration of µSMB run 1 for quantitative assessment of the results. In addition, the measured signals from the calibration experiments (Figure 6.3b) are included for comparison. The concentrations of the calibration standards were multiplied by the expected desalting level to match the x-axis. Furthermore, the mean Tris signal of the third cycle of µSMB run 2 is depicted. The results of both µSMB runs are in good agreement, demonstrating that the µSMB-MS system can achieve reproducible desalting levels and that the performance is independent of the buffer concentration during the startup processes. This is important for PAT applications where variations in product quality need to be detected regardless of the previous process state. Although the measurements of the calibration standards are subject to variation, there is good agreement between the experiment and the calibration, meaning that the expected desalting level of 98% was achieved. This shows that the coupling of the MS system to the µSMB has no negative effect on the latter's performance.

Figure 6.7b shows the effect of the Tris concentration on the MS sensitivity for run 1. Again, for very low Tris concentrations, there is an effect that increases the detected levels of holoMb and heme. At higher concentrations, the detected holoMb concentration as well as the amount of apoMb and heme decrease exponentially. While the detected apoMb is in the expected range from the calibration results, the detected heme level spans a much broader range, which indicates that the apoMb level is more reliable. This was expected, as Tris induces more noise in the detection m/z range of heme. For both the detected amount of holoMb and apoMb, the influence of Tris is less than would have been predicted for a desalting level of 98%, as both signals decrease by only

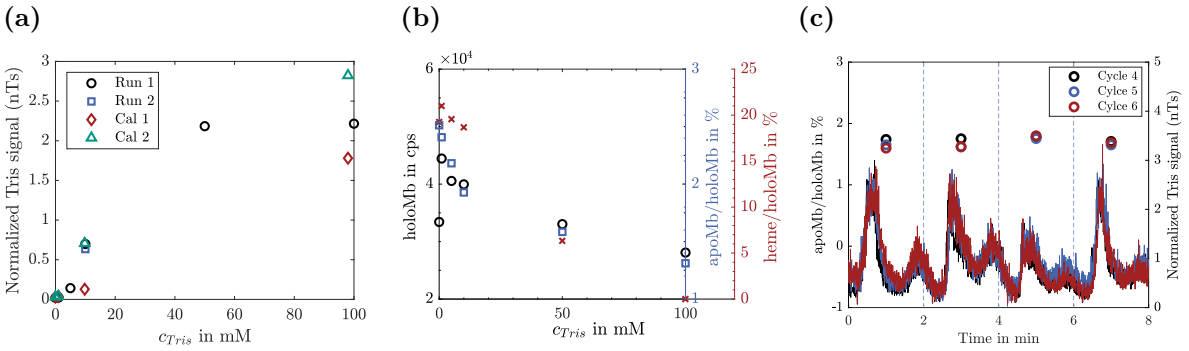

Figure 6.7: (a) Normalized Tris signal as a function of the Tris concentration in the feed of the µSMB experiments. Depicted values are the mean values of the third cycle of each concentration. The Tris concentrations of the calibrations were multiplied with the expected desalting level of 98% in order to match the x-axis. (b) Detected apoMb percentage and detected amount of Mb as a function of the feed Tris concentration during the experiments. The values are mean values of the third cycle of the µSMB process for each concentration. (c) Detected apoMb percentage and Tris signal level for three consecutive cycles (4-6) of µSMB run 2 with a constant Tris concentration of 10 mM in the feed stream. The apoMb level was calculated for each switching interval, as indicated by the dotted vertical lines

10% up to a Tris feed concentration of 10 mM. This could be caused by the positive influence of very low Tris concentrations or the effect of the alternating breakthrough of Tris and Mb described in the previous section. Either way, the detection level of both holoMb and apoMb is highly increased by the hyphenation of the µSMB to the MS.

The results in Figure 6.7a and Figure 6.7b all refer to just one cycle of the µSMB process for the respective concentration. For a continuous on-line analytical application, the system must provide a reliable and comparable performance over a long time. Therefore, Figure 6.7c shows the detected ratio of apoMb to holoMb and the normalized Tris signal for three consecutive SMB cycles of run 2. The percentage of apoMb was calculated for one switching time, as indicated by the dotted vertical lines. The curves of the Tris signal again show differences in the separation performance of the different columns. At the same time, the desalting performance of the same column in different cycles is highly reproducible.

Due to the chosen scale of the plot, it can be observed that there are not one but two Tris peaks per switching time, meaning that there are two different concentration fronts of Tris in acSMB zone III that break through at different times. The fact that the MS system is able to reproducibly capture the dynamic of the Tris breakthrough and the different peak shapes shows that there are no memory effects for the MS measurement that interfere with the long-term measurement. In addition, it is a general indicator of the robustness of the µSMB-MS setup and proves that the µSMB system can provide stable flow rates. The mean detected apoMb percentage remains consistent across switches and cycles, which is reasonable since the mean Tris concentration is also constant. If the apoMb level is calculated over a time period shorter than one switching interval, it is subject to variation (see Figure C.16), because the Tris concentration is not constant. However, if the same time intervals are used for the calculation in all switches, the obtained results are highly reproducible.

6.4 Conclusion

In this study, we successfully hyphenated a µSMB to an ESI-MS system, demonstrating that the µSMB is a valuable tool for on-line sample pre-processing. Throughout the study, we achieved consistent desalting levels of 98% with the µSMB, improving the MS sensitivity significantly. While the detected level of holoMb already dropped below 40% at a Tris concentration of 1 mM without hyphenation to the µSMB, 89% of holoMb still was detected at a 10 mM Tris concentration when the MS system was coupled to the µSMB. The advantage of the µSMB compared to conventional LC systems is not limited to the continuous mode of operation; using the countercurrent principle additionally leads to a high separation efficiency even with poor performance of the single chromatography columns. This makes the µSMB an interesting tool for many applications and challenging separation problems. In addition to SEC, SMB is frequently applied with various other chromatography modes, e.g. for enantioseparation [39]. Future applications of the µSMB-MS principle are not limited to process control at a preparative scale, but can also provide useful insights during process development. At the same time, the system presented here is not restricted to the SMB principle; the setup can be easily adapted to any type of multi-column chromatography and used to hyphenate it to MS, by simply exchanging the 3D printed valve that is used to connect the columns with one fitting the needs of the particular process.

In order to exploit the full potential of µSMB-MS as a PAT application, future studies should investigate the system's response time and residence time distribution, a critical aspect for process optimization. The expected response time of the system is between the µSMB switching time and the cycle time, depending on the phase of the SMB cycle in which a fluctuation occurs, i.e., 2-8 min for the system presented in this study, which is comparable to current LC-MS systems [238]. However, the continuous sampling omits the possibility of undersampling and ensures that each fluctuation is accurately captured with respect to its starting point. In addition, further downscaling of the µSMB system, e.g. by using capillary columns, promises to further reduce the response time and thus increase the applicability of the system.

7. Modeling the Extra Column Volume of a Micro Simulated Moving Bed Chromatography System: Introducing the Equivalent Radial Flow Rate Distribution

Juliane Diehm[1] and Matthias Franzreb[1,*]

[1] Institute of Functional Interfaces, Karlsruhe Institute of Technology, Eggenstein–Leopoldshafen, 76344, Germany

Abstract

Recently, the focus in chromatography model development has expanded to include the modeling of extra column volume (ECV), particularly in small- and lab-scale systems where ECV can constitute a significant portion of the total volume. Typically, ECV is modeled with 1D approaches, for example with combinations of dispersed plug flow reactors (DPFRs) and continuously stirred tank reactors (CSTRs). However, radial inhomogeneities in the ECV concentration profile necessitate higher-dimensional models for more accurate predictions. Searching for a suitable modeling approach for a micro simulated moving bed chromatography (µSMB) system, we investigated whether the 2D laminar flow model can be extended to account for additional dispersion effects, such as Dean vortices, through an equivalent radial flow rate distribution (eqFRD). For this purpose, we conducted 3D CFD simulations of the respective ECV and adapted the radial flow rate profile of a 2D simulation to match the residence time distribution observed in the CFD results.

Applying the eqFRD model led to a significant improvement in prediction accuracy for isolated ECV segments, increasing from 90% to 97% compared to traditional ECV models. However, when these models were applied to the full µSMB system, the choice of ECV model had minimal impact on overall results as long as retention time within the ECV was accurately predicted.

This suggests that, in the studied system, the column has a greater influence on peak shape than the ECV, allowing simpler ECV models to suffice in certain contexts.

Despite these advances, significant deviations between predicted and experimental results were observed, indicating that factors such as the transition between the column and ECV, as well as detector effects, should be considered in future research. The results underscore the importance of selecting an ECV model in the context of the entire system, balancing accuracy with computational efficiency.

Keywords
chromatography modeling; extra column volume; dead volume;small-scale chromatography; multi-column chromatography

published in *Journal of Chromatography A*, `https://doi.org/10.1016/j.chroma.2024.465543`,

CRediT authorship contribution statement
Juliane Diehm: Conceptualization, Methodology, Investigation, Visualization, Software, Writing – original draft. Matthias Franzreb: Conceptualization, Writing – review & editing.

7.1 Introduction

Chromatography is the predominant method for DSP of biopharmaceutical products [10]. As product titers increase, the focus of cost reduction shifts from USP to DSP, with chromatography emerging as the main cost driver [239]. This has prompted a considerable effort to optimize chromatography process development and reduce production expenses [10, 11, 239].

One effective strategy for cost reduction in preparative applications is the implementation of (continuous) multi-column methods, such as SMB and PCC chromatography [10]. These techniques offer numerous benefits, including higher capacity utilization, reduced solvent consumption, and increased productivity [10, 183]. Simultaneously, the adoption of miniaturization and advanced process modeling aims to minimize experimental efforts and associated costs in process development [11, 89].

The use of miniaturized single-column chromatography systems enables material and time efficient determination of important process parameters, often in an automatized fashion [89, 240]. These single-column experiments, combined with chromatography modeling, can be sufficient for multi-column process development. Nonetheless, miniaturized multi-column systems can be advantageous: continuous processes reduce the required equipment scale by approximately a factor of ten compared to batch operations, making batch chromatography systems unsuitable for some applications [11]. Kortmann et al. developed a miniaturized PCC system with potential applications in condition screening or product capture from perfusion cell cultures [95]. Recently, we developed a µSMB system and demonstrated its applicability as a resource-saving tool in small-scale continuous process development [230] (Chapter 5) as well as for process analytics [241] (Chapter 6). The scaled-down equipment significantly conserves resources, especially for long-term studies, while the reduced scale also allows for a fast response time in analytical applications.

Detailed modeling is critical for either performance comparison across scales or optimization of process parameters. While chromatography columns are typically modeled using one-dimensional approaches, such as the general rate model or the equilibrium dispersive model [24, 242], different approaches exists for the modeling of the ECV.

SMB is a quasi-continuous binary separation technique that continuously separates a feed stream into two product streams by using multiple interconnected chromatography columns, divided into four zones by inlets and outlets. This results in a different flow rate in each of the zones and through the timed movement of columns, each zone fulfills a specific function, including separation of components and regeneration of the stationary and mobile phases. A detailed explanation of the SMB principle can be found in literature [39, 40, 46] and Section 2.1.2.1.

In preparative SMB, accurate modeling is essential for determining optimal process points, ensuring efficient separation, and accounting for ECV. ECV is commonly modeled as either an ideal PFR [85], accounting only for time delay without dispersion effects, or as a DPFR [44], considering uniform dispersion and time delay.

DPFRs are also frequently used to model capillaries in lab-scale systems, in conjunction with CSTRs to account for mixing effects in other system components, such as valves and detectors [86, 87, 243]. However, the flow rate dependency of model parameters is often seen as a

drawback in lab-scale systems. To address this, Baran et al. implemented a two-dimensional DPFR considering the radial laminar flow profile, demonstrating good predictability of ECV behavior across a wide range of flow rates [244]. Filip et al. implemented computational fluid dynamics (CFD) models at various geometric levels, showing that under certain conditions, the most detailed model, which includes curvatures and diameter changes, is necessary to accurately predict ECV effects under all tested conditions [88]. Therefore, a trade-off exists between simple DPFR+CSTR models, which offer short computation times but may be inaccurate if the flow rate deviates significantly from the calibration flow rate, and more sophisticated models, such as CFD models, which provide accurate predictions regardless of flow rate but require much longer computation times. This is particularly important when using small chromatography columns, where ECV significantly influences overall dispersion behavior [245], necessitating a more detailed ECV model.

Thus, in the case of the µSMB system, a significant impact of the ECV on the overall system performance is expected and a detailed ECV model required. However, modeling ECV with CFD is impractical for continuous processes where the same portion of ECV must be modeled multiple times, potentially at different flow rates. Consequently, there is a need for a flow rate-independent, accurate prediction of ECV with low computation time.

Given the considerable differences between state-of-the-art ECV modeling in preparative SMB and miniaturized single-column chromatography, we found a limitation in existing ECV models. To address this, we explored the feasibility of transferring the two-dimensional DPFR approach to other flow rate distributions beyond the laminar flow profile, thereby accounting for all ECV effects. This new approach is termed the equivalent radial flow rate distribution (eqFRD).

In this study, we provide a brief overview of current model approaches and the considerations for establishing the eqFRD. We then compare various ECV modeling approaches in different scenarios, ranging from simple capillaries to the ECV of a µSMB system.

7.2 Theoretical Background

7.2.1 Overview of common ECV models

Currently, the most common approach for ECV modeling of lab-scale chromatography systems is with CSTRs, (D)PFRs or a combination thereof [86, 87, 243]. CSTRs are usually applied for modeling elements with distinct mixing effects like valves and mixers [243]. The change in concentration c of component i over time t can be described according to (7.1) with the inlet concentration $c_{i,\mathrm{in}}$ and the average residence time τ [246], which is the quotient of the CSTR's volume V_{CSTR} and the volumetric flow rate Q [247]. PFRs, on the other hand, add a lag time caused by delay volume and are used for the modeling of capillaries [243]. While ideal PFRs solely consider mass transfer by convection, DPFRs have an additional term to include dispersion effects. DPFRs can be described using (7.2) with the mean linear velocity u_{mean}, spatial coordinate z and the dispersion coefficient D_{ECV} [44]. If D_{ECV} is set to zero, the resulting equation describes a PFR; due to the spatial discretization in the simulation process, leading to so called numerical dispersion, the resulting model still will have a dispersion greater than zero. This effect can be utilized to obtain an accurate model with a low number of spatial

grid-points, thus increasing the numerical efficiency. The required number of grid-points N_{ECV} can be approximated with (7.3) [44], with the length of the ECV L_{ECV} [44]; with only one grid-point, the model equals a CSTR model and with infinite grid-points it is a PFR model.

$$\frac{\delta c_i}{\delta t} = \frac{c_{i,\mathrm{in}} - c_i}{\tau} \tag{7.1}$$

$$\frac{\delta c_i}{\delta t} + u_{\mathrm{mean}} \frac{\delta c_i}{\delta z} = D_{\mathrm{ECV}} \frac{\delta^2 c_i}{\delta z^2} \tag{7.2}$$

$$N_{\mathrm{ECV}} = \frac{L_{\mathrm{ECV}} u_{\mathrm{mean}}}{2 D_{\mathrm{ECV}}} \tag{7.3}$$

For certain flow patterns and conditions, D_{ECV} can be calculated. For example, in a straight capillary with laminar flow, it can be calculated using (7.4) with the molecular diffusion coefficient D_{m}, the radius of the capillary R_{cap} and the coefficient $\kappa = 48$ (for laminar flow in a straight tube), if the conditions of Taylor-Aris dispersion are fulfilled [248, 249]. This can be verified with (7.5), which tests if the residence time in the capillary is long enough to reach a radial concentration equilibrium and can thus be treated as a DPFR [244, 248].

$$D_{\mathrm{ECV}} = D_{\mathrm{m}} + \frac{u_{\mathrm{mean}}^2 R_{\mathrm{cap}}^2}{\kappa D_{\mathrm{m}}} \tag{7.4}$$

$$L_{\mathrm{crit}} > \frac{u_{\mathrm{mean}} R_{\mathrm{cap}}^2}{4 D_{\mathrm{m}}} \tag{7.5}$$

If condition (7.5) is not met, the radial flow distribution of the laminar flow profile leads to so called peak splitting, where the convection peak consisting of molecules close to the center of the capillary moves faster compared to the diffusion peak at the perimeters of the capillary. This effect is particularly pronounced for macro molecules due to their lower molecular diffusion coefficient and has already been extensively discussed [244, 250]. To account for this effect, the radial flow profiles as well as radial diffusion have to be considered in (7.2) [244]:

$$\frac{\delta c_i}{\delta t} + u(r) \frac{\delta c_i}{\delta z} = D_{\mathrm{m}} \frac{1}{r} \frac{\delta}{\delta r} \left(\frac{\delta c_i}{\delta r} r \right) + D_{\mathrm{m}} \frac{\delta^2 c_i}{\delta z^2} \tag{7.6}$$

with the radial flow distribution $u(r)$ according to (7.7) in case of laminar flow [244].

$$u(r) = 2 u_{\mathrm{mean}} \left[1 - \left(\frac{r}{R_{\mathrm{cap}}} \right)^2 \right] \tag{7.7}$$

Alongside the temporal dimension, the partial differential equation for describing mass transport in the ECV now has two spatial dimensions, z and r. In real systems, additional effects often occur that are not captured by (7.7), an example are so-called Dean vortices, which can arise in curved capillaries due to centrifugal forces and cause further dispersion [251]. These effects can be modeled, for instance, by 3D CFD models [88]. Whether Dean vortices need to be considered can be determined with the Dean number Dn calculated using (7.8) with the Reynolds number Re_{cap}, the capillary diameter d_{cap}, the curvature radius R_c, the fluid density ρ, the dynamic

viscosity η, and the Schmidt number Sc; if condition (7.10) is met, the centrifugal forces can be neglected [88].

$$Dn = Re_{\mathrm{cap}}\sqrt{\frac{d_{\mathrm{cap}}}{2R_c}} \tag{7.8}$$

$$Re_{\mathrm{cap}} = \frac{\rho u_{\mathrm{mean}} d_{\mathrm{cap}}}{\eta} \tag{7.9}$$

$$Dn^2 Sc < 100 \tag{7.10}$$

$$Sc = \frac{\eta}{\rho D_{\mathrm{m}}} \tag{7.11}$$

Filip et al. used 3D CFD simulations for geometries where the Dean vortices could not be neglected [88]. However, CFD simulations are so far only applied in the context of single-column chromatography, as the computation time is often too long for multi-column chromatography, especially when continuous multi-column chromatography experiments are to be simulated over a long period.

7.2.2 Equivalent radial flow rate distribution

Currently, there is a notable gap in modeling ECV when condition (7.5) is not met, meaning the ECV cannot be described with a combination of DPFRs and CSTRs, and effects like Dean vortices prevent the application of (7.6). This gap is especially evident when the overall system and its application are too complex to model using 3D CFD.

In this work, we tested two different approaches to overcome this issue. In the first approach, we used two DPFRs+CSTRs in parallel to be able to account for radial inhomogeneities in the concentration profile. This approach is quite common when modeling parts with larger volumes that can also exhibit some back-mixing, like mixing chambers [252] or membrane chromatography housings [246], but is usually not applied to other system components. In the second approach, we aimed to reduce the dimensionality required to describe the fluidic effects from 3D to 2D by adjusting the applied flow rate profile and using it in combination with (7.6). As it is not trivial to experimentally measure the ECV effects for single components like short capillaries or microfluidic channels, we used CFD simulations for the determination of the equivalent flow rate profile. To explain the exact procedure for this approach in more detail, we first examine the radial flow rate distribution in case of laminar flow. For the numerical implementation of (7.6), the modeled geometry is usually radially discretized in a number n_{rad} of radial cells. If the discretization is done equidistantly, each radial element k will have the area $A(k)$ according to (7.12). Additionally, a certain percentage of the overall volumetric flow Q, named the flow rate distribution $FRD(k)$, will pass through each radial element according to (7.13), where the mean linear velocity in the radial element $u(k)$ can be approximated using (7.7), resulting in 7.14.

$$A\left(k\right) = \pi\left[\left(r(k) + \frac{R_{\mathrm{cap}}}{n_{\mathrm{rad}}}\right)^2 - r(k)^2\right] \tag{7.12}$$

$$FRD\,(k) = \frac{u\,(k)\,A\,(k)}{Q} \tag{7.13}$$

$$FRD\,(k) = \frac{1}{Q} 2 u_{\text{mean}} \pi \left[1 - \left(\frac{r(k) + 0.5\frac{R_{\text{cap}}}{n_{\text{rad}}}}{R_{\text{cap}}}\right)^2\right] \left[\left(r(k) + \frac{R_{\text{cap}}}{n_{\text{rad}}}\right)^2 - r(k)^2\right] \tag{7.14}$$

If the exact flow profile is unknown, an equivalent radial flow rate distribution ($FRD^*(k)$) can be calculated using a breakthrough curve determined experimentally or through CFD simulation. In many cases, FRD^* does not represent the physical FRD in the respective system but leads to a similar outlet concentration profile. Regardless of the actual geometry of the ECV, which can be quite complex, FRD^* is always approximated with a cylindrical geometry, where diameter and length are chosen to match the physical ECV as closely as possible. Equations (7.15) - (7.17) show the procedure for calculating FRD^* in an iterative process: Without loss of generality, it is assumed that the mean retention time of each radial cell $t_{\text{ret,mean}}(k)$ increases with increasing radius (similar to the laminar flow profile). With the iteratively determined maximum retention time in each radial cell $t_{\text{ret,max}}(k)$, $t_{\text{ret,mean}}(k)$ can be calculated using (7.15). A concentration threshold for the starting point of the breakthrough curve is set (e.g., $c_{\text{out}}(t_{\text{ret,max}}(0)) \geq 10^{-10}\,\text{mM}$) for the calculation of $t_{\text{ret,mean}}\,(1)$. $t_{\text{ret,mean}}\,(k)$ can be used to calculate $FRD^*\,(k)$ with (7.16), which is then used to calculate the outlet concentration $c_{\text{out,cal}}$ with (7.17), which is compared to the actual measured (or CFD calculated) outlet concentration $c_{\text{out}}(t_{\text{ret,max}}(k))$. If (7.17) is not fulfilled, $t_{\text{ret,max}}(k)$ is increased according to the temporal discretization until the smallest possible $t_{\text{ret,max}}(k)$ to fulfill (7.17) is identified. This process is repeated for all radial cells.

$$t_{\text{ret,mean}}\,(k) = t_{\text{ret,max}}(k-1) + 0.5\,(t_{\text{ret,max}}(k) - t_{\text{ret,max}}(k-1)) \tag{7.15}$$

$$FRD^*\,(k) = \frac{A(k) L_{\text{ECV}}}{Q \cdot t_{\text{ret,mean}}\,(k)} \tag{7.16}$$

$$c_{\text{out,cal}} = \sum_{n=1}^{k} FRD^*(n) c_{\text{in}} \leq c_{\text{out}}(t_{\text{ret,max}}(k)) \tag{7.17}$$

7.3 Methods

In this study, various ECV geometries were modeled with different approaches, aiming to accurately represent the ECV of a µSMB system. Even simple test geometries, such as capillaries, were derived from the µSMB's ECV. The µSMB system is an open-loop four-zone system, as depicted in Figure 7.1. In previous studies, this system was used with one SEC column per zone for continuous desalting of proteins [230, 241]. The µSMB functionality is realized through a 3D printed central rotary valve, previously described along with the general setup of the µSMB system [230, 233] (Chapters 4 and 5). The chromatography columns of the system divide the ECV into five distinct segments, as shown in Figure 7.1. Each segment includes the static part of the valve system, the rotating part of the valve system, and capillaries connecting the chromatography columns to the valve. Exemplary, the ECV segment between zones II and III (segment 3) is depicted in Figure 7.2a. Each segment is further divided into several subsegments based on geometric features, six in the case of Figure 7.2a.

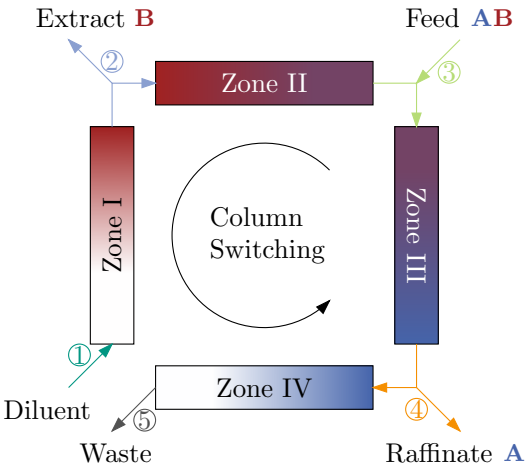

Figure 7.1: Schematic of a four column open-loop SMB system with ECV segments 1-5 between the different zones.

The ECV features diameter changes, curves, and merges (feed) and splits (raffinate/extract). A detailed overview of all dimensions of the individual ECV subsegments of the entire µSMB system is provided in Table D.3 in Appendix D. A technical drawing of the 3D printed stator channel is depicted in Figure D.17.

The ECV was modeled using two methods: a unit-by-unit approach, where each subsegment of the ECV was modeled separately, as shown in Figure 7.2b, and a flow path approach, where all subsegments connecting zone two and zone three and all subsegments connecting the feed and zone three were modeled as a single unit, depicted in Figure 7.2c. Before modeling the entire ECV segments, subsegments 1 and 3 were modeled independently to study the effects of Taylor-Aris dispersion and Dean vortices in greater detail.

A complete SMB process was modeled, and the simulation results were compared to previously published experimental data [230] (Chapter 5). The applied zone flow rates and other process parameters are detailed in Table D.4. The column model, including all parameters, was also previously published. The columns were modeled using the 1D GRM, assuming no radial concentration profile within the columns, thereby neglecting any influence of the columns' outlet profiles on the ECV behavior. Effects caused by frits etc., were not considered separately but were included in the column model. An detailed overview of the units required for SMB modeling with the different approaches is given in Figure D.18. Similar to the experiments, all simulations were performed for BSA (D_m =6.78e-11 m^2/s, calculated according to [234]) and AS (D_m =1.2e-9 m^2/s [253, 254]). The significant size difference between these molecules is advantageous for investigating ECV effects, as molecular size has been reported to play an important role [244].

Seven different approaches for ECV modeling were evaluated, summarized in Table 7.1. In this work, the approaches are categorized into models where all parameters can be calculated based on geometric/literature data (PFR, DPFR, laminar, and CFD) and models requiring a calibration experiment (or CFD simulation) for parameter fitting (DPFR+CSTR, parallel DPFR+CSTR) or parameter calculation (eqFRD). Detailed descriptions of these modeling approaches are provided in the following sections.

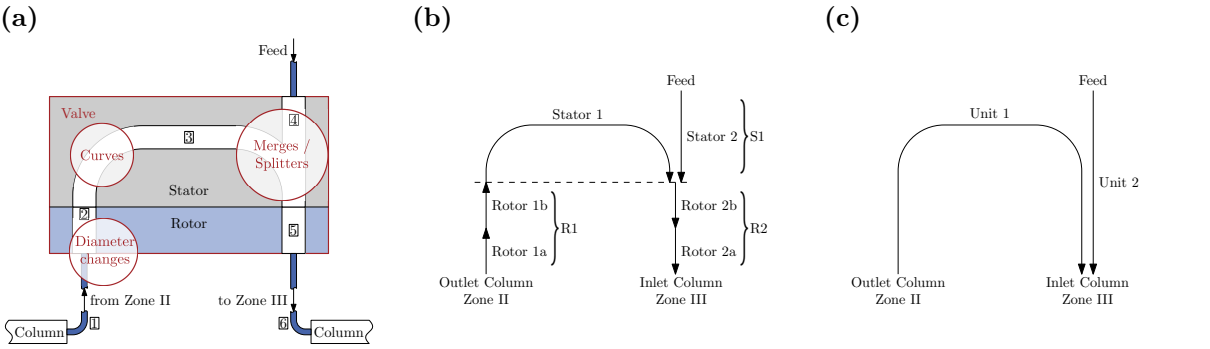

Figure 7.2: Overview of modeled geometries: (a) segment of the µSMB ECV between zones two and three, having distinct geometric properties, such as diameter changes, curves and merges. In accordance with the geometric features, this segment of the ECV was further divided into six subsegments. (b) and (c): different modeling approaches for models with fitted parameters. Either, each of the geometric subsegments is represented by one unit in the model (b), or all subsegment along a flow path are combined in one single unit (c).

7.3.1 CFD models

CFD simulations were performed as a benchmark for the other modeling approaches and also for model calibration (if required). The simulations were conducted using COMSOL Multiphysics version 6.1 (Comsol Multiphysics GmbH, Göttingen, DE), employing the laminar flow and the transport of diluted species physics.

The channels of the valve system (subsegments 2-5 in Figure 7.2a) were modeled in 3D. The capillaries connecting the columns and the valve system (subsegments 1 and 6) were simplified to straight, unbent capillaries, as the real bending radius is to large for the occurrence of Dean vortices and this assumption reduces computational time significantly. Single capillaries were modeled in 2D. All mesh configurations are listed in Table D.5.

Simulations were conducted for both pulse injections and breakthrough curves. The exact inlet profiles are provided in Table D.6. The maximum inlet concentration for both cases was $0.03\,\mathrm{mol/m^3}$. Subsegments 1 and 3 were modeled at flow rates of 1, 10, 100, and 1000 µL/min, while the entire ECV segments were modeled at the respective flow rates of the comparable µSMB experiments.

7.3.2 1D models

All 1D simulations were performed using CADET (Institute of Bio- and Geosciences 1 (IBG-1) of Forschungszentrum Jülich (FZJ), Jülich, DE) [204]. PFRs were modeled using the lumped rate model without pores, setting the column porosity to 1 and the column dispersion to $0\,\mathrm{m^2/s}$. For DPFR models, the column dispersion was calculated using (7.4).

Table 7.1: Overview of different modeling approaches of extra column volume with required model parameters and recommended applications. No superscript: geometric/ physical parameter, ^{a} calculated parameter, ^{b} fitted with genetic algorithm to calibration experiment, ^{c} calculated based on calibration experiment.

Model	Dimension	Parameters	Applications
PFR 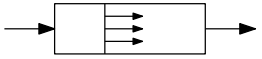	1D	L, d	Low ratio of ECV dispersion to column dispersion
DPFR 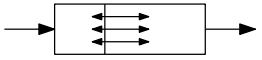	1D	$L, d, D^{a}_{\mathrm{ECV}}$	Laminar flow with (7.5) fulfilled
(D)PFR+CSTR 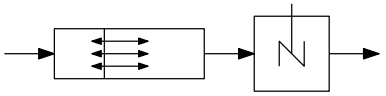	1D	$L^{b}, d, (D^{b}_{\mathrm{ECV}})$, V^{b}_{CSTR}	Geometries with additional dispersion and (7.5) fulfilled
Parallel (D)PFR+CSTR 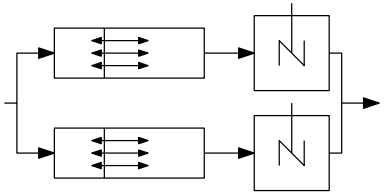	1D	$L^{b}_{1}, d_{1}, (D^{b}_{\mathrm{ECV},1})$, $V^{b}_{\mathrm{CSTR},1}, L^{b}_{2}, d_{2}$, $(D^{b}_{\mathrm{ECV},2})$, $V^{b}_{\mathrm{CSTR},2}$, s^{b}	Geometries with additional dispersion and (7.5) not fulfilled
Laminar 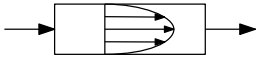	2D	$L, d, D_{\mathrm{m}}, u^{a}(r)$	Laminar flow with (7.5) not fulfilled
eqFRD 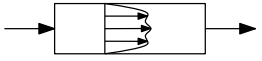	2D	$L, d, u^{c}(r)$	Geometries with additional dispersion and (7.5) not fulfilled under various flow conditions
CFD 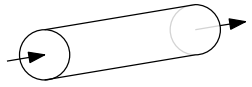	2D/3D	L, d, D_{m}	Complex geometries with high accuracy requirements

A subsequent CSTR model was added to each DPFR for DPFR+CSTR models. The length of the DPFR L, the dispersion coefficient of the DPFR D_{ECV}, and the volume of the CSTR V_{CSTR} were determined through parameter fitting, with a defined diameter. If only a single subsegment was modeled, the actual diameter was used; otherwise, the diameter of the valve system was chosen. The parameter fitting was performed using the differential evolution algorithm of scipy.optimize. The same time steps were used for both the CFD simulation and the parameter fitting. The mean square error between the outlet concentration of the CFD ($c_{\mathrm{CFD}}(t)$) and the respective simulation ($c_{\mathrm{sim}}(t)$) was chosen as the optimization function y according to (7.18). When fitting the parameters of a series of DPFR+CSTR units, the parameters of the first unit were fitted initially, followed by fitting the parameters of the subsequent units, including all previous units in series. For fitting parameters of one unit at varying flow rates, the optimization function was modified to sum the mean square errors of all flow rates. For modeling the entire ECV segment as shown in Figure 7.2b, the units Rotor 1a and 1b (as well as 2a and 2b) were combined.

$$y = \sum_{t=0}^{t_{\mathrm{end}}} \left(c_{\mathrm{CFD}}(t) - c_{\mathrm{sim}}(t)\right)^2 \tag{7.18}$$

The approach for the parallel DPFR+CSTR (P DPFR+CSTR) was similar, except that the volumetric flow rate in each subsegment was divided into two partial flows and modeled separately. The flow rate division ratio s was also determined through parameter fitting. When modeling multiple units in series, the flow rate division ratio remained constant for all units according to the parameter fit of the first unit, resulting in two completely independent flow paths for the entire ECV segment.

7.3.3 2D models

2D models were also implemented in CADET, using the 2D GRM reduced to a 2D lumped rate model without pores by setting the column porosity to one. Unless otherwise stated, an equidistant radial discretization with 50 radial cells was applied. For laminar modeling, the actual diameter and length of the respective geometry were used, along with the molecular diffusion coefficient for radial and axial dispersion. The mean linear velocity of each radial cell was calculated using (7.7).

The eqFRD approach was implemented using a similar 2D GRM in CADET, but the axial and radial dispersion coefficients were set to zero, as molecular diffusion effects were already considered in the parameter calculation based on the CFD simulation results. The radial flow profile FRD^* was calculated based on (7.16).

Equidistant radial discretization was chosen for modeling single units. For modeling a series of different units, the flow in each radial cell was kept constant to prevent artificial simulated mixing effects. Thus, for a series of units, FRD^* was only calculated for the first unit and kept constant for all subsequent units in series. Instead of changing FRD^*, the specific retention time in each subsequent radial subsegment was adjusted using custom radial discretization, with the area of each radial cell calculated similarly to FRD^*.

When modeling an entire ECV segment, subsegments Rotor 1a and 1b (as shown in Figure 7.2b) were modeled using the laminar approach, while Rotor 2a and 2b were modeled as a single unit with eqFRD.

7.4 Results and Discussion

7.4.1 Modeling of straight capillaries

At first, the different model approaches were compared for a straight capillary at varying flow rates. The eqFRD approach was not included, as it equals the laminar approach in case of a straight capillary with laminar flow conditions. Although similar studies have already been conducted [244], we include this for completeness and clarity. The modeled capillary corresponds to subsegments 1 and 6 in Figure 7.2a, representing the capillaries connecting the chromatography columns to the valve system in the µSMB setup. In total, there are eight such capillaries in the µSMB setup, with one at each column's inlet and outlet. The fluidic effects in the capillaries were assumed to be independent of those occurring in the rest of the system for this analysis. The critical flow rate for Taylor-Aris dispersion in this capillary, according to (7.5), is $< 5.6\,\mu L/min$ for BSA and $<99.5\,\mu L/min$ for AS. Given that the µSMB system operates between $48\,\mu L/min$ and $113\,\mu L/min$ for the considered process, dispersed plug flow behavior cannot be assumed for BSA. Therefore, we investigated the effects of flow rate on the outlet profile.

Figure 7.3a displays the outlet profiles from CFD simulations of pulse injections of BSA and AS at flow rates ranging from 1 to $1000\,\mu L/min$. The vertical black line indicates the volume of the capillary. At flow rates below the critical flow rate, the outlet profiles are nearly symmetrical Gaussian peaks with the expected retention volume. Peak height decreases with lower flow rates due to longer residence times, which enhance axial dispersion effects. At higher flow rates, peak splitting caused by the laminar flow profile is observable: Without sufficient residence time, radial diffusion equilibrium is not achieved, resulting in a faster elution of the molecules at the center of the laminar flow profile in contrast to the molecules close to the wall, causing a strong tailing effect. This effect is more distinctive for BSA, where the peak splitting starts at a flow rate of $10\,\mu L/min$, whereas for AS, the effect begins at $100\,\mu L/min$, due to the smaller molecular diffusion coefficient of BSA. The peak height increases again at $1000\,\mu L/min$ because the pulse length had to be increased for numerical stability ($8.33\,\mu L$ for $1000\,\mu L/min$ compared to $0.83\,\mu L$ for other flow rates).

Figures 7.3b and 7.3c depict the breakthrough curves of BSA modeled with different approaches at the flow rates of $1\,\mu L/min$ and $100\,\mu L/min$, respectively. At $1\,\mu L/min$, all models except PFR accurately predict the shape of the breakthrough curve in regard to the CFD model. The PFR model exhibits slight dispersion effects due to numerical dispersion. At $100\,\mu L/min$, above the critical flow rate, the differences between models become more pronounced. For instance, a DPFR with the dispersion coefficient calculated from (7.4) is unsuitable. Using a DPFR+CSTR combination with fitted parameters improves results but still fails to accurately model the breakthrough curve shape. This can only be achieved using a model that allows for radial discretization, accounting for the peak splitting. Two approaches were considered: the parallel DPFR+CSTR, essentially a 2D DPFR+CSTR with two radial cells, and the laminar model.

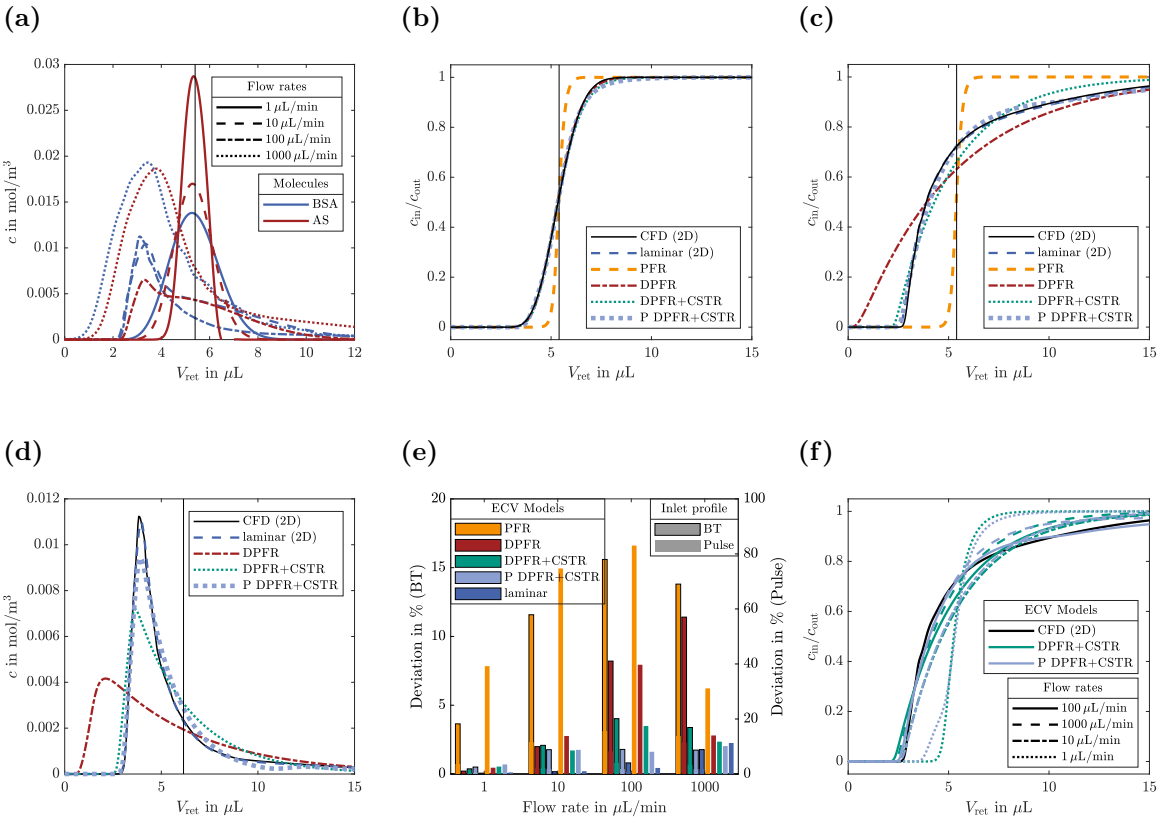

Figure 7.3: Modeling of a straight capillary with a length of 0.11 m and a diameter of 0.25e-3 m with varying flow rates and different ECV model approaches. The vertical black lines represent the volume of the capillary. (a): CFD simulations of a pulse injection at different flow rates for BSA and AS. The injection volume at 1000 µL/min is 8.33 µL and 0.83 µL for all other flow rates. (b), (c): Breakthrough curve of BSA at a flow rate of 1 µL/min (b) and 100 µL/min (c) for different modeling approaches. (d): Pulse injection of BSA at a flow rate of 100 µL/min for different modeling approaches. (e): Deviations of different model approaches from the CFD model for breakthrough and pulse injections of BSA. All values were normalized with the total area of the outlet profile of the CFD simulation. (f): Transfer of fitted ECV models (DPFR+CSTR, P DPFR+CSTR) with parameters (L, D_{ECV}, s) fitted at various flow rates to a flow rate of 100 µL/min.

Due to the low number of radial cells, the parallel DPFR+CSTR was still considered as a 1D approach in this work. Of course, it would be possible to increase the number of parallel DPFR+CSTR units, but for the peak splitting, two cells (one for each peak) are sufficient. While this presents a straight forward model approach, parameter fitting is more complex due to the increased number of parameters, and suitable model parameters for all flow rates could not always be obtained (compare Figure D.19). As previously reported, the laminar approach resulted in comparable results to the CFD simulation, even with a low number of radial cells (10 for BSA and 5 for AS, see Figure D.20), suggesting it should be used more frequently for ECV modeling.

The same models were applied to pulse injections to assess the versatility of the different approaches. Parameters determined from breakthrough curves were used for models requiring parameter fitting (DPFR+CSTR, P DPFR+CSTR). The laminar model again produced results comparable to the CFD model, while the parallel DPFR+CSTR underestimated peak height but predicted the curve shape correctly. This indicates that models not requiring parameter fitting are more robust under varying experimental conditions.

Figure 7.3e summarizes the deviations between the tested ECV simulations and the CFD simulation across different flow rates and injection profiles. All outlet profiles and comparable results for AS are included in Appendix D (Figures D.19, D.21, and D.22). Deviations were normalized with the overall peak area of the CFD outlet profile for better comparability.

Initially, deviations increase with increasing flow rate and stagnate starting from 100 µL/min for most models. Especially at low flow rates, the laminar model shows the smallest deviations as both the laminar and CFD models consider the radial flow rate profile along with axial and radial diffusion. Among the other models, DPFR performs best at flow rates below Q_{crit} but becomes less accurate at higher flow rates. Particularly at higher flow rates, the parallel DPFR+CSTR approach outperforms the DPFR+CSTR. Deviations of the peak injection inlet profile are generally higher than those of the breakthrough curves, likely due to the higher peak area of the breakthrough combined with normalization. In summary, these results illustrate that DPFR with D_{ECV} calculated according to (7.4) is a valid option for flow rates below Q_{crit}, while 2D models are universally applicable under varying conditions, even with a low number of radial cells.

To emphasize this further, Figure 7.3f shows the application of model parameters fitted at different flow rates for simulations performed at 100 µL/min. The deviation from the CFD model increases with the difference between the fitting and simulation flow rates. While this can sometimes be improved by fitting parameters at multiple flow rates, it remains challenging when different fluidic phenomena dominate at different flow rates. On the other hand, for the not-fitted models, the flow rate is used to calculate the model parameters and thus always considered automatically.

7.4.2 Modeling of a curved channel

Next, we focused on modeling the curved structure of the valve's stator (subsegment 3 in Figure 7.2a, without merges or splits) at flow rates ranging from 1 to 1000 µL/min. Due to the presence of Dean vortices, the eqFRD approach differs from the laminar approach and both were

Table 7.2: Overview of flow conditions. At a flow rate of 1000 µL/min, non of the conditions are met for neither molecule. * condition is met.

		1 µL/min	10 µL/min	100 µL/min
BSA	Q_{crit} in µL/min	0.74	0.74	0.74
	Dn^2Sc	2.07*	206.85	20685.48
AS	Q_{crit} in µL/min	13.10*	13.10	13.10
	Dn^2Sc	0.12*	11.69*	1168.73

considered. Table 7.2 provides an overview at which flow rate the criteria for Taylor-Aris dispersion and Dean vortices are met. Dean vortices significantly increase dispersion compared to laminar flow, as illustrated in Figure 7.4, which compares concentration profiles in the center of a longitudinal section of straight and curved channels under identical conditions (L, d, Q, D_m).

Figure 7.5a shows CFD simulations of breakthrough curves for BSA and AS at various flow rates. At low flow rates, the breakthrough curves of BSA are broader than those of AS and the width increases with increasing flow rate. Notably, from a flow rate of 10 µL/min for BSA and 100 µL/min for AS, the curves exhibit a similar shape regardless of flow rate or molecule. Additionally, BSA at 1 µL/min and AS at 10 µL/min display comparable breakthrough curves. These observations are in agreement with Table 7.2 and indicate that flow conditions for Taylor-Aris dispersion and Dean vortices have a greater impact on the outlet profile than molecular diffusion.

Figure 7.5b shows the breakthrough curves of BSA at 100 µL/min with different ECV modeling approaches. The DPFR model deviates significantly from the CFD model, as the residence time is too short for Taylor-Aris dispersion to occur. The laminar model illustrates the outlet profile of a straight channel without Dean vortices, characterized by early breakthrough of molecules near the center and tailing of those near the wall. In the curved capillary, these effects are mitigated by additional dispersion caused by Dean vortices. Other ECV models accurately predict the outlet profile.

Figure 7.5c compares deviations between ECV models and the CFD model across different flow rates and injection profiles for BSA. The outlet profiles for all conditions as well as the comparable results for AS are included in Appendix D (Figures D.23-D.25). Similar to the straight capillary, the deviation increases with flow rate and plateaus at 100 µL/min. Again, deviations for pulse injections are generally higher than those for breakthrough curves and slightly higher than those for the straight capillary but remain below 5% for most breakthrough curves. The eqFRD approach is the most accurate across most flow rates, making it a suitable alternative to the laminar approach when multiple fluidic effects are present. However, achieving high accuracy requires 50 radial cells (see Figure D.26), consequently there is a trade-off between computational time and precision in this case. The increased number of required radial cells likely results from the larger radius compared to the straight capillary rather than the modeling approach itself, as the laminar approach required an increased number as well (see Figure D.27). Unlike the other models, the eqFRD model shows increasing deviations at 1000 µL/min compared to 100 µL/min. This is most likely due to the time discretization used in the simulation as well as the calculation of FRD^*. A time increment of 0.025 s was used across all flow rates, although the total simulation

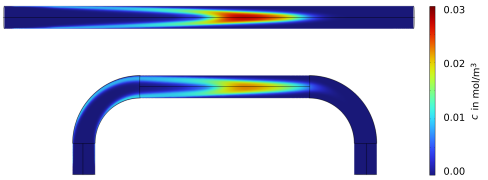

Figure 7.4: CFD calculated concentration profile in a longitudinal section of a straight and curved channel. Except for the geometry, conditions are identical in both cases (pulse injection of BSA, 1.5 s after injection, flow rate of 100 µL/min).

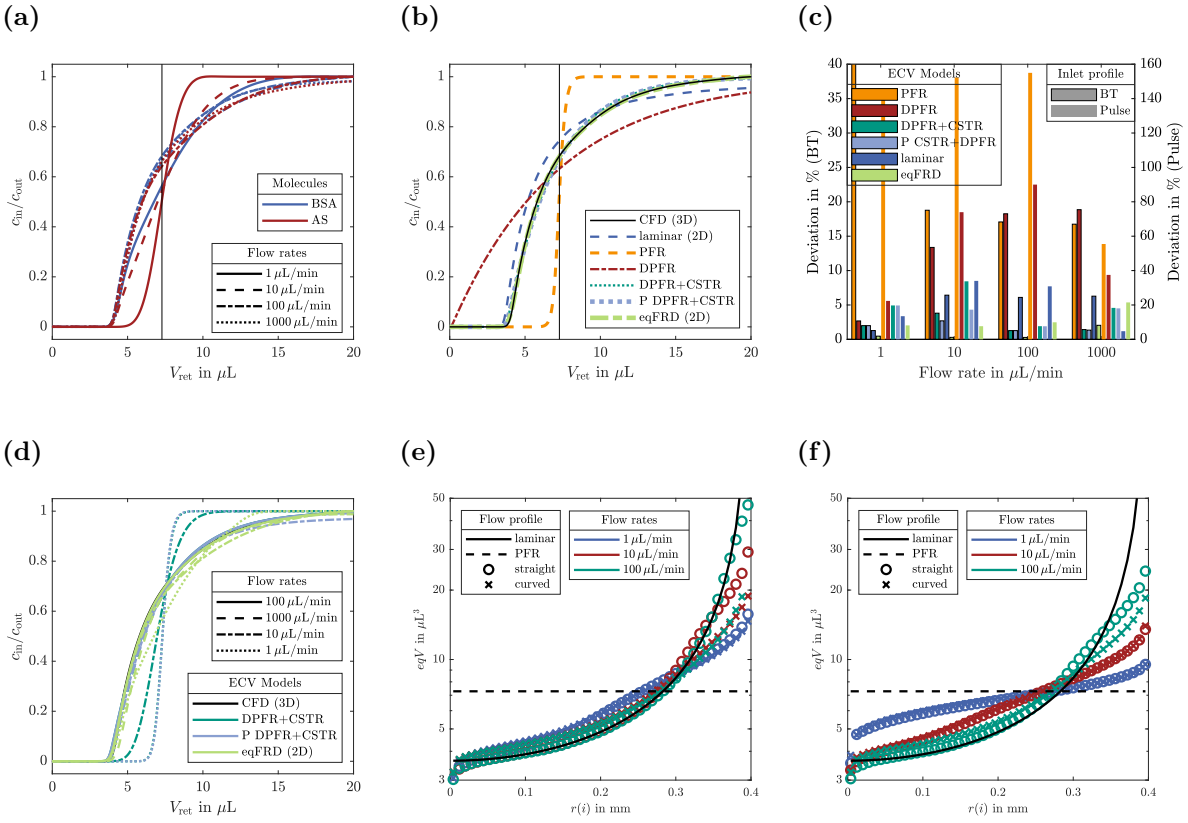

Figure 7.5: Modeling of a curved channel with a length of 0.014 m and a diameter of 0.8e-3 m with varying flow rates and different ECV model approaches. The vertical black lines represent the volume of the channel. (a): CFD simulations of a breakthrough at different flow rates for BSA and AS. (b): Breakthrough curve of BSA at a flow rate of 100 µL/min for different modeling approaches. (c): Deviations of different model approaches from the CFD model for breakthrough and pulse injections of BSA. (d): Transfer of fitted ECV models (DPFR+CSTR, P DPFR+CSTR, eqFRD) with parameters $(L, D_{\mathrm{ECV}}, s, u(r))$ fitted at various flow rates to a flow rate of 100 µL/min. (e), (f): eqV of BSA (e) and AS (f) at different flow rates for a straight and curved structure in comparison with ideal laminar and PFR behavior.

time varied significantly. Consequently, only 36 time steps were required for the breakthrough at a flow rate of 1000 µL/min, compared to 360 and 3600 time steps at flow rates of 100 and 10 µL/min, respectively. Because the precision of the calculated FRD^* is directly linked to the concentration change occurring within each time increment (compare (7.15) - (7.17)), the accuracy at higher flow rates can be improved by reducing the time increment.

Similar to Figure 7.3f, Figure 7.5d shows the transfer of model parameters fitted at various flow rates to simulations performed at 100 µL/min. It is possible to predict the breakthrough curve at 100 µL/min using parameters determined at 1000 µL/min for all methods. However, parameters fitted at 10 µL/min for the DPFR+CSTR model and 1 µL/min for both the DPFR+CSTR and the parallel approach underestimate dispersion effects, resulting in a steeper predicted breakthrough curve. This is because Dean vortices only appear at flow rates above 10 µL/min, with 10 µL/min being at the transition zone. Consequently, these models cannot extrapolate to conditions different from the original flow conditions. In contrast, the eqFRD approach can predict the basic shape of the breakthrough curve even using parameters calculated at 1 µL/min, though deviations from the CFD model increase with the difference between the actual flow rate and the one used for parameter calculation. This demonstrates eqFRD's versatility across various application scenarios, especially when simulating different flow rates over a broad range.

Figures 7.5e and 7.5f compare the eqFRD at different flow rates for the curved channel and an equivalent straight one (with otherwise the same dimensions) for BSA and AS, respectively. For better comparability between the different flow rates, the equivalent volume (eqV), which is FRD^* normalized with the mean retention time, is depicted instead of FRD^*. An ideal PFR and laminar flow are also included. BSA exhibits nearly ideal laminar flow at high flow rates, with almost no radial diffusion. At lower flow rates, the differences between radial cells decrease, and the profile approaches that of a PFR. This is particularly evident for AS at 1 µL/min, the only condition meeting the criterion for Taylor-Aris dispersion. The remaining deviations from the ideal PFR, leading to peak broadening effects, visualize the dispersion. No difference is observable between the straight and curved channels at low flow rates, which aligns with Table 7.2. Interestingly, once a deviation between curved and straight channels occurs, all curved channels exhibit the same eqV, independent of flow rate and molecule. This indicates that Dean vortex-induced dispersion outweighs over molecular diffusion effects. The eqV curves for BSA are more consistent compared to AS, explaining the better transferability of calculated FRD^* across different flow rates. For AS, the transfer results in higher deviations (see Figure D.25b), hence, whether the eqFRD can be generalized over a broad flow rate range needs to be verified for each scenario.

Overall, the new eqFRD approach offers a valuable alternative to 2D simulations with a laminar flow profile, particularly when multiple effects occur simultaneously. It provides a reliable method for various simulation conditions, especially for larger molecules. When strong dispersion effects are present, simpler approaches like DPFRs can also be sufficient. The optimal modeling approach should be determined based on the specific application, balancing modeling accuracy and computational time.

7.4.3 Combination of different subsegments

After analyzing different subsegments of the ECV individually, we proceeded to model entire segments using the different approaches. It is known that dispersion effects occurring in ECV are not additive, nonetheless additive behavior is often assumed for simplification [255, 256]. Here, we investigated whether it is acceptable to assume additive behavior and determine the model parameters of each subsegment independently, or if all subsegments need to be considered together during model development. The results are shown in Figure 7.6a.

As discussed in Section 7.4.1, subsegments 1, 2, 5, and 6 can be effectively modeled with the laminar approach. This holds true even for the diameter changes between subsegments 1 and 2 and 5 and 6 (results not shown here). In implementation S1, all rotor subsegments were modeled as independent units, as depicted in Figure 7.2b, and the rotor subsegments were modeled with the laminar approach and the stator subsegments with eqFRD, assuming no superimposition of the ECV effects between different subsegments. Subsequently, implementations S1+R1 and S1+R2 combined the stator subsegments with one part of the rotor, using eqFRD to model the combined unit. Finally, in implementation S1+R1+R2, all subsegments along a flow path were combined into one unit, as depicted in Figure 7.2c and modeled with eqFRD.

The depicted breakthrough curve features a shoulder resulting from the two inlets of the ECV with different retention times. The shoulder represents the breakthrough of molecules entering subsegment 4, while the main breakthrough is from molecules entering subsegment 1. The end concentration of the first breakthrough is much lower due to the lower flow rate entering subsegment 4 (30 vs. 98 µL/min). Only by considering all subsegments of the ECV segment together during model building, the model is able to accurately predict the CFD breakthrough curve, demonstrating that ECV effects are not simply additive in this example. This was to be expected as no radial mixing occurs between the subsegments.

While these results suggest that modeling all subsegments along a flow path as a single unit is the most accurate and simplest approach, it is not always feasible. In the case of the described µSMB system, for example, each ECV segment consists of rotating and static parts, resulting in different connections between subsegments in the course of one experiment. Consequently, subsegments must be modeled as separate units to implement these changes in connectivity. This is straightforward for models that do not require parameter fitting, as all subsegments can be modeled independently in accordance with Figure 7.2b. For models requiring parameter fitting, it is crucial to consider the flow through all preceding subsegments, as shown in Figure 7.6a.

In the case of SMB, there is one more point to consider: the rotating parts of the ECV switch between the different zones of the SMB system, hence changing flow rates during an experiment. This can be implemented in models that do not require parameter fitting (at least for the ones considered in this study), as only D_{ECV} changes with flow rate and this can be adjusted in CADET. It is more challenging for fitted models, as the stator model also depends on concentration profiles in the rotor parts. Here, it was investigated whether a model applicable at all required flow rates could be implemented. The resulting breakthrough curves and mean residence times of all the model approaches requiring a parameter fit are depicted in Figure 7.6b.

All model approaches match the CFD breakthrough curve when using a single unit and also when using several units for the subsegments. Only when implementing a model for all flow rates, the

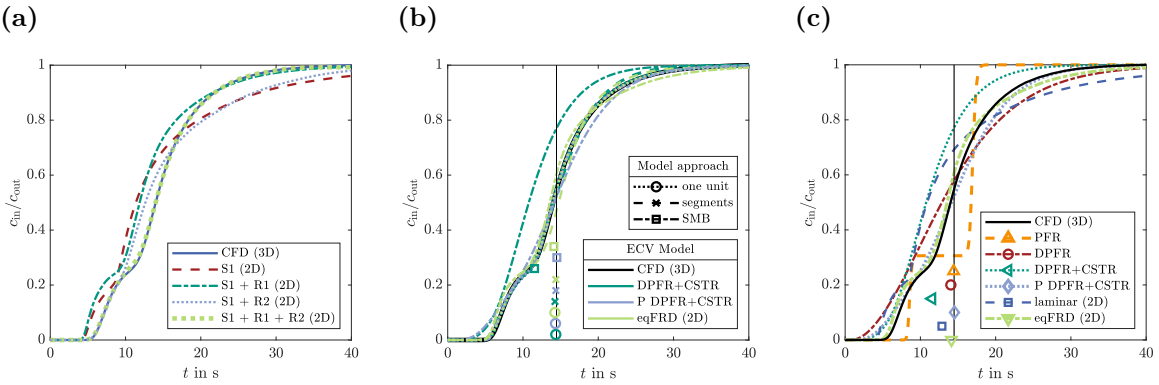

Figure 7.6: Modeling of the ECV segment between zone II and zone III. (a): Modeling with the eqFRD approach, using different subsegments of the ECV for the calculation of the model parameters. For explanation of the subsegments, see Figure 7.2b: S1 - Stator 1 & Stator 2; R1 Rotor 1a & Rotor 1b; R2 - Rotor 2a & Rotor 2b. (b): Breakthrough curves (lines) and mean retention times (first moments, markers) for different model approaches. The ECV was either modeled as one unit (according to Figure 7.2c), as different segments (according to Figure 7.2b), or in µSMB configuration, where the parameters for all rotating parts were calculated considering the breakthrough curves at all four zone flow rates. (c): Breakthrough curves (lines) and mean retention times (first moments, markers) of the µSMB configuration with different modeling approaches.

DPFR+CSTR approach is not able to predict the breakthrough curve any longer, the deviation is also apparent in the mean retention time. Both, eqFRD and the parallel approach predict the peak shape with high accuracy, though the mean retention time is more accurate with the parallel approach. Still, both approaches seem viable options for modeling the whole segment under varying flow rate conditions.

Figure 7.6c provides an overview of all model approaches for the entire ECV segment under SMB conditions. The two breakthroughs from the two inlets become more apparent for the PFR approach. The curve is not perfectly rectangular, which shows the impact of numerical dispersion for the chosen discretization. As previously observed, the parallel approach and eqFRD predict the shape of the breakthrough curve with the highest precision, reducing deviations to the CFD model from 8-11% for all other models to approximately 3%. However, when considering all segments between all the zones, only eqFRD is able to predict the peak shape reliably at all flow rates (compare Figure D.28).

Besides the differences in model complexity and hence computational time, the DPFR and PFR approaches accurately predict the mean retention time as it is not influenced by dispersion. The peak shape, on the other hand, differs significantly. Whether simple 1D models suffice depends on whether peak shape and retention time are crucial or if retention time alone is sufficient. The laminar and DPFR+CSTR approaches underestimate retention time and are unsuitable. For the DPFR+CSTR approach, better model parameters might be found using a different fitting metric, such as considering mean retention time in addition to the mean square error that was applied in this study. The laminar model's shorter retention time results from the not considered dispersion caused by Dean vortices. This effect is compensated in the DPFR model by assuming

increased dispersion due to Taylor-Aris dispersion, leading to comparable retention time but differing peak shape.

7.4.4 Application of ECV models to a µSMB system

Figure 7.7 illustrates the application of the developed ECV models to the µSMB system. The experimental data shown are from the triangle theory process point previously published [230], with the experiments performed in duplicate (labeled as Exp. 1 and Exp. 2). Figure 7.7a displays the first two switches of the third cycle for BSA in the raffinate stream, while Figure 7.7b shows the same for AS in the extract stream. For comparison, a simulation without any ECV model was also performed. The parallel DPFR+CSTR approach is not depicted due to its disproportionately long computational time.

Both plots show the typical cyclic behavior characteristic of an SMB experiment. When comparing these results to Figure 7.6c, it is evident that all models capable of accurately predicting retention time for the ECV between zones II and III yield comparable results in the µSMB simulation. However, the differences in predicted peak shapes between the various approaches are less pronounced than in the standalone ECV modeling. This is primarily because the column model contributes more significantly to overall dispersion than the ECV. By calculating the first and second moments of the column and ECV outlet profiles, it is estimated that the ECV accounts for 17% of the retention time but only 8% of the peak broadening in the case of BSA. This suggests that for the developed µSMB system, a simple ECV model is sufficient, which is advantageous for scale-up modeling, as those are also state of the art for larger scale SMB system and the same model type can be applied across different scales.

However, especially in the case of BSA, there are noticeable differences between the predicted peak shape and retention time compared to the experimental results for all tested ECV models. Figure 7.7c provides an overview of the deviations for the first three cycles of the SMB process. Even between the two duplicate experiments, there is a difference of 14% for BSA and 6% for AS. Overall, the deviations are higher for BSA than for AS. For the PFR, DPFR, laminar, and eqFRD models, the deviation is approximately 25% for BSA and 15% for AS. Among the tested models, the laminar model performs slightly better for AS, likely because the experimental conditions are close to the regime where Taylor-Aris dispersion is expected for AS, but not for BSA. The model that disregards the ECV and the DPFR+CSTR model exhibit the highest deviations, underscoring the importance of accounting for ECV and the challenges in determining suitable model parameters through parameter fitting. These results suggest that all models with calculated parameters would provide a comparable estimation of the SMB process. The influence of the ECV is generally more significant for unretained components [257], as they have a shorter retention time in the column. In this case, both components are unretained, yet their retention times vary significantly. BSA has a pore accessibility of 0, while AS has a pore accessibility of 0.96, resulting in retention volumes of approximately 130 µL and 290 µL, respectively. Consequently, BSA represents the worst-case scenario regarding ECV influence, which also explains the lower deviations observed with AS.

Despite applying the ECV models, significant deviations remain. Possible reasons for these discrepancies include the omission of detector geometry during model parameter determination

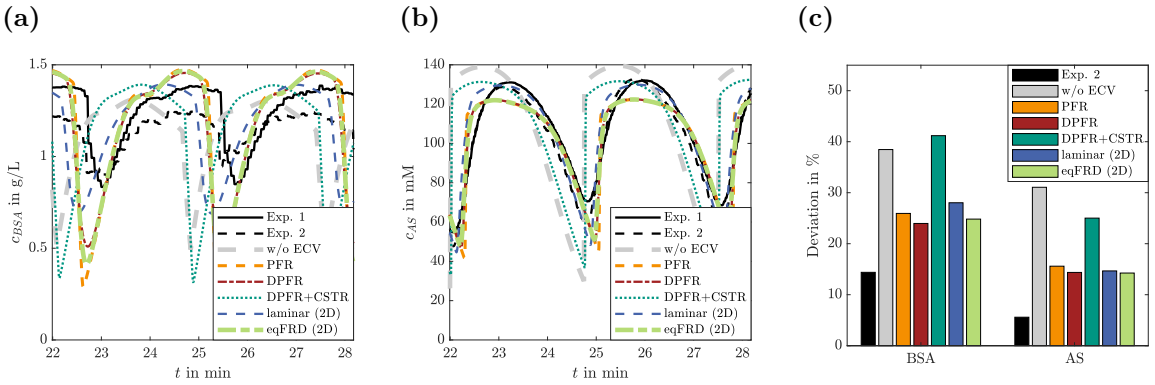

Figure 7.7: Comparison of different ECV model approaches for the application of a µSMB system: (a): BSA concentration in the raffinate stream for the first two switches of the third cycle. Simulated concentrations were post-processed with a moving average with a 10 s time interval to match the experimental settings. (b): AS concentration in the extract stream for the first two switches of the third cycle. (c): Deviations of the tested approaches to the experimental results (Exp. 1) over the first three cycles for BSA in the raffinate stream and AS in the extract stream. For better comparability between the molecules, all values were normalized with the overall area of the experimental results.

or effects related to the column model, such as frits or the transition between the column and ECV, both of which have been previously reported to influence detected peaks [88, 258]. The frits were included in the column model, and the single-column model was tested across various flow rates. However, these single-column results may not be directly transferable to the µSMB system, as we demonstrated in previous sections that the additivity of the influence of single system components on the outlet profile cannot be assumed. The column endpieces and frits used (fixed endpieces for Omnifit Microbore columns with 2 µm stainless steel frits) have an approximate volume of 18 µL per column. This volume is therefore not negligible compared to the system's ECV, which is approximately 21 µL between columns per zone. Thus, the influence of the endpieces and frits should be examined in greater detail in future studies.

The presented results emphasize the importance of considering ECV in relation to the column itself. The selection of a suitable ECV model should not be based solely on the ECV characteristics but also on the performance of the column and the overall system.

7.5 Conclusion

In this study, we systematically evaluated various modeling approaches for predicting the effects of extra column volume in a µSMB chromatography system and its ECV entities. Our results highlight that while the laminar model is highly versatile and provides accurate results for straight capillaries across different flow rates, it is less reliable for curved capillaries and channels where Dean vortices are present. In these cases, the here presented eqFRD model offers a viable alternative, particularly for simulations requiring accurate predictions at varying flow rates. When modeling complex ECVs consisting of multiple subsegments, the model accuracy could be increased significantly from approx. 90% with common ECV models to 97% with the

parallel DPFR+CSTR and eqFRD approaches. However, the eqFRD model proved more reliable when determining process parameters across several flow rates simultaneously, making it a robust choice for complex systems.

When these approaches were applied to model the entire µSMB system, we found that the choice of ECV model had minimal impact, provided it could accurately predict the retention time within the ECV. This suggests that, in the specific scenario considered, the column plays a much more dominant role in determining peak shape than the ECV, and simpler ECV models may be sufficient to achieve reliable results. Therefore, the selection of an ECV model should always be made in the context of the overall system to avoid unnecessary computational complexity.

For all tested model approaches, there remains a significant deviation between the predicted and experimental results of the µSMB experiments. This indicates that other factors, which were not accounted for in this study, such as the transition between the column and ECV, may need to be considered in future research to further improve model accuracy.

8. Integration of Capillary Chromatography Columns into a 3D Printed Microfluidic Multiport Valve for Miniaturized Multi-Column Chromatography

Juliane Diehm[1], David Achauer[1] and Matthias Franzreb[1,*]

[1] Institute of Functional Interfaces, Karlsruhe Institute of Technology, Eggenstein–Leopoldshafen, 76344, Germany

Abstract

Driven by the need for smaller and more efficient continuous chromatographic systems, this study explores the feasibility of further miniaturizing multi-column chromatography by integrating monolithic capillary columns directly into a 3D-printed valve rotor. First, monolith capillary ion-exchange columns were synthesized in PEEK capillaries with a diameter of 0.75 mm and a 3D-printed rotor system that can hold these capillary columns was developed. Single-column experiments confirm that the synthesized monolithic columns can separate the proteins hemoglobin and lysozyme with step elution, although the dynamic binding capacity is significantly lower than that of commercial equivalents. Subsequent multi-column tests reveal that a standard gradient SMB approach faces limitations due to elevated back pressure of the columns, resulting in leakages. To overcome this issue, a continuous multi-column chromatography (CMCC) setup was implemented, enabling promising separations with more than 60% yield and 80% purity for both proteins with switching intervals as low as 30 s, allowing for a fast response time of the system. Although further improvements in monolith morphology, functionalization, and valve sealing are needed, these findings highlight the potential of integrating monolith columns in miniaturized multi-column processes.

Keywords
µSMB; continuous chromatography; small-scale chromatography; multi-column chromatography; monolithic capillary columns; miniaturization

based on the publication https://doi.org/10.1016/j.chroma.2025.466245 in *Journal of Chromatography A*, licensed under a Creative Commons Attribution 4.0 International License (CC BY 4.0)

CRediT authorship contribution statement
Juliane Diehm: Methodology, Visualization, Software, Conceptualization, Writing – original draft. David Achauer: Methodology, Investigation, Conceptualization, Writing – review & editing. Matthias Franzreb: Conceptualization, Writing – review & editing.

8.1 Introduction

In the previous chapters, the development and application of a µSMB system were demonstrated. Although the introduced system is considerably smaller than other SMB systems, it still is large compared to miniaturized analytical single-column chromatography systems: In micro-column liquid chromatography, columns with diameters below 1 mm are generally used [259]. Such columns allow efficient handling of small sample volumes, minimize sample dilution when operated at low flow rates, thus enhancing measurement sensitivity [90].

These successes in analytical micro-column chromatography prompt the question of how far multi-column chromatography processes can be scaled down. Again, one critical factor is the ECV of the system. Halving the column diameter reduces the column volume by a factor of four, which can easily place the column volume and the system's ECV in the same order of magnitude.

A straightforward way to further decrease the ECV of the 3D-printed system is to integrate the chromatography columns directly into the valve. Even without modifying other system components, such a design thereby reduces the ECV of the current setup by 48% just by eliminating the capillaries connecting the columns to the valve.

In the course of this work, three different approaches were tested for directly integrating the columns into the valve. In two approaches, 3D-printed column housings with the same dimensions as used in previous chapters were integrated into the valve rotor. This allowed either dry-packing the columns with conventional SEC stationary phase material or inserting 3D-printed stationary phases. However, the dry-packing did not yield reproducible column packings, and the attempt to 3D print SEC stationary phases did not result in suitable pore-size distributions for protein separations in the printing material.

This chapter therefore focuses on the third approach, which involves monolithic capillary columns directly integrated into the rotor. The column length remained at 50 mm, comparable to previous experiments, but the diameter was reduced from 5 mm to 0.75 mm, resulting in a volume of 22.1 µL per column. Given the complexity of synthesizing monoliths with defined pore size distributions, ion-exchange chromatography (IEX) was selected instead of SEC, aiming to separate lysozyme and hemoglobin in a gradient SMB process. Additionally, the gradient SMB was compared to another continuous multi-column chromatography (CMCC) process, where each step of a typical IEX process (binding, washing, elution, re-equilibration) was performed independently in parallel.

8.2 Material and Methods

8.2.1 Chemicals

Acetone, azobisisobutyronitrile (AIBN), blue dextran, cyclohexanol, 1-dodecanol, ethylene glycol dimethylacrylate (EGDMA), glycidyl methacrylate (GMA), hemoglobin, iminodiacetic acid (IDA), methanol, sodium hydroxide, and sodium chloride were purchased from Sigma Aldrich (St. Louis, US). Lysozyme was obtained from AppliChem (Darmstadt, DE), potassium phosphate from Carl ROTH (Karlsruhe, DE), and sulfuric acid from Merck (Darmstadt, DE). All chemicals were used without further purification.

8.2.2 Monolithic Column Synthesis

The procedure for the in situ polymerization of the monolith structure in PEEK capillaries was adapted from Sýkore et al. [260]: A mixture of 24% GMA, 16% EGDMA, 6% dodecanol, and 54% cyclohexanol, with 4 mg AIBN per mL mixture, was used for monolith synthesis. The mixture was filled in PEEK capillaries with a diameter of 0.75 mm and a length of 30 cm and sealed at both ends. While PEEK capillaries are uncommon in in situ polymer monolith synthesis, they were selected for their flexibility, which facilitates integration into the 3D-printed valve system, unlike stainless steel or fused-silica capillaries. The temperature-induced polymerization process was carried out in an oven (FD 23, Binder, Tuttlingen, DE) at 55 °C for 12 h. Afterwards, the porogens were removed by flushing the monolith with methanol at 50 µL/min, using syringe pumps (Nemesys M, Cetoni, Korbußen, DE). The functionalization process of the monolith with carboxyl groups for weak cation-exchange chromatography was adapted from to Conti et al. [136]: The capillaries were rinsed with water and filled with 2.0 M IDA solution, resulting in the covalent coupling of IDA to the methacrylate backbone via the epoxy group. The capillaries were sealed again and heated at 55 °C for 72 h. Excess IDA was flushed out with water at 50 µL/min, and the capillaries were stored in water for 72 h. Finally, any remaining unfunctionalized epoxy groups were hydrolyzed with 0.1 mM sulfuric acid at 55 °C for 24 h.

8.2.3 Monolith Characterization and Single-Column Experiments

Single-column experiments were performed with an ÄKTA Pure Chromatography System (Cytiva, Uppsala, SE) using a 19 cm long monolithic capillary (83.9 µL column volume). To determine column porosity, 7.5 µL of a 1 g/L blue dextran and 1% (v/v) acetone solution were injected at a flow rate of 50 µL/min, with 20 mM phosphate buffer (pH 6.4) as the mobile phase. For comparison, the same tracer experiment was conducted using an empty capillary instead of the monolith column.

Adsorption experiments were carried out with a feed solution containing 1 g/L hemoglobin and 1 g/L lysozyme. First, 7.5 µL of feed were injected at a flow rate of 50 µL/min with 20 mM phosphate buffer (pH 6.4, buffer A) as mobile phase. The buffer was changed to a 20 mM phosphate buffer with 1 M NaCl (pH 6.4, buffer B) 200 µL after injection for step elution. In another experiment, the elution strength of buffer B was increased in increments of 100 mM NaCl from 0 to 1 M to determine the required elution strength of buffer B. Furthermore, 50 µL of the feed solution was injected into the column at a mobile phase flow rate of 50 µL/min with buffer A as mobile phase, in order to determine the dynamic binding capacity (DBC) of the stationary phase.

8.2.4 Multi-Column Chromatography Experiments

Four monolith ion-exchange columns with an inner diameter of 0.75 mm and a length of 50 mm (column volume of 22.1 µL) were used for all multi-column experiments. Besides the changes in the valve and the chromatography columns, the general SMB setup was as described in Section 5.3.1.1, except that syringe pumps (Nemesys S, Cetoni, Korbußen, DE) were used as flow source instead of the microfluidic flow controller. The feed solution contained 0.5 g/L of each protein (lysozyme and hemoglobin) dissolved in 20 mM phosphate buffer at various pH levels. To

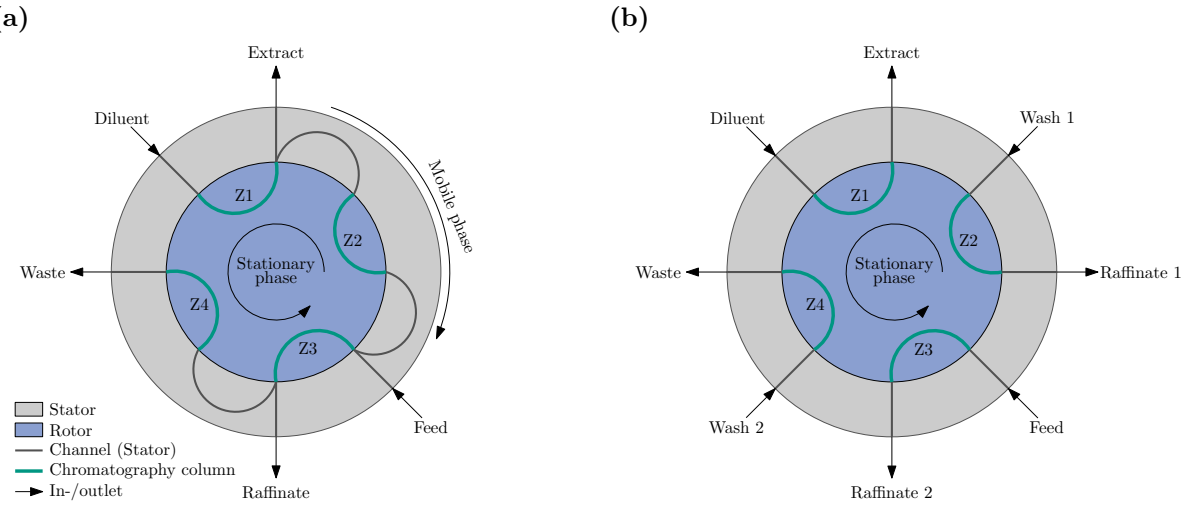

Figure 8.1: Connection schematics for the SMB (a) and CMCC (b) setup including in-/outlets connected to the 3D-printed valve stator, channels in the stator, and capillary chromatography columns integrated into the valve rotor. Z1 – Z4: Zone I – Zone IV.

increase the elution strength of the diluent, 600 mM NaCl were added to the respective phosphate buffer.

Besides SMB, a different CMCC process was evaluated, where the different steps of typical elution chromatography (binding, washing, elution, re-equilibration) were carried out in parallel in separate columns. The syringe pumps were connected to the diluent, extract, feed, and raffinate streams in SMB mode for flow generation, and to all inlets (diluent, wash1, feed, wash2) in CMCC mode (see Figure 8.1). The remaining outlet streams were collected in 1.5 mL centrifuge tubes (Eppendorf, Hamburg, DE). Apart from that, only the stator's connection channels were changed between the SMB and CMCC setups, while all other components of the valve system remained the same. Figure 8.1 schematically depicts the connections in the valve in both setups. For better clarity, the contact surface between rotor and stator is shown in a radial view, although in reality it is axial.

A detailed description of the valve design is provided in the next section. Table 8.1 summarizes the parameters for the SMB process, and Table 8.2 summarizes those for the CMCC processes. Except for CMCC 1 and 2, experiments were performed in triplicate. For easier comparison, flow rates are given both as absolute values in µL/min and as column void volume per switching interval (CVS). A switching time of 30 s was chosen for most experiments to achieve rapid response times.

Following each run, protein concentrations in the different streams were determined with UV/Vis spectroscopy using a Tecan Spark plate reader (Tecan Group, Männerdorf, CH). The total protein concentration was determined at a wavelength of 280 nm, while the hemoglobin concentration was measured at 405 nm. Lysozyme concentration was calculated by subtracting the hemoglobin concentration from the total protein concentration. The required calibration curves are summarized in Tables E.7–E.9. Additional blank runs without protein in the feed solution were performed to determine blank absorption values for the different streams to eliminate possible interference of leached IDA with the UV measurements.

Table 8.1: Process parameters of the SMB experiment

	Zone flow in CVS				Flow rate in µL/min						
Run	Zone I	Zone II	Zone III	Zone IV	Diluent	Extract	Feed	Raffinate	Waste	t_s in s	pH
SMB	2	0.95	1.54	1	33.79	17.74	10	9.15	16.9	30	6.4

Table 8.2: Process parameters of the CMCC experiments

	Zone flow in CVS				Flow rate in µL/min					
Run	Zone I	Zone II	Zone III	Zone IV	Eluent	Wash	Feed	Re-equilibration	t_s in s	pH
CMCC 1	2	2	0.59	2	33.8	33.8	10	33.8	30	6.4
CMCC 2	2.66	2.66	0.59	2.66	45	45	10	45	30	6.4
CMCC 3	2.66	2.66	0.59	2.66	45	45	10	45	30	7.4
CMCC 4	4.73	4.73	0.59	4.73	40	40	5	40	60	7.4
CMCC 5	2.66	2.66	0.59	2.66	45	45	10	45	30	8.2

8.2.5 Adaptions to the Valve System

All valve components were 3D-printed using an Asiga Pro 4K65 printer (Asiga, Alexandria, AU). PlasGray (Asiga, Alexandria, AU) and Loctite® 3D 5015 (Henkel, Düsseldorf, DE) were employed as printing materials.

The general valve concept is the same as in Chapter 4, but several modifications were made to integrate the capillary columns directly into the rotor. The rotor was divided into two parts: the main part (rotor part 1) includes capillary holders and the rotor-stator interface (Figure 8.2b), while rotor part 2 keeps the capillaries in place during experiments and includes a coupling adapter to the motor shaft (Figure 8.2c).

Because both the inlet and outlet of each capillary column must be located at the rotor-stator interface, the columns are integrated in a curved configuration, as shown in Figure 8.2a. Rotor part 1 contains bores sized for the capillaries and consists of two printing materials: PlasGray in the upper region for mechanical stability, and Loctite® 3D 5015 in the lower region. The elastomeric Loctite material secures the capillaries via a press fit and simultaneously seals the gap between capillary and rotor. The transition between these two printing materials is marked with a black line (5) in Figure 8.2b. Loctite® 3D 5015 is also used to print O-ring-like structures on the sealing surface of the rotor (6), both to enhance system tightness and to keep the capillaries in place. The capillaries are inserted into the rotor from the outer bores, the O-ring like structures of the inside bores have a smaller diameter, preventing the capillary from pushing out of the rotor surface on the other side. Alternatively, a steel mesh secured by self-adhesive PTFE film (Hightechflon, Konstanz, DE) can serve a similar function. Both rotor parts have guiding structures (1) for the bent capillaries and contain a groove for another O-ring that seals the space between the rotor parts.

With this new design, there are no external fluidic connections on the valve's rotor, which enables to decrease the distance between the in- and outlets of the columns from 10 mm in the previously introduced design to 5 mm, reducing the stator's connection channel volume from 7.3 µL to 4.6 µL and hence minimizing dispersion effects in the system. Details on the channels' geometry can be found in the appendix, alongside technical drawings for all the 3D-printed parts (Figures E.29-E.33). A detailed explanation of the ECV reduction in the valve system resulting from the integrated chromatography columns is provided in Figure E.34. With the exception of rotor part 1, all other valve components were printed with PlasGray.

A sectional CAD view of the assembled valve with inserted capillary columns is shown in Figure 8.3a. The flow path from the external fluidic ports (8), through the stator channels (7), and into the capillaries (4) aligns smoothly to reduce turbulences in the transition from one part to the other. Switching from the shown SMB to the CMCC layout requires changing only the stator's connection channels and fluidic ports; all other parts remain the same. Figure 8.3b shows the fully assembled valve system.

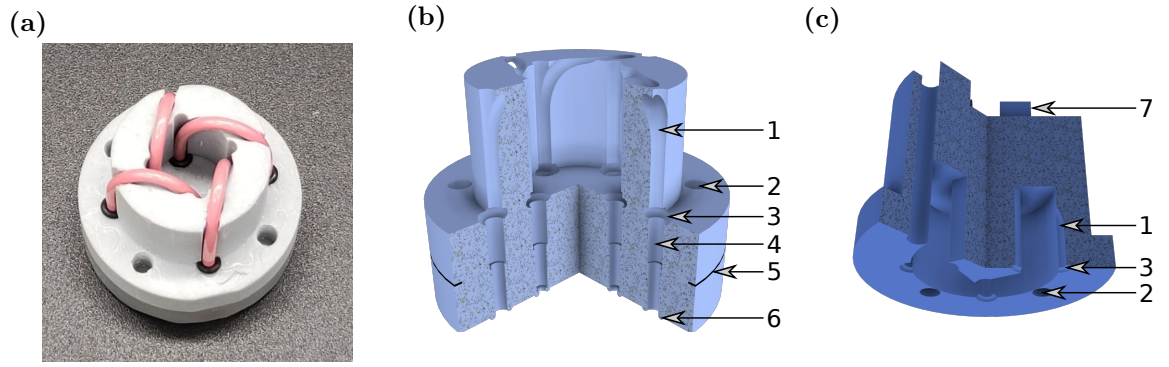

Figure 8.2: (a) 3D-printed rotor (part 1) with inserted capillaries. (b) Section view of rotor part 1 CAD; (c) section view of rotor part 2 CAD. 1 – Guide structure for capillaries; 2 – bore for securing rotor part 1 and 2; 3 – O-ring groove; 4 – capillary holder; 5 – height of material change; 6 – O-ring like structures for sealing the rotor-stator interface; 7 – adapter for motor coupling.

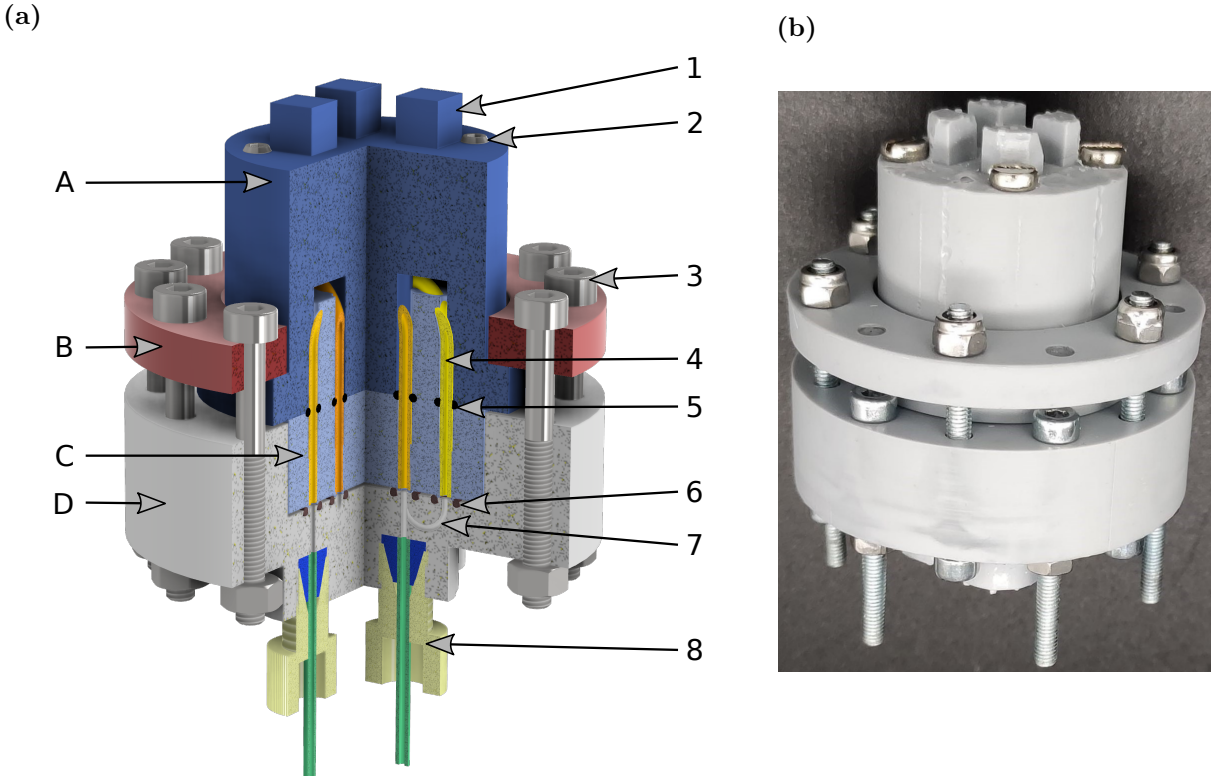

Figure 8.3: (a) Section view of the assembled valve system CAD: A – Rotor part 2 (dark blue); B – cover (red); C – rotor part 1 (light blue); D – stator (gray); 1 – adapter for motor coupling; 2 – screw for joining the two rotor parts; 3 – screw for axial compression of rotor and stator; 4 – capillary chromatography column (different shades of yellow/orange indicate the three different visible columns); 5 – O-ring to prevent fluid bypass around the columns; 6 – O-rings sealing the rotor-stator interface; 7 – connection channels in the stator; 8 – fluidic connection (in/outlet) to the stator. (b) Assembled 3D-printed valve system.

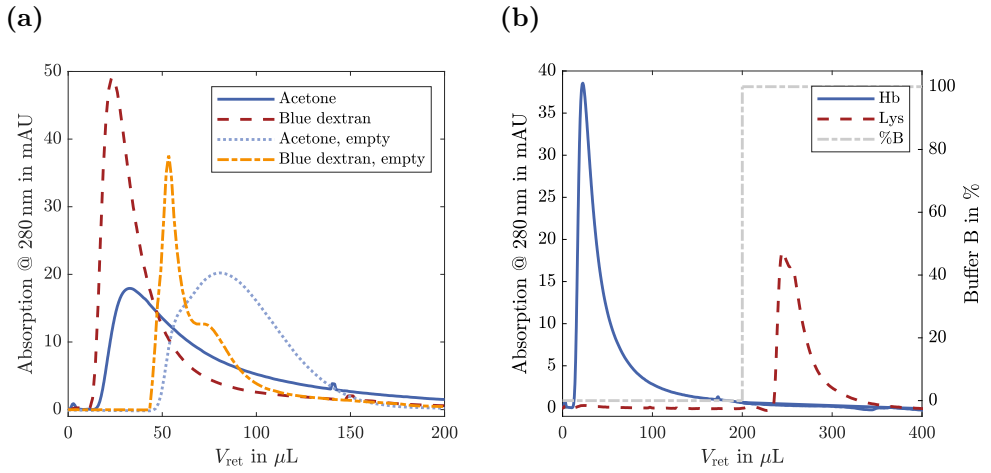

Figure 8.4: (a) Tracer experiments with the monolith column vs. an empty capillary. (b) Single-column experiment for the separation of lysozyme and hemoglobin with step-gradient elution. Hb – hemoglobin; Lys – lysozyme.

8.3 Results and Discussion

8.3.1 Single Column Characterization

Figure 8.4a depicts the results of the tracer experiments with acetone and blue dextran comparing the monolith column to an empty capillary. All peaks exhibit tailing, but because tailing is also observed in the empty capillary, it is likely due to the laminar flow profile in the overall system rather than an inherent property of the monolith. The influence of the laminar flow profile is especially prominent in the empty capillary, where peak splitting can even be observed for acetone, besides its comparable low molecular weight. This effect is not observable for the monolith column, suggesting more plug-flow like behavior in the monolith.

Retention times are shorter with the monolith in comparison to the empty capillary, as the solid phase reduces the accessible void volume. From the retention time of acetone, an overall column porosity ε_T of 0.41 was calculated via (2.2). Since 60% porogen was used in the monomer mixture, some porogen likely remained trapped in non-accessible pores during polymerization. The retention time of blue dextran can be used to determine a theoretical interstitial porosity according to (2.1), describing the amount of large pores that can be accessed by blue dextran. The resulting value of 0.29 indicates that approximately 70% of the total pore volume consists of large pores, resulting in relatively low surface area and limited binding sites for proteins.

Despite this, the monolith can separate lysozyme from hemoglobin, as shown in Figure 8.4b. Hemoglobin does not bind and elutes with the flow-through, whereas lysozyme is only recovered from the column after switching to the elution buffer. The elution profile of hemoglobin is similar to that of blue dextran, indicating that only the larger fraction of the pores is accessible to the protein. A subsequent experiment with stepwise increase of the elution strength of the mobile phase showed that a NaCl concentration of 600 mM is sufficient to fully elute lysozyme, hence this concentration was used in the multi-column experiments.

In another experiment, a larger lysozyme load was injected into the column to record the breakthrough curve and determine the DBC of the monolith, which was 0.88 mg lysozyme per mL solid phase. This is much lower than commercially available ion-exchange monoliths (DBC of 20 mg/mL [261,262]), or other self-synthesized monolithic ion-exchange materials reported in literature (e.g. 5-16 mg/mL [136,263]). The reduced capacity likely stems from the limited surface area due to inhomogeneous pore structure or incomplete functionalization. In literature various protocols to synthesize monoliths with various morphologies and functionalizations exist [264] and although there is substantial room for optimization, this work aims to demonstrate the feasibility of integrating monoliths into the 3D-printed valve system rather than optimizing the monolith itself. Given that these columns can separate low-concentration protein mixtures, it was decided to test them in multi-column experiments despite their low DBC.

8.3.2 Multi-Column Chromatography

The system was first evaluated under gradient SMB conditions at pH 6.4. Figure 8.5a shows that both lysozyme and hemoglobin were recovered in all outlet streams at similar proportions, indicating no effective separation. Additionally, most of both proteins was measured in the raffinate, suggesting insufficient binding of lysozyme. Throughout the experiment, leakages could be observed at the sealing surface between rotor and stator, resulting in an overall volume balance of only 81.2% (±1.7%, n=3) and a protein mass balance of 53.3% (±2.1%, n=3) for lysozyme and 55.7% (±1.9%, n=3) for hemoglobin. Interestingly, the leakages were not evenly distributed among all streams. This was caused by the multiple screws used to compress the rotor and stator, which result in slightly uneven pressure across the sealing surface and thus lead to leakage in specific inlet or outlet streams. This effect is probably enhanced by the comparably high back pressure resulting from connecting the monolith columns in series in comparison to the back pressures of previously used chromatography columns (3 bar compared to 0.2 bar at 50 µL/min). To address this, future studies could reduce leakage by modifying the compression mechanism to ensure uniform pressure across the entire sealing surface.

The observed leakage leads to deviation in the zone flow rates from the desired process point, resulting in an insufficient separation. Especially the flow rate in zone IV was much lower as expected, since all leakages accumulated to that point, resulting in a higher salt concentration in zone IV which is directly transferred to zone III after switching. Hence, the binding of lysozyme to the column is incomplete, even though only approximately 20% of the DBC determined with the single column experiment was used per switch.

Furthermore, even the fraction of lysozyme that did bind may not have been fully eluted because only two column void volumes were used for elution in zone I, whereas the single-column experiments required ten column void volumes to elute 90% of the lysozyme. A higher flow rate in zone I is necessary to ensure complete regeneration of the stationary phase, however, this would either require a higher flow rate in zone I, increasing back pressure and thus leakages, or a longer switching time, increasing analytical times and negating the aim of this study.

These results show that it is not feasible to perform SMB experiments with this setup under the given conditions (DBC, column back pressure, system tightness). Instead, a different continuous multi-column setup was tested by using a different valve stator. In this setup, each column

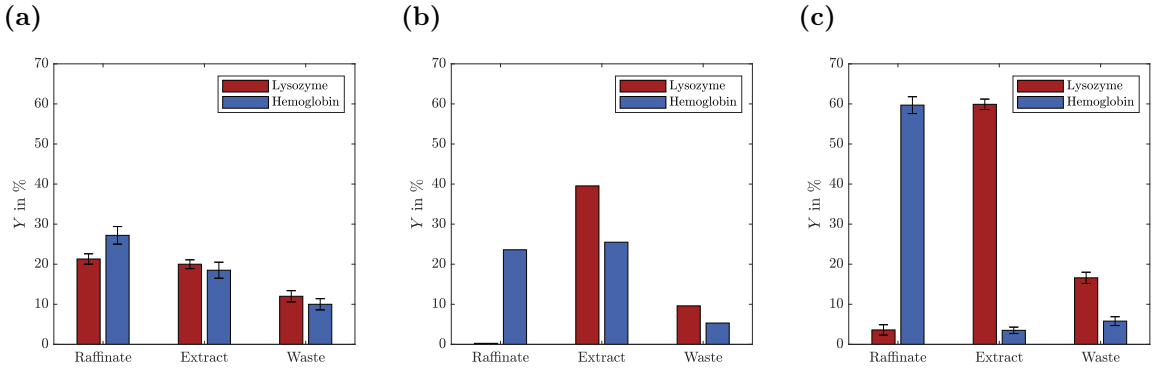

Figure 8.5: (a) SMB experiment at pH 6.4 with a CVS of 2 in zone I; (b) CMCC experiment (CMCC1) at pH 6.4 with a CVS of 2 in zone I; (c) optimized CMCC experiment (CMCC5) at pH 8.2 with a CVS of 2.66 in zone I. Detailed process conditions for all runs are provided in Tables 8.1 and 8.2.

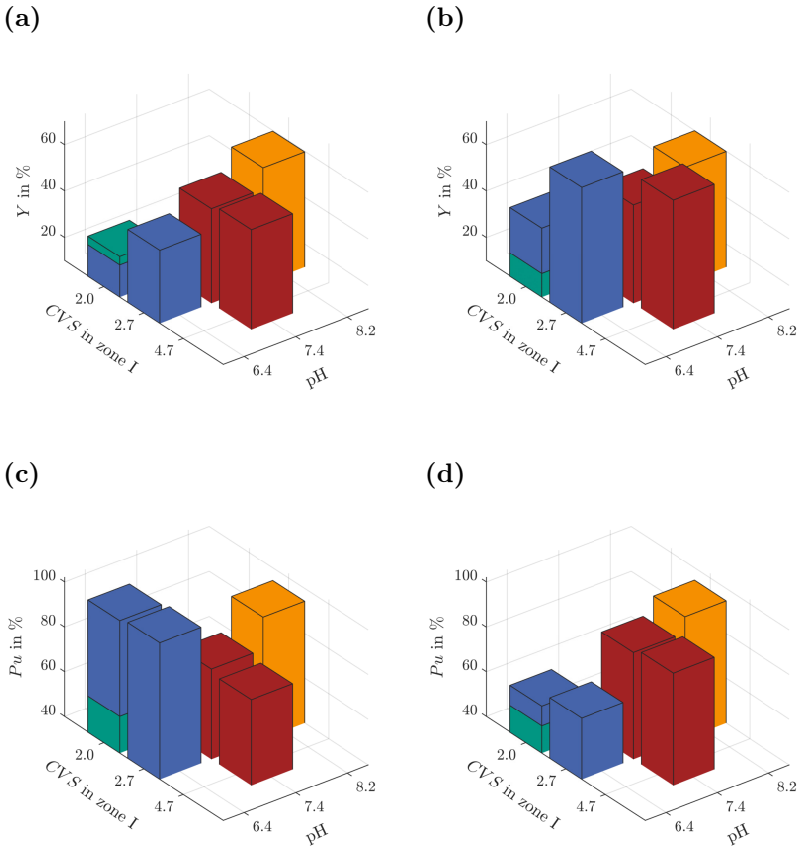

Figure 8.6: Comparison of the SMB experiment with different CMCC runs in dependence of pH and CVS in zone I: (a) Hemoglobin yield in the raffinate; (b) lysozyme yield in the extract; (c) hemoglobin purity in the raffinate; (d) lysozyme purity in the extract. Green bars – SMB run, blue bars – CMCC runs at pH 6.4, red bars – CMCC runs at pH 7.4, orange bars – CMCC runs at pH 8.2. Detailed process conditions for all runs are provided in Tables 8.1 and 8.2.

operates independently in parallel for binding, washing, elution, and re-equilibration, minimizing total back pressure and leaks, allowing for higher flow rates in the single zones. This process features no countercurrent aspect like the more common PCC setup; however, the PCC setup relies on a long loading time in comparison to the time required for the other steps [25], which is not feasible due to the low DBC in combination with the long elution time of lysozyme.

Figure 8.5b depicts the results of a CMCC run performed with the same zone I flow rate and feed flow rate as the SMB run depicted in Figure 8.5a. The flow rates of the wash and re-equilibration step were increased in comparison to the SMB run (compare Tables 8.1 and 8.2). The extract refers to the outlet of the elution step in this case, the raffinate is a pool of the feed and subsequent wash step and the waste is the output of the re-equilibration step. The purity of hemoglobin in the raffinate is greatly improved, indicating successful lysozyme binding. However, hemoglobin also partly binds to the stationary phase, decreasing both the hemoglobin yield in the raffinate and the extract purity. Also, only around 50% of lysozyme and hemoglobin were recovered with a volume balance of 86.4%, indicating that the elution is still incomplete.

Consequently, the flow rate in zone I was increased to enhance the elution process and the pH was increased to reduce hemoglobin binding. The results of a run were the pH was increased from 6.4 to 8.2 and the zone I CVS was increased from 2 to 2.66 is shown in Figure 8.5c. A volume balance of 90.9% (±3.2%, n=3) was achieved under these conditions. The yield of both proteins was increased significantly to approximately 60%; the yield of the lysozyme in the extract could be increased further with a longer elution step, because more than 15% of the total lysozyme is recovered in the re-equilibration step. The purity of the extract is increased, since less hemoglobin bound to the stationary phase at higher pH, however, the purity of the raffinate dropped slightly because more lysozyme did not bind at the higher pH.

Figure 8.6 summarizes the yields and purities across different conditions. Figure 8.6a shows the hemoglobin yield in the raffinate in dependence of CVS in zone I and pH. It indicates that the yield improves with higher pH values, as was expected since a higher mobile phase pH increases the difference to hemoglobin's isoelectric point, preventing its binding to the stationary phase. Literature values for the isoelectric point of hemoglobin range from 6.4-7.0 [265, 266], though it can shift to more acidic values with increasing ionic strength of the buffer [265], or upon interacting with interfaces [266]. Consequently, only at a pH above 7 it can be ensured that the net charge of hemoglobin is negative independent of the respective conditions. At pH 6.4, a slight influence of the CVS in zone I can be observed, but not at pH 7.4. In theory, no influence of the CVS on the raffinate yield is expected for the non-binding hemoglobin.

Figure 8.6b depicts the yield of lysozyme in the extract under the same conditions. The yield increases with higher CVS in zone I at pH 6.4 as well as 7.4. This was expected, since this results in a better elution, as discussed before. The dependence of the yield on the pH is not linear, the yield is lowest at a medium pH of 7.4. The pH influences the yield in two ways: A lower pH results in a better binding of the lysozyme to the column, resulting in less loss to the raffinate stream, while a higher pH probably results in a better elution of the protein, resulting in less loss due to incomplete elution. While at pH 6.4 and 8.2, the respective positive effects seem to outweigh the negative ones, pH 7.4 seems to combine those negative aspects, resulting in a lower yield.

This is also observable for the raffinate purity (Figure 8.6c), where most lysozyme contaminates the raffinate stream at the medium pH of 7.4. At pH 8.2, the better elution results in the preservation of the DBC throughout the experiment, resulting in higher purities. As expected, no influence of the CVS in zone I is observable. Only a slight impact of the CVS in zone I on the extract purity is observable in Figure 8.6d, which is reasonable, since a longer elution step results in the elution of all bound protein. A significant influence of the pH on the extract purity is visible, showing that a pH of 6.4 is to low to prevent the binding of hemoglobin to the stationary phase.

Overall, these results show that the system is able to separate the proteins in CMCC mode. Although the purity and yield still are comparably low for both proteins, the results are encouraging for a first proof of concept, especially given the low DBC of this particular monolith.

8.4 Conclusion

This chapter showcases the limits of downscaling SMB using integrated monolithic capillary columns. The applied columns have a volume of 22 µL each and the valve stator has a channel volume of 24 µL in the case of SMB and 32 µL for the CMCC process. Under the given conditions, the stationary phase's low DBC and high back pressure did not permit the establishment of a suitable process point for SMB separations. However, in a CMCC configuration, the setup successfully achieved protein separation with yields above 60% and purities above 80%. While these processes require further refinement, optimizing process parameters and improving monolith structure and functionalization, these findings underscore the potential of this system as a fast, continuous analytical tool with response times as short as 30 s for proteins recovered in the raffinate stream. The system was operated using the same set of columns for more than ten runs, totaling over 200 min of operation time and more than 400 valve switches, while maintaining consistent performance throughout.

Although valve tightness can be further improved, e.g., by evaluating different sealing materials or by employing an axial compression mechanism that applies more uniform pressure, this study demonstrates the valve's versatility: It shows how capillary columns can be integrated directly into the rotor and how exchanging only the stator enables different multi-column processes (SMB, CMCC) using the same set of columns, enabling the fast comparison of different processes. With these promising initial results, future studies should further explore the potential of combining advances in the miniaturization of single-column and multi-column processes.

9. Summary and Outlook

This thesis explored whether 3D printing can bridge the existing gap in miniaturized continuous chromatography equipment, using SMB as a case study. To address this question, three key aspects were investigated: the development of a 3D-printed valve assembly, the applicability of the resulting µSMB system for process development, and its potential for process analytics.

The valve assembly is a crucial component of any SMB system, as it ensures proper connectivity among multiple chromatography columns. It defines the overall system structure and significantly influences key parameters such as system volume. Thus, the question of whether SMB can be miniaturized using 3D printing can be rephrased as: Is it possible to 3D print a suitable valve system?

While multi-valve configurations are well established in laboratory-scale SMB systems due to their flexibility, a single central valve with rotating chromatography columns was chosen in this work to minimize internal volume. A modular 3D-printed rotor-stator system with axial compression was developed to enable rapid prototyping of customized valve designs. The key challenge lay in achieving reliable sealing between the rotor and stator interfaces, particularly given the relatively rough surfaces produced by 3D printing. Systematic evaluation of different sealing strategies revealed that a combination of a silicone or PTFE sealing mat on one side and O-rings on the opposing surface provided sufficient dynamic tightness up to 8 bar.

The developed valve system was then used in a µSMB setup, which was tested in two proof-of-concept studies. In these studies, SMB experiments were successfully performed, and the valve system remained operational for several hours without failure, demonstrating its suitability for continuous operation.

The valve rotor was then modified to directly integrate chromatography columns, further showcasing the versatility of the concept. However, the use of capillary columns led to leakages due to excessive backpressure. In addition to the adaption of the rotor, the stator was adapted for another continuous chromatography process, where columns were operated in parallel. The same rotor system – including the integrated columns – was compatible with both setups, highlighting the flexibility of the modular system. This capability enables rapid switching between different chromatography configurations, facilitating direct performance comparisons. Overall, this demonstrates that the 3D-printed valve system is fully operational at low and moderate pressures.

The µSMB system's applicability for early-stage process development was evaluated by continuously desalting BSA from AS via SEC. Across multiple process conditions, desalting levels exceeded 94%, with the best process achieving 99.6% desalting while maintaining yields between 65% and 88%. Notably, the feed flow rate during these experiments was as low as 15 µL/min, requiring only ∼3.3 mL of feed to reach cyclic steady state. In subsequent studies, the feed flow rate was further reduced to 10 µL/min for SMB applications and 5 µL/min for CMCC. To the best of the author's knowledge, these are the smallest SMB experiments ever conducted.

To fully leverage the µSMB for process development, cross-scale comparisons are crucial. This necessitates understanding scale-dependent system-wide effects on separation performance. Thus, a system model was developed, integrating both, chromatography columns and the ECV. Since no existing ECV model accurately describes the µSMB's ECV with reasonable computational effort, a novel approach – the equivalent radial flow rate distribution – was developed. This method uses either experimental data or CFD simulations to calculate a radial flow rate profile that approximates the residence time distribution within the ECV. Although eqFRD improved ECV predictions in isolation, increasing accuracy from 90% to 97%, it did not significantly enhance overall µSMB simulation results. This suggests that the ECV only has a minor impact on µSMB performance.

To assess the µSMB's potential for process analytics, it was applied as a sample pre-processing tool for ESI-MS and directly coupled to an ESI-MS system for on-line analysis. Using SEC, myoglobin was continuously transferred from a Tris buffer to an ESI-compatible ammonium acetate buffer. Despite the limited separation performance of the single columns, the µSMB achieved a buffer exchange efficiency of 98%, significantly improving MS measurement quality. Thus, this case study demonstrates how µSMB enables simple and reliable MS integration for process analytics, making this powerful analytical method more accessible for future PAT applications. To fully unlock the potential in this area, future systems must integrate innovative data processing approaches that process measured data in real time and enable its use for active process control.

In conclusion, this thesis presents a successful proof-of-concept for µSMB chromatography, demonstrating significant potential for on-line process analytics, resource-efficient process development with minimal sample requirements, flexible operation, and broad applicability. With its modular design and easy adaptability to other continuous chromatography processes besides SMB, this work lays an important foundation for the broader transition toward continuous bioprocessing in both research and industrial settings.

Beyond the technical aspects, this work can contribute to making process development more flexible and adaptable. As outlined in Section 2.1.2.2, the potential configurations for continuous multi-column chromatography processes are virtually unlimited. The system developed here enables rapid and straightforward experimental validation of diverse operational modes with minimal required product amounts, allowing for the optimization of both the number of columns and their configuration rather than merely optimizing a predefined multi-column process. Moreover, when combined with other miniaturized continuous unit operations, this system could contribute to the creation of a complete miniaturized workflow for continuous biomanufacturing, which would be highly beneficial for the development of integrated manufacturing approaches.

Appendix

A Configurable 3D Printed Microfluidic Multiport Valves with Axial Compression

Figures A.1-A.3 show technical drawings of all 3D-printed parts of the test valve and Figures A.4-A.6 of the upscaled system.

Figure A.7 shows microscope images of sealing surfaces of four test valves. Figure A.7a depicts the sealing surface of a polyjetted valve (sealing concept 1). The surface is quite rough due to circular structures of the printer nozzles, additionally long furrows are visible between the printer heads. Figure A.7b shows a polished polyjetted part (sealing concept 2). It is evident that the circular structures caused by the printer nozzles were smoothed with polishing, but some of the long furrows are still visible. In addition, small grooves that were probably caused by the polishing with the rotary tool are visible. Though the images only allow for a qualitative estimation of the surface roughness, it is obvious that it is reduced with polishing, but the surface is still rough afterwards. For comparison, Figure A.7c shows the surface of a DLP printed valve. It also has some furrows but the surface makes a smoother impression compared to the polyjetted valve. Figure A.7d shows the surface of the silicone mat that was used as a sealing element. The surface is not as rough as for the 3D printed parts but it is neither completely smooth. This suggests that sealing efficiency not only depends on the surface roughness but also on the flexibility of the material.

Figure A.8 shows microscope images of O-rings before and after usage. Figure A.8a depicts a new O-ring for comparison. Figure A.8b depicts an O-ring that was rotated 20 times in a valve with a silicone mat on the opposite sealing surface. Comparing the lower magnification (b1) with the original O-ring (a1), it gets clear that the O-ring is slightly deformed by the compression of the valve and is flattened at the surface. Comparing the structure of the material at higher magnification (a1 & b1), no change is visible, thus the O-ring is still intact. Figure A.8c depicts an O-ring that was rotated 20 times in a valve without a silicone mat on the opposite sealing surface. Figure A.8c1 shows that the O-ring has an uneven surface where it is hard to set the focus level of the microscope and signs of abrasion are visible (white circle). Looking at the material structure (c2), it is obvious that it is less dense compared to the previous two cases with holes of the size of several µm. From these images it can be concluded that the 3D printed parts are no suitable counter surface for sealing with O-rings but the lifetime can be increased using other counterparts, like silicone mats.

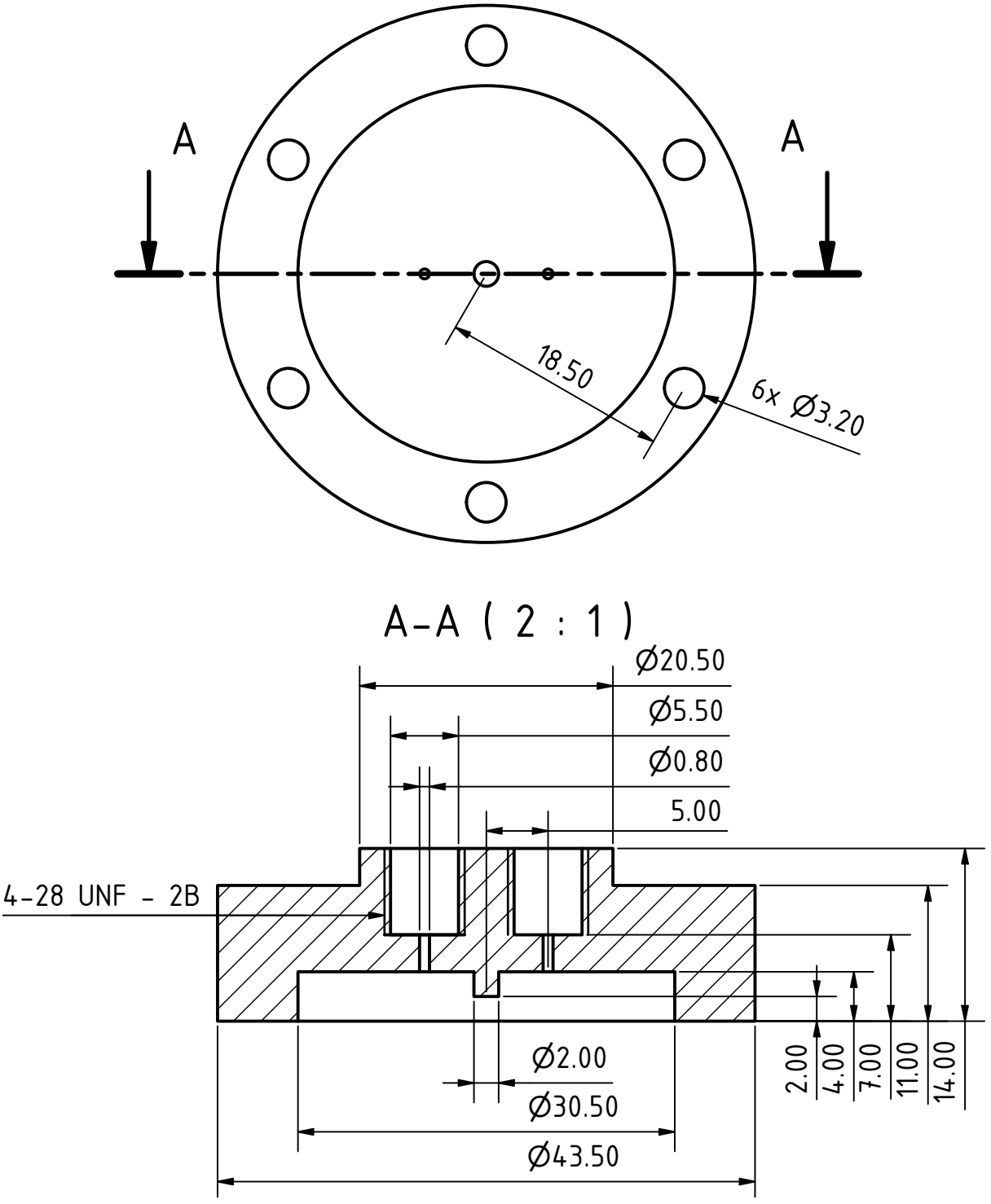

Figure A.1: Technical drawing of the stator of the test valve: top view (top) and section view (bottom) with scale 2:1. All threads were cut after printing, all dimensions in mm.

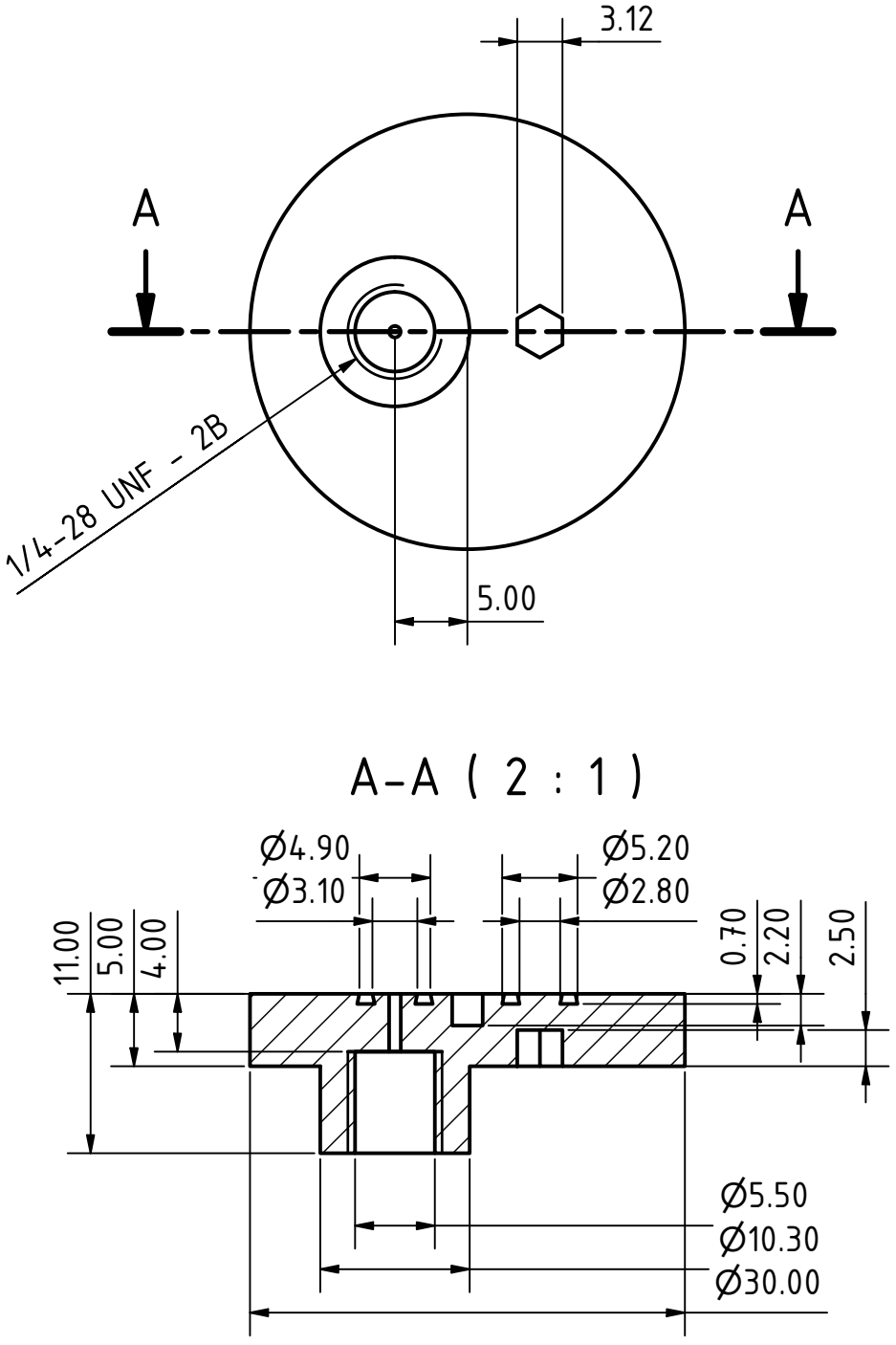

Figure A.2: Technical drawing of the rotor of the test valve: top view (top) and section view (bottom) with scale 2:1. The hexagonal recess in the surface can be used to manually turn the rotor using an Allen key. All threads were cut after printing, all dimensions in mm.

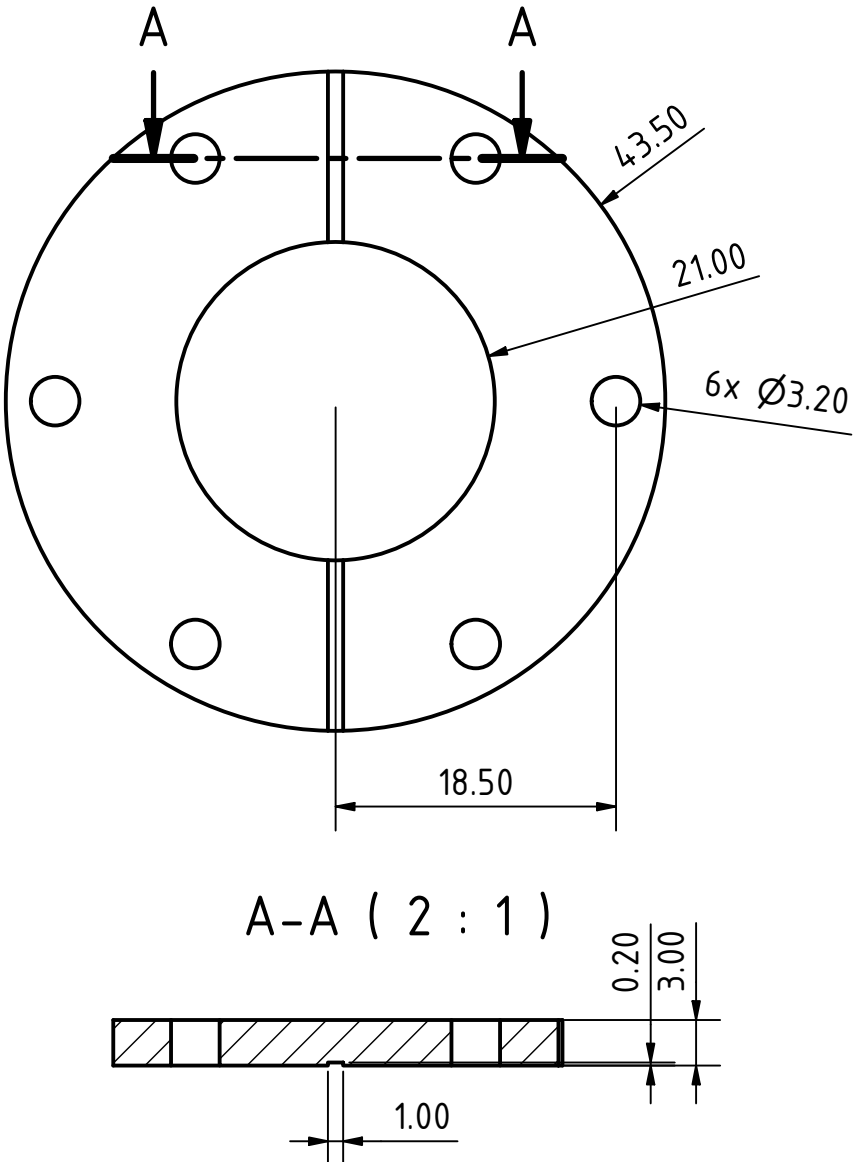

Figure A.3: Technical drawing of the cover of the test valve: top view (top) and section view (bottom) with scale 2:1. All dimensions in mm.

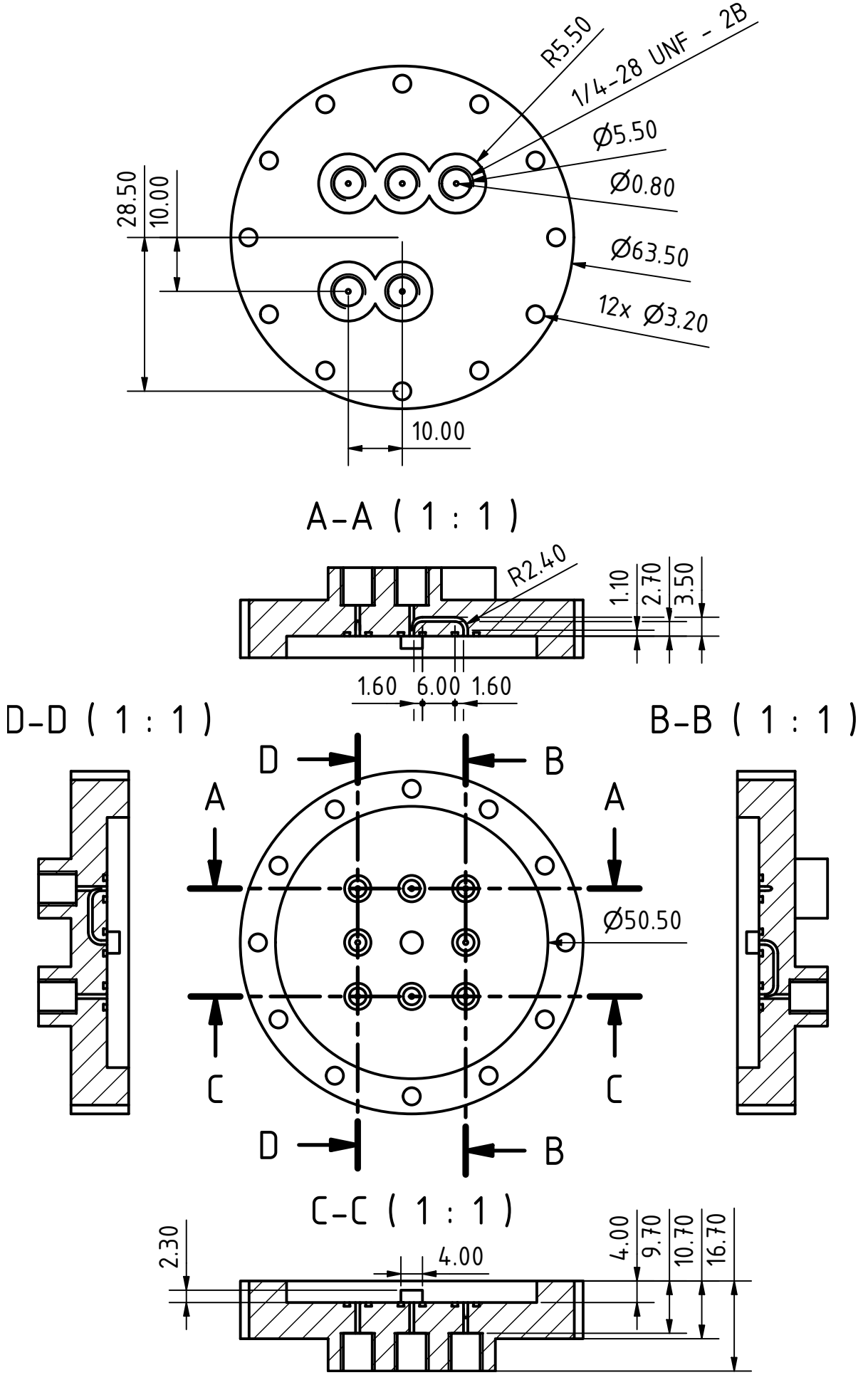

Figure A.4: Technical drawing of the stator of the upscaled valve. Detailed caption on next page.

Figure A.4: Technical drawing of the stator of the upscaled valve: top view (top) and bottom view with several section views (bottom) with scale 1:1. The stator features several channels connecting the in- and outlets, the exact positioning can be seen in the section views. The O-ring grooves have not been dimensioned to increase clarity. The respective dimension can be found in Figure A.2 (bottom). All threads were cut after printing, all dimensions in mm.

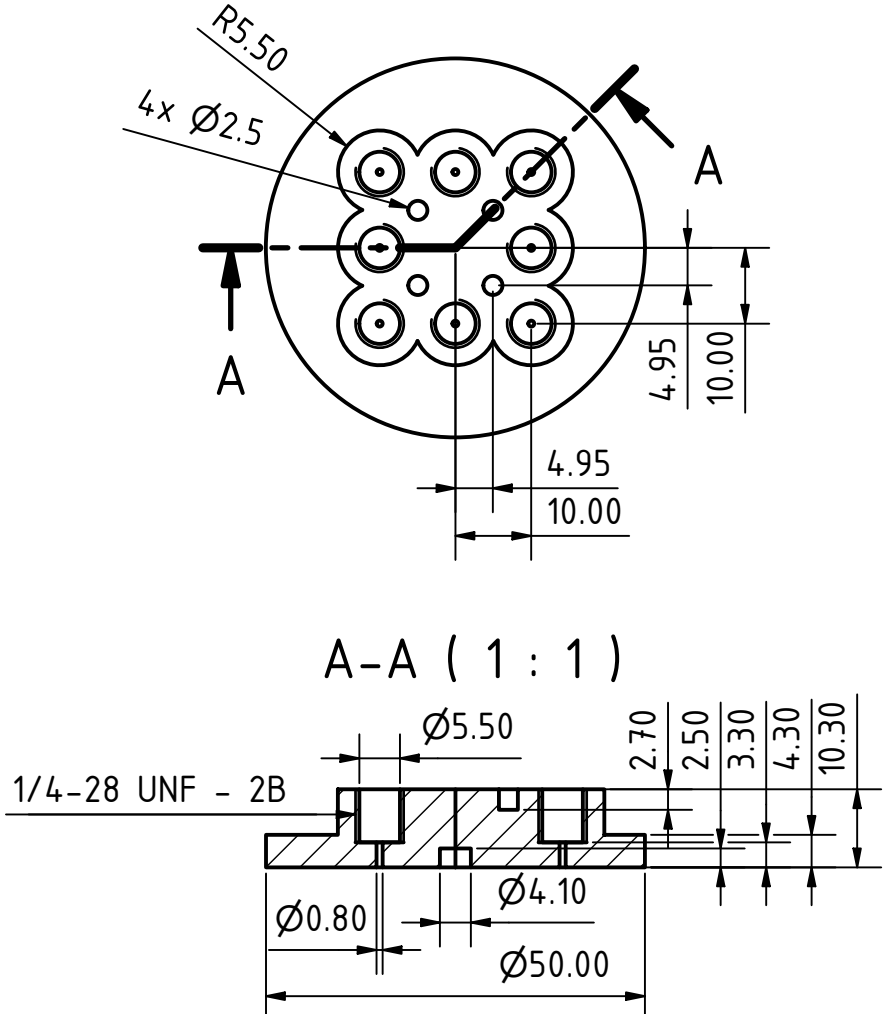

Figure A.5: Technical drawing of the rotor of the upscaled valve: top view (top) and section view (bottom) with scale 1:1. The four recesses in the surface can be used to mount a motor adapter and turn the rotor automatically. All threads were cut after printing, all dimensions in mm.

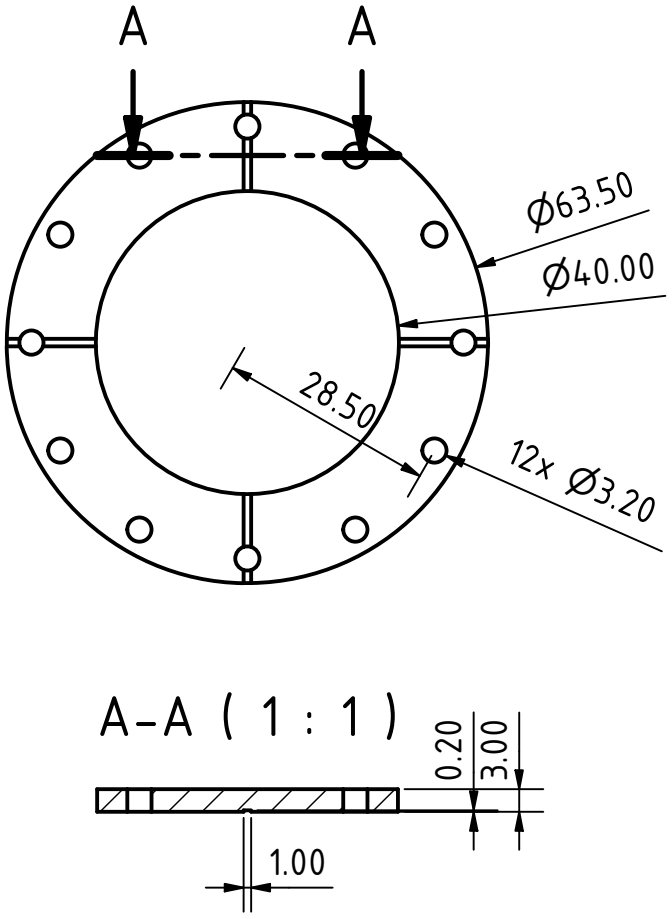

Figure A.6: Technical drawing of the cover of the upscaled valve: top view (top) and section view (bottom) with scale 1:1. All dimensions in mm.

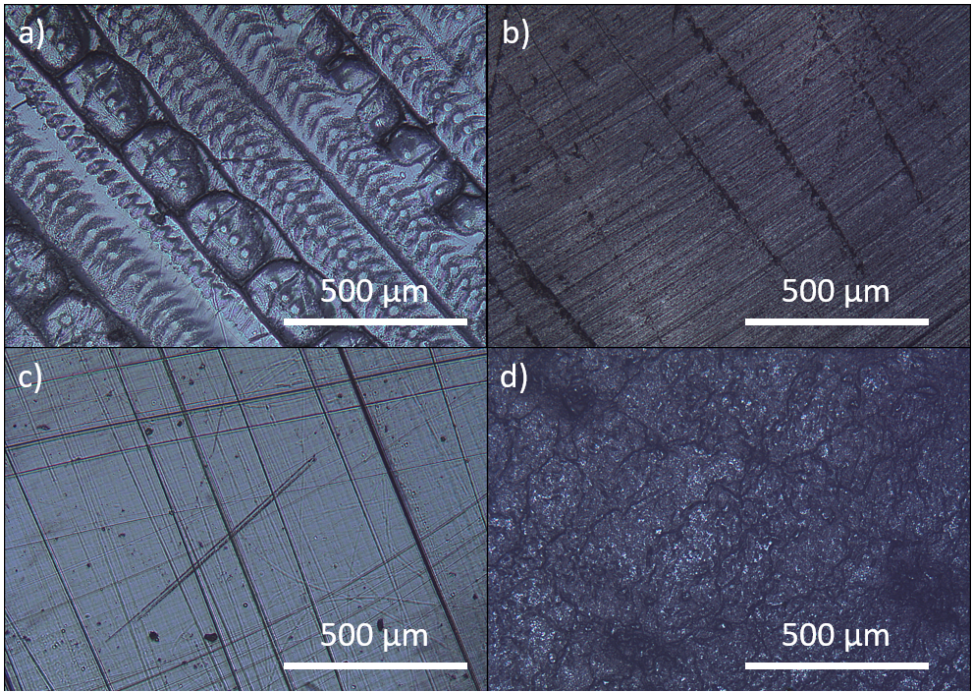

Figure A.7: Microscope images of the sealing surfaces of different valve configurations with 50x magnification; a) polyjetted valve without post-processing; b) polyjetted valve with post-processing (polished); c) DLP printed valve; d) silicone sealing mat.

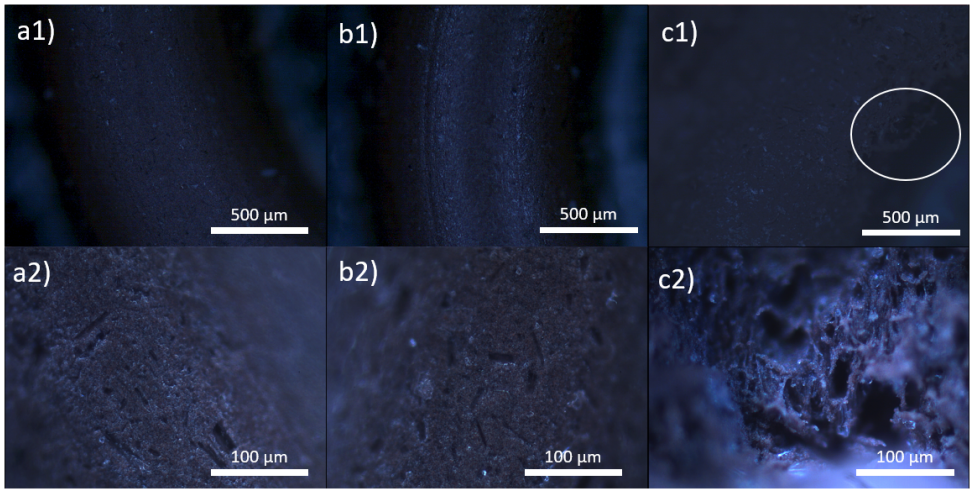

Figure A.8: Microscope images of O-rings at magnifications of 50x (a1-c1) and 200x (a2-c2); a) new O-ring put into the valves O-ring groove; b) O-ring after 20 valve rotations with sealing concept 5 (silicon mat at opposite sealing surface); c): O-ring after 20 valve rotations with sealing concept 4 (without silicone mat).

Figure A.9 depicts the in- and outlet flow rates of the test valve during a switching process in a not tight (a) and tight (b) case, comparable to Figure 4.7a and 4.7b, but using the microfluidic flow controller instead of a piston pump as flow source.

(a) **(b)**

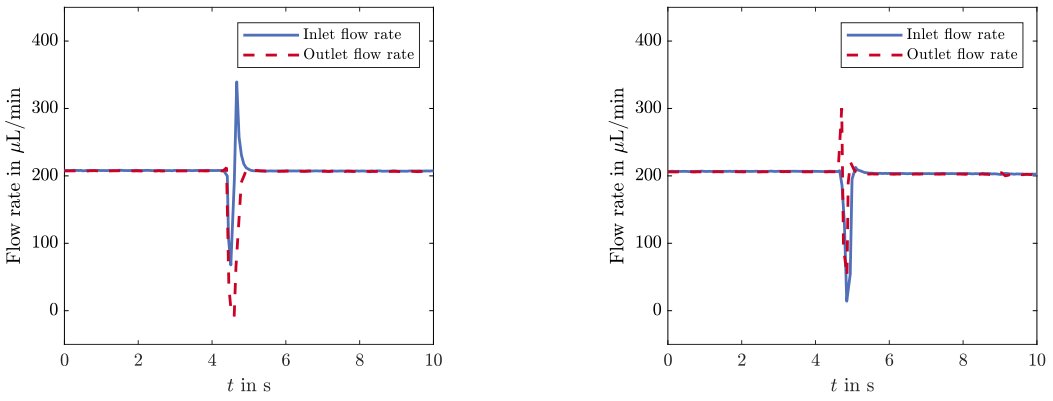

Figure A.9: In- and outlet flow rates during switching process for the 3D printed valve connected to the microfluidic flow control system; (a) not tight case with leakage occurring during the switching process; (b) tight case with no leakage occurring during the switching process.

B Development of a 3D Printed µSMB System

Figure B.10 depicts two different rotor layouts for the connection of four chromatography columns to the rotor. In the first layout (a), all ports are placed on one circle, thus in- and outlet ports follow the same trajectories during the switching process. This leads to cross-contamination, as the flow is not turned off during the switching and hence there will be flow in the "half-turned" position for a short time. The second layout (b) shows a possibility to prevent this problem: The in- and outlet ports are positioned on two concentric circles, hence they follow different trajectories during the switching. In this particular case, all ports form a rectangle as this is the pattern with the smallest footprint for equal spacing of the ports.

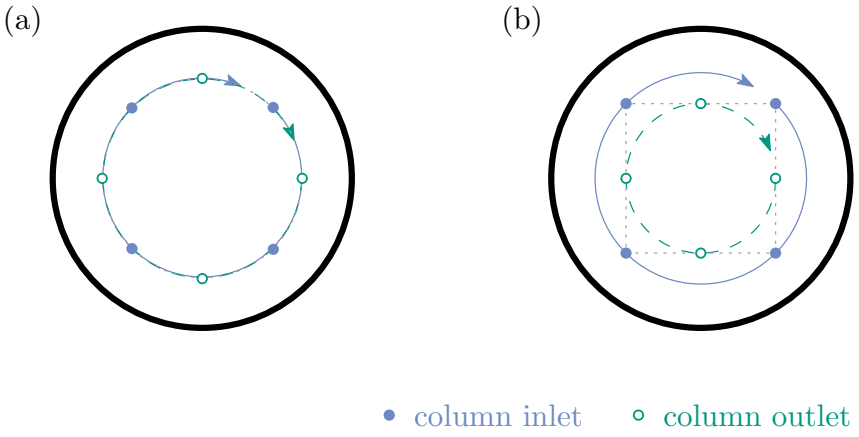

Figure B.10: Valve rotors with different port configurations; a) all ports are located on one circle and follow the same trajectories; b) the in- and outlet ports are positioned on two concentric circles. All ports form a rectangle.

Figure B.11 depicts a screenshot of the GUI that was developed with MATLAB and used for the control and data handling of the µSMB system.

Figure B.12 shows the scheme for the single column simulation. The input concentrations for the column model were generated as a step function. Then the output of the column model was used as input for the system model. The system was modeled with a series of CSTRs. A series of smaller CSTRs was used to model the time delay caused by the dead volume and one bigger CSTR was used to account for the mixing effects in the detector cells. The outlet of this model was compared to the experimental chromatograms. In the real experimental setup, part of the system volume is before the column (injection loop and valve, capillaries to the column) while the other part is located behind the column (capillaries and detectors). Here, we assumed that the peak broadening is independent of the position and treated everything as one unit, as we cannot determine the influence on the peak shape of the single system components experimentally. The number of CSTRs as well as the volume differs for BSA and AS, as they are detected with different detectors.

Table B.1 gives an overview of all required input parameters for the simulations with CADET.

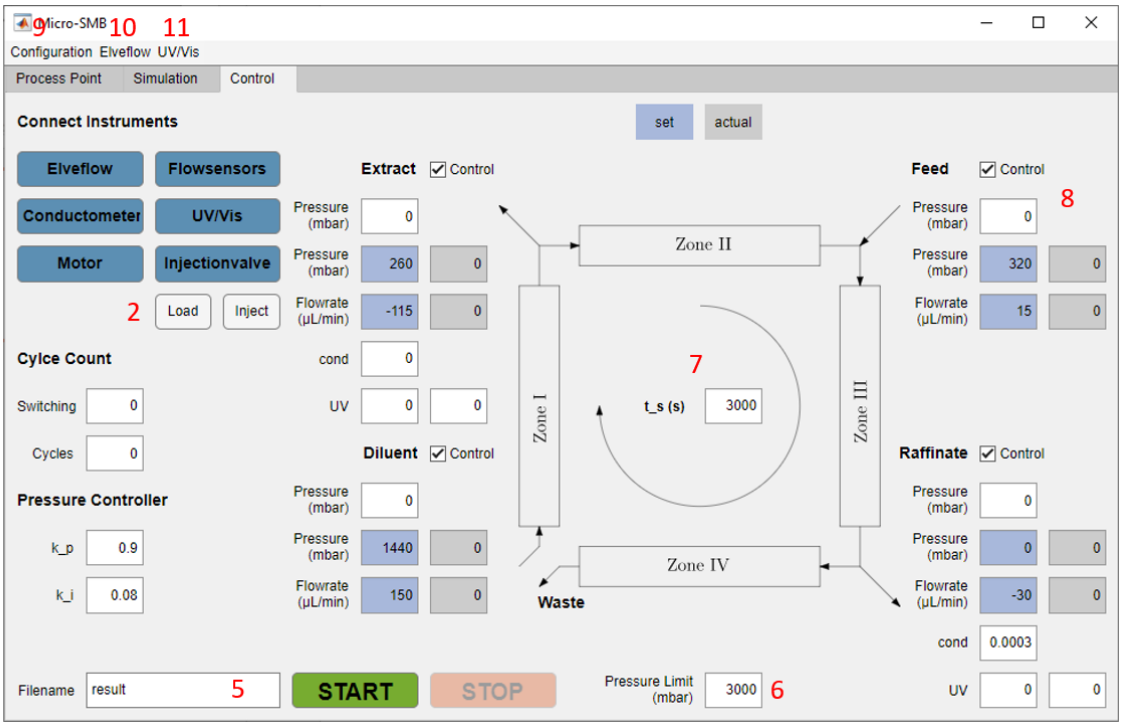

Figure B.11: Screenshot of the GUI for controlling the µSMB system. 1 – buttons to connect different devices; 2 – position change of injection valve (if applicable); 3 – count of performed switches and cycles; 5 – file name for saving of the results; 6 – pressure limit; 7 – switching time; 8 – flow rate and pressure control; 9 – open GUI configuration windwow; 10 – open Elveflow settings window; 11 – open UV/Vis detection setting window.

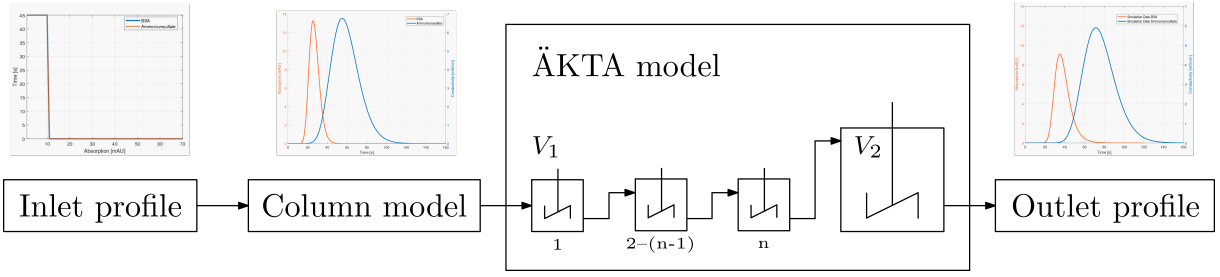

Figure B.12: Schematic of the single column simulation process. For the simulation of ammonium sulfate, the number of small CSTRs was set to 26 with a volume of 1.6 µL and the volume of the bigger CSTR was set to 42 µL. For bovine serum albumin, the number of small CSTRs was set to 13 with a volume of 1.6 µL and the volume of the bigger CSTR was set to 32 µL.

Table B.1: Overview of all model parameters of an SMB simulation with CADET-SMB

Parameter	**Name in CADET**	**Value**
Column length	opt.column.Length	$5.0\times10^{-2}\,\mathrm{m}$
Column diameter	opt.columnDiameter	$3.07\times10^{-3}\,\mathrm{m}$
Particle radius	opt.particleRadius	$2.5\times10^{-5}\,\mathrm{m}$
Bed porosity	opt.porosityColumn	0.394
Particle porosity	opt.porosityParticle	0.743
Accessible porosity	opt.poreAccessibility	BSA: 1×-5 AS: 1
Number of components	opt.nComponents	2
Axial cells per columns	opt.nCellsColumn	40
Radial cells per particle	opt.nCellsParticle	3
Dispersion coefficient	opt.dispersionColumn	$5.21\times10^{-6}Q\,[\mathrm{mL/min}]$
Film transfer coefficient	opt.filmDiffusion	BSA: $1.14\times10^{-5}\,\mathrm{m^2/s}$ AS: $3.00\times10^{-6}\,\mathrm{m^2/s}$
Pore diffusion coefficient	opt.diffusionParticle	BSA: $0\,\mathrm{m^2/s}$ AS: $2.31\times10^{-10}\,\mathrm{m^2/s}$
Surface diffusion coefficient	opt.diffusionParticleSurface	$0\,\mathrm{m^2/s}$
Interstitial velocity	opt.interstitialVelocity	Calculated from volumetric flow rates (see Table 5.1)
Initial particle loading	opt.initialSolid	$0\,\mathrm{mol/m^3}$
Discretization in time	opt.timePoints	1000
Number of zones	opt.nZone	4
Number of columns	opt.nColumn	4
Switching time	opt.switch	See Table 5.1
Feed concentration	concentrationFeed	BSA: $100\,\mathrm{g/m^3}$ AS: $26428\,\mathrm{g/m^3}$
Molar mass	opt.molMass	BSA: $66463.00\,\mathrm{g/mol}$ AS: $132.14\,\mathrm{g/mol}$
Binding model	opt.BindingModel	'NoBinding'

C µSMB-MS as a Continuous On-line Process Analytical Tool

Table C.2 gives an overview of all required input parameters for the process point optimization with CADET-SMB.

Table C.2: Overview of all model parameters of the SMB process point optimization with CADET-SMB. SV – start value; LL – lower limit; UL – upper limit.

Parameter	**Name in CADET**	**Value**
Column length	opt.column.Length	5.0×10^{-2} m
Column diameter	opt.columnDiameter	3.07×10^{-3} m
Particle radius	opt.particleRadius	5.5×10^{-5} m
Bed porosity	opt.porosityColumn	0.376
Particle porosity	opt.porosityParticle	0.547
Accessible porosity	opt.poreAccessibility	Mb: 0.043 Tris: 1
Number of components	opt.nComponents	2
Axial cells per columns	opt.nCellsColumn	40
Radial cells per particle	opt.nCellsParticle	4
Dispersion coefficient	opt.dispersionColumn	$1.27\times10^{-6}Q$ [mL/min] + 4.92×10^{-10}
Film transfer coefficient	opt.filmDiffusion	Mb: 2.20×10^{-5} m^2/s Tris: 7.78×10^{-5} m^2/s
Binding model	opt.BindingModel	'NoBinding'
Initial particle loading	opt.initialSolid	0 mol/m^3
Discretization in time	opt.timePoints	1000
Number of zones	opt.nZone	4
Number of columns	opt.nColumn	4
Switching time	opt.switch	SV: 103 s; LL: 80 s; UL: 300 s
Q_1	-	SV: 2.5×10^{-9} m^3/s; LL: 3.3×10^{-10} m^3/s; UL: 2.5×10^{-9} m^3/s
Q_F	-	SV: 2.5×10^{-10} m^3/s; LL: 2.5×10^{-10} m^3/s; UL: 2.5×10^{-9} m^3/s
Q_E	-	SV: 9.7×10^{-10} m^3/s; LL: 3.3×10^{-10} m^3/s; UL: 2.5×10^{-9} m^3/s
Q_R	-	5×10^{-10} m^3/s;
Interstitial velocity	opt.interstitialVelocity	Calculated from volumetric flow rates
Optimization function	$y = 50Y_{\text{Tris,Raf}} + (1 - Y_{\text{Mb,Raf}})$	

Figure C.13 shows comparably the MS spectra of Mb solutions with different Tris content. For a 1 mM Tris concentration, the highest Tris signal at m/z 593.23 is more than ten times higher compared to the Mb signal at m/z 2196.64.

Figure C.14 shows the single-column desalting experiments of the Mb/Tris system that was used in this study in comparison to the BSA/AS system that was applied in a previous study. The peak height of AS was normalized to match that of Tris for better comparability. The retention time difference of the peak maxima is higher for the BSA/AS separation system. In addition,

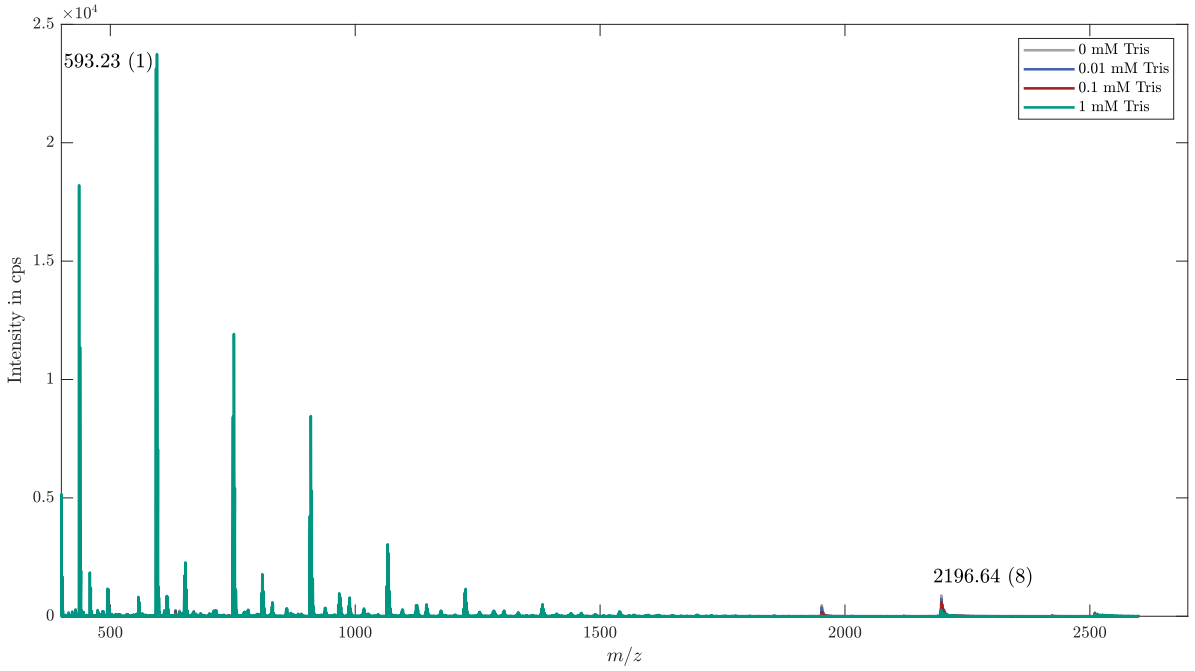

Figure C.13: MS spectra of solutions containing 10 µg/mL Mb and different concentrations of Tris

the resolution at the beginning of the peaks is much better. BSA starts to elute before AS, while Mb and Tris almost elute at the same time. The resolution at the beginning of the separation is most important for the raffinate purity. As the desalting performance of the single-column experiment already is much lower for the Mb/Tris system, it is probably not possible to match the µSMB desalting level of the BSA/AS system with further process point optimization. Rather it would be required to change the separation system itself or the µSMB setup instead. Possible approaches are an increased number of columns per zone, longer chromatography columns or the usage of a stationary phase with higher separation performance.

Figure C.15 depicts the MS signals of Mb, heme and Tris during the third SMB cycle for each Tris concentration of run 1 without baseline correction of the signals. The drop of the Mb signal at Tris concentrations of 50 mM and 100 mM is not as high as with the baseline correction, still the negative influence of Tris on the measurement is clearly observable.

Figure C.16 shows the apoMb level and Tris concentration over five consecutive switches in µSMB-MS run 2. The switches were divided into five subsections (24 s per subsection) and the mean detected apoMb percentage was calculated for each subsection. As the interval that was used to calculate the apoMb level is smaller than one switching interval, the influence of the fluctuations in Tris concentration on the detected apoMb level are observable. Despite the differences of the columns, the mean detected apoMb percentage is comparable between the switches for the different subsections. This is favorable for possible on-line analytical applications, as it shows that different time intervals of the SMB process are comparable as long as they are compared to an equivalent time interval of another switch or cycle. A comparison between different subintervals is not possible, as the detected apoMb percentage differs. Interestingly, there is no direct correlation

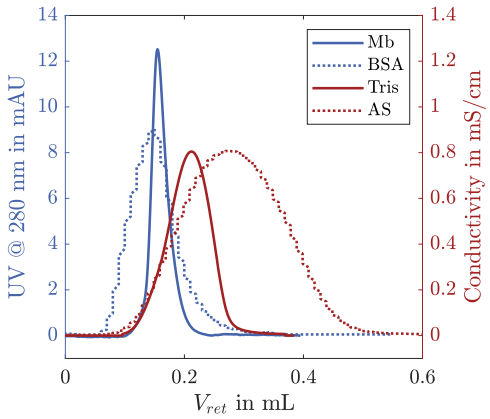

Figure C.14: Single-column experiments for the separation of Mb and Tris with a Sephadex G10 column and for the separation of BSA and AS with a Sephadex G25 fine column. For better comparability, the peak height of the AS peak was normalized to match the Tris peak.

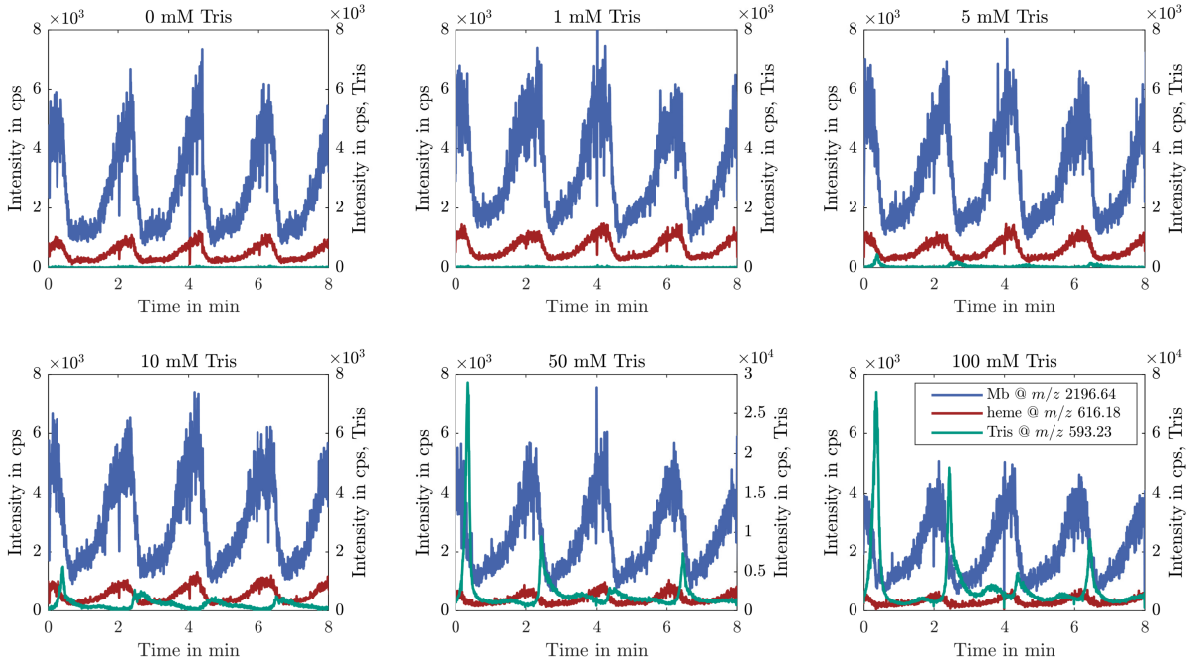

Figure C.15: MS signals of Mb, heme and Tris during the third SMB process cycle for each Tris concentration of µSMB run 1. The depicted signals are not normalized with the baseline signal.

between the Tris concentration and the detected apoMb level, e.g. the detected apoMb level is highest in the third subsection, while the Tris concentration is lowest in the first one. This again suggests that there are is no proportional relationship between the detected apoMb level and the Tris concentration and further investigation is required to clarify the exact effect.

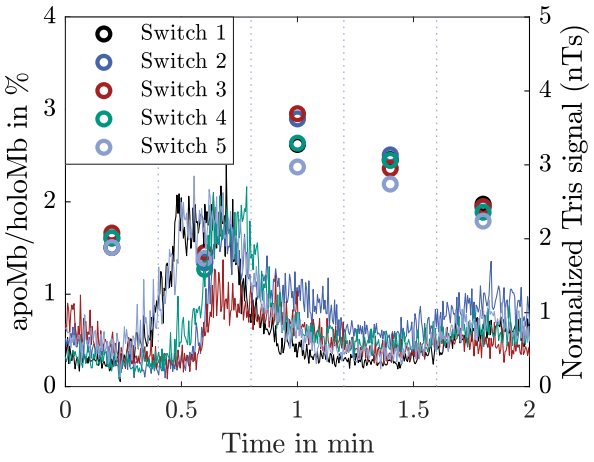

Figure C.16: Detected apoMb level and normalized Tris signal for five consecutive switching intervals of µSMB run 2 (10 mM Tris in feed solution). The apoMb level was calculated over an interval of 24 s, as indicated by the dotted lines

D Modeling the ECV of a µSMB System: Introducing the eqFRD

D.1 Methods

Table D.3 gives an overview of all units of the µSMB model with the laminar approach in CADET. The stator geometry equals a cylinder with the same volume and diameter as the curved channel. If several units are combined to one for other modeling approaches, the diameter of the valve system was always used for the resulting cylindrical geometry and the length was adjusted accordingly.

Table D.3: Overview of units for ECV modeling in CADET

Unit Number	Description	Type	Length in m	Diameter in m
000	Inlet feed	Inlet	-	-
001	Inlet diluent	Inlet	-	-
002	Outlet raffinate	Outlet	-	-
003	Outlet extract	Outlet	-	-
004 – 007	Column models	GRM	5e-2	3e-3
008	Outlet waste	Outlet	-	-
009	Capillary: valve raffinate to conductivity sensor	2DGRM	1e-1	2.5e-4
010	Conductivity sensor (raffinate)	2DGRM	3.5e-2	6.85e-4
011	Capillary: conductivity to UV sensor (raffinate)	2DGRM	1e-1	2.5e-4
012	UV sensor (raffinate)	2DGRM	5e-3	5e-4
013	Capillary: valve extract to conductivity sensor	2DGRM	1e-1	2.5e-4
014 – 021	Capillaries: columns to valve rotor	2DGRM	1.1e-1	2.5e-4
022	Valve stator diluent	2DGRM	5.7e-3	8e-4
023	Valve stator extract pt. 1	2DGRM	14.48e-3	8e-4
024	Valve stator extract pt. 2	2DGRM	5.7e-3	8e-4
025	Valve stator feed pt. 1	2DGRM	14.48e-3	8e-4
026	Valve stator feed pt. 2	2DGRM	5.7e-3	8e-4
027	Valve stator raffinate pt. 1	2DGRM	14.48e-3	8e-4
028	Valve stator raffinate pt. 2	2DGRM	5.7e-3	8e-4
029	Valve stator waste	2DGRM	5.7e-3	8e-4
030 – 037	Channels in valve rotor	2DGRM	3.3e-3	8e-4
038	Conductivity sensor (extract)	2DGRM	3.5e-2	6.85e-4

Figure D.17 shows a technical drawing of the channel in the valve stator between sections two and three of the µSMB. The channels between zones one and two resp. three and four are horizontally mirrored but otherwise identical.

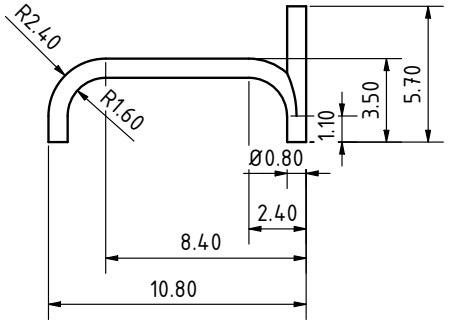

Figure D.17: Technical drawing of the channels in the valve stator between SMB sections two and three (feed-node).

Table D.4 provides the volumetric flow rates and the switching time of the applied SMB process point.

Table D.4: Overview of process parameters of the µSMB process.

Parameter	Value
Q_{D}	113 µL/min
Q_{E}	45 µL/min
Q_{F}	30 µL/min
Q_{R}	50 µL/min
Q_1	113 µL/min
Q_2	68 µL/min
Q_3	98 µL/min
Q_4	48 µL/min
t_{s}	165 s

Figure D.18 gives an overview of the required units and their connectivity for the µSMB model. The eqFRD approach requires the least amount of units due to the combination of several units. The DPFR+CSTR approach combines even more units together but still requires a higher number of total units as each combined unit is modeled with two seperate units (DPFR+CSTR). The parallel DPFR+CSTR approach required by far the most units, using four units per modeled entity.

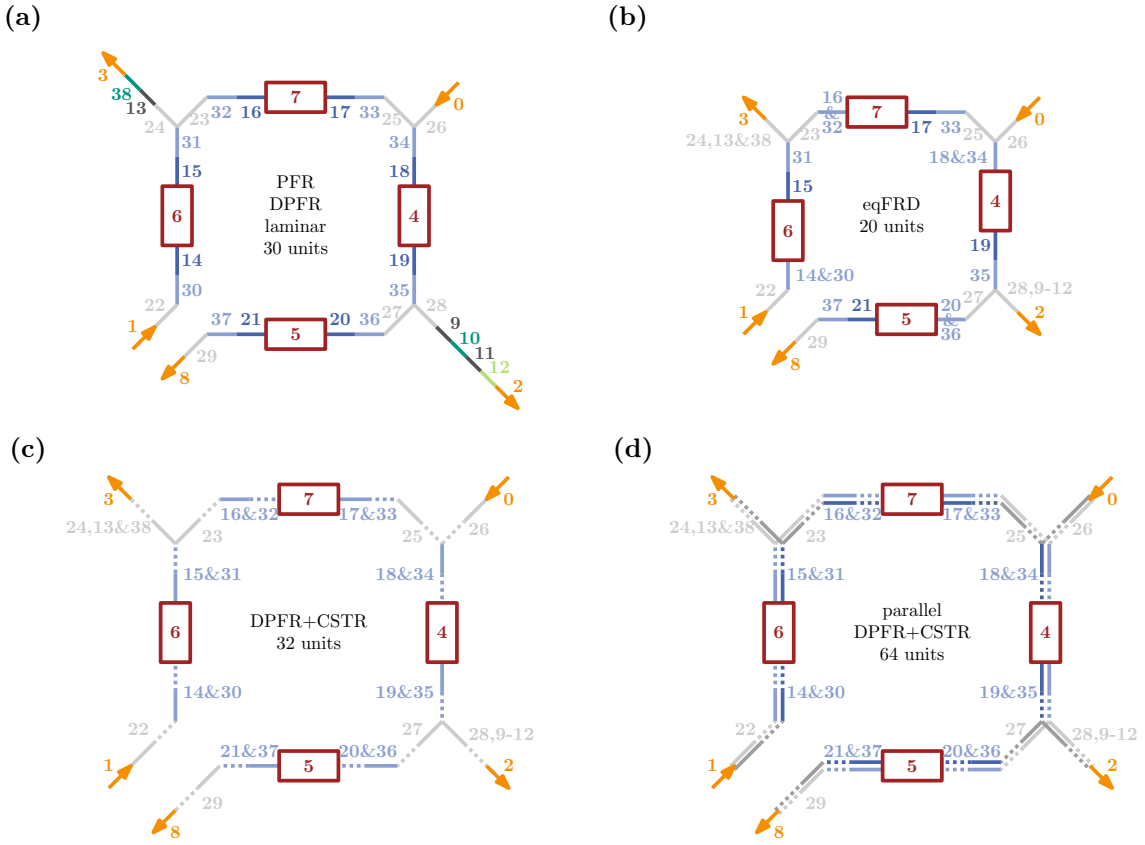

Figure D.18: Overview of required units for modeling the µSMB setup in CADET with different approaches. The red rectangles refer to column models (general rate model), the orange arrows to in- and outlets, the dotted lines to CSTRs and the solid lines either to 2D general rate model units (laminar and eqFRD), PFRs or DPFRs (DPFR, DPFR+CSTR, and parallel DPFR+CSTR). (a): laminar approach; (b): eqFRD approach; (c): DPFR+CSTR approach; (d): parallel DPFR+CSTR approach.

Table D.5 provides an overview of the mesh settings for CFD simulations of the capillaries and the valve's channels. Element sizes were larger for the channels due to their higher diameter. Capillaries were scaled in z-direction in order to reduce computational time.

Table D.5: CFD mesh configurations for different structures.

Setting	Capillary	Valve
Size 1		
Maximum element size	1.56e-5 m	6.20e-5 m
Minimum element size	2.22e-7 m	6.71e-6 m
Maximum element growth rate	1.1	1.1
Curvature factor	0.25	0.4
Resolution of narrow regions	1	0.9
Size 2 (Boundaries)		
Maximum element size	1.95e-5 m	8.89e-5 m
Minimum element size	5.56e-7 m	1.68e-5 m
Maximum element growth rate	1.13	1.13
Curvature factor	0.3	0.5
Resolution of narrow regions	1	0.8
Corner Refinement		
Minimum angle between boundaries	240°	240°
Element size scaling factor	0.25	0.35
Free Triangular/ Tatrahedral		
x-direction scale	1	1
y-direction scale	1	1
z-direction scale	0.05	1
Boundary Layer Properties		
Number of Layers	2	2
Stretching factor	1.2	1.2
Thickness adjusting factor	5	5

Table D.6 provides the shape of the injection profile at different flow rates. To increase the numerical stability, the profile is not a perfect rectangular pulse, instead concentrations were changed over 0.2 s.

Table D.6: Overview of injection profiles for pulse injections at different flow rates.

Flow rate	$t_1(c_{in} = 0)$	$t_2(c_{in} = 0)$	$t_3(c_{in} = c_{max})$	$t_4(c_{in} = c_{max})$	$t_5(c_{in} = 0)$
1 µL/min	0 s	0.15 s	0.25 s	69.95 s	70.05 s
10 µL/min	0 s	0.15 s	0.25 s	6.95 s	7.05 s
100 µL/min	0 s	0.15 s	0.25 s	0.65 s	0.75 s
1000 µL/min	0 s	0.15 s	0.25 s	0.65 s	0.75 s

D.2 Results

D.2.1 Straight capillary

Figure D.19 gives an overview of breakthrough curves and pulse injections of BSA in a straight capillary at different flow rates with various model approaches.

Figure D.20 shows the dependency of the outlet profile on the number of radial cells at a flow rate of 100 µL/min for BSA and AS with the laminar approach.

Figure D.21 gives the results corresponding to Figure D.19 for AS instead of BSA.

Figure D.22a gives an overview of breakthrough curves simulated with CFD for BSA and AS at different flow rates.

Figure D.22b compares the applicability of fitted model approaches for flow rates differing from the calibration flow rate. Depicted are the resulting outlet profiles for AS at a flow rate of 100 µL/min.

Figure D.22c compares the deviations of different model approaches from the CFD model at varying flow rates for breakthrough curves and pulse injections for AS.

D.2.2 Curved channel

Figure D.23 gives an overview of breakthrough curves and pulse injections of BSA in a curved channel at different flow rates with various model approaches. Figure D.24 depicts the corresponding results for AS.

Figure D.25a gives an overview of pulse injection curves simulated with CFD for BSA and AS at different flow rates.

Figure D.25b compares the applicability of fitted model approaches for flow rates differing from the calibration flow rate. Depicted are the resulting outlet profiles for AS at a flow rate of 100 µL/min.

Figure D.25c compares the deviations of different model approaches from the CFD model at varying flow rates for breakthrough curves and pulse injections for AS.

Figure D.26 shows the dependency of the number of radial cells on the outlet profile at a flow rate of 100 µL/min for BSA and AS with the eqFRD approach and Figure D.27 with the laminar approach.

D.2.3 ECV segments

Figure D.28 provides the outlet profiles of the different ECV segments for BSA and AS.

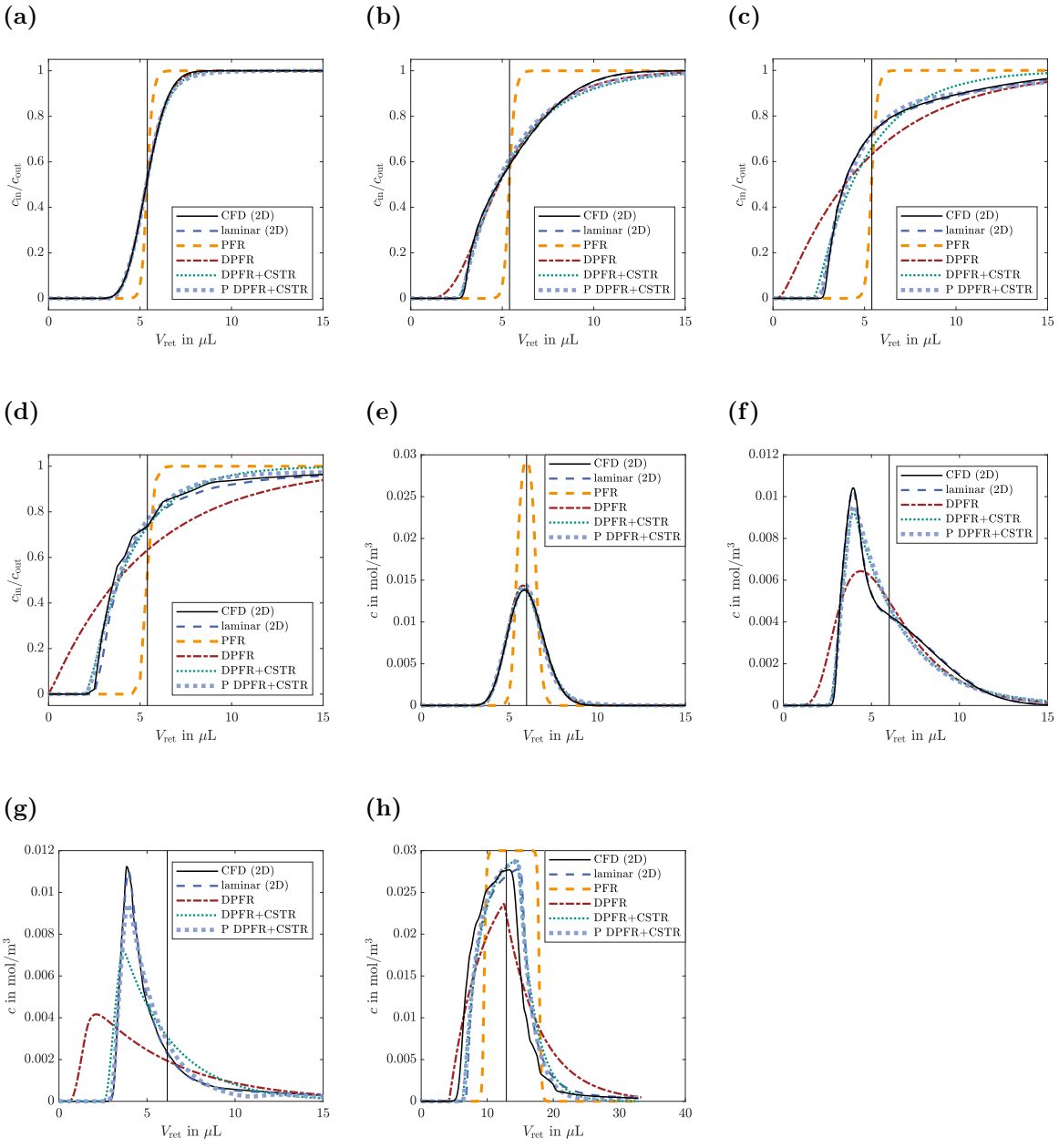

Figure D.19: Overview of breakthrough (BT) curves and pulse injections for BSA with various modeling approaches at different flow rates for a straight capillary. The vertical black lines represent the volume of the capillary. (a): BT, 1 µL/min; (b): BT, 10 µL/min; (c): BT, 100 µL/min; (d): BT, 1000 µL/min; (e): pulse, 1 µL/min; (f): pulse, 10 µL/min; (g): pulse, 100 µL/min; (h): pulse, 1000 µL/min

(a) **(b)**

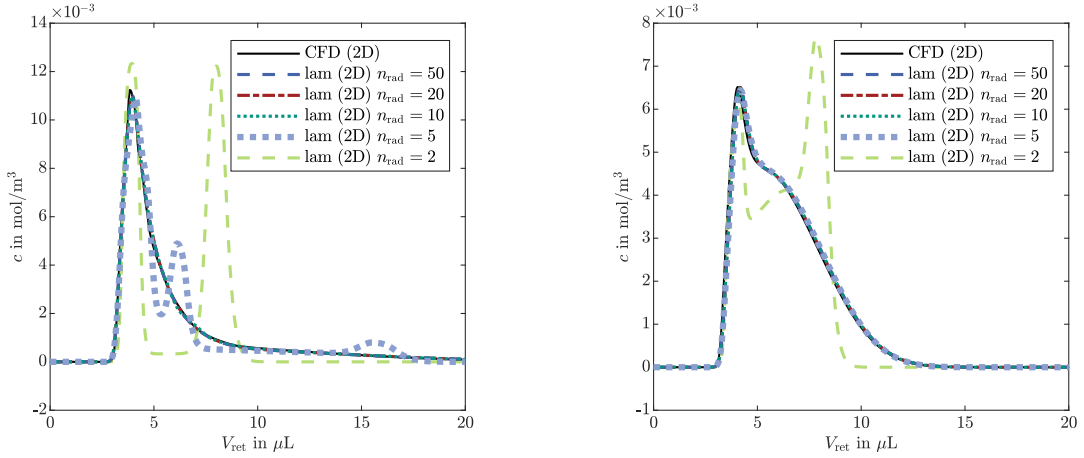

Figure D.20: Influence of the number of radial cells n_{rad} on the outlet profile at a flow rate of 100 µL/min for BSA (a) and AS (b) with the laminar approach.

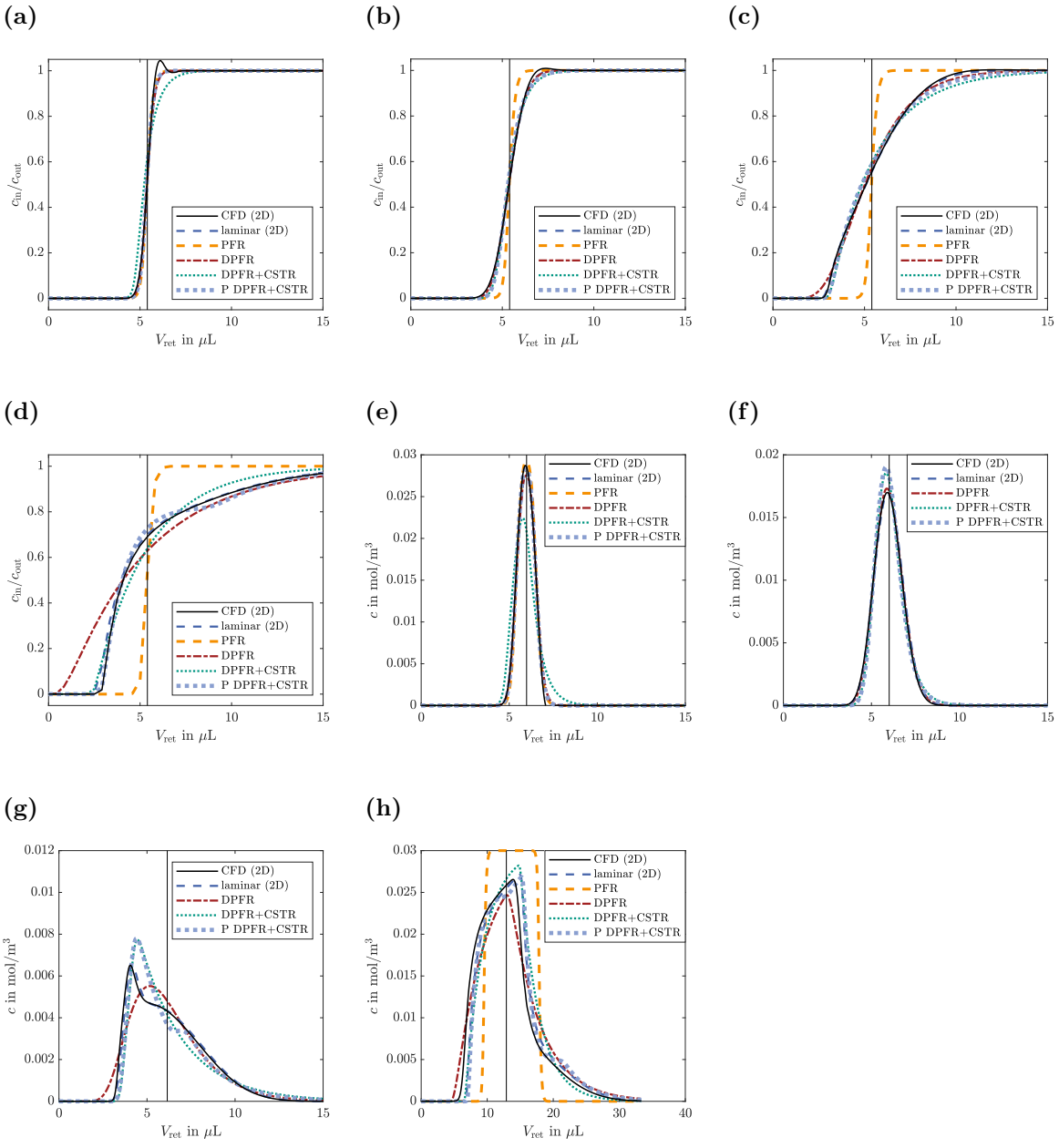

Figure D.21: Overview of breakthrough (BT) curves and pulse injections for AS with various modeling approaches at different flow rates for a straight capillary. The vertical black lines represent the volume of the capillary. (a): BT, 1 µL/min; (b): BT, 10 µL/min; (c): BT, 100 µL/min; (d): BT, 1000 µL/min; (e): pulse, 1 µL/min; (f): pulse, 10 µL/min; (g): pulse, 100 µL/min; (h): pulse, 1000 µL/min

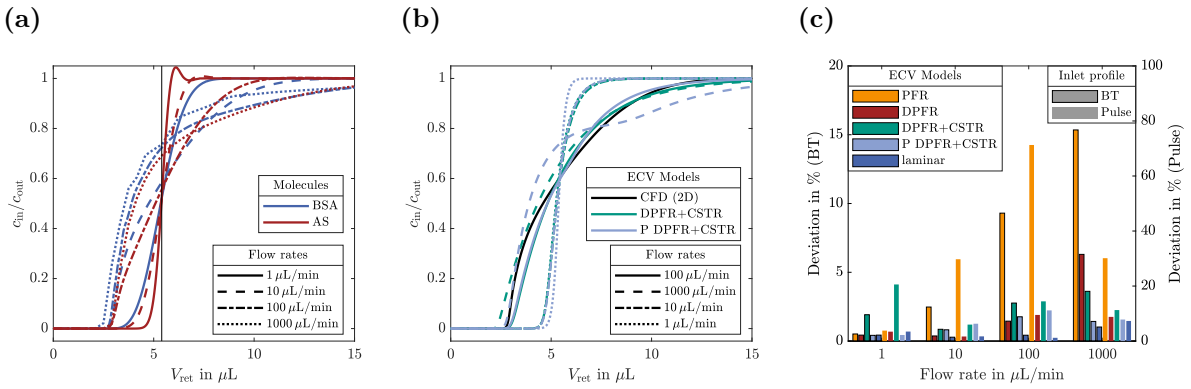

Figure D.22: (a): Overview of breakthrough curves modeled with CFD for BSA and AS at varying flow rates for a straight capillary; (b): Application of fitted model approaches for flow rates differing from the calibration flow rate. Depicted are the resulting outlet profiles for AS at a flow rate of 100 µL/min; (c): deviations of different model approaches from the CFD model at varying flow rates for breakthrough curves and pulse injections for AS. Deviations were normalized with the overall peak area of the CFD outlet profile for better comparability.

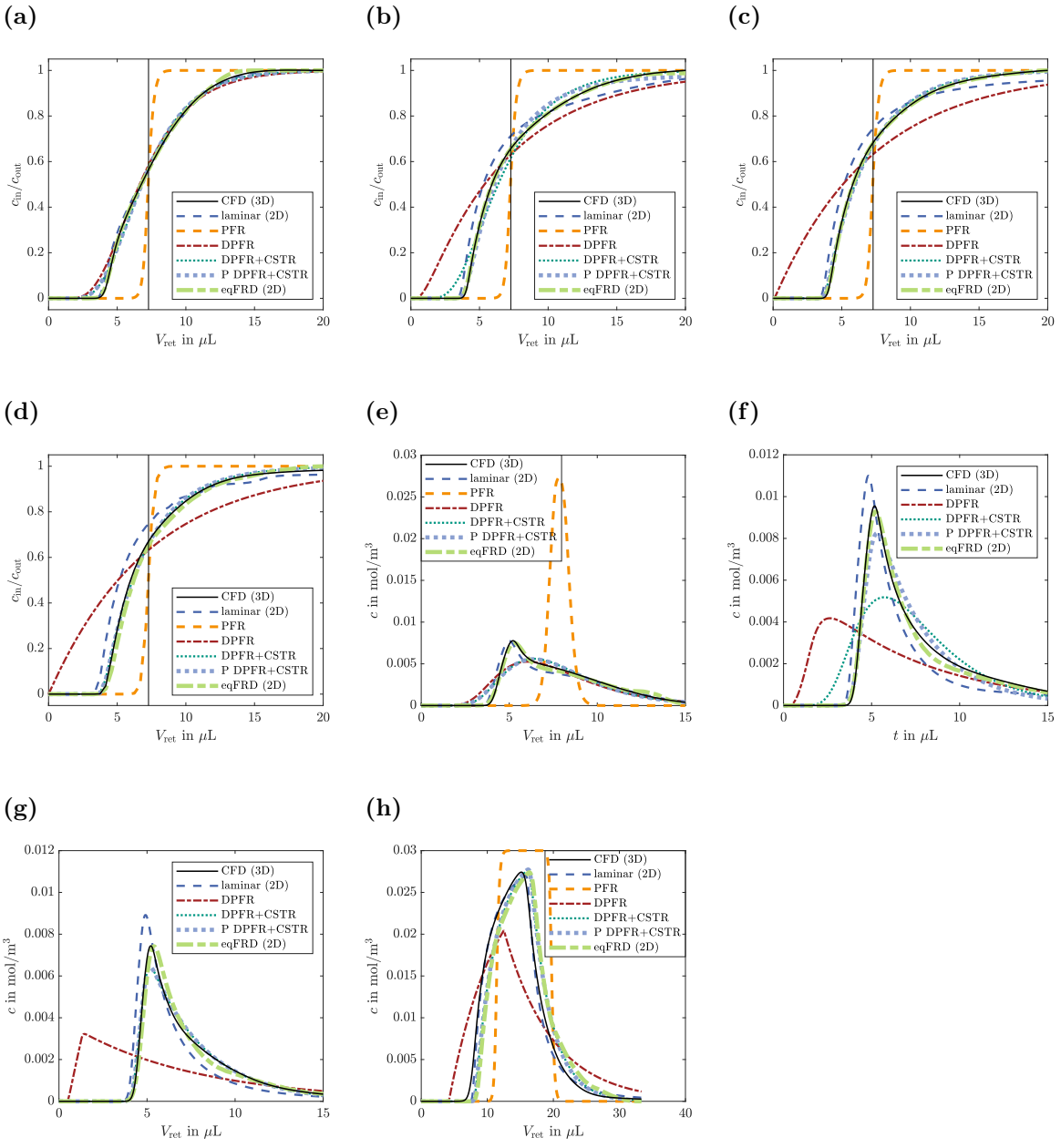

Figure D.23: Overview of breakthrough (BT) curves and pulse injections for BSA with various modeling approaches at different flow rates for a curved channel. The vertical black lines represent the volume of the capillary. (a): BT, 1 µL/min; (b): BT, 10 µL/min; (c): BT, 100 µL/min; (d): BT, 1000 µL/min; (e): pulse, 1 µL/min; (f): pulse, 10 µL/min; (g): pulse, 100 µL/min; (h): pulse, 1000 µL/min

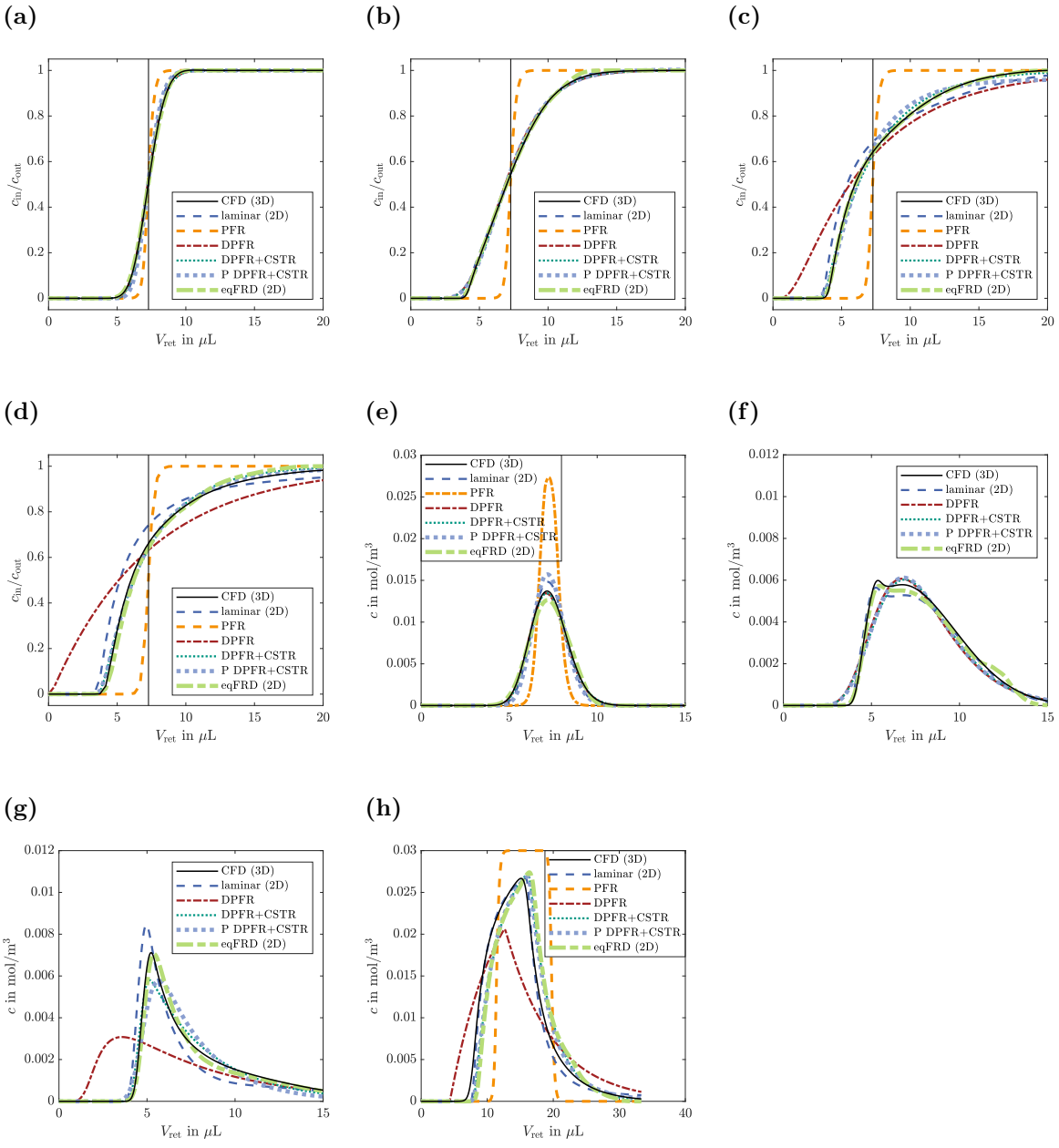

Figure D.24: Overview of breakthrough (BT) curves and pulse injections for AS with various modeling approaches at different flow rates for a curved channel. The vertical black lines represent the volume of the capillary. (a): BT, 1 µL/min; (b): BT, 10 µL/min; (c): BT, 100 µL/min; (d): BT, 1000 µL/min; (e): pulse, 1 µL/min; (f): pulse, 10 µL/min; (g): pulse, 100 µL/min; (h): pulse, 1000 µL/min

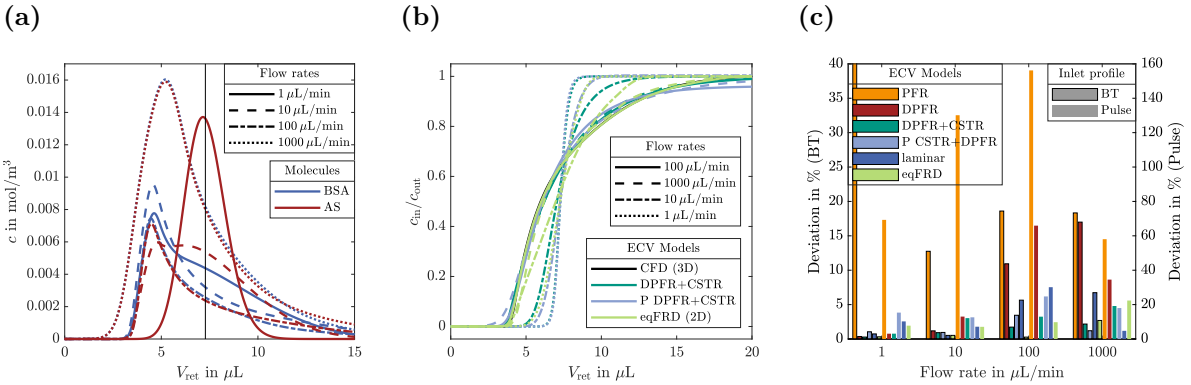

Figure D.25: (a): Overview of pulse injections modeled with CFD for BSA and AS at varying flow rates for a curved channel; (b): Application of fitted model approaches for flow rates differing from the calibration flow rate. Depicted are the resulting outlet profiles for AS at a flow rate of 100 µL/min; (c): deviations of different model approaches from the CFD model at varying flow rates for breakthrough curves and pulse injections for AS. Deviations were normalized with the overall peak area of the CFD outlet profile for better comparability.

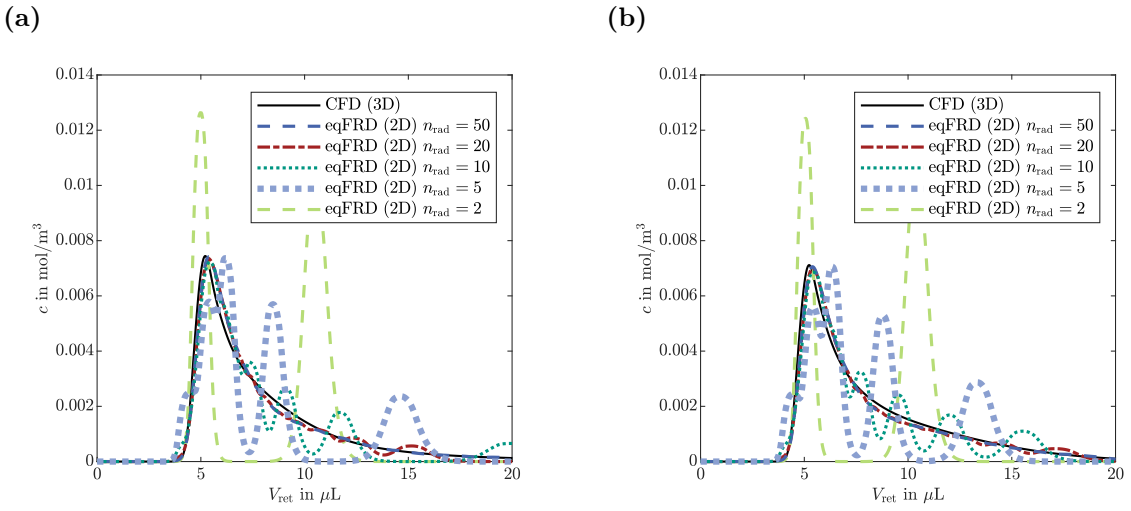

Figure D.26: Influence of the number of radial cells n_{rad} on the outlet profile at a flow rate of 100 µL/min for BSA (a) and AS (b) with the eqFRD approach for a curved channel.

(a) **(b)**

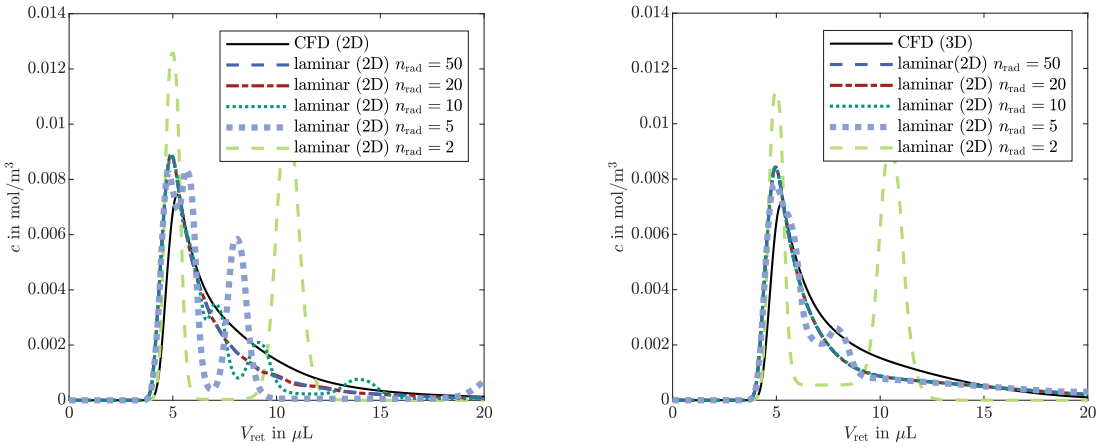

Figure D.27: Influence of the number of radial cells n_{rad} on the outlet profile at a flow rate of 100 µL/min for BSA (a) and AS (b) with the lamianr approach for a curved channel.

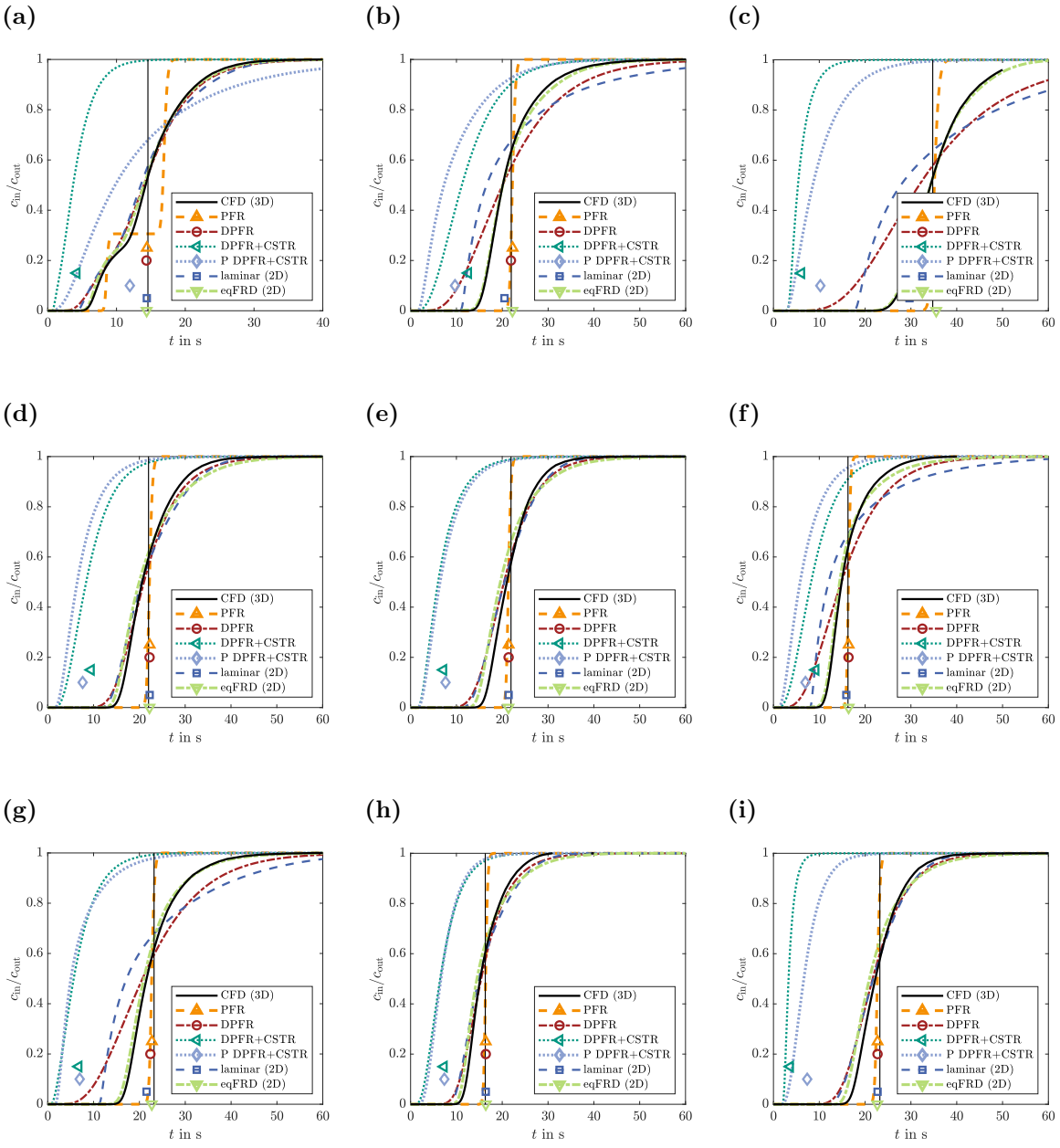

Figure D.28: ECV simulations of the segments of the µSMB system with different model approaches. Simulations were performed with the respective flow rates of the µSMB process. The vertical black line represents the expected retention time and the respective markers the first moment derived from the simulated results. (a): ECV segment between zones two and three (feed-node) for AS; (b): column-outlet of the ECV segment between zones three and four (raffinate-node) for BSA; (c): sensor-outlet of the ECV segment between zones three and four (raffinate-node) for BSA; (d): column-outlet of the ECV segment between zones three and four (raffinate-node) for AS; (e): sensor-outlet of the ECV segment between zones one and two (extract-node) for AS; (f): column-outlet of the ECV segment between zones one and two (extract-node) for BSA; (g): sensor-outlet of the ECV segment between zones zones one and two (extract-node) for BSA; (h): column-outlet of the ECV segment between zones zones one and two (extract-node) for AS; (i): sensor-outlet of the ECV segment between zones zones one and two (extract-node) for AS.

E Integration of Capillary Chromatography Columns into a 3D Printed Microfluidic Multiport Valve for Miniaturized Multi-Column Chromatography

Tables E.7-E.9 list the calibration curves and regression coefficients (R^2) for lysozyme and hemoglobin in dependence of the pH value for different wavelengths. The calibration curves are in the format

$$c_i(\text{g/L}) = a_i^{wv} \cdot absorption(\text{mAU}) + b_i^{wv} \tag{9.1}$$

where the coefficients a_i^{wv} and b_i^{wv} are in dependence of the respective protein and wavelength wv.

Table E.7: Calibration curves with regression coefficients of lysozyme at a wavelength of 280 nm for different pH values.

pH value	a_{lys}^{280}	b_{lys}^{280}	R^2
6.4	0.9377	0.0077	0.9998
7.4	1.0137	0.0062	0.9997
8.2	1.0370	0.0080	0.9985

Table E.8: Calibration curves with regression coefficients of hemoglobin at a wavelength of 280 nm for different pH values.

pH value	a_{heme}^{280}	b_{heme}^{280}	R^2
6.4	1.1078	0.0058	0.9999
7.4	1.1390	-0.0106	0.9989
8.2	1.2078	-0.0048	0.9891

Table E.9: Calibration curves with regression coefficients of hemoglobin at a wavelength of 405 nm for different pH values.

pH value	a_{heme}^{405}	b_{heme}^{405}	R^2
6.4	0.3310	0.0019	0.9999
7.4	0.3615	-0.0008	0.9999
8.2	0.3716	-0.0005	0.9989

Figures E.29-E.33 present the technical drawings of the integrated valve system. Specifically, Figure E.29 illustrates the stator designed for the SMB setup, while Figure E.30 shows the stator variant used in CMCC applications. The remaining components are universally applicable across different processes. A comparison of these drawings with those of the original SMB valve system (Figures A.4-A.6) highlights a significant reduction in the system's overall footprint achieved through the integrated design approach.

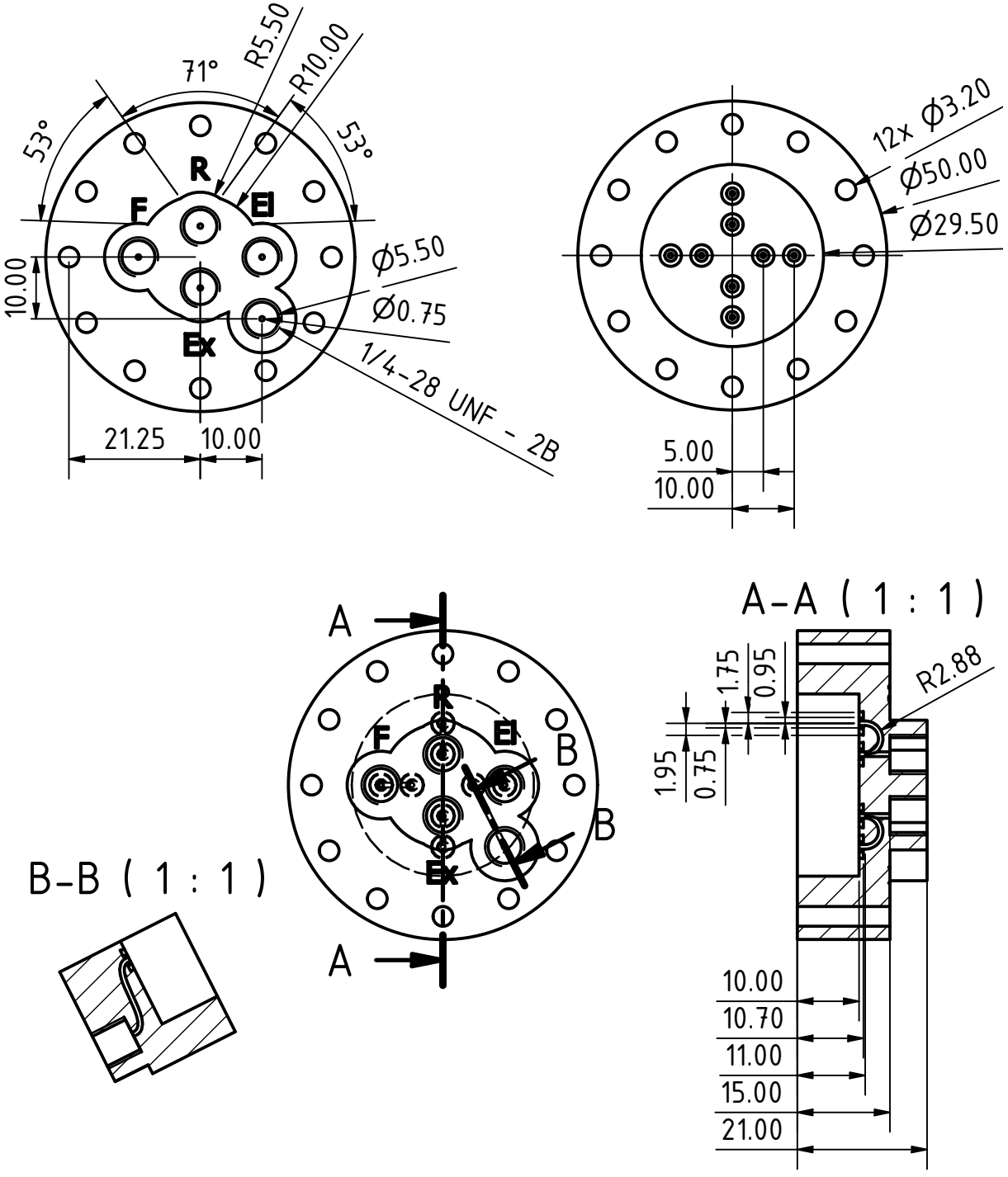

Figure E.29: Technical drawing of the stator of the integrated SMB system: top view (top left), bottom view (top right), and section view (bottom) with scale 1:1. All threads were cut after printing, all dimensions in mm.

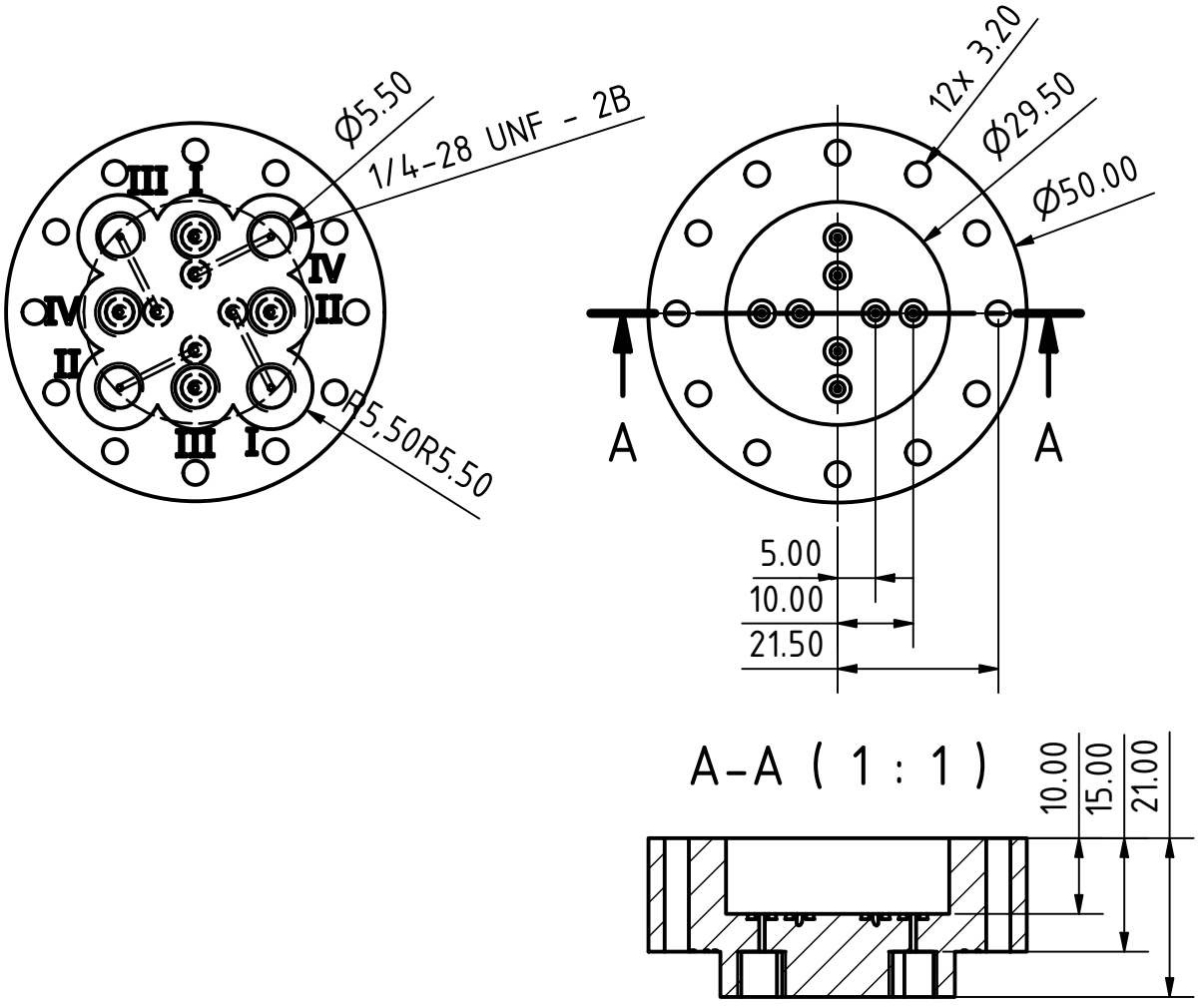

Figure E.30: Technical drawing of the stator of the integrated CMCC system: top view (top left), bottom view (top right), and section view (bottom) with scale 1:1. All threads were cut after printing, all dimensions in mm.

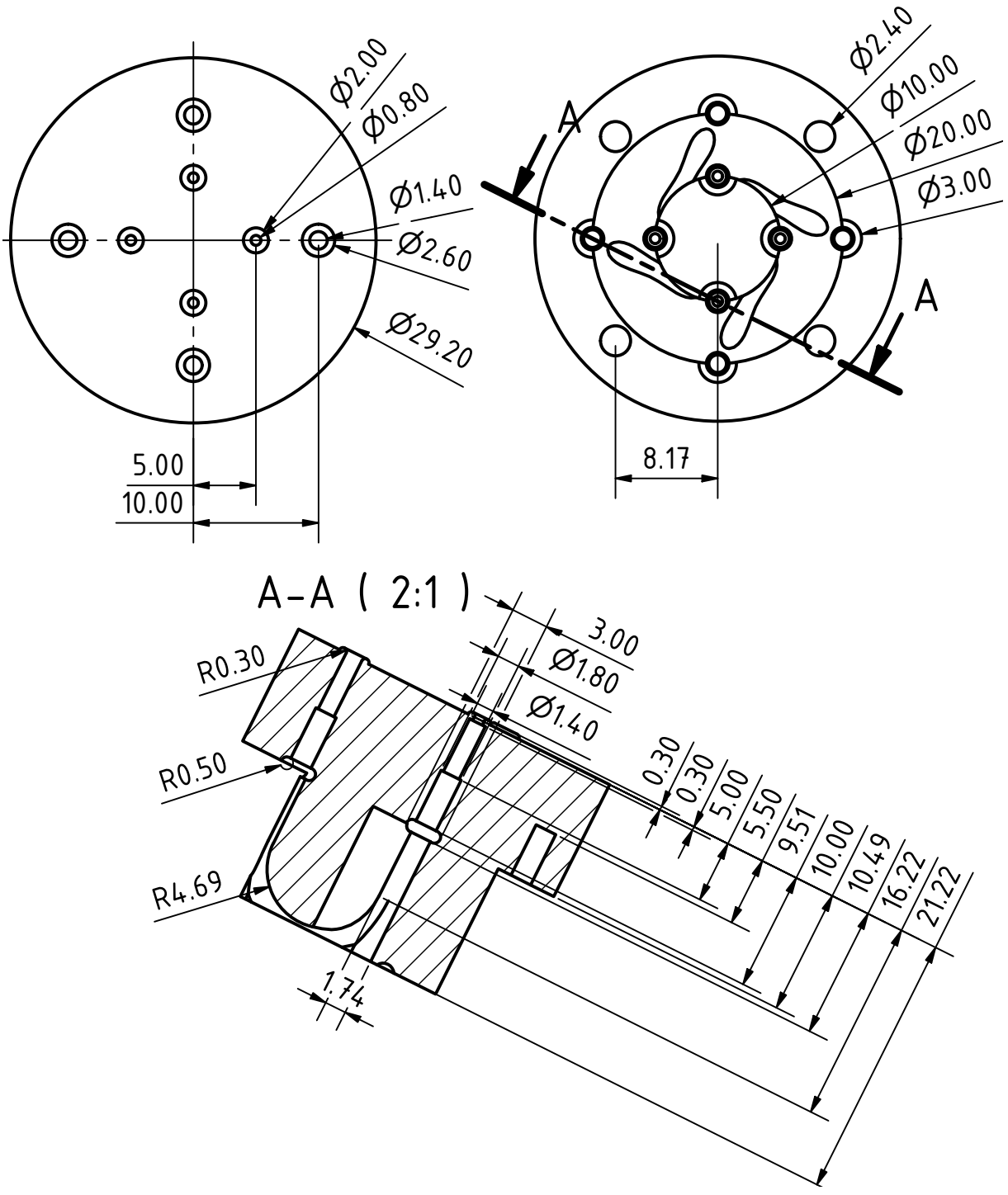

Figure E.31: Technical drawing of the rotor (part 1) of the integrated valve system: bottom view (top left), top view (top right), and section view (bottom) with scale 2:1. All dimensions in mm.

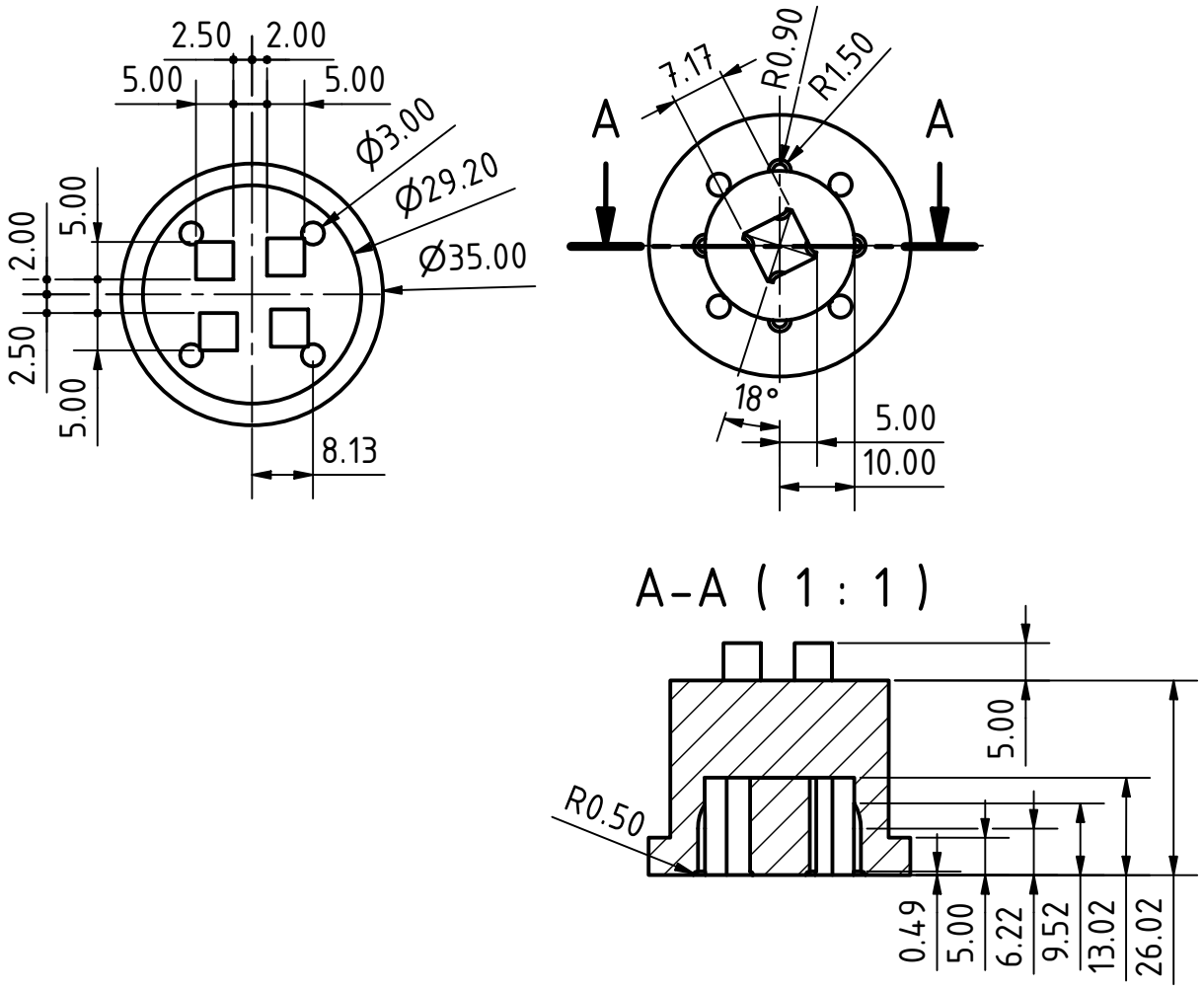

Figure E.32: Technical drawing of the rotor (part 2) of the integrated valve system: top view (top left), bottom view (top right), and section view (bottom) with scale 1:1. All dimensions in mm.

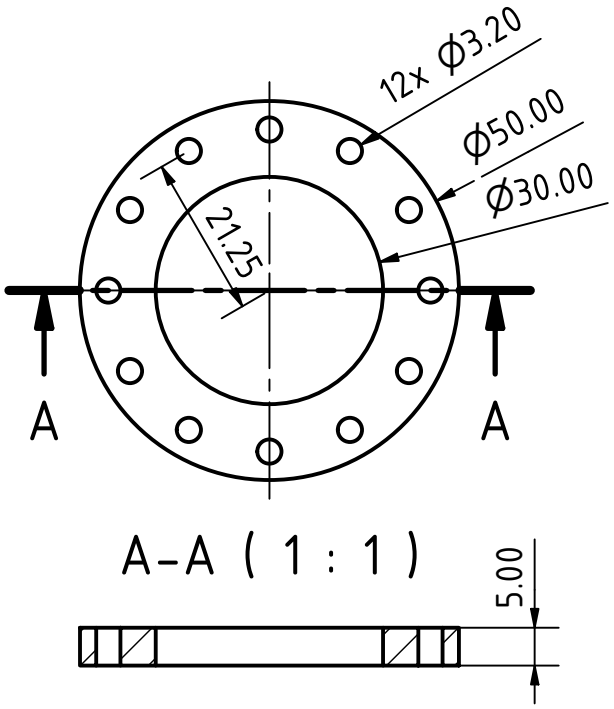

Figure E.33: Technical drawing of the cover of the integrated valve system: top view (top) and section view (bottom) with scale 1:1. All dimensions in mm.

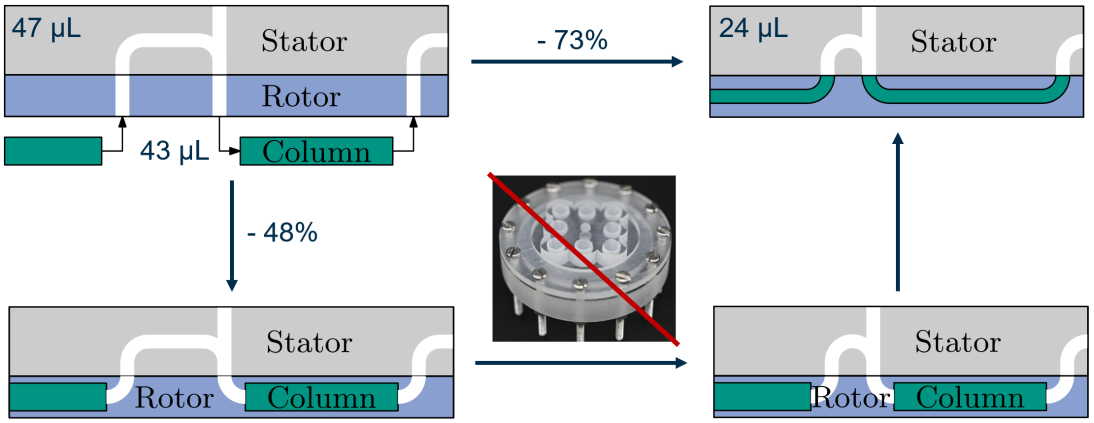

Figure E.34: Comparison of the ECV of different µSMB setups: top-left – central valve system with externally connected chromatography columns; bottom-left – central valve system with integrated chromatography columns; bottom-right – central valve system with integrated chromatography columns and reduced stator-channel volume; top-right – central valve system featuring integrated chromatography columns with adapted column geometry.

Figure E.34 shows the difference in extra-column volume (ECV) for various µSMB implementations. In the µSMB setup with a central valve and external chromatography columns (top-left), the relevant ECV is almost equally distributed between the channels in the valve system (47 µL) and the capillaries connecting the chromatography columns to the valve system (43 µL). Thus, the ECV can be reduced by 48% by integrating the columns directly into the central valve system (bottom-left). Furthermore, the absence of the need for external fluidic connectors for the chromatography columns allows for a reduction in channel volume within the stator (bottom-right). Finally, the ECV in the valve's rotor can be completely eliminated by using curved instead of cylindrical chromatography columns (top-right), resulting in a 73% reduction in ECV compared to a µSMB setup with external columns.

References

[1] I. S. Johnson, Human Insulin from Recombinant DNA Technology, Science 219 (4585) (1983) 632–637. doi:10.1126/science.6337396.

[2] G. Walsh, E. Walsh, Biopharmaceutical benchmarks 2022, Nature Biotechnology 40 (12) (2022) 1722–1760. doi:10.1038/s41587-022-01582-x.

[3] P. Verdin, Top companies and drugs by sales in 2023, Nature Reviews Drug Discovery 23 (4) (2024) 240–240. doi:10.1038/d41573-024-00041-3.

[4] W. R. Strohl, D. M. Knight, Discovery and development of biopharmaceuticals: current issues, Current Opinion in Biotechnology 20 (6) (2009) 668–672. doi:10.1016/j.copbio.2009.10.012.

[5] A. W. Wilson, P. J. Neumann, The cost-effectiveness of biopharmaceuticals: A look at the evidence, mAbs 4 (2) (2012) 281–288. doi:10.4161/mabs.4.2.18812.

[6] A. S. Rathore, F. Shereef, The influence of domestic manufacturing capabilities on biologic pricing in emerging economies, Nature Biotechnology 37 (5) (2019) 498–501. doi:10.1038/s41587-019-0116-0.

[7] A. S. Rathore, D. Sarin, What should next-generation analytical platforms for biopharmaceutical production look like?, Trends in Biotechnology 42 (3) (2024) 282–292. doi:10.1016/j.tibtech.2023.08.008.

[8] J. Erickson, J. Baker, S. Barrett, C. Brady, M. Brower, R. Carbonell, T. Charlebois, J. Coffman, L. Connell-Crowley, M. Coolbaugh, E. Fallon, E. Garr, C. Gillespie, R. Hart, A. Haug, G. Nyberg, M. Phillips, D. Pollard, M. Qadan, I. Ramos, K. Rogers, G. Schaefer, J. Walther, K. Lee, End-to-end collaboration to transform biopharmaceutical development and manufacturing, Biotechnology and Bioengineering 118 (9) (2021) 3302–3312. doi:10.1002/bit.27688.

[9] S. S. Farid, Process Economic Drivers in Industrial Monoclonal Antibody Manufacture, in: Process Scale Purification of Antibodies, John Wiley & Sons, Ltd, 2017, pp. 445–466. doi:10.1002/9781119126942.ch21.

[10] L. Gerstweiler, J. Bi, A. P. Middelberg, Continuous downstream bioprocessing for intensified manufacture of biopharmaceuticals and antibodies, Chemical Engineering Science 231 (2020) 116272. doi:10.1016/j.ces.2020.116272.

[11] A. Jungbauer, P. Satzer, A. Duerauer, A. Azevedo, R. Aires-Barros, B. Nilsson, S. Farid, S. Goldrick, M. Ottens, M. Sponchioni, H. Marcelo Fernandez Lahore, Continuous downstream processing, Separation and Purification Technology 338 (2024) 126439. doi:10.1016/j.seppur.2024.126439.

[12] J. K. Lorek, M. Isaksson, B. Nilsson, Chromatography in Downstream Processing of Recombinant Adeno-Associated Viruses: A Review of Current and Future Practises, Biotechnology and Bioengineering (2025)doi:10.1002/bit.28932.

[13] A. S. Rathore, G. Thakur, N. Kateja, Continuous integrated manufacturing for biopharmaceuticals: A new paradigm or an empty promise?, Biotechnology and Bioengineering 120 (2) (2023) 333–351. doi:10.1002/bit.28235.

[14] M. S. P. Silva, A. E. Rodrigues, J. P. B. Mota, Modeling and simulation of an industrial-scale parex process, AIChE Journal 61 (4) (2015) 1345–1363. doi:10.1002/aic.14732.

[15] D. C. S. Azevedo, A. E. Rodrigues, Fructose–glucose separation in a SMB pilot unit: Modeling, simulation, design, and operation, AIChE Journal 47 (9) (2001) 2042–2051. doi:10.1002/aic.690470915.

[16] M. Kornecki, A. Schmidt, L. Lohmann, M. Huter, F. Mestmäcker, L. Klepzig, M. Mouellef, S. Zobel-Roos, J. Strube, Accelerating Biomanufacturing by Modeling of Continuous Bioprocessing—Piloting Case Study of Monoclonal Antibody Manufacturing, Processes 7 (8) (2019) 495. doi:10.3390/pr7080495.

[17] N. Andersson, J. G. Fons, M. Isaksson, S. Tallvod, D. Espinoza, L. Sjökvist, G. Z. Andersson, B. Nilsson, Methodology for fast development of digital solutions in integrated continuous downstream processing, Biotechnology and Bioengineering 121 (8) (2024) 2378–2387. doi:10.1002/bit.28501.

[18] D. P. Wasalathanthri, R. Shah, J. Ding, A. Leone, Z. J. Li, Process analytics 4.0: A paradigm shift in rapid analytics for biologics development, Biotechnology Progress 37 (4) (2021) e3177. doi:10.1002/btpr.3177.

[19] A. S. Rathore, D. Sarin, S. Bhattacharya, S. Kumar, Multi-attribute monitoring applications in biopharmaceutical analysis, Journal of Chromatography Open 6 (2024) 100166. doi:10.1016/j.jcoa.2024.100166.

[20] N. Bhattacharjee, A. Urrios, S. Kang, A. Folch, The upcoming 3D-printing revolution in microfluidics, Lab on a Chip 16 (10) (2016) 1720–1742. doi:10.1039/C6LC00163G.

[21] A. J. Capel, R. P. Rimington, M. P. Lewis, S. D. R. Christie, 3D printing for chemical, pharmaceutical and biological applications, Nature Reviews Chemistry 2 (12) (2018) 422–436. doi:10.1038/s41570-018-0058-y.

[22] F. Kotz, P. Risch, D. Helmer, B. Rapp, Highly Fluorinated Methacrylates for Optical 3D Printing of Microfluidic Devices, Micromachines 9 (3) (2018) 115. doi:10.3390/mi9030115.

[23] F. Kotz, D. Helmer, B. E. Rapp, Emerging Technologies and Materials for High-Resolution 3D Printing of Microfluidic Chips, in: Advances in Biochemical Engineering/Biotechnology,

Advances in Biochemical Engineering/Biotechnology, Springer, Berlin, Heidelberg, 2020, pp. 1–30. doi:10.1007/10_2020_141.

[24] H. Schmidt-Traub, M. Schulte, A. Seidel-Morgenstern, Preparative Chromatography, 2nd Edition, John Wiley & Sons, Ltd, 2012. doi:10.1002/9783527649280.

[25] L. Gerstweiler, J. Bi, A. P. Middelberg, Continuous downstream bioprocessing for intensified manufacture of biopharmaceuticals and antibodies, Chemical Engineering Science 231 (2021) 116272. doi:10.1016/j.ces.2020.116272.

[26] A. A. Shukla, B. Hubbard, T. Tressel, S. Guhan, D. Low, Downstream processing of monoclonal antibodies—Application of platform approaches, Journal of Chromatography B 848 (1) (2007) 28–39. doi:10.1016/j.jchromb.2006.09.026.

[27] T. Vicente, A. Roldão, C. Peixoto, M. J. T. Carrondo, P. M. Alves, Large-scale production and purification of VLP-based vaccines, Journal of Invertebrate Pathology 107 (2011) S42–S48. doi:10.1016/j.jip.2011.05.004.

[28] K. Kobl, L. Nicoud, E. Nicoud, A. Watson, J. Andrews, E. A. Wilkinson, M. Shahid, C. McKay, B. I. Andrews, B. A. Omer, O. Narducci, E. Masson, S. H. Davies, T. Vandermeersch, Oligonucleotide Purification by Ion Exchange Chromatography: A Step-by-Step Guide to Process Understanding, Modeling, and Simulation, Organic Process Research & Development 28 (7) (2024) 2569–2589. doi:10.1021/acs.oprd.4c00013.

[29] F. Steinebach, T. Müller-Späth, M. Morbidelli, Continuous counter-current chromatography for capture and polishing steps in biopharmaceutical production, Biotechnology Journal 11 (9) (2016) 1126–1141. doi:10.1002/biot.201500354.

[30] G. H. Lathe, C. R. J. Ruthven, The separation of substances and estimation of their relative molecular sizes by the use of columns of starch in water, Biochemical Journal 62 (4) (1956) 665–674.

[31] A. M. Striegel, Size-Exclusion Chromatography: A Twenty-First Century Perspective, Chromatographia 85 (4) (2022) 307–313. doi:10.1007/s10337-022-04143-1.

[32] S. Hussain, M. S. Mehta, J. I. Kaplan, P. L. Dubin, Experimental evaluation of conflicting models for size exclusion chromatography, Analytical Chemistry 63 (11) (1991) 1132–1138. doi:10.1021/ac00011a014.

[33] S. H. Saneii, H. Doosti, Normal Distribution, in: S. H. Saneii, H. Doosti (Eds.), Practical Biostatistics for Medical and Health Sciences, Springer Nature, Singapore, 2024, pp. 115–137. doi:10.1007/978-981-97-3083-4_6.

[34] G. Guiochon, D. G. Shirazi, A. Felinger, A. M. Katti, Fundamentals of preparative and nonlinear chromatography, 2nd Edition, Academic Press, Boston, 2006.

[35] C. Documentary, Binding models — CADET (Feb. 2022).
URL https://cadet.github.io/master/modelling/binding/index.html

[36] C. A. Brooks, S. M. Cramer, Steric mass-action ion exchange: Displacement profiles and induced salt gradients, AIChE Journal 38 (12) (1992) 1969–1978. doi:10.1002/aic.690381212.

[37] G. Guiochon, The limits of the separation power of unidimensional column liquid chromatography, Journal of Chromatography A 1126 (1) (2006) 6–49. doi:10.1016/j.chroma.2006.07.032.

[38] J. J. van Deemter, F. J. Zuiderweg, A. Klinkenberg, Longitudinal diffusion and resistance to mass transfer as causes of nonideality in chromatography, Chemical Engineering Science 5 (6) (1956) 271–289. doi:10.1016/0009-2509(56)80003-1.

[39] M. Juza, M. Mazzotti, M. Morbidelli, Simulated moving-bed chromatography and its application to chirotechnology, Trends in Biotechnology 18 (3) (2000) 108–118. doi:10.1016/S0167-7799(99)01419-5.

[40] A. Seidel-Morgenstern, L. C. Keßler, M. Kaspereit, New Developments in Simulated Moving Bed Chromatography, Chemical Engineering & Technology 31 (6) (2008) 826–837. doi:10.1002/ceat.200800081.

[41] D. B. Broughton, Production-Scale Adsorptive Separations of Liquid Mixtures by Simulated Moving-Bed Technology, Separation Science and Technology 19 (11-12) (1984) 723–736. doi:10.1080/01496398408068590.

[42] M. Schulte, J. Strube, Preparative enantioseparation by simulated moving bed chromatography, Journal of Chromatography A 906 (1-2) (2001) 399–416. doi:10.1016/S0021-9673(00)00956-0.

[43] R. P. Faria, A. E. Rodrigues, Instrumental aspects of Simulated Moving Bed chromatography, Journal of Chromatography A 1421 (2015) 82–102. doi:10.1016/j.chroma.2015.08.045.

[44] C. Migliorini, M. Mazzotti, M. Morbidelli, Simulated moving-bed units with extra-column dead volume, AIChE Journal 45 (7) (1999) 1411–1421. doi:10.1002/aic.690450706.

[45] A. Rajendran, G. Paredes, M. Mazzotti, Simulated moving bed chromatography for the separation of enantiomers, Journal of Chromatography A 1216 (4) (2009) 709–738. doi:10.1016/j.chroma.2008.10.075.

[46] M. Mazzotti, G. Storti, M. Morbidelli, Optimal operation of simulated moving bed units for nonlinear chromatographic separations, J. Chromatogr. A (1997) 22doi:10.1016/S0021-9673(97)00048-4.

[47] C. Migliorini, M. Mazzotti, M. Morbidelli, Continuous chromatographic separation through simulated moving beds under linear and nonlinear conditions, Journal of Chromatography A 827 (2) (1998) 161–173. doi:10.1016/S0021-9673(98)00643-8.

[48] T. Mallmann, B. D. Burris, Z. Ma, N. H. L. Wang, Standing wave design of nonlinear SMB systems for fructose purification, AIChE Journal 44 (12) (1998) 2628–2646. doi:10.1002/aic.690441206.

[49] Y. Kawajiri, Model-based optimization strategies for chromatographic processes: a review, Adsorption 27 (1) (2021) 1–26. doi:10.1007/s10450-020-00251-2.

[50] G. Storti, M. Mazzotti, M. Morbidelli, S. Carrà, Robust design of binary countercurrent adsorption separation processes, AIChE Journal 39 (3) (1993) 471–492. doi:10.1002/aic.690390310.

[51] O. Ludemann-Hombourger, N. R. M., M. Bailly, The "VARICOL" Process: A New Multicolumn Continuous Chromatographic Process, Separation Science and Technology 35 (12) (2000) 1829–1862. doi:10.1081/SS-100100622.

[52] W. Jin, P. C. Wankat, Two-Zone SMB Process for Binary Separation, Industrial & Engineering Chemistry Research 44 (5) (2005) 1565–1575. doi:10.1021/ie040132r.

[53] N. Abunasser, P. C. Wankat, Y.-S. Kim, Y. M. Koo, One-Column Chromatograph with Recycle Analogous to a Four-Zone Simulated Moving Bed, Industrial & Engineering Chemistry Research 42 (21) (2003) 5268–5279. doi:10.1021/ie030283e.

[54] S. Abel, M. U. Bäbler, C. Arpagaus, M. Mazzotti, J. Stadler, Two-fraction and three-fraction continuous simulated moving bed separation of nucleosides, Journal of Chromatography A 1043 (2) (2004) 201–210. doi:10.1016/j.chroma.2004.05.094.

[55] B. J. Hritzko, Y. Xie, R. J. Wooley, N.-H. L. Wang, Standing-wave design of tandem SMB for linear multicomponent systems, AIChE Journal 48 (12) (2002) 2769–2787. doi:10.1002/aic.690481207.

[56] P. C. Wankat, Simulated Moving Bed Cascades for Ternary Separations, Industrial & Engineering Chemistry Research 40 (26) (2001) 6185–6193. doi:10.1021/ie010075r.

[57] H. Schramm, M. Kaspereit, A. Kienle, A. Seidel-Morgenstern, Simulated moving bed process with cyclic modulation of the feed concentration, Journal of Chromatography A 1006 (1) (2003) 77–86. doi:10.1016/S0021-9673(03)00327-3.

[58] Y. Zang, P. C. Wankat, SMB Operation Strategy-Partial Feed, Industrial & Engineering Chemistry Research 41 (10) (2002) 2504–2511. doi:10.1021/ie010832l.

[59] Y.-S. Bae, C.-H. Lee, Partial-discard strategy for obtaining high purity products using simulated moving bed chromatography, Journal of Chromatography A 1122 (1) (2006) 161–173. doi:10.1016/j.chroma.2006.04.040.

[60] P. Li, G. Xiu, A. E. Rodrigues, Proteins separation and purification by salt gradient ion-exchange SMB, AIChE Journal 53 (9) (2007) 2419–2431. doi:10.1002/aic.11259.

[61] L. C. Keßler, L. Gueorguieva, U. Rinas, A. Seidel-Morgenstern, Step gradients in 3-zone simulated moving bed chromatography: Application to the purification of antibodies and bone morphogenetic protein-2, Journal of Chromatography A 1176 (1) (2007) 69–78. doi:10.1016/j.chroma.2007.10.087.

[62] J. Y. Clavier, R. M. Nicoud, M. Perrut, A new efficient fractionation process: The simulated moving bed with supercritical eluent, in: P. R. von Rohr, C. Trepp (Eds.), Process Technology Proceedings, Vol. 12 of High Pressure Chemical Engineering, Elsevier, 1996, pp. 429–434. doi:10.1016/S0921-8610(96)80074-4.

[63] L. Kuger, C.-R. Arlt, M. Franzreb, Magnetic/flow controlled continuous size fractionation of magnetic nanoparticles using simulated moving bed chromatography, Talanta 240 (2022) 123160. doi:10.1016/j.talanta.2021.123160.

[64] J. W. Lee, Double-Layer Simulated Moving Bed Chromatography for Ternary Separations: Serialized Layer Configurations, Industrial & Engineering Chemistry Research 60 (24) (2021) 8911–8926. doi:10.1021/acs.iecr.1c01268.

[65] D. B. Broughton, C. G. Gerhold, Continuous sorption process employing fixed bed of sorbent and moving inlets and outlets, US2985589A (1961).
URL https://patents.google.com/patent/US2985589A/en

[66] M. A. T. Bisschops, J. A. M. Pennings, J. A. Tijsterman, Device for chromatographic separations, US7846335B2 (2010).
URL https://patents.google.com/patent/US7846335B2/en

[67] F. Schmitz, E. Knöchelmann, T. Kruse, M. Minceva, M. Kampmann, Continuous multi-column capture of monoclonal antibodies with convective diffusive membrane adsorbers, Biotechnology and Bioengineering 121 (6) (2024) 1859–1875. doi:10.1002/bit.28695.

[68] N. Nitika, G. Thakur, A. S. Rathore, Continuous manufacturing of monoclonal antibodies: Dynamic control of multiple integrated polishing chromatography steps using BioSMB, Journal of Chromatography A 1690 (2023) 463784. doi:10.1016/j.chroma.2023.463784.

[69] J. Gomis-Fons, N. Andersson, B. Nilsson, Optimization study on periodic counter-current chromatography integrated in a monoclonal antibody downstream process, Journal of Chromatography A 1621 (2020) 461055. doi:10.1016/j.chroma.2020.461055.

[70] M. Angarita, T. Müller-Späth, D. Baur, R. Lievrouw, G. Lissens, M. Morbidelli, Twin-column CaptureSMB: A novel cyclic process for protein A affinity chromatography, Journal of Chromatography A 1389 (2015) 85–95. doi:10.1016/j.chroma.2015.02.046.

[71] L. Aumann, M. Morbidelli, A continuous multicolumn countercurrent solvent gradient purification (MCSGP) process, Biotechnology and Bioengineering 98 (5) (2007) 1043–1055. doi:10.1002/bit.21527.

[72] C. D. Luca, S. Felletti, G. Lievore, A. Buratti, S. Vogg, M. Morbidelli, A. Cavazzini, M. Catani, M. Macis, A. Ricci, W. Cabri, From batch to continuous chromatographic purification of a therapeutic peptide through multicolumn countercurrent solvent gradient purification, Journal of Chromatography A 1625 (2020) 461304. doi:10.1016/j.chroma.2020.461304.

[73] N. Walch, A. Jungbauer, Continuous desalting of refolded protein solution improves capturing in ion exchange chromatography: A seamless process, Biotechnology Journal 12 (6) (2017) 1700082. doi:10.1002/biot.201700082.

[74] B. Napadensky, O. Shinkazh, A. Teella, A. L. Zydney, Continuous Countercurrent Tangential Chromatography for Monoclonal Antibody Purification, Separation Science and Technology 48 (9) (2013) 1289–1297. doi:10.1080/01496395.2013.767837.

[75] L.-M. Herlevi, M. Fernandez-Lahore, G. Ferreira, A fluidized-bed-riser adsorption system for continuous bioproduct recovery from crude feedstock, Biotechnology and Bioengineering 120 (10) (2023) 2969–2976. doi:10.1002/bit.28458.

[76] V. Kumar, S. Leweke, E. von Lieres, A. S. Rathore, Mechanistic modeling of ion-exchange process chromatography of charge variants of monoclonal antibody products, Journal of Chromatography A 1426 (2015) 140–153. doi:10.1016/j.chroma.2015.11.062.

[77] V. Kumar, A. M. Lenhoff, Mechanistic Modeling of Preparative Column Chromatography for Biotherapeutics, Annual Review of Chemical and Biomolecular Engineering 11 (Volume 11, 2020) (2020) 235–255. doi:10.1146/annurev-chembioeng-102419-125430.

[78] H. Narayanan, M. F. Luna, M. von Stosch, M. N. Cruz Bournazou, G. Polotti, M. Morbidelli, A. Butté, M. Sokolov, Bioprocessing in the Digital Age: The Role of Process Models, Biotechnology Journal 15 (1) (2020) 1900172. doi:10.1002/biot.201900172.

[79] M. O. Besenhard, A. Tsatse, L. Mazzei, E. Sorensen, Recent advances in modelling and control of liquid chromatography, Current Opinion in Chemical Engineering 32 (2021) 100685. doi:10.1016/j.coche.2021.100685.

[80] V. S. Joshi, V. Kumar, A. S. Rathore, Optimization of ion exchange sigmoidal gradients using hybrid models: Implementation of quality by design in analytical method development, Journal of Chromatography A 1491 (2017) 145–152. doi:10.1016/j.chroma.2017.02.058.

[81] A. Schmidt, H. Helgers, L. J. Lohmann, F. Vetter, A. Juckers, M. Mouellef, S. Zobel-Roos, J. Strube, Process analytical technology as key-enabler for digital twins in continuous biomanufacturing, Journal of Chemical Technology & Biotechnology 97 (9) (2022) 2336–2346. doi:10.1002/jctb.7008.

[82] Q. He, Advanced System Simulation, Parameter Estimation and Process Design in Preparative Chromatography, Dissertation.

[83] P. V. Danckwerts, Continuous flow systems. Distribution of residence times, Chemical Engineering Science 50 (24) (1953) 3857–3866. doi:10.1016/0009-2509(96)81811-2.

[84] Z. Ma, R. D. Whitley, N.-H. L. Wang, Pore and surface diffusion in multicomponent adsorption and liquid chromatography systems, AIChE Journal 42 (5) (1996) 1244–1262. doi:10.1002/aic.690420507.

[85] S. Katsuo, C. Langel, P. Schanen, M. Mazzotti, Extra-column dead volume in simulated moving bed separations: Theory and experiments, Journal of Chromatography A 1216 (7) (2009) 1084–1093. doi:10.1016/j.chroma.2008.12.031.

[86] V. Kumar, O. Khanal, M. Jin, Modeling the Impact of Holdup Volume from Chromatographic Workstations on Ion-Exchange Chromatography, Industrial & Engineering Chemistry Research 61 (28) (2022) 10195–10204. doi:10.1021/acs.iecr.2c01266.

[87] D. Espinoza, S. Tallvod, N. Andersson, B. Nilsson, Automatic procedure for modelling, calibration, and optimization of a three-component chromatographic separation, Journal of Chromatography A 1720 (2024) 464805. doi:10.1016/j.chroma.2024.464805.

[88] B. Filip, R. Bochenek, K. Baran, D. Strzałka, D. Antos, Influence of the geometry of extra column volumes on band broadening in a chromatographic system. Predictions by computational fluid dynamics, Journal of Chromatography A 1653 (2021) 462410. doi:10.1016/j.chroma.2021.462410.

[89] T. C. Silva, M. Eppink, M. Ottens, Small, smaller, smallest: Miniaturization of chromatographic process development, Journal of Chromatography A 1681 (2022) 463451. doi:10.1016/j.chroma.2022.463451.

[90] L. Shan, B. R. Jones, Nano-LC: An updated review, Biomedical Chromatography 36 (5) (2022) e5317. doi:10.1002/bmc.5317.

[91] A. A. Shukla, S. Rameez, L. S. Wolfe, N. Oien, High-Throughput Process Development for Biopharmaceuticals, in: B. Kiss, U. Gottschalk, M. Pohlscheidt (Eds.), New Bioprocessing Strategies: Development and Manufacturing of Recombinant Antibodies and Proteins, Springer International Publishing, Cham, 2018, pp. 401–441. doi:10.1007/10_2017_20.

[92] M. Bensch, P. Schulze Wierling, E. von Lieres, J. Hubbuch, High Throughput Screening of Chromatographic Phases for Rapid Process Development, Chemical Engineering & Technology 28 (11) (2005) 1274–1284. doi:10.1002/ceat.200500153.

[93] K. M. Łącki, High-throughput process development of chromatography steps: Advantages and limitations of different formats used, Biotechnology Journal 7 (10) (2012) 1192–1202. doi:10.1002/biot.201100475.

[94] S. Nagamatsu, O. Ludemann-Hombourger, J. Filou, Simulated moving bed device, US6544413B1 (2003).
URL https://patents.google.com/patent/US6544413B1/en

[95] C. Kortmann, T. Habib, C. Heuer, D. Solle, J. Bahnemann, A Novel 3D-Printed and Miniaturized Periodic Counter Current Chromatography System for Continuous Purification of Monoclonal Antibodies, Micromachines 15 (3) (2024) 382. doi:10.3390/mi15030382.

[96] Y. Bian, C. Gao, B. Kuster, On the potential of micro-flow LC-MS/MS in proteomics, Expert Review of Proteomics 19 (3) (2022) 153–164. doi:10.1080/14789450.2022.2134780.

[97] F. a. D. Administration, Guidance for Industry PAT - A Framework for Innovative Pharmaceutical Development, manufacturing, and Quality Assurance (2004).
URL https://www.fda.gov/media/71012/download

[98] A. S. Rathore, R. Bhambure, V. Ghare, Process analytical technology (PAT) for biopharmaceutical products, Analytical and Bioanalytical Chemistry 398 (1) (2010) 137–154. doi:10.1007/s00216-010-3781-x.

[99] L. Rolinger, M. Rüdt, J. Hubbuch, A critical review of recent trends, and a future perspective of optical spectroscopy as PAT in biopharmaceutical downstream processing, Analytical and Bioanalytical Chemistry 412 (9) (2020) 2047–2064. doi:10.1007/s00216-020-02407-z.

[100] M. Rüdt, N. Brestrich, L. Rolinger, J. Hubbuch, Real-time monitoring and control of the load phase of a protein A capture step, Biotechnology and Bioengineering 114 (2) (2017) 368–373. doi:10.1002/bit.26078.

[101] M. Pathak, A. S. Rathore, Implementation of a fluorescence based PAT control for fouling of protein A chromatography resin, Journal of Chemical Technology & Biotechnology 92 (11) (2017) 2799–2807. doi:10.1002/jctb.5358.

[102] L. Rolinger, M. Rüdt, J. Diehm, J. Chow-Hubbertz, M. Heitmann, S. Schleper, J. Hubbuch, Multi-attribute PAT for UF/DF of Proteins—Monitoring Concentration, particle sizes, and Buffer Exchange, Analytical and Bioanalytical Chemistry 412 (9) (2020) 2123–2136. doi:10.1007/s00216-019-02318-8.

[103] B. A. Patel, A. Gospodarek, M. Larkin, S. A. Kenrick, M. A. Haverick, N. Tugcu, M. A. Brower, D. D. Richardson, Multi-angle light scattering as a process analytical technology measuring real-time molecular weight for downstream process control, mAbs 10 (7) (2018) 945–950. doi:10.1080/19420862.2018.1505178.

[104] F. Feidl, S. Garbellini, M. F. Luna, S. Vogg, J. Souquet, H. Broly, M. Morbidelli, A. Butté, Combining Mechanistic Modeling and Raman Spectroscopy for Monitoring Antibody Chromatographic Purification, Processes 7 (10) (2019) 683. doi:10.3390/pr7100683.

[105] Y. Chen, O. Yang, C. Sampat, P. Bhalode, R. Ramachandran, M. Ierapetritou, Digital Twins in Pharmaceutical and Biopharmaceutical Manufacturing: A Literature Review, Processes 8 (9) (2020) 1088. doi:10.3390/pr8091088.

[106] J. Wang, J. Chen, J. Studts, G. Wang, Simultaneous prediction of 16 quality attributes during protein A chromatography using machine learning based Raman spectroscopy models, Biotechnology and Bioengineering 121 (5) (2024) 1729–1738. doi:10.1002/bit.28679.

[107] J. Chen, J. Wang, R. Hess, G. Wang, J. Studts, M. Franzreb, Application of Raman spectroscopy during pharmaceutical process development for determination of critical quality attributes in Protein A chromatography, Journal of Chromatography A 1718 (2024) 464721. doi:10.1016/j.chroma.2024.464721.

[108] S. Bhattacharya, S. Joshi, A. S. Rathore, A native multi-dimensional monitoring workflow for at-line characterization of mAb titer, size, charge, and glycoform heterogeneities in cell culture supernatant, Journal of Chromatography A 1696 (2023) 463983. doi:10.1016/j.chroma.2023.463983.

[109] I. Apostol, P. V. Bondarenko, D. Ren, D. J. Semin, C.-H. Wu, Z. Zhang, C. T. Goudar, Enabling development, manufacturing, and regulatory approval of biotherapeutics through advances in mass spectrometry, Current Opinion in Biotechnology 71 (2021) 206–215. doi:10.1016/j.copbio.2021.08.001.

[110] I. A. Kaltashov, G. Wang, S. Wang, Mass Spectrometry in Biopharmaceutical Analysis, De Gruyter, 2021. doi:10.1515/9783110546187.
URL https://www.degruyter.com/document/doi/10.1515/9783110546187/html

[111] S. Banerjee, S. Mazumdar, Electrospray Ionization Mass Spectrometry: A Technique to Access the Information beyond the Molecular Weight of the Analyte, International Journal of Analytical Chemistry 2012 (1) (2012) 282574. doi:10.1155/2012/282574.

[112] S. Rogstad, A. Faustino, A. Ruth, D. Keire, M. Boyne, J. Park, A Retrospective Evaluation of the Use of Mass Spectrometry in FDA Biologics License Applications, Journal of the American Society for Mass Spectrometry 28 (5) (2017) 786–794. doi:10.1007/s13361-016-1531-9.

[113] S. C. Nanita, L. G. Kaldon, Emerging flow injection mass spectrometry methods for high-throughput quantitative analysis, Analytical and Bioanalytical Chemistry 408 (1) (2016) 23–33. doi:10.1007/s00216-015-9193-1.

[114] G. Wu, C. Yu, S. Yin, J. Du, Y. Zhang, Z. Fu, L. Wang, J. Wang, A native SEC-MS workflow and validation for analyzing drug-to-antibody ratio and drug load distribution in cysteine-linked antibody-drug conjugates, Journal of Chromatography B 1241 (2024) 124167. doi:10.1016/j.jchromb.2024.124167.

[115] K. Muneeruddin, J. J. Thomas, P. A. Salinas, I. A. Kaltashov, Characterization of Small Protein Aggregates and Oligomers Using Size Exclusion Chromatography with Online Detection by Native Electrospray Ionization Mass Spectrometry, Analytical Chemistry 86 (21) (2014) 10692–10699. doi:10.1021/ac502590h.

[116] Y. Lyubarskaya, K. Kobayashi, P. Swann, Application of mass spectrometry to facilitate advanced process controls of biopharmaceutical manufacture, Pharmaceutical Bioprocessing 3 (4) (2015) 313–321. doi:10.4155/pbp.15.10.

[117] M. Scigelova, M. Hornshaw, A. Giannakopulos, A. Makarov, Fourier Transform Mass Spectrometry, Molecular & Cellular Proteomics 10 (7). doi:10.1074/mcp.M111.009431.

[118] A. El-Aneed, A. Cohen, J. Banoub, Mass Spectrometry, Review of the Basics: Electrospray, MALDI, and Commonly Used Mass Analyzers, Applied Spectroscopy Reviews 44 (3) (2009) 210–230. doi:10.1080/05704920902717872.

[119] M. N. São Pedro, M. E. Klijn, M. H. Eppink, M. Ottens, Process analytical technique (PAT) miniaturization for monoclonal antibody aggregate detection in continuous downstream processing, Journal of Chemical Technology & Biotechnology 97 (9) (2022) 2347–2364. doi:10.1002/jctb.6920.

[120] M. Maier, L. Weiß, N. Zeh, V. Schmieder-Todtenhaupt, A. Dehghani, M. N. Felix, D. Heinzelmann, B. Lindner, M. Schmidt, J. Studts, P. Schulz, B. Reisinger, K. Otte, M. Franzreb, D. Lakatos, S. Fischer, Illuminating a biologics development challenge: systematic characterization of CHO cell-derived hydrolases identified in monoclonal antibody formulations, mAbs 16 (1) (2024) 2375798. doi:10.1080/19420862.2024.2375798.

[121] C. Heuer, J.-A. Preuß, T. Habib, A. Enders, J. Bahnemann, 3D printing in biotechnology—An insight into miniaturized and microfluidic systems for applications from cell culture to bioanalytics, Engineering in Life Sciences 22 (12) (2022) 744–759. doi:10.1002/elsc.202100081.

[122] C. W. Hull, S. Gabriel, Apparatus for production of three-dimensional objects by stereolithography, US4575330A (1986).
URL https://patents.google.com/patent/US4575330A/en?oq={US4575330A}

[123] S. Bechtold, 3D Printing, Intellectual Property and Innovation Policy, IIC - International Review of Intellectual Property and Competition Law 47 (5) (2016) 517–536. doi:10.1007/s40319-016-0487-4.

[124] S. F. Iftekar, A. Aabid, A. Amir, M. Baig, Advancements and Limitations in 3D Printing Materials and Technologies: A Critical Review, Polymers 15 (11) (2023) 2519. doi:10.3390/polym15112519.

[125] A. A. Demircali, D. Yilmaz, A. Yilmaz, O. Keskin, M. Keshavarz, H. Uvet, Enhancing mechanical properties and surface quality of FDM-printed ABS: A comprehensive study on cold acetone vapor treatment, The International Journal of Advanced Manufacturing Technology 130 (7) (2024) 4027–4039. doi:10.1007/s00170-023-12929-2.

[126] M. Qamar Tanveer, G. Mishra, S. Mishra, R. Sharma, Effect of infill pattern and infill density on mechanical behaviour of FDM 3D printed Parts- a current review, Materials Today: Proceedings 62 (2022) 100–108. doi:10.1016/j.matpr.2022.02.310.

[127] R. B. Kristiawan, F. Imaduddin, D. Ariawan, Ubaidillah, Z. Arifin, A review on the fused deposition modeling (FDM) 3D printing: Filament processing, materials, and printing parameters, Open Engineering 11 (1) (2021) 639–649. doi:10.1515/eng-2021-0063.

[128] C. Yang, X. Tian, D. Li, Y. Cao, F. Zhao, C. Shi, Influence of thermal processing conditions in 3D printing on the crystallinity and mechanical properties of PEEK material, Journal of Materials Processing Technology 248 (2017) 1–7. doi:10.1016/j.jmatprotec.2017.04.027.

[129] B. I. Oladapo, S. A. Zahedi, S. O. Ismail, F. T. Omigbodun, 3D printing of PEEK and its composite to increase biointerfaces as a biomedical material- A review, Colloids and Surfaces B: Biointerfaces 203 (2021) 111726. doi:10.1016/j.colsurfb.2021.111726.

[130] Y. Wang, Y. Wang, C. Mao, D. Mei, Printing depth modeling, printing process quantification and quick-decision of printing parameters in micro-vat polymerization, Materials & Design 227 (2023) 111698. doi:10.1016/j.matdes.2023.111698.

[131] I. Turkyilmaz, G. N. Wilkins, 3D printing in dentistry – Exploring the new horizons, Journal of Dental Sciences 16 (3) (2021) 1037–1038. doi:10.1016/j.jds.2021.04.004.

[132] Z. Dong, H. Cui, H. Zhang, F. Wang, X. Zhan, F. Mayer, B. Nestler, M. Wegener, P. A. Levkin, 3D printing of inherently nanoporous polymers via polymerization-induced phase separation, Nature Communications 12 (1) (2021) 247. doi:10.1038/s41467-020-20498-1.

[133] F. Kotz, K. Arnold, W. Bauer, D. Schild, N. Keller, K. Sachsenheimer, T. M. Nargang, C. Richter, D. Helmer, B. E. Rapp, Three-dimensional printing of transparent fused silica glass, Nature 544 (7650) (2017) 337–339. doi:10.1038/nature22061.

[134] G. Varghese, M. Moral, M. Castro-García, J. J. López-López, J. R. Marín-Rueda, V. Yagüe-Alcaraz, L. Hernández-Afonso, J. C. Ruiz-Morales, J. Canales-Vázquez, Fabrication and characterisation of ceramics via low-cost DLP 3D printing, Boletín de la Sociedad Española de Cerámica y Vidrio 57 (1) (2018) 9–18. doi:10.1016/j.bsecv.2017.09.004.

[135] Y. Jia, C. A. Spiegel, J. Diehm, D. Zimmermann, B. Huber, H. Mutlu, M. Franzreb, M. Wilhelm, P. Théato, E. Blasco, M. Tsotsalas, Investigating Dynamic Changes in 3D-Printed Covalent Adaptable Polymer Networks, Macromolecular Materials and Engineering 309 (9) (2024) 2300438. doi:10.1002/mame.202300438.

[136] M. Conti, J. A. Symington, J. R. Pullen, R. Mravljak, A. Podgornik, S. Dimartino, Porous Platform Inks for Fast and High-Resolution 3D Printing of Stationary Phases for Downstream Processing, Advanced Materials Technologies 8 (19) (2023) 2300801. doi:10.1002/admt.202300801.

[137] J. R. Tumbleston, D. Shirvanyants, N. Ermoshkin, R. Janusziewicz, A. R. Johnson, D. Kelly, K. Chen, R. Pinschmidt, J. P. Rolland, A. Ermoshkin, E. T. Samulski, J. M. DeSimone, Continuous liquid interface production of 3D objects, Science 347 (6228) (2015) 1349–1352. doi:10.1126/science.aaa2397.

[138] R. Janusziewicz, J. R. Tumbleston, A. L. Quintanilla, S. J. Mecham, J. M. DeSimone, Layerless fabrication with continuous liquid interface production, Proceedings of the National Academy of Sciences 113 (42) (2016) 11703–11708. doi:10.1073/pnas.1605271113.

[139] M. Rafiee, R. D. Farahani, D. Therriault, Multi-Material 3D and 4D Printing: A Survey, Advanced Science 7 (12) (2020) 1902307. doi:10.1002/advs.201902307.

[140] A. K. Au, W. Huynh, L. F. Horowitz, A. Folch, 3D-Printed Microfluidics, Angewandte Chemie International Edition 55 (12) (2016) 3862–3881. doi:https://doi.org/10.1002/anie.201504382.

[141] S. Waheed, J. M. Cabot, N. P. Macdonald, T. Lewis, R. M. Guijt, B. Paull, M. C. Breadmore, 3D printed microfluidic devices: enablers and barriers, Lab on a Chip 16 (11) (2016) 1993–2013. doi:10.1039/C6LC00284F.

[142] L. Wang, M. Pumera, Recent advances of 3D printing in analytical chemistry: Focus on microfluidic, separation, and extraction devices, TrAC Trends in Analytical Chemistry 135 (2021) 116151. doi:10.1016/j.trac.2020.116151.

[143] D. J. Cocovi-Solberg, M. Rosende, M. Michalec, M. Miró, 3D Printing: The Second Dawn of Lab-On-Valve Fluidic Platforms for Automatic (Bio)Chemical Assays, Analytical Chemistry 91 (1) (2019) 1140–1149. doi:10.1021/acs.analchem.8b04900.

[144] G. M. Whitesides, The origins and the future of microfluidics, Nature 442 (7101) (2006) 368–373. doi:10.1038/nature05058.

[145] J. K. Hamilton, M. T. Bryan, A. D. Gilbert, F. Y. Ogrin, T. O. Myers, A new class of magnetically actuated pumps and valves for microfluidic applications, Scientific Reports 8 (1) (2018) 933. doi:10.1038/s41598-018-19506-8.

[146] A. Mansoorifar, A. Tahayeri, L. E. Bertassoni, Bioinspired reconfiguration of 3D printed microfluidic hydrogels via automated manipulation of magnetic inks, Lab on a Chip 20 (10) (2020) 1713–1719. doi:10.1039/D0LC00280A.

[147] M. Nadgorny, Z. Xiao, C. Chen, L. A. Connal, Three-Dimensional Printing of pH-Responsive and Functional Polymers on an Affordable Desktop Printer, ACS Applied Materials & Interfaces 8 (42) (2016) 28946–28954. doi:10.1021/acsami.6b07388.

[148] S. E. Bakarich, R. Gorkin, M. i. h. Panhuis, G. M. Spinks, 4D Printing with Mechanically Robust, Thermally Actuating Hydrogels, Macromolecular Rapid Communications 36 (12) (2015) 1211–1217. doi:https://doi.org/10.1002/marc.201500079.

[149] A. K. Au, N. Bhattacharjee, L. F. Horowitz, T. C. Chang, A. Folch, 3D-printed microfluidic automation, Lab on a Chip 15 (8) (2015) 1934–1941. doi:10.1039/C5LC00126A.

[150] Y.-S. Lee, N. Bhattacharjee, A. Folch, 3D-printed Quake-style microvalves and micropumps, Lab on a Chip 18 (8) (2018) 1207–1214. doi:10.1039/C8LC00001H.

[151] C. I. Rogers, K. Qaderi, A. T. Woolley, G. P. Nordin, 3D printed microfluidic devices with integrated valves, Biomicrofluidics 9 (1) (2015) 016501. doi:10.1063/1.4905840.

[152] D. H. Kang, N. K. Kim, S.-W. Park, W. Lee, H. W. Kang, A microfluidic circuit consisting of individualized components with a 3D slope valve for automation of sequential liquid control, Lab on a Chip 20 (23) (2020) 4433–4441. doi:10.1039/D0LC00501K.

[153] F. Momeni, S. M.Mehdi Hassani.N, X. Liu, J. Ni, A review of 4D printing, Materials & Design 122 (2017) 42–79. doi:10.1016/j.matdes.2017.02.068.

[154] E. Wilhelm, C. Richter, B. Rapp, Phase change materials in microactuators: Basics, applications and perspectives, Sensors and Actuators A: Physical 271 (2018) 303–347. doi:10.1016/j.sna.2018.01.043.

[155] H. Chu, W. Yang, L. Sun, S. Cai, R. Yang, W. Liang, H. Yu, L. Liu, 4D Printing: A Review on Recent Progresses, Micromachines 11 (9) (2020) 796. doi:10.3390/mi11090796.

[156] K. Morioka, H. Sato, K. Morita, H. Akihide, H. Nakajima, A. Shoji, A. Yanagida, Development of an on-chip sample injection system with a 6-port valve incorporated in a microchip, RSC Advances 10 (59) (2020) 35848–35855. doi:10.1039/D0RA07043B.

[157] C.-K. Su, S.-C. Hsia, Y.-C. Sun, Three-dimensional printed sample load/inject valves enabling online monitoring of extracellular calcium and zinc ions in living rat brains, Analytica Chimica Acta 838 (2014) 58–63. doi:10.1016/j.aca.2014.06.037.

[158] H. N. Chan, Y. Shu, B. Xiong, Y. Chen, Y. Chen, Q. Tian, S. A. Michael, B. Shen, H. Wu, Simple, Cost-Effective 3D Printed Microfluidic Components for Disposable, Point-of-Care Colorimetric Analysis, ACS Sensors 1 (3) (2016) 227–234. doi:10.1021/acssensors.5b00100.

[159] A. S. Munshi, C. Chen, A. D. Townsend, R. S. Martin, Use of 3D printing and modular microfluidics to integrate cell culture, injections and electrochemical analysis, Analytical Methods 10 (27) (2018) 3364–3374. doi:10.1039/C8AY00829A.

[160] R. Gundelfinger, Two position rotary valve for injecting sample liquids into an analysis system, US4068528A (1978).
URL https://patents.google.com/patent/US4068528A/en?q=Rheodyne&assignee=Rheodyne%2c+Llc&sort=old

[161] S. R. Bakalyar, R. E. Sylvester, Sample injector, US4182184A (1980).
URL https://patents.google.com/patent/US4182184A/en?q=Rheodyne&assignee=Rheodyne%2c+Llc&sort=old

[162] S. R. Bakalyar, Injector with minimal flow-interrupt transient, US4506558A (4506558A).

[163] E. Mattio, F. Robert-Peillard, L. Vassalo, C. Branger, A. Margaillan, C. Brach-Papa, J. Knoery, J.-L. Boudenne, B. Coulomb, 3D-printed lab-on-valve for fluorescent determination of cadmium and lead in water, Talanta 183 (2018) 201–208. doi:10.1016/j.talanta.2018.02.051.

[164] G. Poll, Dichtungen, in: B. Sauer (Ed.), Konstruktionselemente des Maschinenbaus 2, Springer Berlin Heidelberg, Berlin, Heidelberg, 2018, pp. 195–234. doi:10.1007/978-3-642-39503-1_3.
URL http://link.springer.com/10.1007/978-3-642-39503-1_3

[165] M. T. Guler, P. Beyazkilic, C. Elbuken, A versatile plug microvalve for microfluidic applications, Sensors and Actuators A: Physical 265 (2017) 224–230. doi:10.1016/j.sna.2017.09.001.

[166] Amersham Pharmacia Biotech, Instructions Valve INV-907 (Oct. 2021).
URL https://btiscience.org/wp-content/uploads/2014/04/Valve_Instructions.pdf

[167] R. Flitney, M. W. Brown, Seals and sealing handbook, 5th Edition, Elsevier/Butterworth-Heinemann, Oxford ; Burlington, MA, 2007.

[168] L. Sooväli, E.-I. Rõõm, A. Kütt, I. Kaljurand, I. Leito, Uncertainty sources in UV-Vis spectrophotometric measurement, Accreditation and Quality Assurance 11 (5) (2006) 246–255. doi:10.1007/s00769-006-0124-x.

[169] A. Jungbauer, Continuous downstream processing of biopharmaceuticals, Trends in Biotechnology 31 (8) (2013) 479–492. doi:10.1016/j.tibtech.2013.05.011.

[170] A. S. Rathore, H. Agarwal, A. K. Sharma, M. Pathak, S. Muthukumar, Continuous Processing for Production of Biopharmaceuticals, Preparative Biochemistry & Biotechnology 45 (8) (2015) 836–849. doi:10.1080/10826068.2014.985834.

[171] F. Feidl, S. Vogg, M. Wolf, M. Podobnik, C. Ruggeri, N. Ulmer, R. Wälchli, J. Souquet, H. Broly, A. Butté, M. Morbidelli, Process-wide control and automation of an integrated continuous manufacturing platform for antibodies, Biotechnology and Bioengineering 117 (5) (2020) 1367–1380. doi:https://doi.org/10.1002/bit.27296.

[172] A. C. Fisher, M.-H. Kamga, C. Agarabi, K. Brorson, S. L. Lee, S. Yoon, The Current Scientific and Regulatory Landscape in Advancing Integrated Continuous Biopharmaceutical Manufacturing, Trends in Biotechnology 37 (3) (2019) 253–267. doi:10.1016/j.tibtech.2018.08.008.

[173] R.-M. Nicoud, The Amazing Ability of Continuous Chromatography To Adapt to a Moving Environment, Industrial & Engineering Chemistry Research 53 (10) (2014) 3755–3765. doi:10.1021/ie5005866.

[174] M. Wellhoefer, W. Sprinzl, R. Hahn, A. Jungbauer, Continuous processing of recombinant proteins: Integration of refolding and purification using simulated moving bed size-exclusion chromatography with buffer recycling, Journal of Chromatography A 1337 (2014) 48–56. doi:10.1016/j.chroma.2014.02.016.

[175] J. Andersson, B. Mattiasson, Simulated moving bed technology with a simplified approach for protein purification: Separation of lactoperoxidase and lactoferrin from whey protein concentrate, Journal of Chromatography A 1107 (1) (2006) 88–95. doi:10.1016/j.chroma.2005.12.018.

[176] J. Strube, F. Grote, J. P. Josch, R. Ditz, Process Development and Design of Downstream Processes, Chemie Ingenieur Technik 83 (7) (2011) 1044–1065. doi:10.1002/cite.201100017.

[177] J. F. Buyel, R. Fischer, Scale-down models to optimize a filter train for the downstream purification of recombinant pharmaceutical proteins produced in tobacco leaves, Biotechnology Journal 9 (3) (2014) 415–425. doi:10.1002/biot.201300369.

[178] T. Tajsoleiman, L. Mears, U. Krühne, K. V. Gernaey, S. Cornelissen, An Industrial Perspective on Scale-Down Challenges Using Miniaturized Bioreactors, Trends in Biotechnology 37 (7) (2019) 697–706. doi:10.1016/j.tibtech.2019.01.002.

[179] H. J. Subramani, A. S. Kurup, Micro-simulated moving bed (µSMB) systems: A numerical study, Chemical Engineering Journal 120 (3) (2006) 169–179. doi:10.1016/j.cej.2006.04.002.

[180] J. W. Baier, R. C. Mierendorf, A. C. Grabski, A. P. Wilke, A. R. Oroskar, Valve module and methods for simulated moving bed chromatography, US8807164B2 (2014).
URL https://patents.google.com/patent/US8807164B2/en

[181] R. T. Sprague, G. P. Towler, A. R. Oroskar, Miniature actual moving bed assembly, US6979402B1 (2005).
URL https://patents.google.com/patent/US6979402B1/en

[182] A. R. Oroskar, S. P. Parikh, A. A. Oroskar, K. U. Johnson, A. J. Escarcega, Valve and process for interrupted continuous flow chromatography, US7544293B2 (2009).
URL https://patents.google.com/patent/US7544293B2/en

[183] M. Pedeferri, G. Zenoni, M. Mazzotti, M. Morbidelli, Experimental analysis of a chiral separation through simulated moving bed chromatography, Chemical Engineering Science 54 (17) (1999) 3735–3748. doi:10.1016/S0009-2509(99)00031-7.

[184] T. Kröber, M. W. Wolff, B. Hundt, A. Seidel-Morgenstern, U. Reichl, Continuous purification of influenza virus using simulated moving bed chromatography, Journal of Chromatography A 1307 (2013) 99–110. doi:10.1016/j.chroma.2013.07.081.

[185] A. Rodrigues, Simulated Moving Bed Technology: Principles, Design and Process Applications, Butterworth-Heinemann, 2015.

[186] K. Hashimoto, S. Adachi, Y. Shirai, Continuous Desalting of Proteins with a Simulated Moving-bed Adsorber, Agricultural and Biological Chemistry 52 (9) (1988) 2161–2167. doi:10.1080/00021369.1988.10869005.

[187] A. G. Rios, A. M. Ribeiro, A. E. Rodrigues, A. F. P. Ferreira, Bovine serum albumin and myoglobin separation by size exclusion SMB, Journal of Chromatography A 1628 (2020) 461431. doi:10.1016/j.chroma.2020.461431.

[188] Y. Xie, S. Mun, J. Kim, N.-H. Wang, Standing Wave Design and Experimental Validation of a Tandem Simulated Moving Bed Process for Insulin Purification, Biotechnology Progress 18 (6) (2002) 1332–1344. doi:10.1021/bp025547r.

[189] Tosoh, Octave 12 Pump (Sep. 2022).
URL https://sembabio.com/octave-12-pump-chromatography/

[190] Sartorius, BioSMB PD (Sep. 2022).
URL https://www.sartorius.com/en/products/process-chromatography/chromatography-systems/continuous-chromatography/biosmb-pd

[191] K. B. Lynch, A. Chen, S. Liu, Miniaturized high-performance liquid chromatography instrumentation, Talanta 177 (2018) 94–103. doi:10.1016/j.talanta.2017.09.016.

[192] L. Li, X. Wang, Q. Pu, S. Liu, Advancement of electroosmotic pump in microflow analysis: A review, Analytica Chimica Acta 1060 (2019) 1–16. doi:10.1016/j.aca.2019.02.004.

[193] W. Zeng, S. Li, Z. Wang, Characterization of syringe-pump-driven versus pressure-driven microfluidic flows, in: 2015 International Conference on Fluid Power and Mechatronics (FPM), 2015, pp. 711–715. doi:10.1109/FPM.2015.7337207.

[194] N. Mavrogiannis, M. Ibo, X. Fu, F. Crivellari, Z. Gagnon, Microfluidics made easy: A robust low-cost constant pressure flow controller for engineers and cell biologists, Biomicrofluidics 10 (3) (2016) 034107. doi:10.1063/1.4950753.

[195] J. Knoška, L. Adriano, S. Awel, K. R. Beyerlein, O. Yefanov, D. Oberthuer, G. E. Peña Murillo, N. Roth, I. Sarrou, P. Villanueva-Perez, M. O. Wiedorn, F. Wilde, S. Bajt, H. N. Chapman, M. Heymann, Ultracompact 3D microfluidics for time-resolved structural biology, Nature Communications 11 (1) (2020) 657. doi:10.1038/s41467-020-14434-6.

[196] M. Minceva, A. E. Rodrigues, Influence of the Transfer Line Dead Volume on the Performance of an Industrial Scale Simulated Moving Bed for p-Xylene Separation, Separation Science and Technology 38 (7) (2003) 1463–1497. doi:10.1081/SS-120019088.

[197] W. Jin, P. C. Wankat, Thermal Operation of Four-Zone Simulated Moving Beds, Industrial & Engineering Chemistry Research 46 (22) (2007) 7208–7220. doi:10.1021/ie070047u.

[198] P. S. Gomes, M. Zabkova, M. Zabka, M. Minceva, A. E. Rodrigues, Separation of chiral mixtures in real SMB units: The FlexSMB-LSRE®, AIChE Journal 56 (1) (2010) 125–142. doi:10.1002/aic.11962.

[199] V. Gnyawali, M. Saremi, M. C. Kolios, S. S. H. Tsai, Stable microfluidic flow focusing using hydrostatics, Biomicrofluidics 11 (3) (2017) 034104. doi:10.1063/1.4983147.

[200] R. Bermejo, F. Gabriel Acién, M. J. Ibáñez, J. M. Fernández, E. Molina, J. M. Alvarez-Pez, Preparative purification of B-phycoerythrin from the microalga Porphyridium cruentum by expanded-bed adsorption chromatography, Journal of Chromatography B 790 (1) (2003) 317–325. doi:10.1016/S1570-0232(03)00168-5.

[201] J. G. Ziegler, N. B. Nichols, Optimum Settings for Automatic Controllers, Journal of Dynamic Systems, Measurement, and Control 115 (2B) (1993) 220–222. doi:10.1115/1.2899060.

[202] R. Qin, C. Duan, The principle and applications of Bernoulli equation, Journal of Physics: Conference Series 916 (2017) 012038. doi:10.1088/1742-6596/916/1/012038.

[203] A. Podgornik, Pressure drop in liquid chromatography, Journal of Separation Science 42 (1) (2019) 72–88. doi:10.1002/jssc.201800882.

[204] S. Leweke, E. von Lieres, Chromatography Analysis and Design Toolkit (CADET), Computers & Chemical Engineering 113 (2018) 274–294. doi:10.1016/j.compchemeng.2018.02.025.

[205] Q.-L. He, S. Leweke, E. von Lieres, Efficient numerical simulation of simulated moving bed chromatography with a single-column solver, Computers & Chemical Engineering 111 (2018) 183–198. doi:10.1016/j.compchemeng.2017.12.022.

[206] A. Püttmann, S. Schnittert, U. Naumann, E. von Lieres, Fast and accurate parameter sensitivities for the general rate model of column liquid chromatography, Computers & Chemical Engineering 56 (2013) 46–57. doi:10.1016/j.compchemeng.2013.04.021.

[207] A. Püttmann, S. Schnittert, S. Leweke, E. von Lieres, Utilizing algorithmic differentiation to efficiently compute chromatograms and parameter sensitivities, Chemical Engineering Science 139 (2016) 152–162. doi:10.1016/j.ces.2015.08.050.

[208] I. of Bio-and Geosciences 1 (IBG-1) of Forschungszentrum Jülich, General rate model (GRM) — CADET.
URL https://cadet.github.io/master/modelling/unit_operations/general_rate_model.html

[209] S. F. Chung, C. Y. Wen, Longitudinal dispersion of liquid flowing through fixed and fluidized beds, AIChE Journal 14 (6) (1968) 857–866. doi:10.1002/aic.690140608.

[210] E. J. Wilson, C. J. Geankoplis, Liquid Mass Transfer at Very Low Reynolds Numbers in Packed Beds, Industrial & Engineering Chemistry Fundamentals 5 (1) (1966) 9–14. doi:10.1021/i160017a002.

[211] C. N. Satterfield, C. K. Colton, W. H. Pitcher Jr., Restricted diffusion in liquids within fine pores, AIChE Journal 19 (3) (1973) 628–635. doi:10.1002/aic.690190332.

[212] C. Chen, B. T. Mehl, A. S. Munshi, A. D. Townsend, D. M. Spence, R. Scott Martin, 3D-printed microfluidic devices: fabrication, advantages and limitations—a mini review, Analytical Methods 8 (31) (2016) 6005–6012. doi:10.1039/C6AY01671E.

[213] S. V. Luis, E. García-Verdugo, Chemical Reactions and Processes Under Flow Conditions, Royal Society of Chemistry, 2010.

[214] W. Xie, G. Pedrielli, From Discovery to Production: Challenges and Novel Methodologies for Next Generation Biomanufacturing, in: 2022 Winter Simulation Conference (WSC), 2022, pp. 238–252, iSSN: 1558-4305. doi:10.1109/WSC57314.2022.10015464.

[215] N. Lingg, P. Zhang, Z. Song, M. Bardor, The sweet tooth of biopharmaceuticals: Importance of recombinant protein glycosylation analysis, Biotechnology Journal 7 (12) (2012) 1462–1472. doi:10.1002/biot.201200078.

[216] V. Dotz, R. Haselberg, A. Shubhakar, R. P. Kozak, D. Falck, Y. Rombouts, D. Reusch, G. W. Somsen, D. L. Fernandes, M. Wuhrer, Mass spectrometry for glycosylation analysis of biopharmaceuticals, TrAC Trends in Analytical Chemistry 73 (2015) 1–9. doi:10.1016/j.trac.2015.04.024.

[217] F. Füssl, K. Cook, K. Scheffler, A. Farrell, S. Mittermayr, J. Bones, Charge Variant Analysis of Monoclonal Antibodies Using Direct Coupled pH Gradient Cation Exchange Chromatography to High-Resolution Native Mass Spectrometry, Analytical Chemistry 90 (7) (2018) 4669–4676. doi:10.1021/acs.analchem.7b05241.

[218] J. Dai, J. Lamp, Q. Xia, Y. Zhang, Capillary Isoelectric Focusing-Mass Spectrometry Method for the Separation and Online Characterization of Intact Monoclonal Antibody Charge Variants, Analytical Chemistry 90 (3) (2018) 2246–2254. doi:10.1021/acs.analchem.7b04608.

[219] B. Kükrer, V. Filipe, E. van Duijn, P. T. Kasper, R. J. Vreeken, A. J. R. Heck, W. Jiskoot, Mass Spectrometric Analysis of Intact Human Monoclonal Antibody Aggregates Fractionated by Size-Exclusion Chromatography, Pharmaceutical Research 27 (10) (2010) 2197–2204. doi:10.1007/s11095-010-0224-5.

[220] D. D. Vallejo, C. K. Jeon, K. F. Parson, H. R. Herderschee, J. D. Eschweiler, D. I. Filoti, B. T. Ruotolo, Ion Mobility–Mass Spectrometry Reveals the Structures and Stabilities of Biotherapeutic Antibody Aggregates, Analytical Chemistry 94 (18) (2022) 6745–6753. doi:10.1021/acs.analchem.2c00160.

[221] R. Disela, O. L. Bussy, G. Geldhof, M. Pabst, M. Ottens, Characterisation of the E. coli HMS174 and BLR host cell proteome to guide purification process development, Biotechnology Journal n/a (n/a) (2023) 2300068. doi:10.1002/biot.202300068.

[222] R. Kufer, M. Haindl, H. Wegele, S. Wohlrab, Evaluation of Peptide Fractionation and Native Digestion as Two Novel Sample Preparation Workflows to Improve HCP Characterization by LC–MS/MS, Analytical Chemistry 91 (15) (2019) 9716–9723. doi:10.1021/acs.analchem.9b01259.

[223] F. Yang, D. E. Walker, J. Schoenfelder, J. Carver, A. Zhang, D. Li, R. Harris, J. T. Stults, X. C. Yu, D. A. Michels, A 2D LC-MS/MS Strategy for Reliable Detection of 10-ppm Level Residual Host Cell Proteins in Therapeutic Antibodies, Analytical Chemistry 90 (22) (2018) 13365–13372. doi:10.1021/acs.analchem.8b03044.

[224] L. Wang, S. Zeng, T. Chen, H. Qu, Direct analysis in real time mass spectrometry, a process analytical technology tool for real-time process monitoring in botanical drug manufacturing, Journal of Pharmaceutical and Biomedical Analysis 91 (2014) 202–209. doi:10.1016/j.jpba.2013.12.034.

[225] B. Yan, T. Chen, Z. Xu, H. Qu, Rapid process development of chromatographic process using direct analysis in real time mass spectrometry as a process analytical technology tool, Journal of Pharmaceutical and Biomedical Analysis 94 (2014) 106–110. doi:10.1016/j.jpba.2014.01.033.

[226] A. Venter, M. Nefliu, R. Graham Cooks, Ambient desorption ionization mass spectrometry, TrAC Trends in Analytical Chemistry 27 (4) (2008) 284–290. doi:10.1016/j.trac.2008.01.010.

[227] J. H. Gross, Direct analysis in real time—a critical review on DART-MS, Analytical and Bioanalytical Chemistry 406 (1) (2014) 63–80. doi:10.1007/s00216-013-7316-0.

[228] I.-F. Shieh, C.-Y. Lee, J. Shiea, Eliminating the Interferences from TRIS Buffer and SDS in Protein Analysis by Fused-Droplet Electrospray Ionization Mass Spectrometry, Journal of Proteome Research 4 (2) (2005) 606–612. doi:10.1021/pr049765m.

[229] C.-T. Chien, F.-A. Li, J.-L. Huang, G.-R. Her, CE-MS of antihistamines using nonvolatile phosphate buffer, ELECTROPHORESIS 28 (9) (2007) 1454–1460. doi:10.1002/elps.200600542.

[230] J. Diehm, T. Ballweg, M. Franzreb, Development of a 3D printed micro simulated moving bed chromatography system, Journal of Chromatography A 1695 (2023) 463928. doi:10.1016/j.chroma.2023.463928.

[231] G. Brenner-Weiss, F. Kirschhöfer, B. Kühl, M. Nusser, U. Obst, Analysis of non-covalent protein complexes by capillary electrophoresis–time-of-flight mass spectrometry, Journal of Chromatography A 1009 (1) (2003) 147–153. doi:10.1016/S0021-9673(03)00553-3.

[232] I. K. Ventouri, D. B. A. Malheiro, R. L. C. Voeten, S. Kok, M. Honing, G. W. Somsen, R. Haselberg, Probing Protein Denaturation during Size-Exclusion Chromatography Using Native Mass Spectrometry, Analytical Chemistry 92 (6) (2020) 4292–4300. doi:10.1021/acs.analchem.9b04961.

[233] J. Diehm, V. Hackert, M. Franzreb, Configurable 3D Printed Microfluidic Multiport Valves with Axial Compression, Micromachines 12 (10) (2021) 1247. doi:10.3390/mi12101247.

[234] A. Polson, The Some Aspects of Diffusion in Solution and a Definition of a Colloidal Particle., The Journal of Physical and Colloid Chemistry 54 (5) (1950) 649–652. doi:10.1021/j150479a007.

[235] V. Katta, B. T. Chait, Observation of the heme-globin complex in native myoglobin by electrospray-ionization mass spectrometry, Journal of the American Chemical Society 113 (22) (1991) 8534–8535. doi:10.1021/ja00022a058.

[236] J. Zaia, R. S. Annan, K. Biemann, The correct molecular weight of myoglobin, a common calibrant for mass spectrometry, Rapid Communications in Mass Spectrometry 6 (1) (1992) 32–36. doi:10.1002/rcm.1290060108.

[237] K. Sugiyama, R. Highet, A. Woods, R. Cotter, Y. Osawa, Hydrogen peroxide-mediated alteration of the heme prosthetic group of metmyoglobin to an iron chlorin product: Evidence for a novel oxidative pathway, Proceedings of the National Academy of Sciences of the United States of America 94 (1997) 796–801. doi:10.1073/pnas.94.3.796.

[238] M. Beccaria, D. Cabooter, Current developments in LC-MS for pharmaceutical analysis, Analyst 145 (4) (2020) 1129–1157. doi:10.1039/C9AN02145K.

[239] O. Ötes, H. Flato, J. Winderl, J. Hubbuch, F. Capito, Feasibility of using continuous chromatography in downstream processing: Comparison of costs and product quality for a hybrid process vs. a conventional batch process, Journal of Biotechnology 259 (2017) 213–220. doi:10.1016/j.jbiotec.2017.07.001.

[240] T. C. Silva, M. Eppink, M. Ottens, Automation and miniaturization: enabling tools for fast, high-throughput process development in integrated continuous biomanufacturing, Journal of Chemical Technology & Biotechnology 97 (9) (2022) 2365–2375. doi:10.1002/jctb.6792.

[241] J. Diehm, L. Witting, F. Kirschhöfer, G. Brenner-Weiß, M. Franzreb, Micro simulated moving bed chromatography-mass spectrometry as a continuous on-line process analytical tool, Analytical and Bioanalytical Chemistrydoi:10.1007/s00216-023-05023-9.

[242] J. M. Breuer, S. Leweke, J. Schmölder, G. Gassner, E. von Lieres, Spatial discontinuous Galerkin spectral element method for a family of chromatography models in CADET, Computers & Chemical Engineering 177 (2023) 108340. doi:10.1016/j.compchemeng.2023.108340.

[243] L. K. Shekhawat, A. S. Rathore, An overview of mechanistic modeling of liquid chromatography, Preparative Biochemistry & Biotechnology 49 (6) (2019) 623–638. doi:10.1080/10826068.2019.1615504.

[244] K. Baran, W. K. Marek, W. Piątkowski, D. Antos, Effect of flow behavior in extra-column volumes on the retention pattern of proteins in a small column, Journal of Chromatography A 1598 (2019) 154–162. doi:10.1016/j.chroma.2019.03.060.

[245] D. Iurashev, S. Schweiger, A. Jungbauer, J. Zanghellini, Dissecting peak broadening in chromatography columns under non-binding conditions, Journal of Chromatography A 1599 (2019) 55–65. doi:10.1016/j.chroma.2019.03.065.

[246] E. von Lieres, J. Wang, M. Ulbricht, Model Based Quantification of Internal Flow Distributions from Breakthrough Curves of Flat Sheet Membrane Chromatography Modules, Chemical Engineering & Technology 33 (6) (2010) 960–968. doi:10.1002/ceat.200900614.

[247] Y. Qu, I. Baker, J. Black, L. Fabri, S. L. Gras, A. M. Lenhoff, S. E. Kentish, Application of mechanistic modelling in membrane and fiber chromatography for purification of biotherapeutics — A review, Journal of Chromatography A 1716 (2024) 464588. doi:10.1016/j.chroma.2023.464588.

[248] G. I. Taylor, Dispersion of soluble matter in solvent flowing slowly through a tube, Proceedings of the Royal Society of London. Series A. Mathematical and Physical Sciences 219 (1137) (1953) 186–203. doi:10.1098/rspa.1953.0139.

[249] R. Aris, G. I. Taylor, On the dispersion of a solute in a fluid flowing through a tube, Proceedings of the Royal Society of London. Series A. Mathematical and Physical Sciences 235 (1200) (1997) 67–77. doi:10.1098/rspa.1956.0065.

[250] A. Shankar, A. M. Lenhoff, Dispersion in round tubes and its implications for extracolumn dispersion, Journal of Chromatography A 556 (1) (1991) 235–248. doi:10.1016/S0021-9673(01)96224-7.

[251] W. Dean, Note on the motion of fluid in a curved pipe, The London, Edinburgh, and Dublin Philosophical Magazine and Journal of Science 4 (20) (1927) 208–223. doi:10.1080/14786440708564324.

[252] J. Beck, W. Heymann, E. von Lieres, R. Hahn, Compartment Model of Mixing in a Bubble Trap and Its Impact on Chromatographic Separations, Processes 8 (7) (2020) 780. doi:10.3390/pr8070780.

[253] J. G. Albright, J. P. Mitchell, D. G. Miller, Interdiffusion coefficients, densities, and refractive indices of ammonium chloride + water and ammonium sulfate + water at 25.degree.C, Journal of Chemical & Engineering Data 39 (1) (1994) 195–200. doi:10.1021/je00013a055.

[254] R. Mohan, O. Kaytancioglu, A. S. Myerson, Diffusion and cluster formation in supersaturated solutions of ammonium sulfate at 298K, Journal of Crystal Growth 217 (4) (2000) 393–403. doi:10.1016/S0022-0248(00)00528-5.

[255] J. G. Atwood, M. J. E. Golay, Dispersion of peaks by short straight open tubes in liquid chromatography systems, Journal of Chromatography A 218 (1981) 97–122. doi:10.1016/S0021-9673(00)82050-6.

[256] G. Desmet, K. Broeckhoven, Extra-column band broadening effects in contemporary liquid chromatography: Causes and solutions, TrAC Trends in Analytical Chemistry 119 (2019) 115619. doi:10.1016/j.trac.2019.115619.

[257] F. Gritti, A. Felinger, G. Guiochon, Influence of the errors made in the measurement of the extra-column volume on the accuracies of estimates of the column efficiency and the mass transfer kinetics parameters, Journal of Chromatography A 1136 (1) (2006) 57–72. doi:10.1016/j.chroma.2006.09.074.

[258] S. Schweiger, A. Jungbauer, Scalability of pre-packed preparative chromatography columns with different diameters and lengths taking into account extra column effects, Journal of Chromatography A 1537 (2018) 66–74. doi:10.1016/j.chroma.2018.01.022.

[259] J. P. C. Vissers, Recent developments in microcolumn liquid chromatography, Journal of Chromatography A 856 (1) (1999) 117–143. doi:10.1016/S0021-9673(99)00692-5.

[260] D. Sýkora, F. Svec, J. M. J. Fréchet, Separation of oligonucleotides on novel monolithic columns with ion-exchange functional surfaces, Journal of Chromatography A 852 (1) (1999) 297–304. doi:10.1016/S0021-9673(99)00004-7.

[261] T. Scientific, ProSwift Ion-Exchange Monolith Columns for Protein Analysis (Jan. 2025). URL https://assets.fishersci.com/TFS-Assets/CMD/Specification-Sheets/65843-DS-ProSwift-IEX-29Mar2010-LPN2020-02.pdf

[262] Sartorius, CIMmultus® SO3 4 mL Monolithic Column (2 µm) | Chromatography Monoliths | Sartorius eShop (Jan. 2025). URL https://shop.sartorius.com/de/p/cimmultus-so3-4-ml-monolithic-column-2-m/414.6157-2#

[263] N. P. Dinh, Q. M. Cam, A. M. Nguyen, A. Shchukarev, K. Irgum, Functionalization of epoxy-based monoliths for ion exchange chromatography of proteins, Journal of Separation Science 32 (15-16) (2009) 2556–2564. doi:10.1002/jssc.200900243.

[264] E. G. Vlakh, T. B. Tennikova, Preparation of methacrylate monoliths, Journal of Separation Science 30 (17) (2007) 2801–2813. doi:10.1002/jssc.200700284.

[265] H. Shirahama, K. Suzuki, T. Suzawa, Bovine hemoglobin adsorption onto polymer latices, Journal of Colloid and Interface Science 129 (2) (1989) 483–490. doi:10.1016/0021-9797(89)90462-1.

[266] S. Devineau, K.-i. Inoue, R. Kusaka, S.-h. Urashima, S. Nihonyanagi, D. Baigl, A. Tsuneshige, T. Tahara, Change of the isoelectric point of hemoglobin at the air/water interface probed by the orientational flip-flop of water molecules, Physical Chemistry Chemical Physics 19 (16) (2017) 10292–10300. doi:10.1039/C6CP08854F.

List of Publications

PhD-Related Publications

Diehm, J., Achauer, D., Franzreb M. Integration of capillary chromatography columns into a 3D-printed microfluidic multiport valve for miniaturized multi-column chromatography, *J. Chromatogr. A* 1760, 466245 (2025).

Diehm, J., Franzreb M. Modeling the extra column volume of a micro simulated moving bed chromatography system: Introducing the equivalent radial flow rate distribution, *J. Chromatogr. A* 1740, 465543 (2025).

Diehm, J., Witting, L., Kirschhöfer, F. et al. Micro simulated moving bed chromatography-mass spectrometry as a continuous on-line process analytical tool. *Anal Bioanal Chem* 416, 373–386 (2024).

Diehm, J., Ballweg, T., Franzreb M. Development of a 3D printed micro simulated moving bed chromatography system, *J. Chromatogr. A* 1695, 463928 (2023).

Diehm, J., Hackert, V., Franzreb, M. Configurable 3D Printed Microfluidic Multiport Valves with Axial Compression. *Micromachines* 12, 1247 (2021).

Conference Contributions

Diehm, J., Franzreb, M. Integration of Capillary Chromatography Columns into a 3D-Printed Microfluidic Multiport Valve for Miniaturized Multi-Column Chromatography *20th International PhD Seminar on Chromatographic Separation Science (SoCSS 2025)*, Munich (DE) – Presentation.

Diehm, J., Franzreb, M. Efficient Simulation of Extra Column Volume in Small-Scale Multi-Column Chromatography. *Recovery of Biological Products (RXX 2024)*, Sun River, Oregon (US) – Poster.

Diehm, J., Franzreb, M. Modeling of Extra Column Volume in Small-Scale Multi-Column Chromatography Systems. *19th International PhD Seminar on Chromatographic Separation Science (SoCSS 2024)*, Lund (SE) – Presentation.

Diehm, J., Franzreb, M. Efficient Simulation of 3D Dead Volumes of Chromatography Systems by 2D Simulation with Equivalent Radial Flow Distribution. *15th Mediterranean Congress of Chemical Engineering (MECCE 2023)*, Barcelona (ES) – Presentation (Keynote Lecture).

Diehm, J., Witting, L., Kirschhöfer, F. et al. Micro-Simulated Moving Bed Chromatography – Mass Spectrometry (µSMB-MS): Continuous On-line Sample Preparation for Process Analytical Technology. *EuroPACT (2023)*, Copenhagen (DK) – Presentation.

Diehm, J., Witting, L., Kirschhöfer, F. et al. Simulated Moving Bed Chromatography – Mass Spectrometry (SMB-MS): Continuous On-line Sample Preparation for Process Analytical Technology. *18th International Symposium on Preparative and Industrial Chromatography and Allied Techniques (SPICA 2022)*, Lisbon (PT) – Presentation and Poster (Best Poster Award).

Diehm, J., Witting, L., Kirschhöfer, F. et al. On-line Simulated Moving Bed Chromatography –Continuous Sample Preparation for Mass Spectrometry as Process Analytical Tool. *Recovery of Biological Products (RXIX 2022)*, Rome (IT) – Poster

Diehm, J., Ballweg, T., Hackert, V. et al. Development of a 3D Printed Micro SMB Device as Process Analytical Tool. *40th International Symposium on the Purification of Proteins, Peptides and Polynucleotides (ISPPP 2021)*, Porto (PT) – Presentation.

Diehm, J., Hackert, V., Franzreb, M. Development of a Micro Simulated Moving Bed System. *16th International PhD Seminar on Chromatographic Separation Science (SoCSS 2020/21)*, Vienna (AT) – Presentation.

Diehm, J., Hohmann, S., Hackert, V., et al. Development of 3D printed rotatory microfluidic valves for the application of an analytical micro SMB device. *IS2M annual meetings (2019)*, Mulhouse (FR) – Poster.

Diehm, J., Hohmann, S., Brenner-Weiß, G., et al. Development of a rotatory microfluidic multiport valve using 3D printing technologies for application of an analytical micro SMB device. *ANAKON (2019)*, Münster (DE) – Poster.

Patent Applications

Diehm, J., Meutelet, R., Franzreb M. Functional Microvalve DE102022100987A1 / WO2023135046A1 (2023).

Additional Publications

Jia, Y., Spiegel, C. A., Diehm, J. et al. Investigating Dynamic Changes in 3D-Printed Covalent Adaptable Polymer Networks. *Macromol. Mater. Eng.* 309, 2300438 (2024).

Rolinger, L., Rüdt, M., Diehm, J. et al. Multi-attribute PAT for UF/DF of Proteins—Monitoring Concentration, particle sizes, and Buffer Exchange. *Anal Bioanal Chem* 412, 2123–2136 (2020).

Fraas, R., Hübner, J.F., Diehm, J. et al. A Compartmented Microfluidic Reactor for Protein Modification Via Solid-phase Reactions — Semi-automated Examination of Two PEGylation Routes. *Biotechnol Bioproc E* 24, 382–394 (2019).

Fraas, R., Diehm, J., Franzreb, M. Automated Solid-Phase Protein Modification with Integrated Enzymatic Digest for Reaction Validation: Application of a Compartmented Microfluidic Reactor for Rapid Optimization and Analysis of Protein Biotinylation. *Front. Bioeng. Biotechnol.* 5, 72 (2017).